

**Fundamental Studies of Combustion of Droplet and Vapour  
Mixtures**

by

Aminuddin Saat

Submitted in accordance with the requirements for the degree of  
Doctor of Philosophy

The University of Leeds  
School of Mechanical Engineering

November 2010

This copy has been supplied on the understanding that it is copyright material and  
that no quotation from the thesis may be published without proper  
acknowledgement.

## **Intellectual Property and Publication Statements**

The candidate confirms that the work submitted is his own, except where work which has formed part of jointly-authored publications has been included. The contribution of the candidate and the other authors to this work has been explicitly indicated below. The candidate confirms that appropriate credit has been given within the thesis where reference has been made to the work of others.

1. Sections 5.3 and 6.4 of this thesis is based on a jointly-authored conference paper: Lawes, M. and Saat, A., "Burning rate enhancement in the explosion of isooctane and air aerosols", Proceedings of the Sixth International Seminar on Fire and Explosion Hazards, April 2010, Paper No. 126, Leeds, UK. The candidate undertook major tasks of the work presented in this paper, such as undertaking experimental works, analysing and presenting the results. Being a supervisor of the candidate, Dr. Malcolm Lawes guided the candidate throughout the process and providing valuable discussion.
2. Sections 5.5 and 6.5 of this thesis is based on a jointly-authored journal paper: Lawes, M. and Saat, A., "Burning rates of turbulent isooctane aerosol mixtures in spherical flame explosions", Proceedings of the Combustion Institute, 2011, 33 (2), 2047-2054. Similar to the previous paper, the candidate performed major tasks including experimental works, analysing and presenting the results. Dr. Malcolm Lawes helped the candidate by providing valuable discussion throughout the publication process.

## **Acknowledgements**

I would like to express my sincere thanks to Dr. Malcolm Lawes, for his support, guidance and motivation throughout this study. I would also like to thank him for his constructive criticisms during the preparation of this thesis. My thanks are also forward to Prof. Derek Bradley, Dr. Alexey Burluka and Prof. Chris Sheppard for their discussion and valuable advice in my work.

My thanks are due to John Groves, Brian Leach, Mark Batchelor and Ron Cellier from the Thermodynamics Laboratory for their support and assistance during the preparation of the experimental work. Also thanks to Fiona Slade and C. McLaughlin for their help in arranging my meetings with supervisor.

Many thanks are also due to all combustion group members: Navanshu Tripathi, Markous Mansour, Allaa Dawood, Pascal Nicholas, Shaharin Sulaiman, Matthew Harker, Phil Roberts, Tawfiq Al-Mughanam, Ahmed Eldein Hussin, Ibrahim Mohamed, Luay Zayed, Ahmed Faraz, Graham Conwy and all the other colleagues for their friendship and assistance throughout the period of research.

The financial and moral support from Universiti Teknologi Malaysia and Ministry of Higher Education Malaysia throughout the period of this study is gratefully acknowledged.

Finally, I would like to express my thanks to my parents for their endless encouragement, and to my wife and children for their understanding and support throughout the study.

## Abstract

There are few experimental data of a fundamental nature that clearly demonstrate the similarities and differences in burning rates between single phase and two phase combustion, either in laminar or turbulent conditions. Such data are essential towards a better understanding of the spray combustion phenomena as well as a whole system. In the present study, experimental investigations of combustion of droplet and vapour air mixtures under quiescent and turbulence conditions have been conducted in a fan stirred combustion vessel. Aerosols were generated by expansion of gaseous pre-mixture to produce a homogeneously distributed suspension of fuel droplets. Spherically expanding flames following central ignition were employed to quantify the flame structure and propagation rate. The effect of droplets on flame propagation was investigated by comparing the burning rate of gaseous mixtures at initial pressure and temperature close to those of aerosol mixtures.

In quiescent conditions, aerosols of two different fuels, isooctane and ethanol, were investigated at near atmospheric conditions. The effect of fuel droplets, up to 31  $\mu\text{m}$  diameter, on laminar flame propagation was examined at a wide range of equivalence ratios. In the early stages of flame development, inertia of fuel droplets leads to local enrichment in equivalence ratio which increases the initial burning rate of lean aerosols but decreases that of rich ones. For the later stages of flame propagation, the presence of liquid droplets causes earlier onset of instabilities and cellularity than for gaseous flames, particularly at rich conditions. This leads to an enhanced burning rate and is probably due to heat loss from the flame and local disturbances due to droplet evaporation and subsequent diffusion processes.

In turbulent studies, the effect of isooctane droplets up to 14  $\mu\text{m}$  in diameter on flame propagation was examined at various values of root mean square turbulence velocities between zero and 4.0 m/s. It is suggested that during early flame development, the turbulence was found to induce droplet motion before flame initiation which dominated over those resulting from the flame, negating the effect of droplet inertia. In the later stages, the presence of droplets in a low turbulent flame resulted in a significant burning rate enhancement. However, this enhancement became progressively less important as turbulent wrinkling became dominant. Between low and high turbulence, there was a transition regime between instability dominated and turbulence dominated regimes. As a consequence, the burning rate enhancement due to droplets under this transition range was rather complex.

## Contents

<b>Intellectual Property and Publication Statements .....</b>	<b>ii</b>
<b>Acknowledgements.....</b>	<b>iii</b>
<b>Abstract.....</b>	<b>iv</b>
<b>Contents .....</b>	<b>v</b>
<b>List of Figures.....</b>	<b>viii</b>
<b>List of Tables .....</b>	<b>xv</b>
<b>Nomenclature.....</b>	<b>xvi</b>
<b>Chapter 1 Introduction.....</b>	<b>1</b>
1.1 General introduction.....	1
1.2 Objectives of the present study.....	2
1.3 Thesis outline .....	3
<b>Chapter 2 Review of Droplet Combustion.....</b>	<b>5</b>
2.1 Introduction .....	5
2.2 Applications and challenges in droplet combustion.....	5
2.3 Premixed combustion and burning rate.....	7
2.3.1 Laminar flames .....	7
2.3.2 Instabilities in laminar flames.....	12
2.3.3 Turbulent flames .....	17
2.4 Droplet generation.....	19
2.5 Droplet characterisation .....	20
2.6 Studies of droplet combustion.....	23
2.6.1 Group combustion modes .....	23
2.6.2 Laminar combustion .....	25
2.6.3 Instabilities in aerosol flame .....	26
2.6.4 Oscillating flames .....	27
2.6.5 Turbulent combustion .....	28
<b>Chapter 3 Experimental Apparatus and Techniques.....</b>	<b>39</b>
3.1 Introduction .....	39
3.2 Combustion apparatus .....	39
3.2.1 Explosion vessel .....	40
3.2.2 Expansion vessel.....	41
3.2.3 Ignition system.....	42
3.2.3.1 Fixed energy ignition unit.....	42

3.2.3.2	Variable energy ignition unit .....	42
3.3	Mixture preparation.....	43
3.3.1	Fuels.....	44
3.3.2	Pre-heating of explosion vessel .....	44
3.3.3	Preparation of gaseous pre-mixtures.....	45
3.3.4	Generation of aerosol.....	45
3.4	Data acquisition and synchronisation.....	46
3.5	Instrumentation for aerosol characterisation and flame analysis.....	47
3.5.1	Phase Doppler Anemometry (PDA).....	47
3.5.2	Laser attenuation system .....	49
3.5.3	High speed schlieren photography .....	50
3.5.3.1	Image recording .....	50
3.5.3.2	Image processing .....	51
<b>Chapter 4</b>	<b>Characterisation of Aerosol Mixtures.....</b>	<b>57</b>
4.1	Introduction .....	57
4.2	Determination of aerosol properties.....	57
4.2.1	Gas phase equilibrium.....	58
4.2.2	Mass fraction and equivalence ratio.....	59
4.3	Pressure and temperature variation .....	63
4.3.1	Initially quiescent conditions .....	63
4.3.2	Turbulent conditions .....	64
4.4	Droplet size distribution.....	64
4.4.1	Initially quiescent conditions .....	65
4.4.2	Turbulent conditions .....	66
4.5	Droplet number density.....	67
4.5.1	Initially quiescent conditions .....	67
4.5.2	Turbulent conditions .....	68
4.6	Effect of particles on aerosol formation.....	69
4.7	Summary of aerosol characterisation .....	70
<b>Chapter 5</b>	<b>Flame Observations and Burning Rates.....</b>	<b>88</b>
5.1	Introduction .....	88
5.2	Observations of laminar iso-octane-air flames.....	88
5.2.1	Flame development with different ignition systems .....	88
5.2.2	Ignition.....	89
5.2.3	Aerosol and gaseous flame development.....	90
5.3	Laminar burning rates in iso-octane-air mixtures .....	92
5.3.1	Flame speed development of gaseous mixtures.....	92

5.3.2	Aerosol flame speed and comparisons with gaseous flames .....	92
5.3.3	Flames with early onset of instabilities.....	95
5.3.4	Markstein length and unstretched burning velocity.....	95
5.3.5	Oscillating flames .....	97
5.4	Turbulent flame observations.....	98
5.4.1	Ignition.....	98
5.4.2	Aerosol and gaseous flame development.....	98
5.5	Turbulent burning rates in isooctane-air mixture.....	101
5.5.1	Flame speed development in gaseous mixtures.....	101
5.5.2	Aerosol flame speed and comparisons with gaseous flames ..	101
5.6	Burning rates of quiescent ethanol aerosol mixtures.....	103
5.6.1	Flame observations .....	103
5.6.2	Burning rates of laminar gaseous and aerosol mixtures.....	104
<b>Chapter 6</b>	<b>Discussions .....</b>	<b>137</b>
6.1	Introduction .....	137
6.2	Effect of ignition unit on comparisons with previous work.....	137
6.3	Evaporation of droplets in laminar and turbulent flames.....	139
6.4	Effect of droplets on laminar flames .....	141
6.4.1	Early stage of flame propagation .....	142
6.4.2	Later stage of flame propagation.....	144
6.4.3	Instabilities in aerosol flames.....	145
6.4.4	Unstretched burning velocity of isooctane and ethanol aerosols .....	148
6.5	Effect of droplets on turbulent flames.....	149
6.5.1	Early stage propagation.....	149
6.5.2	Later stage propagation .....	150
<b>Chapter 7</b>	<b>Conclusions and Suggestions .....</b>	<b>168</b>
7.1	Conclusions .....	168
7.2	Suggestions for further work.....	172
<b>References</b>	<b>.....</b>	<b>175</b>

## List of Figures

Figure 2.1: Measured flame speeds of stoichiometric iso-octane-air with initial temperature of 358 K and pressure of 100 kPa at different flame radii. Reproduced from Bradley <i>et al.</i> (1998). .....	32
Figure 2.2: Variation of flame speed with flame stretch for stoichiometric methane-air at 500 kPa and 300 K. Reproduced from Gu <i>et al.</i> (2000). .....	32
Figure 2.3: Schematic of a planar flame situated in a divergent stagnation flow.....	33
Figure 2.4: Comparison of flame structure using schlieren images between a (a) smooth flame and (b) cellular flame. Reproduced from Mandilas (2008). .....	33
Figure 2.5: Schematic diagram of the hydrodynamic instability mechanism. Reproduced from Law (1988). .....	34
Figure 2.6: Schematic diagram of the thermo-diffusive instability mechanism. Reproduced from Law (2006). .....	34
Figure 2.7: Conceptual diagrams of the effects of stretch on the flame motion for an expanding spherical flame at (a) $t = 0$ , (b) $t = \delta t$ . Reproduced from Law (2006). .....	35
Figure 2.8: Theoretical wave numbers, $n$ , at limits of flame stability for different $Ma_{sr}$ , as function of Peclet number. Shaded area is a peninsular of instability for $Ma_{sr} = 8$ . Reproduced from Bradley <i>et al.</i> (2000). .....	35
Figure 2.9: Instability peninsula, with limiting wave numbers $fn_i$ , and $n_i$ . Critical Peclet number, $Pe_{cl}$ at tip of peninsula. Reproduced from Al-Shahrany <i>et al.</i> (2005). .....	36
Figure 2.10: Correlation of turbulent burning velocities. Broken curves show $R_L/(Le)^2$ , with $R_L$ evaluated for fully developed r.m.s. turbulent burning velocity, $u'$ , equal to $u'_k$ . Reproduced from Bradley <i>et al.</i> (1992). .....	36
Figure 2.11: Different types of droplet generators. Reproduced from Gökalp <i>et al.</i> (1999). .....	37
Figure 2.12: Variation of burning velocity at different droplet size of stoichiometric medium diesel oil-air sprays. Reproduced from Polymeropoulos (1984).....	37
Figure 2.13: Variation of flame speed with time for oscillating flames of iso-octane-air aerosols at $\phi_{ov} = 0.8$ and $1.0$ . Also shown are oscillation periods. Reproduced from Atzler (1999). .....	38
Figure 2.14: Effect of a variation of $u_D$ on the local $\phi$ and resulting values of $S_n$ , $u_g$ and $u_l$ for aerosol mixture with $\phi_{ov} = 1.0$ and $\phi_g = 0.75$ . Reproduced from Atzler <i>et al.</i> (2001). .....	38



Figure 3.1: Photograph of the cylindrical explosion vessel, with one end plate removed.....	52
Figure 3.2: Schematic of combustion apparatus with schlieren system. Reproduced from Atzler (1999).....	53
Figure 3.3: Circuit diagram for fixed energy ignition unit. Reproduced from Atzler (1999). .....	54
Figure 3.4: Circuit diagram for variable energy ignition unit. Reproduced from Ali (1995). .....	54
Figure 3.5: PDA system and laser attenuation apparatus for aerosol characterisation experiment.....	55
Figure 3.6: Experimental setup for high speed schlieren cine photography.....	55
Figure 3.7: Schematic of control circuit for ignition and schlieren cine photography.....	56
Figure 4.1: Expansion paths for phase change in present work on (a) $P$ - $v$ diagram, and (b) $T$ - $s$ diagram. Reproduced from Sulaiman (2007). .....	74
Figure 4.2: Generalised compressibility chart for low pressure condition. Reproduced from Cengel <i>et al.</i> (1998).....	75
Figure 4.3: Variation of pressure and temperature with time during the expansion of initially quiescent stoichiometric iso-octane and air mixture from 200 kPa and 303 K. ....	75
Figure 4.4: Variation of pressure and temperature with time during expansion of initially quiescent stoichiometric ethanol and air mixture from 200 kPa and 313 K. ....	76
Figure 4.5: Variation of pressure and temperature with time for initially quiescent iso-octane and air mixtures at various $\phi_{ov}$ . All mixtures were expanded from 200 kPa and 303 K.....	76
Figure 4.6: Variation of pressure and temperature with time for stoichiometric turbulent iso-octane and air mixture expanded from 200 kPa and 303 K at $u'$ of 1.0 m/s.....	77
Figure 4.7: Variation of pressure and temperature with time for stoichiometric turbulent iso-octane and air mixtures at various $u'$ . All mixtures were expanded from 200 kPa and 303 K. ....	77
Figure 4.8: Variation of individual and averaged droplet diameter, $D_{10}$ , and standard deviation, $\sigma_D$ , with time for initially quiescent stoichiometric iso-octane and air mixture expanded from 200 kPa and 303 K.....	78
Figure 4.9: Variation of individual and averaged droplet diameter, $D_{10}$ , and standard deviation, $\sigma_D$ , with time for initially quiescent stoichiometric ethanol and air mixture expanded from 200 kPa and 313 K.....	78
Figure 4.10: Spatial variation of individual droplet diameter and $\sigma_D$ with time for stoichiometric iso-octane and air mixture expanded from 250 kPa and	

303 K at six different positions in explosion vessel. Reproduced from Marquez (2003).....	79
Figure 4.11: Variation of $D_{10}$ with time for initially quiescent iso-octane and air mixtures at various $\phi_{ov}$ . All mixtures were expanded from 200 kPa and 303 K.....	79
Figure 4.12: Variation of $D_{10}$ with time for initially quiescent ethanol and air mixtures at various $\phi_{ov}$ . All mixtures were expanded from 200 kPa and 313 K.....	80
Figure 4.13: Variation of $D_{10}$ with time for turbulent iso-octane and air mixtures at various $\phi_{ov}$ . All mixtures were expanded from 200 kPa and 303 K at $u'$ of 1.0 m/s .....	80
Figure 4.14: Variation of $D_{10}$ with time for turbulent stoichiometric iso-octane and air mixtures at various $u'$ . All mixtures were expanded from 200 kPa and 303 K. ....	81
Figure 4.15: Variation of laser power attenuation and droplet number density with time for initially quiescent iso-octane and air mixtures at various $\phi_{ov}$ . All mixtures were expanded from 180 kPa and 303 K. ....	81
Figure 4.16: Variation of laser power attenuation and droplet number density with time for initially quiescent of ethanol and air mixtures at various $\phi_{ov}$ . All mixtures were expanded from 200 kPa and 313 K. ....	82
Figure 4.17: Variation in calculated mass of liquid fuel with time for stoichiometric iso-octane air mixture. Mixture was expanded from initial conditions of 200kPa and 303K. ....	82
Figure 4.18: Variation of laser power attenuation and droplet number density with time for turbulent stoichiometric iso-octane and air mixtures at various $u'$ . All mixtures were expanded from 200 kPa and 303 K. ....	83
Figure 4.19: Variation of pressure and temperature with time during expansion of initially quiescent stoichiometric iso-octane and air mixtures from 200 kPa and 303 K under different mixture preparation conditions.....	83
Figure 4.20: Variation of $D_{10}$ with time for expanded mixtures in Fig. 4.18. ....	84
Figure 4.21: Variation of laser power attenuation and $N_D$ with time for expanded mixtures in Fig. 4.18.....	84
Figure 4.22: Comparison of aerosol generation at different initial pressures: (a) variation of $D_{10}$ with instantaneous pressure and (b) schematic representation of expansion process on a $P$ - $v$ diagram. Stoichiometric iso-octane and air under initially quiescent conditions at initial temperature of 303 K.....	85
Figure 4.23: Comparison of aerosol generation at different initial temperatures: (a) variation of $D_{10}$ with instantaneous pressure and (b) schematic	

representation of expansion on $P$ - $v$ diagram. Stoichiometric ethanol and air under initially quiescent conditions at initial pressure of 200 kPa.....	85
Figure 4.24: Comparison of aerosol generation at different $\phi_{ov}$ : (a) variation of $D_{10}$ with instantaneous pressure and (b) schematic representation of expansion on $P$ - $v$ diagram. Both mixtures were iso-octane and air, expanded from initially quiescent conditions at 200 kPa and 303 K.....	86
Figure 4.25: Comparison of aerosol generation at different types of fuel: (a) variation of $D_{10}$ with instantaneous pressure and (b) schematic representation of expansion on $P$ - $v$ diagram. Both mixtures were expanded from 200 kPa and 313 K at initially quiescent and stoichiometric conditions. ....	86
Figure 4.26: Comparison of aerosol generation at different expansion rates: (a) variation of $D_{10}$ with instantaneous pressure and (b) schematic representation of expansion on $P$ - $v$ diagram. Stoichiometric iso-octane and air under initially quiescent conditions at 200 kPa and 303 K.....	87
Figure 5.1: Comparison of effect of ignition system on laminar flame propagation for gaseous iso-octane-air.....	107
Figure 5.2: Effects of droplets on ignition and initial flame growth of initially quiescent iso-octane-air mixtures, $\phi_{ov}=1.4$ . ....	108
Figure 5.3: Effects of droplets on ignition and initial flame growth of initially quiescent iso-octane-air mixtures, $\phi_{ov}=0.9$ . ....	109
Figure 5.4: Typical development of laminar iso-octane-air flames at $\phi_{ov} = 1.2$ for, (a) gaseous mixture, (b) aerosol at $D_{10} = 5 \mu\text{m}$ and (c) aerosol at $D_{10} = 14 \mu\text{m}$ .....	110
Figure 5.5: Comparison of flame schlieren images at radius approximately 48 mm for gaseous and aerosol .....	111
Figure 5.6: Variation of flame speed with (a) time, (b) radius, for gaseous iso-octane-air mixtures at $\phi_{ov} = 0.9$ , 97 kPa and 279 K. ....	112
Figure 5.7: Variation of flame speed with stretch rate for the gaseous flame in.....	112
Figure 5.8: Variation of flame speed with radius for aerosols iso-octane-air mixture at $D_{10} = 5 \mu\text{m}$ and at $\phi_{ov} = 0.8, 1.0$ and $1.2$ . Also shown for each case are last flame images within field of view of access windows. ....	113
Figure 5.9: Variation of flame speed with stretch rate for aerosol flames in .....	113
Figure 5.10: Variation of flame speed with time and radius for gaseous and aerosol iso-octane-air mixtures at $\phi_{ov} = 0.9, 1.4$ and $2.0$ . ....	114
Figure 5.11: Comparison of $S_{n,48}$ for gaseous and aerosol iso-octane-air at various $\phi_{ov}$ . ....	115
Figure 5.12: Typical variation of flame speed with stretch rate for iso-octane-air mixtures at $\phi_{ov} = 1.4$ for (a) gaseous, (b) aerosol at $D_{10} = 5 \mu\text{m}$ , (c)	

aerosol at $D_{10} = 14 \mu\text{m}$ and (d) aerosol at $D_{10} = 20 \mu\text{m}$ .....	116
Figure 5.13: Effect of fuel droplets on relationship between $\phi_{ov}$ and $L_b$ of iso-octane-air mixtures. ....	117
Figure 5.14: Variation of averaged $u_l$ with $\phi_{ov}$ and $D_{10}$ for iso-octane-air mixtures. ....	117
Figure 5.15: Variation of $u_l$ with $D_{10}$ for iso-octane-air mixtures at $\phi_{ov} = 0.8, 1.0$ and $1.2$ . ....	118
Figure 5.16: Typical variation of flame speed with radius for oscillating flame of iso-octane-air aerosol mixture. Also shown are corresponding schlieren images throughout propagation. ....	119
Figure 5.17: Variation of flame speed with time for iso-octane-air aerosol at $\phi_{ov} = 0.8$ at $D_{10}$ between 0 and 20 $\mu\text{m}$ , pressures between 93 and 120 kPa and temperatures between 263 and 276 K. ....	119
Figure 5.18: Effects of droplets on early stage of flame propagation under turbulent condition, $u' = 0.5 \text{ m/s}$ for iso-octane-air mixtures at $\phi_{ov} = 0.9$ .....	120
Figure 5.19: Effects of droplets on early stage of flame propagation under turbulent condition, $u' = 0.5 \text{ m/s}$ for iso-octane-air .....	121
Figure 5.20: Typical development of turbulent gaseous and aerosol flames propagation at $u' = 0.5 \text{ m/s}$ and $\phi_{ov} = 0.9$ .....	122
Figure 5.21: Typical development of turbulent gaseous and aerosol flames propagation at $u' = 0.5 \text{ m/s}$ and $\phi_{ov} = 1.2$ .....	123
Figure 5.22: Typical development of turbulent gaseous and aerosol flames propagation at $u' = 4.0 \text{ m/s}$ and $\phi_{ov} = 1.2$ . ....	124
Figure 5.23: Typical flame structure at radius approximately 40 mm of turbulent gaseous and aerosol flames at $\phi_{ov} = 0.9$ .....	125
Figure 5.24: Typical flame structure at radius approximately 40 mm of turbulent gaseous and aerosol flames at $\phi_{ov} = 1.2$ .....	126
Figure 5.25: Flame radius against time for turbulent gaseous iso-octane-air at $\phi_{ov} = 1.2, 100 \text{ kPa}, 303 \text{ K}$ and $u'$ of 0.5 and 4.0 m/s. ....	127
Figure 5.26: Variation of $S_l$ with time for turbulent gaseous flames in Fig. 5.25.....	127
Figure 5.27: Variation of $S_l$ with radius for turbulent gaseous flames in Fig. 5.25.....	128
Figure 5.28: Variation of flame speed with time, radius and $u'$ for iso-octane-air gaseous and aerosol mixtures at $\phi_{ov} = 0.9$ .....	129
Figure 5.29: Variation of flame speed with time and radius for iso-octane-air gaseous and aerosol mixtures at $\phi_{ov} = 1.2$ and $u'$ of 0, 0.5 and 1.0 m/s.....	130
Figure 5.30: Variation of flame speed with time and radius for iso-octane-air gaseous and aerosol mixtures at $\phi_{ov} = 1.2$ and $u'$ of 2.0 and 4.0 m/s.....	131
Figure 5.31: Typical development of laminar ethanol-air flames at $\phi_{ov} = 1.2$ for, (a) gaseous mixture, (b) aerosol at $D_{10} = 5 \mu\text{m}$ and (c) aerosol at $D_{10} = 12 \mu\text{m}$ .....	132

Figure 5.32: Comparison of flame schlieren images at radius approximately 48 mm for gaseous and aerosol .....	133
Figure 5.33: Comparison of $S_{n,48}$ for gaseous and aerosol ethanol-air at various $\phi_{ov}$ .....	134
Figure 5.34: Effect of fuel droplets on relationship between $\phi_{ov}$ and $L_b$ of ethanol-air mixtures. ....	134
Figure 5.35: Variation of $u_l$ with $D_{10}$ for ethanol-air mixtures at various $\phi_{ov} = 0.8, 1.0$ and $1.2$ . ....	135
Figure 5.36: Variation of averaged $u_l$ with $\phi_{ov}$ and $D_{10}$ for ethanol-air mixtures. Also shown is the variation of averaged $u_l$ with $\phi_{ov}$ for gaseous iso-octane-air mixtures as in Fig. 5.14. ....	136
Figure 6.1: Natural light imaging of spark ignition in air using fixed energy ignition unit at 100 kPa and 303 K. Reproduced from Sulaiman (2007). ....	154
Figure 6.2: Schlieren image of black clouds in turbulent stoichiometric iso-octane aerosol flame at $u' = 4.0$ m/s, ignited by fixed energy ignition unit. Reproduced from Sulaiman (2007). ....	154
Figure 6.3: Variation of flame speed with time for gaseous isooctane-air mixtures at $\phi_{ov} = 1.2, 100$ kPa and 303 K. ....	155
Figure 6.4: Estimation of droplet lifetime using $D^2$ -law for stoichiometric iso-octane-air aerosol at 100 kPa and 273 K, assuming $T_\infty = 2275$ K. ....	155
Figure 6.5: Illustration of turbulent flame and region ahead of the flame. ....	156
Figure 6.6: A modified Borghi phase diagram showing different regimes in turbulent combustion (Abdel-Gayed <i>et al.</i> , 1989). ....	156
Figure 6.7: Effect of turbulence on estimation of droplet lifetime using $D^2$ -law for stoichiometric iso-octane-air aerosol at 100 kPa and 273 K, assuming $T_\infty = 2275$ K. ....	157
Figure 6.8: Variation of $S_n$ with time during early stage of flame propagation of iso-octane-air mixtures at, (a) fuel-lean mixture, (b) fuel-rich mixture. ....	157
Figure 6.9: Effect of droplet diameter on minimum ignition energy of isooctane sprays. Adapted from Ballal and Lefebvre (1978). ....	158
Figure 6.10: Effect of variation of $u_D$ on local equivalence ratio at reaction zone and resulting values of $S_n$ , $u_g$ and $u_l$ for aerosol mixture at $\phi_{ov} = 1.0$ . Adapted from Atzler <i>et al.</i> (2001). ....	158
Figure 6.11: Gas velocity at a point in space as an unconfined flame propagation past. ....	159
Figure 6.12: Measured and computed gas temperature and velocity for a methane-air flame at 0.16 atm and $\phi = 1.07$ . Reproduced from Bradley <i>et al.</i> (1994). ....	159
Figure 6.13: Computed composition and temperature profiles for stoichiometric methane-air mixture at 1 atm and 300 K. Reproduced from Haq (1998). ....	160

Figure 6.14: Variation of normalised flame speed with $D_{10}$ and $\phi_{ov}$ for isooctane-air aerosol mixtures. ....	160
Figure 6.15: Variation of normalised flame speed with normalised droplet diameter and $\phi_{ov}$ ; solid curves are for isooctane and chain dashed curves are for ethanol. ....	161
Figure 6.16: Variations of $Pe_{cl}$ with $D_{10}$ at different $\phi_{ov}$ for iso-octane-air aerosol flames. ....	161
Figure 6.17: Variations of $Pe_{cl}$ with $Ma_{sr}$ for iso-octane-air aerosol flames. Also shown, curve fit for gaseous flames (Bradley <i>et al.</i> , 2009).....	162
Figure 6.18: Variations of $K_{cl}$ with $Ma_{sr}$ for isooctane-air aerosol flames. Also shown curve fit for gaseous flames (Bradley <i>et al.</i> , 2009).....	162
Figure 6.19: Comparison of laminar flame structure of propane-air mixtures at 60 mm radius, (a) without water, (b) with water aerosol, at $\phi_{ov} = 1.3$ , 105-110 kPa, 260-265 K. Reproduced from Atzler (1999). ....	163
Figure 6.20: Effect of $D_{10}$ on normalised unstretched burning velocity of iso-octane and ethanol aerosol mixtures at stoichiometric condition.....	163
Figure 6.21: Estimation of droplet lifetime using $d^2$ -law for stoichiometric isooctane and ethanol aerosols at 100 kPa and 273 K, assuming $T_{\infty} = 2275$ K.....	164
Figure 6.22: Variation of flame speed with time and $u'$ during early stage of flame propagation of isooctane-air mixtures at $\phi_{ov} = 0.9$ and 1.2. ....	165
Figure 6.23: Variation of flame speed normalisation at a radius of 40 mm with different normalised droplet diameter and $u'$ of isooctane-air mixtures at $\phi_{ov} = 1.2$ . ....	166
Figure 6.24: Variation of flame speed normalisation at a radius of 40 mm with different normalised droplet diameter and $u'$ of isooctane-air mixtures at $\phi_{ov} = 0.9$ . ....	166
Figure 6.25: Variation of flame speed normalisation with normalised droplet diameter, $D_{10}/\delta_l$ as a function of ratio of $u'/u_l$ . ....	167
Figure 6.26: Variation of flame speed normalisation at different ratio of $u'/u_l$ and $D_{10}/\delta_l = 0.11$ .....	167

## List of Tables

Table 2.1: Main characteristics of different droplet generator types. Reproduced from Gökalp <i>et al.</i> (1999). .....	30
Table 2.2: Characteristics of group combustion regimes (Chiu & Liu, 1977). Reproduced from Nakamura <i>et al.</i> (2005). .....	31
Table 4.1: Initial (pre-expansion) conditions for aerosol characterisation experiment in present work. ....	73

## Nomenclature

$\bar{Q}_e$		mean extinction efficiency (laser attenuation)
$\bar{R}$	J/mol.K	universal gas constant
$A$	m <sup>2</sup> , mm <sup>2</sup>	flame area
$B$		Spalding number or transfer number
$c_p$	J kg <sup>-1</sup> K <sup>-1</sup>	specific heat (at constant pressure)
$D$		mass diffusivity, droplet diameter
$D_{10}$	μm	length mean droplet diameter
$D_{20}$	μm	area mean droplet diameter
$D_{32}$	μm	sauter mean droplet diameter
$E$	mJ	discharged ignition energy
$f_u$	Hz	frequency of flow velocity fluctuation
$G$		group combustion number
$gmf$		gas mass fraction
$h$	W m <sup>-2</sup> K <sup>-1</sup>	convective heat transfer coefficient
$I$	A	current
$K$		Karlovitz stretch factor
$k$	W m <sup>-1</sup> K <sup>-1</sup>	thermal conductivity
$K_{cl}$		critical Karlovitz stretch factor
$K_o$		fuel evaporation constant of quiescent mixture
$K_t$		fuel evaporation constant of turbulent mixture
$L$	mm	integral length scale of turbulence
$L_b, L_c, L_{cr},$ $L_s, L_{sr}$	mm	Markstein lengths, as defined
$l_D$	μm	interdrop distance
$Le$		Lewis number
$lmf$		liquid mass fraction
$m$	kg	mass
$M$	kg/kmol	molar mass
$Ma_s, Ma_c,$ $Ma_{sr}, Ma_{cr}$		Markstein number, as defined
$n$		cell wavenumber, number of moles



$N_D$	$m^{-3}$	droplet number density
$n_l$		lower limit wave number
$n_s$		upper limit wave number
$N_T$		total number of droplet in a cluster
$P$	kPa	pressure
$Pe_{cl}$		critical Peclet number for onset of acceleration
$Pe_{cr}$		critical Peclet number for onset of instability
$P_v$	kPa	vapour pressure
$r$	mm	flame radius
$Re$		Reynolds number
$R_L$		turbulent Reynolds number based on the integral length scale
$r_{sch}$	mm	schlieren flame radius
$r_v$	mm	flame radius at which the volume of unburned gas inside a sphere of this radius is equal to the volume of burned gas outside it
$S$		correction factor to account the effect of the flame thickness, see Eq. (2.4)
$s$	kJ/kmol.K	entropy
$Sc$		Schmidt number ( $Sc = \nu/D$ )
$S_n$	m/s	stretched flame speed
$S_{n,48}$	m/s	stretched flame speed at $r \approx 48$ mm
$S_s$	m/s	unstretched flame speed
$S_t$	m/s	turbulent flame speed
$t$	s, ms	time
$T$	K	temperature
$u'$	m/s	root mean square turbulent velocity
$u'_k$	m/s	effective root mean square turbulent velocity
$u_D$	m/s	droplet velocity
$u_g$	m/s	gas velocity
$u_l$	m/s	unstretched burning velocity
$u_n$	m/s	stretched laminar burning velocity, based on rate of disappearance of cold unburned gas
$u_{nr}$	m/s	stretched mass burning velocity, based on rate of appearance of burned gas
$u_t$	m/s	turbulent burning velocity

$V$	V, m <sup>3</sup>	Voltage, volume
$v$	m/kg	specific volume
$Z$		compressibility factor

*Greek symbols*

$\alpha$	s <sup>-1</sup> , ms <sup>-1</sup>	stretch rate, thermal diffusivity
$\rho$	kg m <sup>-3</sup>	density
$\nu$	m <sup>2</sup> /s	kinematic viscosity
$\Lambda$		cell wavelength
$\sigma$		density ratio, $\sigma = \rho_w/\rho_b$
$\lambda$	nm	wave length, Taylor microscale of turbulence
$\phi$		equivalence ratio
$\tau_D$	s	droplet lifetime
$\delta_l$	m	flame thickness
$\omega$	rpm	fan speed
$\sigma_e$	m <sup>2</sup>	extinction cross section (laser attenuation)
$\sigma_D$	μm	standard deviation of droplet diameter
$\gamma$		isentropic expansion index
$\mu$	kgs/m	fluid viscosity

*Subscripts*

$l$	pre-expansion
$2$	during expansion
$a$	air
$b$	burned
$c$	curvature
$D$	droplet
$f$	fuel
$g$	gas
$l$	liquid
$ov$	overall
$r$	reduced
$s$	flow strain

<i>t</i>	turbulent
<i>u</i>	unburned
<i>v</i>	vapour

# Chapter 1

## Introduction

### 1.1 General introduction

The combustion of sprays of droplets has been the subject of research studies for more than five decades. Much work has concentrated on achieving substantial improvements in fuel efficiency of the combustion system, while other research has been directed at complying with environmental issues and stringent emission requirements. Such developments in any practical combustion system always necessitate a better understanding of the combustion process, particularly that dealing with fundamental knowledge. Nevertheless, studies in practical systems are difficult due to the multiplicity of dependent parameters and this is also associated with the complexity of the systems themselves.

In practice, every combustion process occurs in a turbulent environment. However, it is well established that the laminar burning rate plays an important role in turbulent combustion (Bradley *et al.*, 1992). Information on laminar burning rates for fuel sprays and gas-liquid mixtures are still inadequate. There are few experimental data of a fundamental nature that clearly demonstrate the similarities and differences in burning rates, either laminar or turbulent, between single and two-phase combustion (Lawes *et al.*, 2006). Several workers, Ballal and Lefebvre (1981), Nakabe *et al.* (1988) and Richards and Lefebvre (1989), suggested that this was due to the more complex nature of two-phase combustion and the resulting increase in difficulties in experimental as well as theoretical study. Nevertheless, a significant number of fundamental studies related to droplet combustion have been made and these are reviewed in Section 2.6. Under laminar condition, a few studies (Hayashi and Kumagai, 1975; Polymeropoulos, 1984; Greenberg *et al.*, 1998; Nomura *et al.*, 2000) suggested that flame propagation through droplet clouds can be faster than that in fully vapourised homogeneous mixtures. However, under turbulent conditions, there is little fundamental data to show the differences.

Since the important aspects of single droplet combustion have become well understood, fundamental investigation of droplet cloud combustion provided a further approach towards a better understanding of spray combustion systems (Hayashi *et al.*, 1976). Such elementary study is essential in order to enhance our understanding, particularly to provide correct interpretations of the observed phenomena related to spray combustion. As a simple model of spray combustion, idealised systems are needed in which monosized droplets are suspended uniformly in a fuel vapour air mixture. One such system can be realised by employing the principle of the Wilson cloud chamber (as in the present work) in which a fuel vapour becomes supersaturated and some portion of the vapour condenses into droplets.

## 1.2 Objectives of the present study

The general idea that emerges from previous studies on droplet cloud combustion, presented in Section 2.6, was a promotion in the burning rate due to droplets at certain conditions, under both laminar and turbulent conditions. Yet, these studies are limited by the fact that the enhancement in burning rate, although observed by many researchers, was not properly quantified. In the very few cases of experimental study where it was quantified (Nomura *et al.*, 2000; 2007), the size of the flame considered was quite small, leading to ambiguities in transition regimes. Furthermore, there were only a few experimental works (Hayashi *et al.*, 1976; Lawes *et al.*, 2006) that identify the similarities and differences between single phase and two phase combustion. Therefore, in the present study, experimental investigation of spherically propagating flames of droplet and vapour air mixture in a cylindrical, fan stirred combustion apparatus was undertaken. The effect of droplets on flame propagation was investigated by comparing the burning rate of gaseous mixtures at initial pressure and temperature close to those of aerosols at a wide range of equivalence ratios.

The objectives of the present study are:

- to provide fundamental experimental data on the laminar burning characteristics of droplet and vapour air mixtures;
- to quantify the enhancement in burning rates of aerosol and gaseous mixtures at a wide range of equivalence ratios and droplet sizes;

- to investigate the effect of fine droplets during two stages of flame propagation: early and later stage propagation, under laminar and turbulent conditions.

### 1.3 Thesis outline

An essential prerequisite for the study of droplet clouds combustion is an understanding of the experimental concepts and theoretical descriptions of gaseous pre-mixed combustion under laminar and turbulent conditions. Those important concepts for the present study are presented in Chapter 2. A number of important studies related to droplet clouds and aerosol combustion are also described in this chapter, together with some practical applications. Of particular interest are the works on experimental and theoretical study which found the burning rate promotion of aerosol combustion at a particular range of conditions. The experimental apparatus and techniques involved in the present study are presented in Chapter 3. The combustion vessel consists of two vessels, with the main one fitted with optical access to allow observation during flame development. It was equipped with fans which allowed combustion experiments in a controlled turbulent environment and for mixture preparation. Aerosols were generated using the Wilson cloud chamber principle (Wilson, 1897), which produced a homogeneous spatial droplet distribution and nearly monosized droplets across the vessel. The mixture, generated under laminar and turbulent conditions, was characterised using laser diagnostic techniques to obtain the droplet size and the number density of fuel droplets. Simultaneously, pressure and temperature were also recorded and used as a basis to calculate aerosol properties. Characterisation results are presented in Chapter 4. Also in Chapter 4, there is a brief description of factors that influence aerosol formation.

Results from laminar and turbulent combustion are presented in Chapter 5. At each condition, all results were presented in terms of flame observations and burning rates measurements. For each experiment, details of flame propagation during the early and later stages are presented. The effects of several parameters on flame propagation was investigated. These include the overall equivalence ratio, droplet diameter and rms turbulence velocity. Variations of burning rates at a wide range of conditions were presented to demonstrate the differences between gaseous and aerosol combustion. Chapter 6 discusses the results. These include the observations

of flame development, possible mechanisms of burning rate enhancement, the mechanism of flame instability and the determination of unstretched burning velocity. The effect of turbulence on aerosol flames is also discussed in this Chapter. Finally, Chapter 7 summarises the outcomes of the present work and gives recommendations for further work.

## **Chapter 2**

### **Review of Droplet Combustion**

#### **2.1 Introduction**

Droplet combustion has relevance to many practical combustion devices. These varied applications have led to numerous studies of both spray combustion and associated processes, such as droplet atomisation and evaporation. Such studies are important in order to establish criteria for designing an efficient and reliable system with due regard to the environment. This chapter presents a review of droplet combustion studies and their applications. Section 2.2 presents an overview of some of the practical applications of droplet combustion and the recent trends in their development. In Section 2.3, a brief review of the burning rate of homogeneous mixtures is presented, since this forms the foundation for the present study. This includes the phenomenon of laminar flame instability and a brief description of turbulent burning velocity. In order to study droplet, or aerosol, combustion, it is necessary to understand the underlying principles of droplet generation. Thus, a review of droplet generation techniques is described in Section 2.4, followed by that of droplet characterisation in Section 2.5. Finally, a review of previous work related to the combustion of droplet and vapour mixtures under laminar and turbulent conditions is presented in Section 2.6.

#### **2.2 Applications and challenges in droplet combustion**

Droplet combustion is of practical importance in a wide range of technological applications that include automotive engines, gas turbines, power generation, furnaces, boiler and space heating. However, there are several phenomena relating to the burning of droplets that are still not fully understood due to the complexity of practical spray combustion systems. The following descriptions present an overview of some of the practical applications of droplet combustion and the recent challenges which draw interest for the present study.



In relation to automotive engines, much of the combustion-related research has been dedicated to combining the trends in increasing power and fuel economy with the minimisation of noxious emissions such as carbon monoxide, nitric oxides and particulates. Traditionally, automotive engines can be classified into gasoline engines and diesel engines (Heywood, 1988). In terms of mixture introduction and combustion, gasoline engines can be sub-divided into port-fuel-injected, PFI, homogeneous-charge-compression-ignition, HCCI, and gasoline-direct-injection, GDI (Zhao *et al.*, 1999). PFI and HCCI engines use homogeneous mixtures, and therefore are not relevant to the present study. In GDI engines, fuel is introduced in two modes, namely early injection for homogeneous charge operation at full loads and late injection for stratified charge operation under part loads (Lee *et al.*, 2002). Stratified charge is a possible technique for increasing engine efficiency because a relatively rich mixture is required for ignition close to spark gap but a lean mixture is required elsewhere for increased thermal efficiency (Zhao *et al.*, 1999). However, a stratified charge may result in a heterogeneous mixture of droplets and vapour due to the limited time available between the required late fuel injection and ignition (Zhao *et al.*, 1999). As a result, there is a possibility of fine fuel droplets in the reaction zone. Therefore, understanding the effect of fuel droplets on flame propagation has become essential.

In aero-engines, the combustion process involves the burning of a fuel spray in air. Different from automotive engines, the combustion occurs in a continuous mode rather than intermittent and the typical operating droplet sizes ranges to a few hundred microns (Lefebvre, 1989). A crucial criterion of an aero-engine is its ignition performance (Mokhtar, 2001) at a wide range of operating conditions that range from normal start to altitude relight at which the pressure and temperature are very low. In the event of flame extinction at altitudes above which the low pressure and temperature prevents successful ignition, it would be necessary to reduce altitude before re-igniting combustion (Liou *et al.*, 1994; Lefebvre, 1989). Several investigations have focused in this area to understand the behavior of the ignition (Tian-Yu *et al.*, 1981; Mokhtar, 2001). Mokhtar (2001) suggested that the use of laser ignition could be a potential solution to this problem. However, it would probably take another decade before an appropriate lightweight laser system is applicable for application in aircraft. Nevertheless, the relighting issue in aero-engines is a complex process and is still not fully understood.

The combustion processes mentioned above are carefully controlled and efficient, and effective combustion is a requirement. Conversely, an accidental ignition of any flammable fuel vapour or vapour-droplet mixture, perhaps after an accidental spillage, may have serious consequences in terms of damage to plant and injury or death. The aim of research in this area is to understand the combustion process in order to assess more accurately risk and potential consequences as well as to provide recommendations that minimise such dangers. The potential explosion hazard created from flammable gases has been much discussed (Rasbash, 1979; Shebeko *et al.*, 1995) but the hazards generated from releases of two-phase liquid vapour mixtures often have been underestimated (Bowen and Cameron, 1999). Yet, there is evidence, theoretical (Polymeropoulos, 1984; Greenberg *et al.*, 1999) and experimental (Hayashi and Kumagai, 1975; Myers and Lefebvre, 1986; Nomura *et al.*, 2000), to suggest that aerosol explosions may, under certain circumstances, burn faster than those of homogeneous mixtures. Clearly, this can result in disastrous consequences in the hazards context. Several incidents of explosions which were believed to be of two-phase air-fuel mixtures (HSE, 1975; 2008) draw the need for understanding the contributing mechanism and also for explosion mitigation.

### **2.3 Premixed combustion and burning rate**

A necessary precursor to the understanding of droplet combustion is to understand the combustion of premixed gaseous mixtures. Several workers, Ballal and Lefebvre (1981), Polymeropoulos (1984) and Lawes *et al.* (2006), used the theoretical description of premixed flames to estimate and calculate the burning rates in two-phase combustion. Hayashi and Kumagai (1975) suggested that the investigation of premixed flames at similar conditions to those for droplet combustion is essential to understand the effect of droplets on flame propagation in two-phase environments. The following sections present a brief review of the burning rate of homogeneous gaseous mixtures, under laminar and turbulent conditions.

#### **2.3.1 Laminar flames**

Premixed laminar burning rates have been derived from spherical expanding flames technique with central ignition (Lewis and Von Elbe, 1987; Bradley *et al.*,

1998). This technique is well established for premixed flames and has also been used previously for aerosol flame studies (Atzler, 1999; Marquez, 2003; Sulaiman, 2007). The velocity of the spherical flame front, also known as the stretched flame speed,  $S_n$ , is calculated from the measured flame front radius,  $r$ , of spherical flames by

$$S_n = \frac{dr}{dt} \quad (2.1)$$

Shown in Fig. 2.1 is a typical variation of flame speed with radius of stoichiometric iso-octane-air mixture at initial conditions of 358 K and 100 kPa (Bradley *et al.*, 1998). As described by Ali (1995), after spark ignition, the flame speed is high due to the high temperature and active radicals provided by the spark energy. At approximately 5 mm radius, the flame speed attains a minimum value as the effect of the spark decay and before normal flame chemistry develops. After this point, spark plasma dynamics and flame stretch are operative in a regime of spark assisted flame propagation and this is followed by self-sustaining flame propagation. Flame speed is not a fundamental property of a combustible mixture. It is the sum of the stretched laminar burning velocity,  $u_n$ , and the gas expansion velocity,  $u_g$ , adjacent to the flame front:

$$S_n = u_n + u_g \quad (2.2)$$

From mass conservation, the relationship between  $S_n$  and  $u_n$  is expressed by

$$u_n = S S_n \left( \frac{\rho_b}{\rho_u} \right) \quad (2.3)$$

where  $\rho_b$  and  $\rho_u$  are the burned and unburned gas densities, calculated using the *Gaseq* equilibrium program (Morley, 2001).  $S$  is a generalised function that accounts for the effects of flame thickness on the mean density of the burned gases (Bradley *et al.*, 1996), and this is given by

$$S = 1 + 1.2 \left[ \frac{\delta_l}{r} \left( \frac{\rho_u}{\rho_b} \right)^{2.2} \right] - 0.15 \left[ \frac{\delta_l}{r} \left( \frac{\rho_u}{\rho_b} \right)^{2.2} \right]^2 \quad (2.4)$$

where  $\delta_l$  is the laminar flame thickness based on a hydrodynamic length and  $r$  is flame front radius.

The laminar flame thickness can be described by a distance between completely unburned gas (at the unburned gas temperature) and completely burned gas (at the burned gas temperature). However, it is difficult to quantify this distance because the change from unburned gas to burned gas occurs gradually. As a result, there are various definitions of flame thickness in the literature (Haq, 1998; Gillespie *et al.*, 2000) to estimate this distance such as based on a mass diffusion length,  $\delta_D = D_{ij}/u_l$  (where  $D_{ij}$  is the binary mass diffusion coefficient and  $u_l$  is the unstretched laminar burning velocity), a thermal diffusion length,  $\delta_T = D_T/u_l$  (where  $D_T$  is the thermal diffusivity of the mixture) and a hydrodynamic length,  $\delta_\nu = \nu/u_l$  (where  $\nu$  is the kinematic viscosity of the mixture). In the present work, flame thickness is defined based on a hydrodynamic length.

Derivation of Eq. (2.4) was produced by Bradley *et al.* (1996) from a modeled methane-air mixture at 100 kPa and 300 K for a wide range of equivalence ratios. Although, they did not calculate a value for iso-octane air mixtures, used in the present work, but they suggested that it is unlikely to be significantly different to that of methane-air mixtures. Values of unstretched laminar burning velocity,  $u_l$ , are based on the linear extrapolation of  $S_n$  to the zero stretch (illustrated in Fig. 2.2), and hence are not sensitive to the value of  $S$ . However, Bradley *et al.* (1998) suggested that the calculation of Markstein number (described in later paragraph) might be affected by small errors in using Eq. (2.4). With such potential of errors and the application mainly for gaseous premixed flames, the present work did not use Eq. (2.4) for aerosol flames.

For a non-planar flame, the rate at which unburned gas is entrained into the flame front is not the same as the rate of formation of the burned products due to finite flame thickness. Bradley *et al.* (1996) presented two definitions of laminar burning velocity. The first is based on the entrainment of the unburned gas into the flame front, expressed by

$$u_n = \frac{1}{\rho_u} \left( \frac{\dot{m}_e}{A} \right) \quad (2.5)$$

where  $\dot{m}_e$  is the rate of mass entrainment of the unburned gas into the flame front and  $A$  is the flame area defined at the cold flame front. The second definition is based on the rate of production of reacted gas and is given by

$$u_{nr} = \frac{1}{\rho_u} \left( \frac{\dot{m}_r}{A} \right) \quad (2.6)$$

where  $\dot{m}_r$  is the rate of formation of the burned product. At small flame radii, the effect of  $\delta_l$  is important. However, it is less so at larger flame radii. As the flame radius tends to infinity, both  $u_n$  and  $u_{nr}$  tend towards  $u_l$ . Bradley *et al.*, (1996) show that  $u_n$  and  $u_{nr}$  are related by

$$u_{nr} = \frac{\rho_b}{\rho_b - \rho_u} (u_n - S_n) \quad (2.7)$$

In a realistic situation, flame is subjected to aerodynamic influences such as flow non-uniformity, curvature and non-stationary. The flame in this case is known as a stretched flame. A simple explanation to understand a stretched flame is by considering a planar flame situated in a divergent stagnation flow as shown in Fig. 2.3. Assuming a potential flow moves through the streamtube and because the flow is divergent, the resultant of the flow is stretching out the flame. This effect is clearly due to pure stretch as represented by the divergence of the flow when it traverses the reaction region. For a stationary flame, Wu and Law (1984) show that there are three factors that result a stretched flame, which due to pure stretch, preferential diffusion and non-uniformity flow field. However, since diffusion effect is parallel to the normal of flame surface, the importance of preferential diffusion is significant in the dynamics of stretched flames. Explanation on the influence of preferential diffusion on the response of stretched flame is given in Section 2.3.2. A general definition of stretch acting on the flame,  $\alpha$ , is defined as the time derivative of the area,  $A$ , of an infinitesimal element divided by the area (Law, 1988)

$$\alpha = \frac{1}{A} \frac{dA}{dt} \quad (2.8)$$

In a case of spherical flame, the surface area is  $4\pi r^2$ . Hence Eq. (2.8) becomes

$$\alpha = \frac{1}{A} \frac{dA}{dt} = \frac{1}{4\pi r^2} \frac{d(4\pi r^2)}{dt} = \frac{2}{r} \frac{dr}{dt} = \frac{2}{r} S_n \quad (2.9)$$

The change in flame speed due to the stretch rate is given by

$$S_s - S_n = L_b \alpha \quad (2.10)$$

where  $L_b$  is the Markstein length which represents the sensitivity of flame speed to the stretch rate and  $S_s$  is the unstretched flame speed. This is a linear equation in which the gradient is defined by  $L_b$ , and  $S_s$  is obtained when  $\alpha = 0$ , as shown in Fig. 2.2. A positive value of  $L_b$  indicates a stable flame with little tendency towards instabilities. Conversely, a negative value of  $L_b$  indicates greater propensity towards unstable flame propagation (Bradley *et al.*, 1998). As the flame stretch tends towards zero value, the use of Eq. (2.3) is applicable to calculate the unstretched laminar burning velocity from  $S_s$  by

$$u_l = S_s \frac{\rho_b}{\rho_u} \quad (2.11)$$

In a spherically expanding flame within the pre-pressure period, there are two mechanisms that contribute to stretch. Firstly from curvature, given by

$$\alpha_c = 2 \frac{u_n}{r} \quad (2.12)$$

and secondly, from flow field aerodynamic strain, expressed by

$$\alpha_s = 2 \frac{u_g}{r} \quad (2.13)$$

The total stretch is given by the sum of these two mechanisms

$$\alpha = \alpha_c + \alpha_s \quad (2.14)$$

Combined with the two definitions of stretched burning velocity,  $u_n$  and  $u_{nr}$ , Bradley *et al.* (1996) presented the variation in the stretched burning velocity with these two components of flame stretch. For  $u_n$ ,

$$u_l - u_n = L_c \alpha_c + L_s \alpha_s \quad (2.15)$$

where  $L_s$  is the Markstein length associated with aerodynamic strain and  $L_c$  is the Markstein length associated with curvature. Grott and De Goey (1992) show that these values are different because they depend strongly on the stage of flame propagation and on the isotherm on which the Markstein length is defined.

For  $u_{nr}$ ,

$$u_l - u_{nr} = L_{cr} \alpha_c + L_{sr} \alpha_s \quad (2.16)$$

where  $L_{cr}$  is the Markstein length associated with curvature and  $L_{sr}$  is the Markstein lengths associated with strain. Normalisation of these Markstein lengths by the flame thickness,  $\delta_f$ , yields dimensionless Markstein numbers  $Ma_s$ ,  $Ma_c$ ,  $Ma_{sr}$  and  $Ma_{cr}$ . In a spherical flame, Bradley *et al.* (1996) showed that  $u_g$  is usually much larger than  $u_n$ , hence the flame stretch due to flow strain,  $\alpha_s$  is typically 4 to 5 times higher than that due to curvature,  $\alpha_c$ . For this reason, Bradley *et al.* (1996) emphasised that  $Ma_{sr}$  (strain rate Markstein number) is the most relevant for many aspects of combustion.

### 2.3.2 Instabilities in laminar flames

The phenomenon of flame front instability plays an important role in the investigation of premixed laminar flames and their burning rates. A smooth flame front subjected to non-planar disturbances experiences wrinkles and cells uniformly over the flame surface. Such typical structure of cellular spherical flame is shown in Fig. 2.4 together with comparison to that of smooth flame. This cellularity results in an increase in the flame surface area followed by a relative increase in laminar flame speed (Bradley *et al.*, 1998). Similar to experimental work (Groff, 1982; Kwon *et al.*, 1992; Gu *et al.*, 2000), theoretical studies of flame instability have reported the development of instability in the form of wrinkles and cells as precursors to a cellular structure of the flame front (Sivashinsky, 1977; Bradley and Harper, 1994; Ashurst, 1997). In the present study, cellular flames were observed under many conditions (see Chapter 5). Therefore, the mechanism of instabilities is likely to be important in aerosol flames. Hence, they are reviewed here.

Law (1988) described that there are two fundamental modes that contribute to the flame instabilities, namely hydrodynamic instability and thermal diffusive effects. Hydrodynamic instability is caused by the density jump across the flame. In this mode, as shown in Fig. 2.5, the flame is assumed to propagate with the laminar burning velocity,  $u_n$ . As the reactants move towards the convex flame front they diverge and as a result the reactants flow slows down because of widening of the streamtube. However, since the burning velocity remains unchanged, a dynamic imbalance then results which leads to a further protrusion of this flame segment. Following a similar approach, for the concave segment, it will further recede into the burned gas region. Clearly, this flow variation deforms the flame surface and as a consequence, the overall flame speed is increased. This type of instability, also

known as a Darrieus-Landau instability, results from the interaction of the flame with the hydrodynamic disturbances.

The instability induced due to the hydrodynamic disturbances can be balanced or strengthened by a thermal diffusive mechanism. The thermal diffusive mechanism for such cellularity is shown in Fig. 2.6. With a wavelike flame (stretched flame) as shown in Fig. 2.6, there is a diverging conductive thermal flux away from the flame surface into the unburned gas ahead of it and a converging diffusive mass flux of the deficient reactant into the flame surface at the crest of the wave. At the trough of the wave, the opposite situation arises where conductive thermal flux is converging while diffusive mass flux is diverging. In this context, the relationship between conductive thermal flux and diffusive mass flux in terms of magnitudes plays a main role in characterising the flame as either stable or unstable, depending on which one dominates. This diffusion coefficient, which known as the Lewis number,  $Le$ , is defined by

$$Le = \frac{\alpha}{D} \quad (2.17)$$

where  $\alpha$  is the thermal diffusivity of the mixture and  $D$  is the mass diffusivity of the deficient reactant. If the diffusion coefficient in the Lewis number expression is less than unity (dominated by thermal), there is a resulting increase in enthalpy by the flame and the local burning velocity increases at the crest. The converse situation occurs at the trough where there is a loss of enthalpy and the local burning velocity decreases. The crest then propagates faster than the trough and the amplitude of the wavy flame increases. Hence, the flame becomes more unstable. However, if  $Le$  is greater than unity (dominated by mass), similar effects result in local burning velocity, but to decrease at the crest and to increase at the trough. Consequently, this effect tends to flatten the wavy flame and stabilise the flame. This demonstrates that flame propagation can be influenced by stretch through preferential diffusion which tends to increase or decrease the flame temperature and burning rate depending on the effective Lewis number.

Initially, all spherically propagating laminar flames are stable because of high stretch rate at small flame radii. This can be described by understanding the effect of stretch due to flame motion on spherical flame propagation (Law, 2006). Consider an expanding spherical flame, as shown in Fig. 2.7a, with flame radius,  $r_f$  larger than the flame thickness. After an interval  $\delta x$ , as shown in Fig. 2.7b, the flame



radius grows by an amount of  $\delta r_f$  which is smaller than  $r_f$ ,  $r_T$  and  $r_M$ . Here  $r_T$  and  $r_M$  represent the radii of thermal and limiting reactant layers. As the flame expands, the volume of thermal energy increases as well as that of reactant concentration. The increase in thermal energy in flame structure represents an increased extent of heat transfer away from the reaction zone, while an increase in reactant concentration represents an increased amount of reactant supply to the reaction zone. Since the effect of flame thickness is significant for the small flame radii (Bradley *et al.*, 1996), this results in the ratio of  $r_T/r_M$  becoming larger, which means more heat release than the amount of reactant supply. This can be further interpreted by the Lewis number,  $Le$ , expressed in Eq. (2.17), which implies that for this condition  $Le$  is larger than unity and the flame tends to be more stable.

As the flame expands, the flame radius increases and the flame stretch rate decreases. Subsequently, a critical radius is reached at which the rate of stretch no longer provides sufficient stabilising effects and cellularity develops. This early cellularity appears in the form of cracks which further propagate across the flame surface. At this stage, the critical radius,  $r_{cr}$ , defines a critical Peclet number,  $Pe_{cr}$ , given by Harper (1989) as

$$Pe_{cr} = \frac{r_{cr}}{\delta_l} \quad (2.18)$$

After the onset of cellularity, at  $Pe_{cr}$ , there is no significant change in burning rate since it takes time for its effect to manifest itself. Cross-cracking develops until eventually the flame surface becomes completely cellular. At this stage, the cellular flame gives rise to an increase in flame speed at a higher critical radius,  $r_{cl}$ , which defines another critical Peclet number,  $Pe_{cl}$  (Bradley *et al.*, 1998; Gu *et al.*, 2000):

$$Pe_{cl} = \frac{r_{cl}}{\delta_l} \quad (2.19)$$

This point is also shown in Fig. 2.2 and indicates the point at which the flame speed rapidly accelerates as stretch is reduced during flame growth.

The Peclet number in Eqs. (2.18) and (2.19) is traditionally a ratio of convective to diffusive transport and this is expressed by

$$Pe = \frac{LV}{\alpha} \quad (2.20)$$

where  $L$  is the characteristic length scale,  $V$  is the velocity scale, and  $\alpha$  is thermal diffusivity. Thermal diffusivity can be calculated by

$$\alpha = \frac{k}{\rho c_p} \quad (2.21)$$

where  $k$  is the thermal conductivity,  $\rho$  is the density and  $c_p$  is the heat capacity. By combining the thermal diffusivity expression in the Peclet number expression in Eq. (2.20), this becomes

$$Pe = \frac{LV\rho c_p}{k} \quad (2.22)$$

Bechtold and Matalon (1987) showed that the expression of  $\frac{k}{V\rho c_p}$  characterises the thickness of the flame,  $\delta_l$  where  $\rho$  is density of unburned gas and  $V$  is the adiabatic flame speed. In the case of spherical flame, the characteristic length scale,  $L$  can be represented by radius of the flame,  $r$ .

In the analysis of Bechtold and Matalon (1987) the perturbation of a spherical flame was investigated using linear stability analysis. They showed that, based on the Markstein number, there can exist a range of perturbing wavelengths with upper and lower limits inside which the flame is unstable. These limits are defined by the wave number,  $n$ ,

$$n = \frac{2\pi Pe}{\Lambda} \quad (2.23)$$

where  $Pe$  is the Peclet number and  $\Lambda$  is the wavelength associated with  $n$ , normalised by the flame thickness (Bradley, 1999). Figure 2.8 shows the results of the analysis by Bechtold and Matalon (1987) in terms of theoretical values of  $n$  and  $Pe$  for different Markstein Number,  $Ma_{sr}$  with a density ratio,  $\sigma = \rho_u/\rho_b$ , of 6. The lowest value of  $Pe$  for instability at the tip of the peninsular is  $Pe_{cr}$ . The lower limit wave number,  $n_l$ , is associated with the longest unstable wavelength. The upper limit wave number,  $n_s$ , is associated with the shortest unstable wavelength. Within the peninsula, the amplitude of the flame disturbance is amplified. At the boundary wave numbers, there is no amplification or attenuation of the disturbance. Outside the peninsula, the flame is stable. It can be seen that the range of unstable wave numbers increases with an increase in  $Pe$  and a decrease in  $Ma_{sr}$ . However, full cellularity and an associated increase in flame speed only occur at  $Pe_{cl}$ . Thus,

Bradley (1999) modified the analysis of Bechtold and Matalon (1987) to allow for a lag in the full development of the instability by introducing  $f(n_s/n_l)$ , where  $f$  is a numerical constant less than unity. An idealised and simplified of instability peninsula for particular values of  $Ma_{sr}$  and  $\rho_u/\rho_b$  is shown in Fig. 2.9. The value of  $Pe_{cl}$  is obtained experimentally by observing when full cellularity has developed and the flame speed begins to accelerate.

Experimental values of  $Pe_{cl}$  have been correlated in terms of Markstein Number,  $Ma_{sr}$  (defined in Section 2.3.1) by Bradley *et al.* (1998) and Gu *et al.* (2000). The latter showed that  $Pe_{cl}$  can be correlated linearly with  $Ma_{sr}$  by

$$Pe_{cl} = 177Ma_{sr} + 2177 \quad (2.24)$$

This correlation was derived from various experimental results of gaseous mixtures of methane-air, iso-octane-air and 90% iso-octane / 10% n-heptane-air at a wide range of equivalence ratios, pressures and temperatures. This correlation demonstrates some generality in the onset of cellular instabilities in gaseous flames as a function of  $Ma_{sr}$ . However, Eq. (2.24) is only an approximate guide to the previous experimental results although this relationship is less reliable for negative values of  $Ma_{sr}$  (Bradley *et al.*, 2007). In a recent work, Bradley *et al.* (2009) modified this correlation to have a better relation through the latest and previous experimental results, expressed by

$$Pe_{cl} = 1808.6 \exp^{0.103 Ma_{sr}} \quad (2.25)$$

Since a spherical flame is initially stabilised by the high stretch rate, Bradley *et al.* (2007) proposed a critical Karlovitz stretch factor for replacing the experimental and theoretical values of  $Pe_{cl}$ , given by

$$K_{cl} = \alpha_{cl} \frac{\delta_l}{u_l} \quad (2.26)$$

where  $\alpha_{cl}$  is critical total stretch rate at which the flame speed starts to accelerate. Bradley *et al.* (2009) suggested that  $K_{cl}$  seems to be a more reasonable parameter for quantifying flame instability than  $Pe_{cl}$ , since  $K_{cl}$  was expressed in terms of the critical stretch rate at the onset of flame instability. Using available experimental and theoretical data, Bradley *et al.* (2009) also correlated  $K_{cl}$  with  $Ma_{sr}$  and this is given by

$$K_{cl} = 0.075 \exp^{-0.123 Ma_r} \quad (2.27)$$

### 2.3.3 Turbulent flames

Measurements of turbulent burning velocity is complicated and still remains challenging due to the influence of turbulence parameters such as the root mean square turbulence velocity,  $u'$ , and the resulting flame brush (Gillespie *et al.*, 2000). At Leeds, the mean schlieren flame front radius,  $r_{sch}$ , has been used historically in measurements of turbulent flame propagation (Abdel Gayed *et al.*, 1986). Yet this neither represents the leading edge at which reactants enter the flame nor the mean flame front more readily obtained from laser sheet images. Haq (1998) introduced a flame radius,  $r_v$ , at which the volume of unburned mixture inside a sphere of this radius is equal to the volume of burned mixture outside it. Bradley *et al.* (2003) showed that at the spherical surface defined by  $r_v$ , the rate of disappearance of cold unburned mixture is equal to the rate of appearance of burned mixture, and showed that  $r_v$  can be estimated by planar sheet imaging.

Using experimental findings, Bradley *et al.* (2003) demonstrated that the relationship between  $r_v$  and the schlieren radius,  $r_{sch}$ , is given by

$$r_v = \left( \frac{1}{1.11} \right) r_{sch} - 2.1 \quad (2.28)$$

for  $r_v$  between 2 and 40 mm. The calculation of flame speeds and burning velocities of turbulent flames is very similar to that described in Section 2.3.1 for laminar flames. Schlieren flame radius,  $r_{sch}$ , is defined based on the projected flame area using schlieren technique, and the turbulent flame speed,  $S_t$ , is expressed by

$$S_t = \frac{dr_{sch}}{dt} \quad (2.29)$$

Then, the turbulent burning velocity can be calculated by

$$u_t = \left( 0.9 \frac{\rho_b}{\rho_u} \right) S_t \quad (2.30)$$

where the constant value of 0.9 is obtained from Eq. (2.28) which relates the  $r_{sch}$  to  $r_v$ .

In order to generalise the measurement of turbulent flames, Bradley *et al.* (1992) presented a correlation of turbulent burning velocity from about 1650 experimental values, obtained in both combustion bombs and burners. The correlation suggests that

$$\frac{u_t}{u_l} = f\left(\frac{u'_k}{u_l}, K, Le(\text{or } Ma)\right) \quad (2.31)$$

Here  $u'_k$  is the effective r.m.s. turbulent velocity influencing the flame (Bradley *et al.*, 1992). The ratio of  $u_t/u_l$  indicates the effect of the increase in burning velocity due to turbulence, and  $u'_k/u_l$  is an indication of flame wrinkling. The Karlovitz stretch factor,  $K$  in Eq. (2.31) represents turbulent flame stretch and is given by

$$K = \left(\frac{u'}{\lambda}\right) / \left(\frac{u_l}{\delta_l}\right) \quad (2.32)$$

where the numerator is the turbulent strain rate (Abdel-Gayed *et al.*, 1984), in which  $\lambda$  is the Taylor micro scale of turbulence, and the denominator represents a chemical strain rate. Alternatively, Eq. (2.32) can be considered to be a ratio of chemical to eddy lifetimes:  $(\delta_l/u_l) / (\lambda/u')$ . For isotropic turbulence, with  $\lambda$  related to the integral length-scale,  $L$  by Abdel Gayed *et al.* (1984)

$$\frac{\lambda^2}{L} = 40.4 \frac{\nu}{u'} \quad (2.33)$$

With Eqs. (2.32) and (2.33), it can be shown that

$$K = 0.157 \left(\frac{u'}{u_l}\right)^2 R_L^{-0.5} \quad (2.34)$$

where  $R_L$  is the turbulent Reynolds number based on the integral scale of turbulence:  $(R_L = u'L/\nu)$ . In a more recent work, Bradley *et al.* (2005) used a different constant in Eq. (2.33) and this changed Eq. (2.34) and becomes

$$K = 0.25 \left(\frac{u'}{u_l}\right)^2 R_L^{-0.5} \quad (2.35)$$

Bradley *et al.* (1992) suggested that for laminar flamelet modelling of turbulent combustion, the group  $(KMa)$  expresses the reduction in burning velocity due to stretch. However, at that time, there was insufficient data on  $Ma$  value to

generate a correlation. Therefore, pending the availability of more data on  $Ma$ , Bradley *et al.* (1992) decided to correlate experimental values of  $u_t/u_l$  in terms of the wrinkling factor,  $u_k'/u_l$ , with the flame stretch factor  $KLe$ , as shown in Fig. 2.10. The correlation in Eq. (2.31) and in Fig. 2.10 is described approximately by

$$\frac{u_t}{u_l} = 0.88 \frac{u_k'}{u_l} (KLe)^{-0.3} \quad (2.36)$$

The negative exponential suggests that increasing the turbulent stretch rate decreases the turbulent burning velocity. Bradley *et al.* (1992) also emphasised that the experimental points, which are not shown in Fig. 2.10, correlate better with  $KLe$  than solely with  $K$ . This correlation has been widely used in the validation of mathematical models of turbulent combustion in general, and in determining combustion rates in engine cycle and explosion models (Bradley *et al.*, 1992).

## 2.4 Droplet generation

In spray combustion, it is necessary to atomise and distribute the liquid fuel in a controlled manner within the combustion chamber. The performance of the spray combustion process is, in general, dependent upon the size of the droplets produced and the homogeneity of the droplet distribution. Gökalp *et al.* (1999) identified several different techniques of droplet generation and summarised some criteria used for their selection. A brief description of the principle behind each technique, along with its major advantages and disadvantages, is discussed below. These descriptions are based mainly on the review of Gökalp *et al.* (1999) and the schematic of each system is given in Fig. 2.11.

- i) *Liquid jet atomiser and air assisted atomiser.* A large velocity difference between liquid jet and the co-flowing gas stimulates surface instabilities on the jet surfaces, thus shearing off droplets from the jet surface. The advantage is that this type of system is capable of handling large fuel flow rates but the disadvantages are that the size distribution of the droplets is highly dispersed and produces droplets with high velocity.
- ii) *Jet instabilities.* Droplets are formed by breaking up of jet due to surface dynamic instabilities induced by external excitation, commonly created by superimposed oscillations at ultrasonic frequencies, or by some other means.

The advantage is that a monodispersed spray is produced in this case but the liquid flow rate is extremely low.

- iii) *Surface instabilities*. Droplets are formed by instabilities created on the surface of a planar liquid surface by ultrasonic actuators based on piezoelectric or magnetostrictive systems. These create low-dispersed sprays for reasonable flow rates. However, there are limitations to the sizes of droplet that can be studied and technical realisation in handling a large bulk of fluid can be a problem.
- iv) *Electrostatic spray*. The spray is obtained by feeding a liquid which is sufficiently conductive through a capillary metallic tube maintained at a potential of a few kilovolts with respect to an electrode located a few centimetres away. Under the action of this electric field, spray is formed from the thin jet originating from the capillary. The electrostatically generated droplets are advantageous in that size of the droplets can be controlled and with low dispersion. However, for studying combustion, this poses a huge disadvantage, as the electrostatically charged droplets may result in micro-explosions, leading to ambiguity in overall results.
- v) *Condensation spray*. Droplets are generated by condensation process during the rapid gas expansion. The main advantage of this type is the narrow droplet dispersion and near zero initial droplet velocity field. But the main disadvantages are that this method is not suitable for high initial pressure and that fabrication is difficult.

Table 2.1 summarises the above description and clearly shows that there is no ideal solution of droplet generation that can perfectly meet all the criteria required. In many circumstances, it is essential to consider the quality of the spray in terms of physical parameters such as the droplet size distribution or the mean velocity field. For an application intended to study flame propagation in a droplet spray, these two criteria seem to be the most relevant (Gökalp *et al.*, 1999).

## 2.5 Droplet characterisation

Depending on the nature of formation, described in Section 2.4, droplets may exist in the form of sprays in engines, or droplets-vapour-air mixtures as in an

aerosol generated by expansion of gaseous fuel. In order to study the combustion of these mixtures, the parameters involved in characterising them must be clarified.

The simplest and perhaps the most practical parameter, used by most researchers (e.g. Burgoyne and Cohen, 1954; Hayashi and Kumagai, 1975; Nomura *et al.*, 2000) to define a mixture that contains fuel droplets, is the overall equivalence ratio,  $\phi_{ov}$ . This includes all fuel present, irrespective of phase. Since, as suggested by Myers and Lefebvre (1986), the propagation of an aerosol flame might be primarily dependent on the gaseous equivalence ratio,  $\phi_g$ , this also is a key parameter. The two different equivalence ratios are therefore defined to accommodate the fraction of gaseous and liquid phases. These are described in detail in Section 4.2.

Atzler (1999) suggested that the evaporation of droplets ahead of the flame front may change both the gaseous and liquid equivalence ratios. Therefore, the actual amount of gaseous fuel that exists in the reaction zone is difficult to determine experimentally and no measurements were attempted in the works included in the present review. However, in a theoretical study, this parameter was used by Polymeropoulos (1984) in the prediction of burning rates in an aerosol flame. Other researchers, for example Burgoyne and Cohen (1954), calculated the change in drop size and the subsequent change in  $\phi_g$ , in the preheat zone of the flame from the scaled temperature profile of a homogeneous flame. However, this is not without problems since aerosol flames can be much thicker than gaseous ones. Therefore, experimental results have usually been correlated in terms of cold gas parameters.

The droplet size is the most frequent parameter used for the correlation of flame propagation of an aerosol flame. If all droplets in an aerosol mixture are of the same size, then the obvious statement is that of droplet diameter. Such an aerosol is termed monosized or monodispersed. However, sprays produced by injectors are rarely monosized. Thus, a form of averaging to determine a suitable mean size that correctly represents the physical properties of droplets is necessary (Lefebvre, 1989). A brief description of several mean droplet size terminologies has been given in, for example, Schick (1997). One of the commonly used mean droplet sizes in spray is the Sauter Mean Diameter (SMD), or  $D_{32}$ , expressed by

$$D_{32} = \frac{\sum_{i=1}^k n_i D_i^3}{\sum_{i=1}^k n_i D_i^2} \quad (2.37)$$



where  $n_i$  is the number of droplets within a range centred on diameter  $D_i$ , and  $k$  is the number of ranges. The SMD is an average diameter with a volume to surface area ratio equal to that of the droplets. It is also used as an indicator of the degree of atomisation produced by an injector. Another representative of droplet diameters is the surface mean diameter,  $D_{20}$ . It represents an average diameter with a surface area equal to the mean surface area of all the droplets. It is expressed by

$$D_{20} = \sqrt{\frac{\sum_{i=1}^k n_i D_i^2}{\sum n_i}} \quad (2.38)$$

$D_{20}$  is used for surface controlled applications such as absorption. Another term that also can be used for representing droplet diameters is the mean arithmetic diameter,  $D_{10}$ . This is expressed by

$$D_{10} = \frac{\sum_{i=1}^k n_i D_i}{\sum n_i} \quad (2.39)$$

In the case of monodispersed or near monodispersed aerosols, the use of  $D_{10}$  is suitable since all mean droplet diameters (Eqs. 2.37 to 2.39) tend towards the same value. It is worth noting that, in the context of spray flame instability, the use of mean diameters such as SMD to characterise flame cellularity may lead to inaccurate conclusions since it is important to differentiate the homogeneity of the droplet spatial distribution (Greenberg, 2002).

Conditions in the mixture containing fuel droplets can also be expressed in terms of the liquid volume of fuel present per unit volume of mixture. This is a function of the average size of the droplets and the average inter-drop distance. This is illustrated in a study by Cekalin (1962) who showed that the sensitivity of burning velocity to the inter-drop distance was a function of the vapour fraction. Burgoyne and Cohen (1954) combined the droplet size and the inter-drop distance to the non-dimensional droplet spacing to express the limiting conditions for flame propagation, in terms of flammability of the aerosol. This parameter was developed further to accommodate more complex process such as combustion in droplet clouds (Chiu and Liu, 1977; Correa and Sichel, 1982).

## 2.6 Studies of droplet combustion

### 2.6.1 Group combustion modes

Studies of droplet combustion in practical systems are too complex because of the complex interaction between important parameters such as evaporation rate, burning rate and turbulence, which are closely coupled (Faeth, 1977). To accommodate these complex interactions, Chiu and Liu (1977) introduced the group combustion number,  $G$ , which characterises different combustion modes. It corresponds to the ratio of the gross droplet evaporation rate to the inward oxygen diffusion rate and is given by

$$G = 1.5Le \left( 1.0 + 0.276Re^{\frac{1}{2}} Sc^{\frac{1}{3}} \right) N_T^{\frac{2}{3}} \left( \frac{D}{l_D} \right) \quad (2.40)$$

where  $Le$  is the Lewis number,  $Re$  is the droplet Reynolds number,  $Sc$  is the Schmidt number,  $N_T$  is the total number of droplets in a cluster,  $D$  is the mean droplet diameter and  $l_D$  is the inter-drop distance. Using this parameter, four modes of droplet combustion have been identified: single droplet combustion, internal group combustion, external group combustion and external sheath combustion. These modes are suggested to progress from single droplet combustion to external sheath combustion as the group combustion number increases. The characteristics of each mode are presented in Table 2.2. These four different combustion regimes were re-defined into more detailed subsections by Annamalai and Ryan (1992). The applicability of  $G$  was verified qualitatively in experiments by Akamatsu *et al.* (1996) by applying advanced laser-based diagnostics with high temporal and spatial resolutions to the spray flames in a turbulent jet. Nevertheless, this group combustion number only investigates the interaction between droplets in terms of evaporation, and the location of the reaction zone is predicted to be a function only of the local mixture composition. Furthermore, this group combustion number does not account for hydrodynamic interaction between the flame and the droplet clouds. Therefore, the group combustion number is likely valid for application in a burner and gas turbine engines, in which fuel is sprayed directly into the flame. In a case where there is homogeneous distribution of fuel droplets in a combustible mixture, such as in the present work, the use of group combustion number might be not relevant.

In order to provide fundamental understanding of phenomena in practical droplet combustion, idealised and simplified systems such as the single droplet theory may provide further understanding on important parameters such as evaporation, mixing and burning in a well-defined environment. Godsave (1953) showed that the time required for a single droplet suspended in stagnant air to burn out is a square function of its diameter. He established the so-called  $D^2$ -law for the condition in which the difference in temperature between the droplet and the surrounding atmosphere is significant:

$$D_t^2 = D_o^2 - K_o t \quad (2.41)$$

Here,  $D_o$  and  $D_t$  are the droplet sizes initially and at time,  $t$ , respectively, and  $K_o$  is the fuel evaporation constant, determined directly from the gradient of plots of  $D^2$  against  $t$ . From Eq. (2.41), the value of droplet lifetime,  $\tau_D$ , can be estimated by equating  $D_t$  to zero value,

$$\tau_D = \frac{D_o^2}{K_o} \quad (2.42)$$

In a case of a quiescent mixture,  $K_o$  can be estimated by

$$K_o = \frac{8k_g}{c_{pg}\rho_l} \ln(1+B) \quad (2.43)$$

where  $k_g$  and  $c_{pg}$  are the specific thermal conductivity and specific heat for the gas phase, respectively, and  $\rho_l$  is the liquid phase density of the fuel (Turns, 2000). The constant  $B$ , which is referred as the mass transfer number or Spalding number (Spalding, 1953), given by

$$B = \frac{c_{pg}(T_\infty - T_s)}{h_{fg}} \quad (2.44)$$

where  $T_\infty$  is the far field temperature,  $h_{fg}$  is the heat of vaporisation and  $T_s$  is the surface temperature of the fuel.  $T_s$  is approximated by the fuel boiling temperature since the situation of the fuel droplet is exposed to the intense heating during steady state combustion. This allows a further assumption that the surface temperature is constant and uniform. As described by Law (1982), the above assumption implies that the droplet transient heating effect is neglected. This is consistent since the

droplet transient heating proceeds fairly rapidly during the droplet lifetime estimation.

In practice, droplets are not usually stationary, as was assumed by Godsave (1953). However, it has been experimentally confirmed by Gökalp *et al.* (1992) that the  $D^2$ -law given in Eq. (2.41) is still applicable. Using an empirically derived relation, they showed that the fuel evaporation constant under turbulence environment,  $K_t$ , can be estimated by

$$K_t = K_o \left( 1.0 + 0.276 Re^{\frac{1}{2}} Sc^{\frac{1}{3}} \right) \quad (2.45)$$

where  $Sc$  is the Schmidt number,  $Re$  is the droplet Reynolds number and  $K_o$  is the fuel evaporation constant under quiescent condition. In many situations involving droplet combustion, mixing and burning, to a first approximation, can be assumed to be very fast (Spalding, 1953). Thus, evaporation rate is the important parameter which may control the burning rate of droplet combustion. This is particularly so for large droplets, where reduction in droplet burning rate was reported to occur when the droplet size is bigger than 40  $\mu\text{m}$  (Ballal and Lefebvre, 1981). This is discussed in the following section.

### 2.6.2 Laminar combustion

Flame propagation in an initially quiescent mixture of uniformly-dispersed spray has been widely studied (Burgoyne and Cohen, 1954; Hayashi and Kumagai, 1975; 1976; Nomura *et al.*, 2000; 2007; Lawes *et al.*, 2006). Burgoyne and Cohen (1954) reported that, within a range of droplet diameters between 10 and 40  $\mu\text{m}$ , the flames resembled a brush-like spray of discrete burning drops. For a droplet size of 17  $\mu\text{m}$  and  $\phi_{ov}=0.70$ , the burning velocity was nearly 60% higher than that of a stoichiometric mixture at 10  $\mu\text{m}$ . Similar enhancement in the burning velocity was evident in the results of Hayashi and Kumagai (1975, 1976) for n-octane and ethanol. They showed that the burning rate of aerosol flames was a function of droplet size and gas-vapour concentration. They suggested that the effect of flame wrinkling due to isolated droplet burning and the burning of the gaseous fuel around isolated droplets at the optimum fuel-to-air ratio were the probable mechanisms which increase the burning rate. Nomura *et al.* (2000, 2007) studied ethanol aerosol combustion under microgravity conditions. At a range of equivalence ratio, the

liquid fraction was maintained constant by varying the expansion rate. They showed that a flame speed enhancement was obtained with overall lean mixtures. However, in both studies, the flame size under consideration was relatively small at about 10 mm in radius. They concluded that the flame speed in aerosol mixtures was influenced by the overall equivalence ratio, liquid equivalence ratio and droplet size. Lawes *et al.* (2006) attributed the higher burning rates in iso-octane aerosol mixtures, as compared to gaseous mixtures at the same  $\phi_{ov}$ , to the development of flame front instabilities in the aerosol mixtures. They suggested that this was due to the wrinkling of the flame by the droplets which increased the flame surface area and enhanced flame propagation. A similar burning rate promotion was observed in other experimental works using an ultrasonic atomiser with a centrally ignited flame (Mizutani *et al.*, 1973b), a condensation aerosol generator in a flame tube (Chan and Jou, 1988) and flame propagation in a cylindrical tube (Nunome *et al.*, 2002).

Although most of the previous works observed that the burning rate of aerosol mixtures generally increased with droplet size, the opposite effect was shown experimentally by Ballal and Lefebvre (1981). They studied aerosol mixtures of iso-octane, diesel oil and heavy fuel oil at drop sizes between 30 and 100  $\mu\text{m}$ . They proposed that the reduction in the aerosol burning rate was related to the rate of droplet evaporation which is small when the droplet size is bigger than 40 $\mu\text{m}$ . From their results, they presented a model to predict burning rate in quiescent aerosol mixtures which is based on considerations of evaporation rates and chemical reaction rates. Later, Polymeropoulos (1984) extended the work of Ballal and Lefebvre (1981) and predicted a significant burning rate enhancement for monodispersed aerosol fuel-air mixtures in the so-called “transitional range” in which droplet diameters are between 5 and 20  $\mu\text{m}$ . However, due to lack of experimental data within this transition range, his prediction could not be validated. Fig. 2.12 shows the effect of fuel droplets on the burning rate of stoichiometric medium diesel oil-air sprays predicted by the model (Polymeropoulos, 1984) and from the experiments (Ballal and Lefebvre, 1981). In similar work by Greenberg *et al.* (1998), the enhancement in burning rate was suggested to be due to instabilities induced by the use of a spray of fuel droplets.

### 2.6.3 Instabilities in aerosol flame

The phenomenon of gaseous flame instability discussed in Section 2.3.2 has also been observed in aerosol flames. In aerosol combustion, the presence of liquid fuel droplets has been shown to influence instabilities by causing earlier onset of cellularity than for gases, which further leads to burning rate enhancement (Burgoyne and Cohen, 1954; Hayashi *et al.*, 1976; Atzler, 1999; Sulaiman; 2007).

Early observation of such phenomena was recorded by Burgoyne and Cohen (1954) where flame propagation in tetralin droplets resembled a brush-like spray of discrete burning drops. This was followed by a significant promotion in the flame velocity propagation. Hayashi *et al.* (1976) reported that there was a rough appearance of the flame for ethanol droplets as small as 7  $\mu\text{m}$ , growing with flame propagation. They observed, for a droplet size around 20  $\mu\text{m}$ , the flame front was rugged, undulated and thickened. They suggested that this cellularity was due to the local variations in temperature and mixture strength and further increase in the burning rates. Similar observations were found in later works by Atzler (1999), Marquez (2003) and Sulaiman (2007).

Several mechanisms responsible for these instabilities have been discussed by Atzler (1999) and Sulaiman (2007). These include self-tubularisation by droplets, flame distortion due to droplets passing through the reaction zone, heat loss from the flame and local expansion due to droplet evaporation. Atzler (1999) suggested that the possible mechanisms that play a main roles in aerosol flame instability were related to the heat loss from the reaction zone and local rapid expansion through droplet evaporation.

### 2.6.4 Oscillating flames

At some condition, the aerosol flames appeared to have periodic fluctuation of flame structure and speed during its development. This was termed an oscillating flame and reported by several workers (Atzler, 1999; Marquez, 2003; Sulaiman, 2007). This oscillation, also categorised as flame instability behaviour, was simply described by alternating fast and slow modes of flame propagation, as shown in Fig. 2.13 together with changes in a flame structure alternating between cellular and smooth, respectively. Atzler (1999) reported that this phenomenon was found only in aerosol flames of overall lean and stoichiometric mixtures, with droplet diameter

greater than 15  $\mu\text{m}$ . Several factors have been discussed by Atzler (1999) to explain the mechanism responsible for oscillating behaviour in aerosol flames. These include the effect of acoustic wave oscillation, radiation from burning particles and the effect of droplet inertia. Atzler (1999) suggested that the possible mechanism for this oscillation was the effect of droplet inertia.

Figure 2.14 shows a possible mechanism to explain the oscillating spherical flame for an aerosol mixture with  $\phi_{ov} = 1.0$  and  $\phi_g = 0.75$  due to droplet inertia (Atzler *et al.*, 2001). It shows the effect of a variation in droplet velocity,  $u_D$ , on the local equivalence ratio,  $\phi$ , (thick line) at the reaction zone and resulting values of flame speed,  $S_n$ , gas velocity,  $u_g$ , and burning velocity,  $u_l$ . Initially, following ignition,  $u_D$  near the flame front is equal to zero. Therefore, the equivalence ratio in the reaction zone is  $\phi_{max}$ . The flame causes the gas droplet velocity to begin to accelerate. Hence, fewer droplets are entrained by the flame and  $\phi$  decrease, as in regime 1. As the stoichiometric equivalence ratio is approached, the droplets continue to accelerate towards that of  $u_g$ , while  $u_l$  and  $u_g$  reduce as their peak values are passed, as in regime 2. The point at which  $S_n$  and  $u_g$  reach their maximum values is defined as the critical equivalence ratio,  $\phi_{critical}$ . The droplet and gas velocities become equal at  $\phi_{ov}=1.0$ . After this, inertia results in  $u_D$  higher than  $u_g$  as the latter continues to reduce. Hence, the equivalence ratio within the reaction zone tends towards  $\phi = \phi_g$  (regime 3), and would attain this value when  $u_D = S_n$ . Eventually, the droplets approach equilibrium with the surrounding gas and more droplets are entrained as  $\phi$  begins to increase through  $\phi_{ov}$  and  $\phi_{critical}$  (regime 4) as the droplets once again lag behind the gas velocity. The cycle is then repeated. Figure 2.14 clearly shows that a variation in local  $\phi$  will affect local  $S_n$ ,  $u_l$  and  $u_g$ . This results in fluctuations in the burning rate in which the minimum burning rate is equivalent to that of a gaseous flame with  $\phi = \phi_g$ , while the maximum burning rate can correspond to that of a gaseous flame richer than  $\phi_{ov}$ . Marquez (2003) and Sulaiman (2007) supported the view of Atzler *et al.* (2001) by verifying his oscillation model with experimental works which measured simultaneously droplet velocity, flame speed and gas velocity ahead of the flame front.

### 2.6.5 Turbulent combustion

Under turbulent conditions, there are few experimental data of a fundamental nature that demonstrate the similarities and differences in burning rate between single and two-phase combustion, and such data are contradictory. Mizutani *et al.* (1972) investigated the effects of flow velocity and turbulence on combustion of a two-phase fuel-air mixture on a burner. They found that the flame speed increased in proportion to  $u'$  and in inverse proportion to the droplet diameter. A similar trend was observed in other experimental works using various fuels: kerosene (El-Banhawy and Whitelaw, 1981; Myers and Lefebvre, 1986), decane and toluene (Richards and Lefebvre, 1989) and kerosene with propane drops (Nakabe *et al.*, 1988). It was suggested (El-Banhawy and Whitelaw, 1981; Myers and Lefebvre, 1986) that droplet evaporation rate was a controlling factor for turbulent flame speed when the level of turbulence is low, at  $u' < 2.0$  m/s. However, these works used large droplets of between 40 to 100  $\mu\text{m}$ , at which conditions there are no comparative laminar experiments to form a reference. For example, typical laminar aerosol studies have been undertaken with droplets between 10 to 40  $\mu\text{m}$  (Hayashi and Kumagai, 1975; Polymeropoulos, 1984). Marquez (2003) and Sulaiman (2007) suggested that the burning rate of turbulent iso-octane-air aerosol mixtures with droplets of about 4 to 15  $\mu\text{m}$  could be significantly lower than that of gaseous flames. They also performed laminar studies with similar sized droplets. However, these works were inconclusive because they were unable to maintain the same initial pressure and temperature for both the aerosol and gaseous mixtures as well as the limitation in the turbulence conditions.

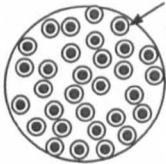
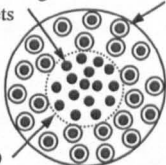
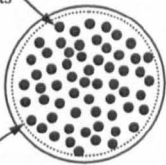
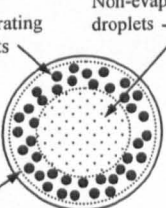
Contradictory evidence was provided by Mizutani and Nakajima (1973a) in which they observed that the addition of kerosene drops into a turbulent ( $u' = 0.13$  m/s) propane-air flame yielded a higher burning rate than for the propane-air flame without drops. However, they also observed that as turbulence increased, this combustion-promoting effect became less significant until, ultimately, burning approximated that of a gaseous flame and droplet size and number density were not significant variables. It was suggested (Mizutani and Nakajima, 1973a) that this was because of increased evaporation and mixing and demonstrates that increased turbulence may reduce or eliminate the burning rate enhancing effect of droplets in aerosol flames that have been reported for initially quiescent mixtures (Hayashi and Kumagai, 1975; Polymeropoulos, 1984).



Table 2.1: Main characteristics of different droplet generator types. Reproduced from Gökalp *et al.* (1999).

Method Criteria	Liquid jet atomiser (Fig. 2.11a)	Air assisted atomiser (Fig. 2.11b)	Jet instabilities (Fig. 2.11c)	Surface instabilities (Fig. 2.11d)	Electrostatic spray (Fig. 2.11e)	Condensation spray (Fig. 2.11f)
Droplet size dispersion	Broad	Broad	Very narrow	Narrow	Very narrow	Narrow
Possible liquid flow rate	Small to large	Small to large	Very small	Small	Small	Very small
Initial droplet kinetic energy	Very high	High	High	Small	Small	Very small
Design and fabrication	Intermediate	Easy	Difficult	Intermediate	Intermediate	Difficult
Use at high pressure	Easy	Intermediate	Easy	Easy	Easy	Difficult

Table 2.2: Characteristics of group combustion regimes (Chiu & Liu, 1977).  
 Reproduced from Nakamura *et al.* (2005).

Combustion Mode	Group Number	Characteristics	
Single droplet	$G < 0.01$	All droplets in group burn with envelope flames, unaffected by other droplets	
Internal group	$0.01 < G < 0.1$	Droplets inside group flame just evaporate and droplets outside group flame burn with envelope flames	
External group	$0.1 < G < 100$	Group flame encloses whole droplet group	
External sheath	$G > 100$	Non-evaporating region found inside evaporating region in droplet group	

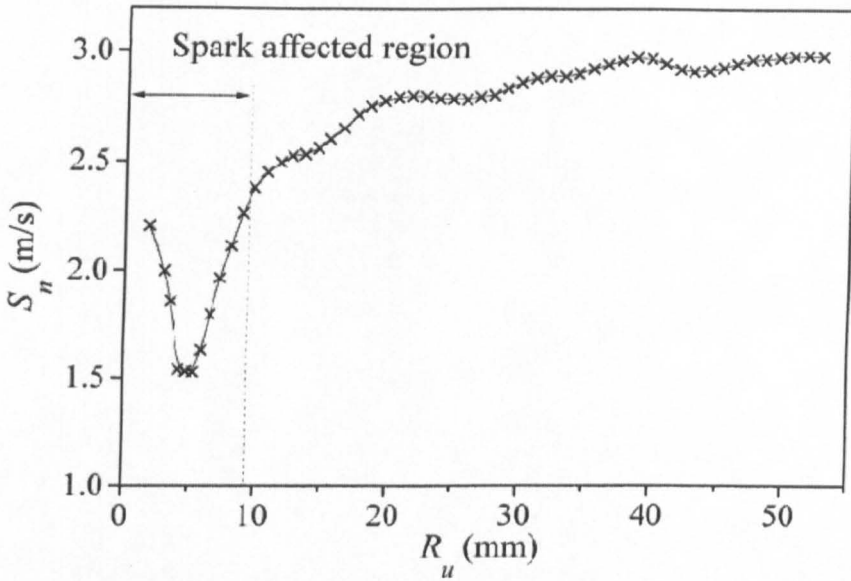


Figure 2.1: Measured flame speeds of stoichiometric iso-octane-air with initial temperature of 358 K and pressure of 100 kPa at different flame radii. Reproduced from Bradley *et al.* (1998).

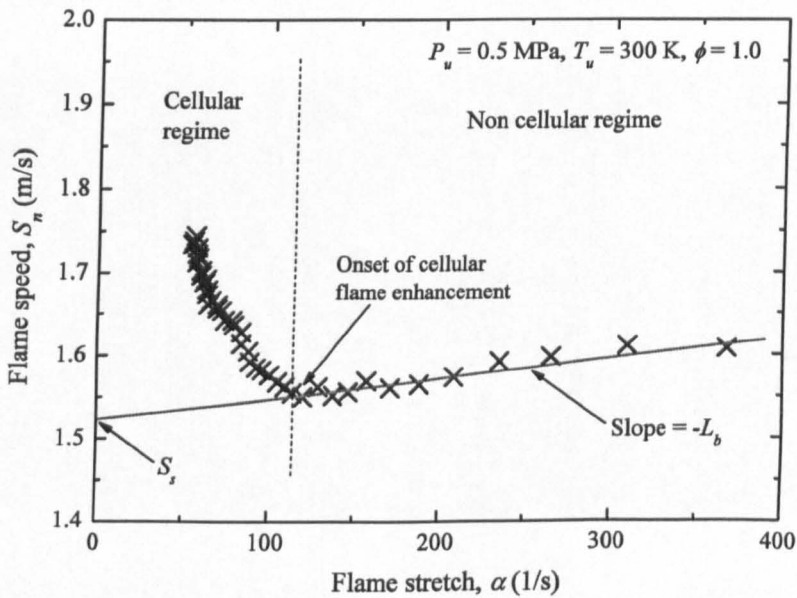


Figure 2.2: Variation of flame speed with flame stretch for stoichiometric methane-air at 500 kPa and 300 K. Reproduced from Gu *et al.* (2000).

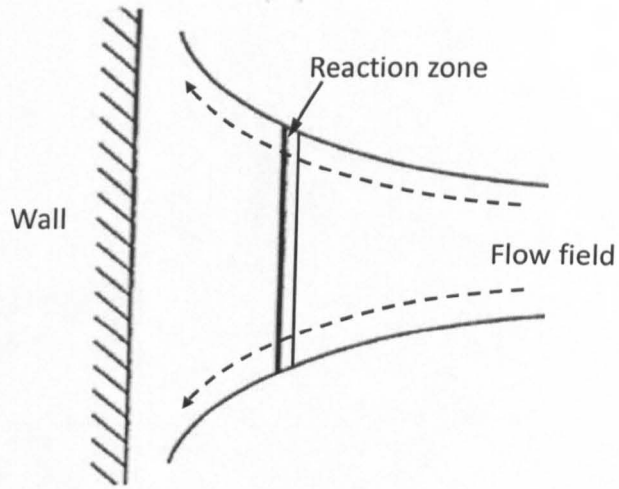


Figure 2.3: Schematic of a planar flame situated in a divergent stagnation flow.

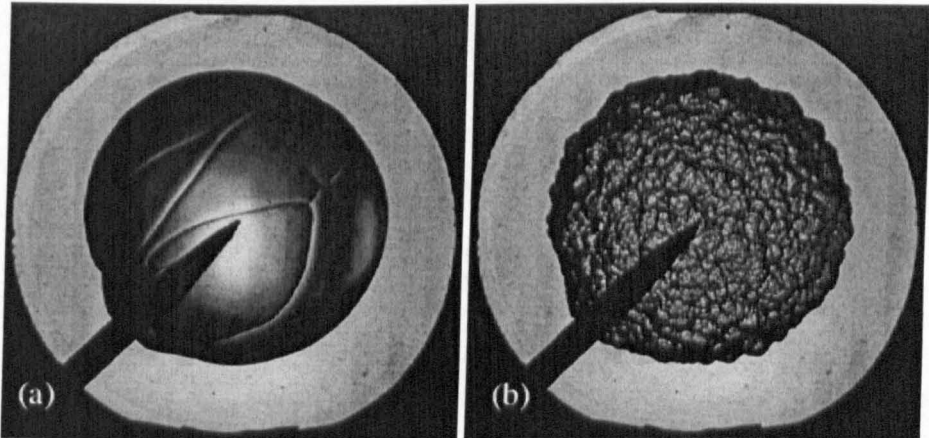


Figure 2.4: Comparison of flame structure using schlieren images between a (a) smooth flame and (b) cellular flame. Reproduced from Mandilas (2008).

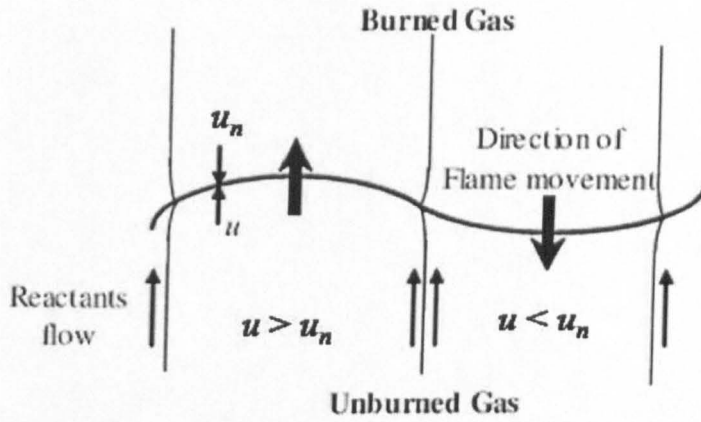


Figure 2.5: Schematic diagram of the hydrodynamic instability mechanism. Reproduced from Law (1988).

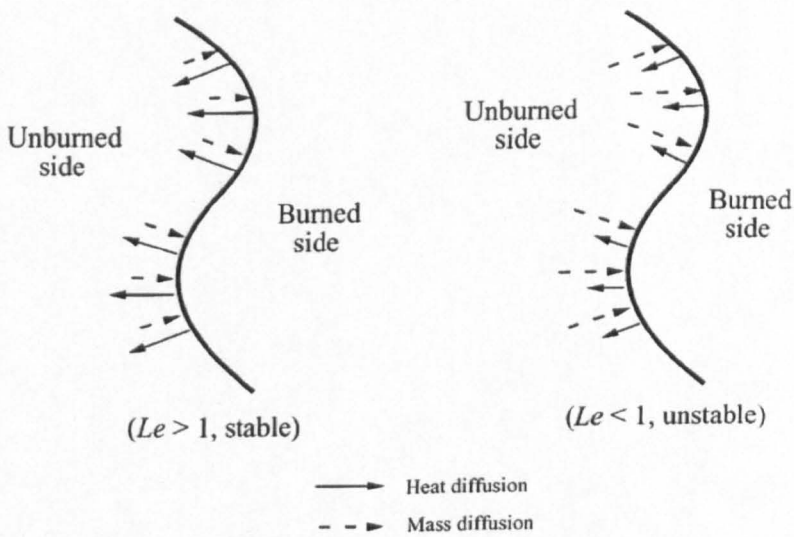


Figure 2.6: Schematic diagram of the thermo-diffusive instability mechanism. Reproduced from Law (2006).

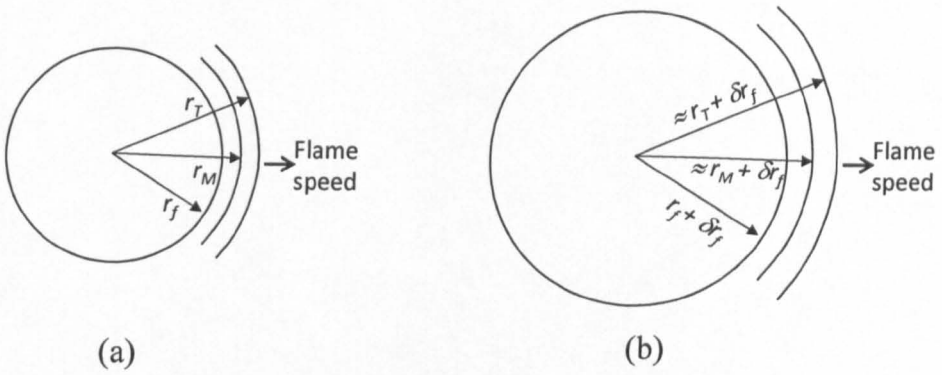


Figure 2.7: Conceptual diagrams of the effects of stretch on the flame motion for an expanding spherical flame at (a)  $t = 0$ , (b)  $t = \delta t$ . Reproduced from Law (2006).

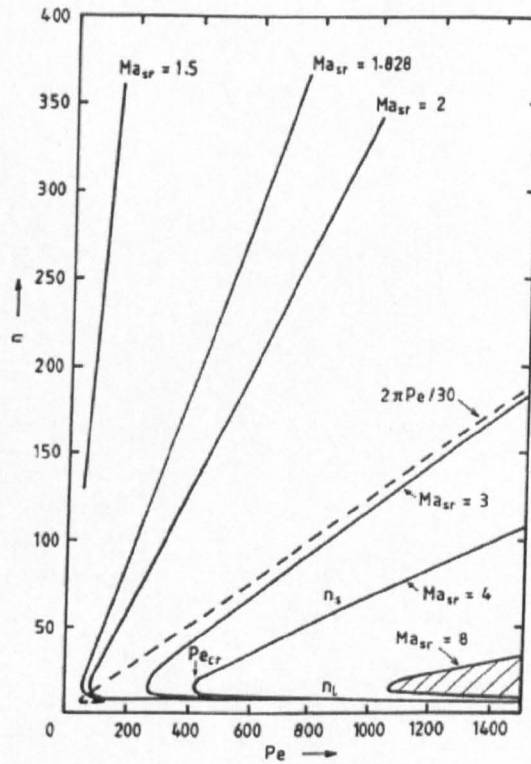


Figure 2.8: Theoretical wave numbers,  $n$ , at limits of flame stability for different  $Ma_{sr}$ , as function of Peclet number. Shaded area is a peninsula of instability for  $Ma_{sr} = 8$ . Reproduced from Bradley *et al.* (2000).

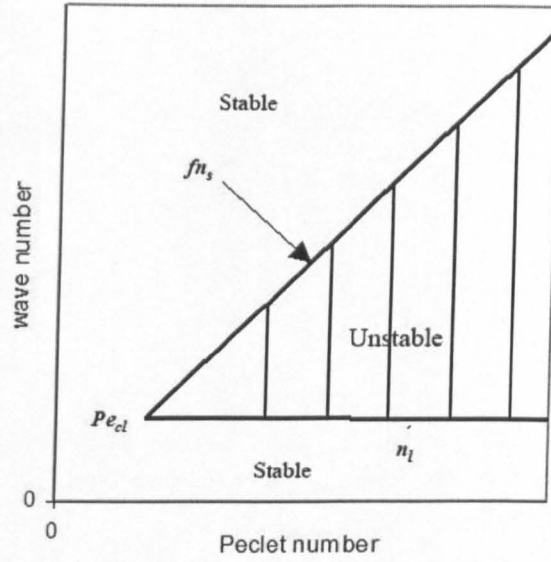


Figure 2.9: Instability peninsula, with limiting wave numbers  $fn_s$  and  $n_l$ . Critical Peclet number,  $Pe_{cl}$  at tip of peninsula. Reproduced from Al-Shahrany *et al.* (2005).

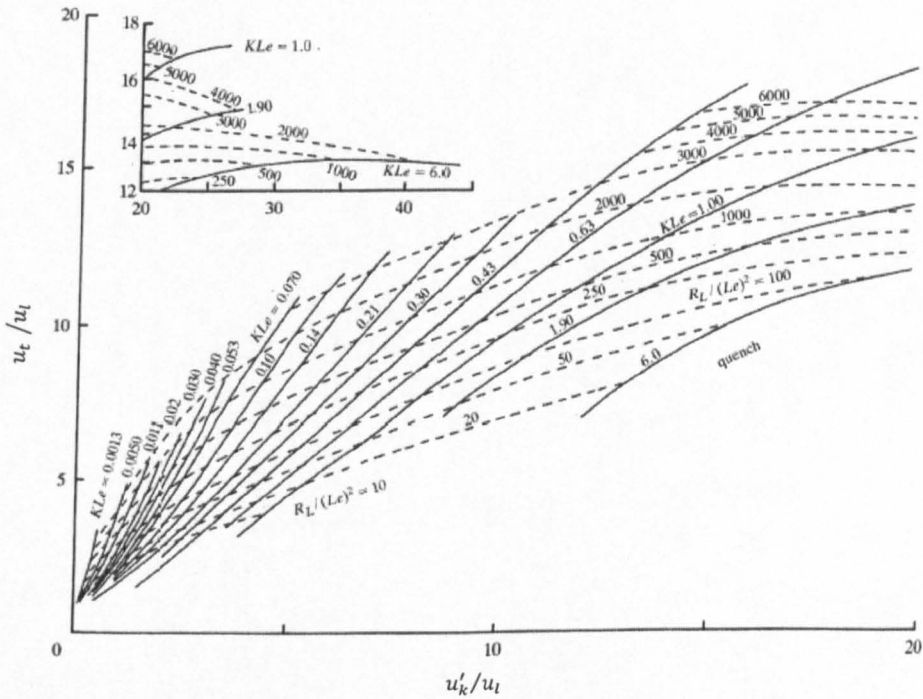


Figure 2.10: Correlation of turbulent burning velocities. Broken curves show  $R_L / (Le)^2$ , with  $R_L$  evaluated for fully developed r.m.s. turbulent burning velocity,  $u'$ , equal to  $u'_k$ . Reproduced from Bradley *et al.* (1992).

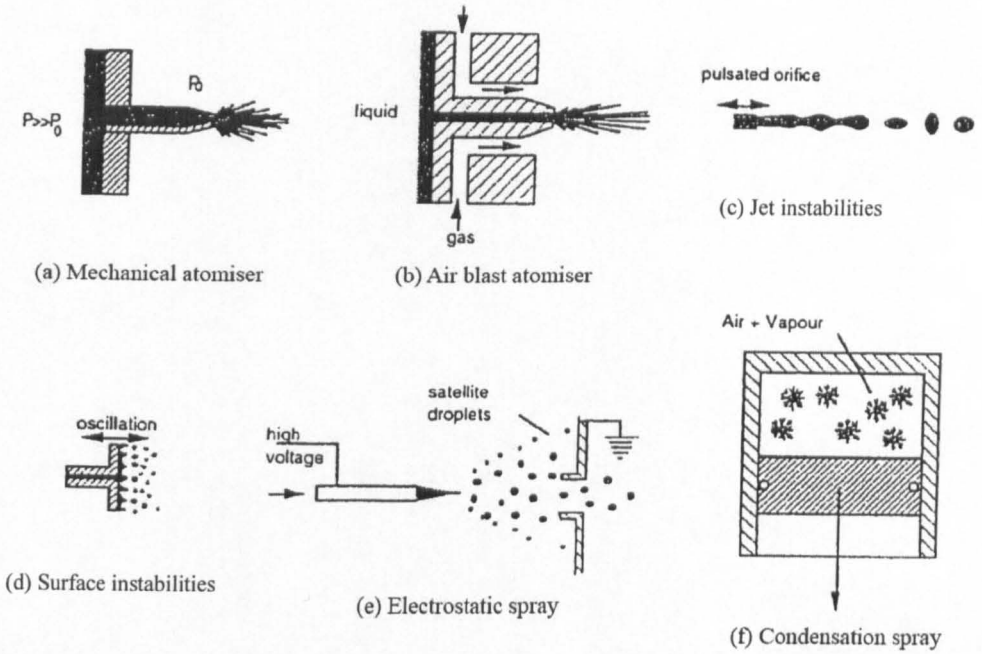


Figure 2.11: Different types of droplet generators. Reproduced from Gökalp *et al.* (1999).

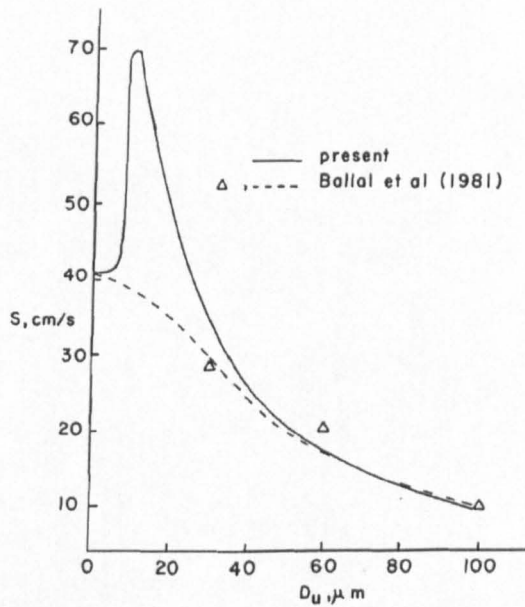


Figure 2.12: Variation of burning velocity at different droplet size of stoichiometric medium diesel oil-air sprays. Reproduced from Polymeropoulos (1984).



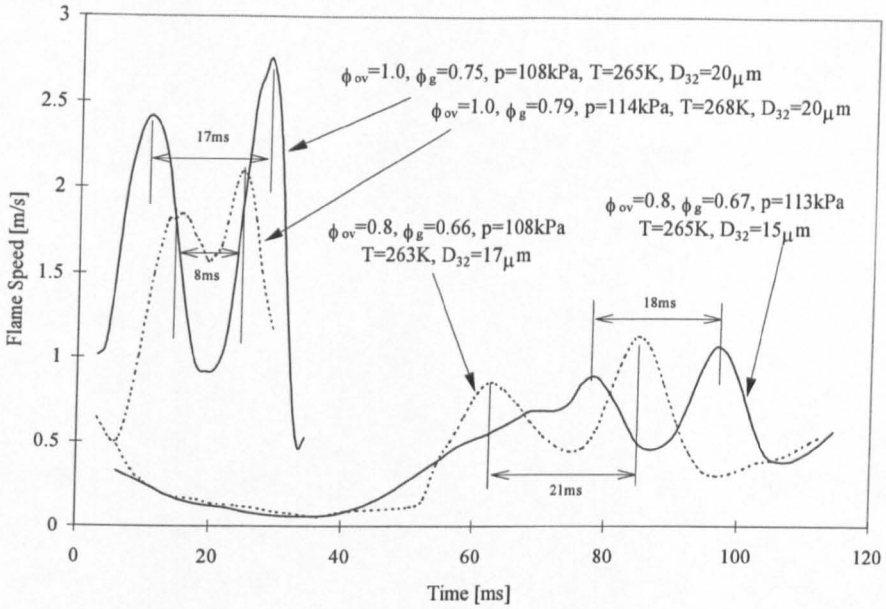


Figure 2.13: Variation of flame speed with time for oscillating flames of iso-octane-air aerosols at  $\phi_{ov} = 0.8$  and  $1.0$ . Also shown are oscillation periods. Reproduced from Atzler (1999).

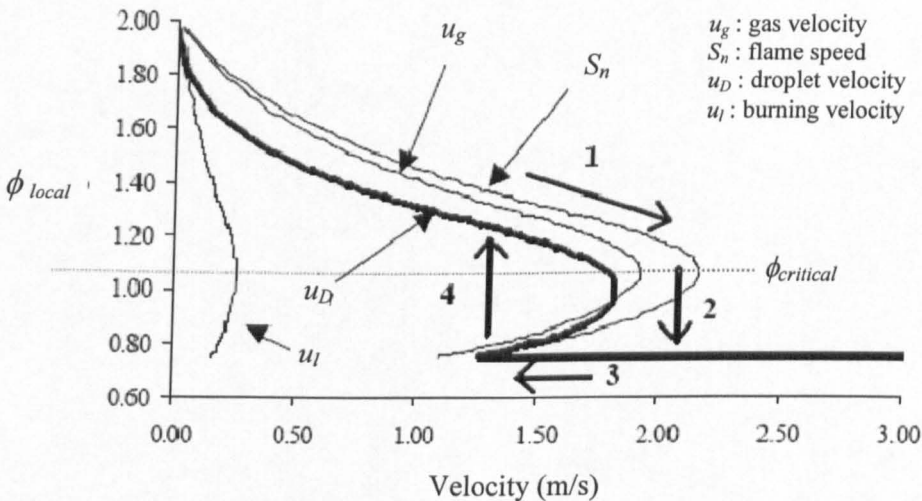


Figure 2.14: Effect of a variation of  $u_D$  on the local  $\phi$  and resulting values of  $S_n$ ,  $u_g$  and  $u_l$  for aerosol mixture with  $\phi_{ov} = 1.0$  and  $\phi_g = 0.75$ . Reproduced from Atzler *et al.* (2001).

## Chapter 3

### Experimental Apparatus and Techniques

#### 3.1 Introduction

In this chapter, the apparatus and techniques for the study of aerosol characterisation and flame propagation are described. The rig and apparatus for the experimental work is described in Section 3.2 and the mixture preparation technique is presented in Section 3.3. Section 3.4 refers to instrument synchronisation and acquisition during the expansion process and the combustion events. In Section 3.5, the description of laser diagnostic systems used for characterising the aerosol mixture is presented. This comprises measurement of droplet size using Phase Doppler Anemometry and droplet density using laser attenuation. During combustion events, flames were recorded using high speed schlieren photography. This technique, including the processing of flame images, is also presented in Section 3.5. Only brief descriptions are given when detailed information exists elsewhere.

#### 3.2 Combustion apparatus

The combustion rig is shown photographically in Fig. 3.1 and schematically in Fig. 3.2. It comprised an explosion vessel, an expansion tank and interconnecting pipework, various valves and control systems and measurement instrumentation. A description of each component is presented in Sections 3.2.1 and 3.2.2.

The present rig was developed by Atzler (1999) and used by Marquez (2003) and Sulaiman (2007) for aerosol combustion studies. Aerosol mixtures were generated in situ, using the Wilson cloud chamber principle (Wilson, 1897). In this technique, a homogeneous fuel air mixture is cooled by expansion until the fuel vapour condenses into a cloud of liquid droplets as described in Section 3.3. In addition to the previous studies in Leeds (Atzler, 1999; Marquez, 2003; Sulaiman, 2007), this method has been used for aerosol combustion studies by Hayashi and Kumagai (1975, 1976) and Nomura *et al.* (2000, 2007).

### 3.2.1 Explosion vessel

A comprehensive description of the present system can be found in Atzler (1999). As shown in Fig. 3.1, it comprised a cast steel cylinder of 305 mm diameter and 305 mm length with a working volume of 23.2 litres. Optical quality BK7 windows, 150 mm diameter and 39 mm thick, were fitted in each end plate. Four identical eight-bladed fans were fitted, equi-spaced around the central circumferential plane at 45° to the horizontal. These were connected to 3-phase 1.5 kW motors and electronic motor controllers. In laminar studies, prior to the experiment, the fans were used only for mixing of fuel and air. For studies of turbulent combustion, the fans provided the required flow field and generated nearly isotropic turbulence within the field of view of the windows. Turbulence was characterised by Lawes (1987) in gaseous mixtures and it was found by Marquez (2003) to be unchanged in the presence of aerosols. Full details, including power spectra, velocity and lengths scale for this vessel are given in Abdel-Gayed *et al.* (1987). The turbulence root mean square velocity,  $u'$ , was found to be a linear function of fan speed given by

$$u' = 0.0016\omega \quad (3.1)$$

where  $\omega$  is the fan speed in rpm, and the integral length scale is approximately constant at 40 mm (Lawes, 1987; Marquez, 2003).

As shown in Fig. 3.1 and 3.2, the explosion vessel was connected by a ½" BSP fitting at the top of it to a central fill and discharge valve, which linked the vessel to the air supply and the exhaust. A pressure transducer, used to monitor the mixture initial pressure, was also connected to this port. The pressure transducer was protected from combustion pressure by an additional isolating valve fitted immediately adjacent to the port. Four 1" BSP ports were equi-spaced around the explosion vessel, as shown in Fig. 3.2. The top port was permanently connected to the expansion pipe and the others were used as appropriate for ignition, thermometry and an additional 25.4 mm (1") diameter window. Two electrical heaters with a total installed power of 4.5 kW were used to heat up the vessel to the temperature required for an experiment. As shown in Fig. 3.1, each heater was mounted close to the surface of an end plate and, in conjunction with the running fans during heating, provided a homogeneous temperature distribution throughout the vessel. Both heaters were controlled by a CAL 3200 electronic controller.

Temperature measurements during expansion were required to enable the determination of initial conditions for combustion experiments. Two sizes of K-type thermocouples were used. For the required high frequency response during calibration studies of the expanding mixture, a 25  $\mu\text{m}$  fine wire thermocouple was used. However, fine wires were too fragile to be used during combustion studies. Hence, in all work that did not require a fast response, a 200  $\mu\text{m}$  thermocouple was employed. The thermocouples were connected, as required, through a home-built 12-way input selector to a Digitron 2751-K digital readout, with analogue output. The analogue output was used for the computer recording of temperature histories. Measurements of total static absolute pressure and fuel partial pressure, as well the pressure change during expansion, were made using a precision pressure transducer-amplifier/readout system, DRUCK PDCR 820 and DPI 280. It was fitted in the expansion pipe, 400 mm from the inner surface of the explosion vessel, behind the isolating valve. This transducer had a range of 0 to 350 kPa gauge, with a resolution of 0.1 kPa, and was calibrated by the manufacturer.

### **3.2.2 Expansion vessel**

Aerosol mixtures were prepared, as described in Section 3.3, by expanding at a controlled rate, a gaseous pre-mixture from the explosion vessel into the expansion vessel with a volume of 28 litres. As shown in Fig. 3.1, this tank was connected to the explosion vessel through the top port. The tank was linked to the exhaust system through a ball valve which was connected to a  $\frac{1}{2}$ " BSP port. Prior to its use in the present system, the expansion tank was used as a combustion vessel and, hence was, capable of withstanding combustion pressure. Therefore, the expansion tank could safely withstand any explosion of the fuel-air mixture that was expanded into it.

The explosion vessel and expansion tank were connected by a pipeline of 38 mm internal diameter, into which was fitted an expansion valve comprising a ball valve of 26 mm internal diameter. This was operated pneumatically and was used to separate the explosion vessel and the expansion tank. It was placed immediately outside the explosion vessel. Mixture expansion was controlled by a throttle, which comprised of interchangeable orifice plates. For example, in laminar studies, an orifice of 6 mm produced an expansion time to reach pressure equilibrium between the two vessels of approximately four seconds. This long duration, relative to that for combustion, allowed

for easy synchronisation of the spark and diagnostics with respect to the desired state of mixture expansion. The slow expansion also minimised any resulting flow disturbances within the combustion chamber.

### **3.2.3 Ignition system**

In the present work, two ignition systems were available. The first was used in previous studies (Atzler, 1999; Marquez, 2003; Sulaiman, 2007) and is described in Section 3.2.3.1. This system was found to be unreliable particularly in providing a consistent observation of ignition as described in Section 5.2.1. The second system was a variable energy ignition unit, described in Section 3.2.3.2. Using each system, fuel-air mixtures were ignited centrally in the explosion vessel with a standard Miniglo model aircraft engine spark plug. The plug was held on an extension screwed into one of the horizontal 1" BSP ports of the vessel. The electrodes and outside earth shell were stainless steel wire and tube, respectively. The insulator was made of a ceramic tube and all components were bonded together. The body length was 60 mm and 4 mm diameter approximately.

#### **3.2.3.1 Fixed energy ignition unit**

This unit was used and described by Atzler (1999), Marquez (2003) and Sulaiman (2007). As shown by a circuit diagram in Fig. 3.3, it comprised a capacitor discharge unit and a discharge trigger switch. The capacitor was charged to typically between 35 and 40 Volts using an adjustable DC power supply. The voltage across the capacitor was monitored by a voltmeter. The trigger produced a small coil generated spark at the spark electrodes, thus providing an ionised electrical path for the release of the capacitor discharge, which supplied the main spark. This unit produced a spark with energy of approximately 300-400 mJ (Atzler, 1999). The limitation of this unit was due to the production of an excessive ignition energy with long spark duration. Based on indirect measurement by Sulaiman (2007), who used natural light imaging, the average duration of the spark discharge from this unit was about 8 ms.

#### **3.2.3.2 Variable energy ignition unit**

This unit was developed by Lung (1986) and modified by Ali (1995). A schematic is shown in Fig. 3.4 and a comprehensive description is given in Ali (1995).

This unit allowed spark energy and duration to be controlled separately. The main spark unit was designed to discharge a 40  $\mu\text{F}$  capacitor through the spark gap by means of a bank of resistors which controlled the current. The capacitor was charged by a 600 Volts DC power supply. Control of the spark current was achieved by the series resistors which could be isolated or included within the circuit through switches. Increasing the series resistance of the circuit reduced the current through the spark gap, while reducing the series resistance increased the current. Steps of 0.1A and 0.5A were used for the low energy setting which varied current from 0 to 3A and steps of 0.75A was used for the high energy setting which varied current from 6A to 12A. This unit enabled the spark duration to be varied from 0 to 1 ms in steps of 10  $\mu\text{s}$ .

The voltage and current outputs could be monitored by an oscilloscope for measuring the discharge energy. The time of discharge across the spark gap was obtained from the recorded pulse width. The discharged energy,  $E$  (mJ), across the spark gap is given by (Ballal and Lefebvre, 1975)

$$E = \int_0^t VI dt \quad (3.2)$$

where  $V$  is the voltage drop in volts,  $I$  is the current in amperes and  $t$  is the total spark duration in seconds. In the present study, combustible mixtures were ignited at a settings of 6 A and fixed spark duration of 800  $\mu\text{s}$ . For this setting, the ignition energy was estimated of about 180 mJ. Since this energy was calculated based on the stored energy, the delivered energy should be lower by up to 50% (Maly and Vogel, 1979) as current and voltage might have been lost between the points of measurement and the electrodes.

### 3.3 Mixture preparation

In this study, two fuels were used and these are described in Section 3.3.1. The preparation of aerosol mixtures consists of three stages which include pre-heating of the explosion vessel, preparation of gaseous pre-mixtures and an expansion process that generates the aerosol mixtures. These are discussed below.

### 3.3.1 Fuels

The principal fuel for this study was iso-octane, which is the single component fuel closest to gasoline. It was chosen because data for its gaseous combustion have been obtained at Leeds for a wide range of experimental conditions and are available for comparison with results from the present study. Atzler (1999) demonstrated that the evaporation and condensation properties of iso-octane were suitable for the current research apparatus, with regard to the temperature and pressure limitations of the vessel. Iso-octane, 2-2-4 trimethylpentane, was supplied by Ultrafine Ltd. and was specified to be at least 99.9% pure with 50 ppm maximum water content.

The other fuel that used for this study was ethanol. It was supplied by Fisher Scientific UK Ltd. and was specified at 99.7% purity. It was considered because this fuel has been widely recognised as one of the promising alternative fuels for engines. It has been identified as offering a potential solution to improve air quality when used to replace conventional gasoline in engines because of its good anti-knock characteristics and the reduction of CO and unburned HC emissions (Moreira and Goldemberg, 1999). This fuel has a lower molecular weight and higher heat of vaporisation than iso-octane (Yaws, 1992). Since the vapour pressure of ethanol was nearly close to that of iso-octane, the condensation process to generate ethanol aerosols was similar to that with iso-octane.

### 3.3.2 Pre-heating of explosion vessel

Prior to experiments, the explosion vessel was heated by its internal heaters to a temperature of 303 K for the iso-octane and 313 K for the ethanol, according to the experimental requirements. This temperature ensured complete evaporation of the liquid fuel. It also provided the required temperature datum to enable comparison with the data of other workers, for both gaseous and aerosol experiments.

In order to ensure a spatially homogeneous condensation, a uniform temperature throughout the mixture was required. For this, the explosion vessel was heated to a preliminary value above the desired initial temperature and then left to cool and homogenise for approximately one hour. Temperature uniformity was ascertained by monitoring the temperature at several points around the outside of the vessel. Good temperature homogeneity across the vessel was assumed when the difference between the measurements was less than 2 K.

### 3.3.3 Preparation of gaseous pre-mixtures

Before the introduction of fresh combustible mixture, the explosion vessel and expansion tank were evacuated and flushed with air to remove residuals from previous experiments. After flushing, the explosion vessel and expansion tank were evacuated again before the valve connecting was closed. Liquid fuel was then injected slowly into the explosion vessel through a needle valve at a pressure close to vacuum, to aid complete and fast evaporation. The fuel was injected using either a 5 ml or 10 ml Hamilton Microliter glass syringe. Atzler (1999) found that the accuracy of the injected volumes using this syringe was better than  $\pm 0.015$  ml and  $\pm 0.03$  ml, respectively, yielding an equivalence ratio accuracy of within  $\pm 0.5\%$ . All fans were run at 1500 rpm to improve vaporisation of the liquid fuel. During fuel injection, the pressure in the explosion vessel was monitored to provide an independent check of the equivalence ratio and to ensure complete fuel vaporisation. The appropriate volume of liquid fuel for given initial conditions in terms of temperature, pressure and overall equivalence ratio, was calculated using the stoichiometric equation and the ideal gas law as described in Chapter 4. After fuel injection was completed, a settling time of 40 seconds was allowed to ensure proper evaporation of fuel. It was important to use the same settling time in all cases during mixture preparation for consistency of results. Such difference in aerosol calibration due to settling time is discussed in Section 4.6.

After fuel injection, clean dried air was injected into the explosion vessel to take the final pressure of air-fuel mixture up to that required for an experiment. Bottled industrial grade dry air was used in the fuel-air mixtures to minimise the possibility of water droplet generation during the expansion process. It also minimised the presence of impurities which might affected aerosol formation as described in Section 4.6. The dried air was supplied by BOC Ltd., with a specified composition of: 78% N<sub>2</sub>, 21% O<sub>2</sub>, 0.9% Ar, H<sub>2</sub>O < 250 ppm, CO < 10 ppm, CO<sub>2</sub> < 500 ppm and oil < 1 ppm. The effects of foreign species on combustion were assumed to be negligible. The air-fuel mixture was then allowed to blend for about 40 seconds with the fans running at 1500 rpm to achieve homogeneity.

### 3.3.4 Generation of aerosol

Following mixture preparation as described above, the expansion valve was opened and the mixture was allowed to expand into the expansion tank. When the



temperature became lower than the saturation temperature of the fuel, condensation occurred. A detailed thermodynamic analysis of the process is given in Chapter 4.

For combustion studies, the aerosol mixtures were ignited at selected times after the start of expansion, allowing variation of the initial conditions at ignition, in terms of liquid and gaseous phase equivalence ratio, droplet size, pressure and temperature. Combustion occurred while the mixture was expanding. However, since the combustion duration was short, typically of the order of 20 to 60 ms, relative to the expansion duration of about four seconds for laminar conditions, quasi steady state was assumed in the unburned mixture.

For turbulent experiments, it was necessary to make the expansion time to pressure equilibrium much faster than for laminar conditions, which was approximately 0.5 seconds with 25 mm orifice. This was required because the rapid heat transfer from explosion walls when the fans were switched on, allowed the maintenance of an aerosol for only a very short period. In this case, the combustion duration was typically less than 20 ms and hence the assumption of quasi steady condition was also applied for turbulent conditions.

### **3.4 Data acquisition and synchronisation**

Accurate control of experimental conditions and data acquisition required the precise synchronisation of measurement equipment and data acquisition systems with the expansion and combustion events. The datum parameter for all experiments was the start of expansion. All equipment was triggered by a primary trigger switch, PTS, fitted to the expansion valve, as shown in Fig. 3.1. This consisted of a micro switch which was actuated by the expansion valve lever, within 2° of lever movement and before the actual start of valve opening. Consistency of valve opening was assessed and discussed by Atzler (1999).

Measurements of pressure and temperature were synchronised with the start of expansion. Pressure and temperature records were digitised on a 16-bit National Instruments analogue-to-digital conversion board, model PCI-6034E. The signal inputs to the ADC were analogue voltages from the thermometer and pressure transducer amplifier. The output sensitivity of the thermometer was 1 mV/K and that of the transducer amplifier 1 mV/kPa. A typical temperature measurement had a bandwidth of

approximately 50 K or 50 mV and a typical pressure measurement had one of approximately 100-200 kPa or 100-200 mV.

In addition to error associated with the thermometer and ADC systems, the raw data displayed fluctuations of approximately  $\pm 1.2$  K at a frequency of approximately 50 Hz, which indicated electro-magnetic noise from the mains electricity supply. This was minimised by using a 5-point moving average smoothing routine, which reduced the fluctuations to about  $\pm 0.2$  K. The control and monitoring of the measurements were done using LabView version 8.5 installed into a desktop computer.

### **3.5 Instrumentation for aerosol characterisation and flame analysis**

In the present work, two laser diagnostic systems were used simultaneously for characterising the aerosol mixtures. These were PDA, described in Section 3.5.1 and laser attenuation, described in Section 3.5.2. Aerosol properties were also determined by equilibrium calculations based on pressure, temperature and overall equivalence ratio, as discussed in Chapter 4. Flame propagation was recorded with high speed schlieren digital movie photography to obtain flame speeds and burning velocities and this is described in Section 3.5.3.

#### **3.5.1 Phase Doppler Anemometry (PDA)**

PDA is an established optical technique that measures, simultaneously, size and velocity of spherical particles. Advantages of PDA are that it is a non-intrusive measurement, can be used on-line and in-situ. It is an absolute measurement technique which means no calibration is required, has very high accuracy and very high spatial resolution (small measurement volume). This system was available to the author from the EPSRC (Engineering and Physical Science Research Council) loan pool for a period of three months during the present work. A similar PDA system was used in the present vessel (Marquez, 2003; Sulaiman, 2007) and described in detail by Marquez (2003). Hence, the following is a brief description about the technique as detailed information exist elsewhere.

Phase doppler anemometry is an extension of laser doppler anemometry (LDA) and is based on light scattering interferometry (Ofner, 2001). Laser doppler anemometry is a well known technique for measuring velocity of particles at a point. The

measurement point is defined by the intersection of two coherent laser beams and the measurements are performed on single particle as it move through this point. When a particle passes through this measurement point, the scattered light forms an optical interference fringe pattern. The scattered interference sweeps past a receiver unit at the Doppler difference frequency, which is proportional to the velocity of the particle. The spatial frequency of the interference fringe pattern is inversely proportional to the diameter of the particle.

The arrangement of PDA apparatus in the present work is shown in Fig. 3.5, where it was used simultaneously with laser attenuation measurements. Detail of laser attenuation measurements are described in the following section. The PDA system and the instrumentation was manufactured by TSI Instruments Ltd and comprised the following:

1. An argon-ion laser source, Spectra Physics, model Stabilite 2017, with an output power of 2W.
2. TSI multicolour laser beam separator, model 9201, capable of separating the beam into two wavelengths: 514 nm (green) and 488 nm (cyan).
3. TSI transmitter probe with focal length of 363 mm
4. Optical fibre cables to convey the beams to the transmitter
5. Fibreoptic receiver, model 450300, with focal length of 500 mm
6. Photo detector module, model PDM 1000: receives optical signals from receiver and send as electric signals to FSA signal processor.
7. Signal processor, Multibit digital processor model FSA3500: receives and processes electric signals from PDM such as frequency, phase, burst transit time and arrival time, and sends to the computer.
8. TSI traverse system, Isel® Traverse controller, to place the transmitter-receiver arrangement.

For the present work, the receiver and transmitter were positioned at an angle of  $32^\circ$  as shown in Fig. 3.5, being the optimal angle for PDA measurements. A rising logic level signal (5V) from the expansion controller was connected to the pulse input connection located on the back of PDA signal processor box. This was used to synchronise the expansion event with PDA data acquisition by resetting the time stamp during data collection. Data from signal processor were processed using a software from TSI, Flowsizer 2.0.3 installed on a computer. The program requires input of droplet-media

refractive index and transmitter-receiver angle. The outputs from this program were diverse, but of particular interest to the present work were: individual and arithmetic mean droplet diameter,  $D_{10}$ .

### 3.5.2 Laser attenuation system

This technique measures the attenuation of a laser beam due to its passage through a specific fluid medium. Syzmanski and Wagner (1990) claimed that this technique was suitable for measuring aerosol concentrations with diameters larger than  $0.1 \mu\text{m}$  and concentrations up to the order of  $10^{10} \text{ m}^{-3}$ . For the present study, this technique was used for two reasons. First, laser attenuation enabled assessment of the starting point of condensation by measuring the reduction in laser power when the first droplets appeared. Second, laser attenuation during the expansion event was used to estimate the number density of droplets generated using the Beer-Lambert law (Bachalo *et al.*, 1988):

$$\frac{I}{I_o} = \exp(-N_D \sigma_e L) \quad (3.3)$$

where  $I_o$  and  $I$  are the intensities of the original and attenuated laser beam, respectively,  $N_D$  is the number density,  $L$  is the optical path length taken to be 305 mm, which is the length of the vessel, and  $\sigma_e$  is the extinction cross-section which is constant for visible light frequencies. It is defined by Bachalo *et al.* (1988):

$$\sigma_e = \frac{\pi}{4} \overline{Q}_e D_{20}^2 \quad (3.4)$$

where  $\overline{Q}_e$  is the mean extinction efficiency taken to be 1 for uniform sprays (Payne *et al.*, 1986; Nicolas, 2009) and  $D_{20}$  is the surface mean diameter of droplet (defined in Section 2.5). During the present work, values of  $D_{20}$  were not measured, but were substituted with values of arithmetic mean diameter,  $D_{10}$  that was obtained from PDA measurement described in Section 3.5.1. This was considered to be a reasonable approximation because the narrow distribution of droplet size that obtained in the present vessel resulted in a little difference between  $D_{20}$  and  $D_{10}$ .

The laser attenuation system was arranged simultaneously with the PDA system, as shown in Fig. 3.5. It comprised a uniphase 20 mW He-Ne source laser with a wavelength of 632 nm and a laser power meter as a receiver. The laser beam was

expanded to a diameter of 150 mm by an Olympus A40 microscope lens, where it was collimated by a 150 mm diameter plano-convex lens with a focal length of 1000 mm. After the beam passed through the two windows of the explosion vessel, a second, identical lens was used to refocus the parallel beam onto a pinhole. The laser was detected by a laser power meter which produced an analogue voltage output which was proportional to the laser input. This was received by the ADC system, described in Section 3.4.

An input-output calibration undertaken by Marquez (2003), who uses the same technique, using absorptive neutral density filters of known attenuation, showed that the laser power meter has a linear response in voltage for intensity attenuation throughout the whole range of operating conditions. This is given by:

$$\frac{I}{I_o} = \frac{\left( \frac{V}{V_o} + 0.0279 \right)}{1.0483} \quad (3.5)$$

where the voltage ratio  $V/V_o$  was the ratio of attenuated and non-attenuated laser beam obtained from experiment.

### 3.5.3 High speed schlieren photography

The growth rate of spherically expanding flames was recorded using high speed schlieren cine photography. This technique is a visual process that used to photograph the flow of fluids of varying density. In the present work, it was used to visualise the density gradients between burned and unburned mixtures. Using the path-integrated image from analysed high speed flame movies, flame radius against time data was measured to derive flame speed and burning velocity, following the image processing technique presented in Section 3.5.3.2. The schlieren images were also used to study the onset and development of cellularity in aerosol flames as discussed in Chapter 5.

#### 3.5.3.1 Image recording

The arrangement of the image recording system is shown in Fig. 3.6. In this setup, a 50W tungsten light was focused by a 45 mm diameter plano-convex lens with 70 mm focal length onto a pinhole. Then the light was collimated by a 150 mm diameter plano-convex lens with 1000 mm focal length. After the light passed through the two windows of the explosion vessel, a second, identical lens was used to refocus the

parallel beam onto a pinhole. A high-speed digital camera (see details below) fitted with a Nikkor 50 mm lens was positioned behind the schlieren focus to record the flame propagation. In laminar experiments, a Phantom V4 high-speed digital camera was used with full resolution at 512x512 pixels. At this resolution, it is capable of recording schlieren movies at 1000 frames per second. For turbulent experiments, a Photron Ultima APX-RS high-speed digital camera with a 10-bit CMOS type chip was used. This camera was operated at between 3000 and 5000 frames per second, depending on the level of rms turbulence velocity. At both frame rates, the image resolution was 480x480 pixels.

A synchronisation unit, the circuit of which is shown in Fig. 3.7, was used to synchronise the start of camera operation with that of the expansion process with ignition. When the expansion valve opened, it activated the primary trigger switch, PTS, which sent a signal to start an Omron H8GN countdown timer. The signal from the timer was converted by the signal converter into break (OFF) and make (ON) signals for the camera and ignition systems, respectively.

### **3.5.3.2 Image processing**

The processing technique for the schlieren images was described by Orsmy (2005) and Mandilas (2008), and only brief details are given here. For each combustion experiment, about 30-100 schlieren images were recorded. These images covered the period from just before ignition until the flame edge was no longer visible, due to the window size. The flame images were originally in a grayscale format. Using an algorithm coded in the Matlab software environment, by Mandilas (2008), the flame radius for each image was calculated by thresholding the grayscale image to yield a white flame image on a black background. The flame radius was calculated as the radius of a white circle. A transparent grid of 10 mm x 10 mm attached to the window of the vessel was first photographed with the setup used for flame studies to provide a scale with which measurements could be scaled to true distances. From the time interval between images and flame radius measurements, flame speed and burning velocity were calculated.

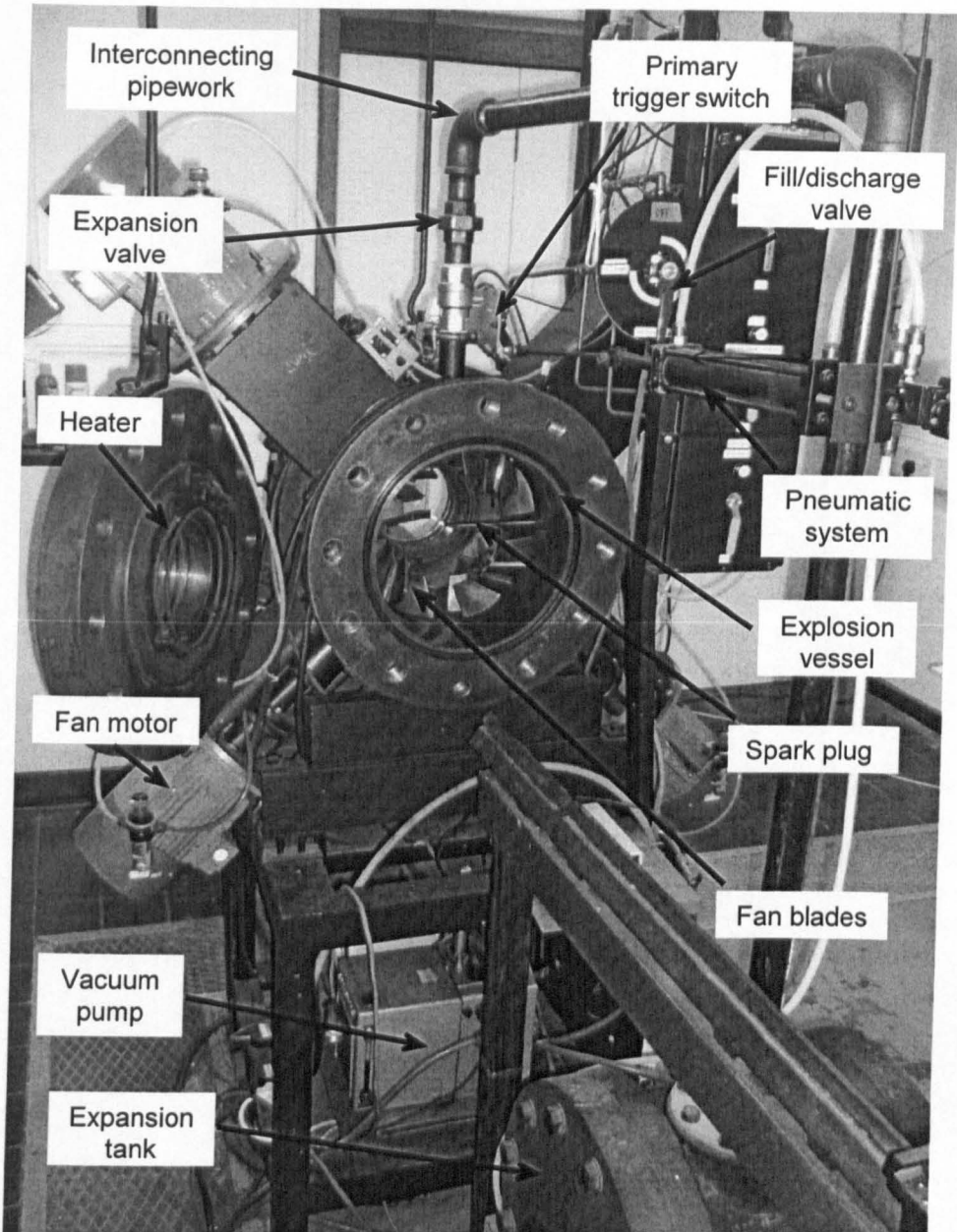


Figure 3.1: Photograph of the cylindrical explosion vessel, with one end plate removed.

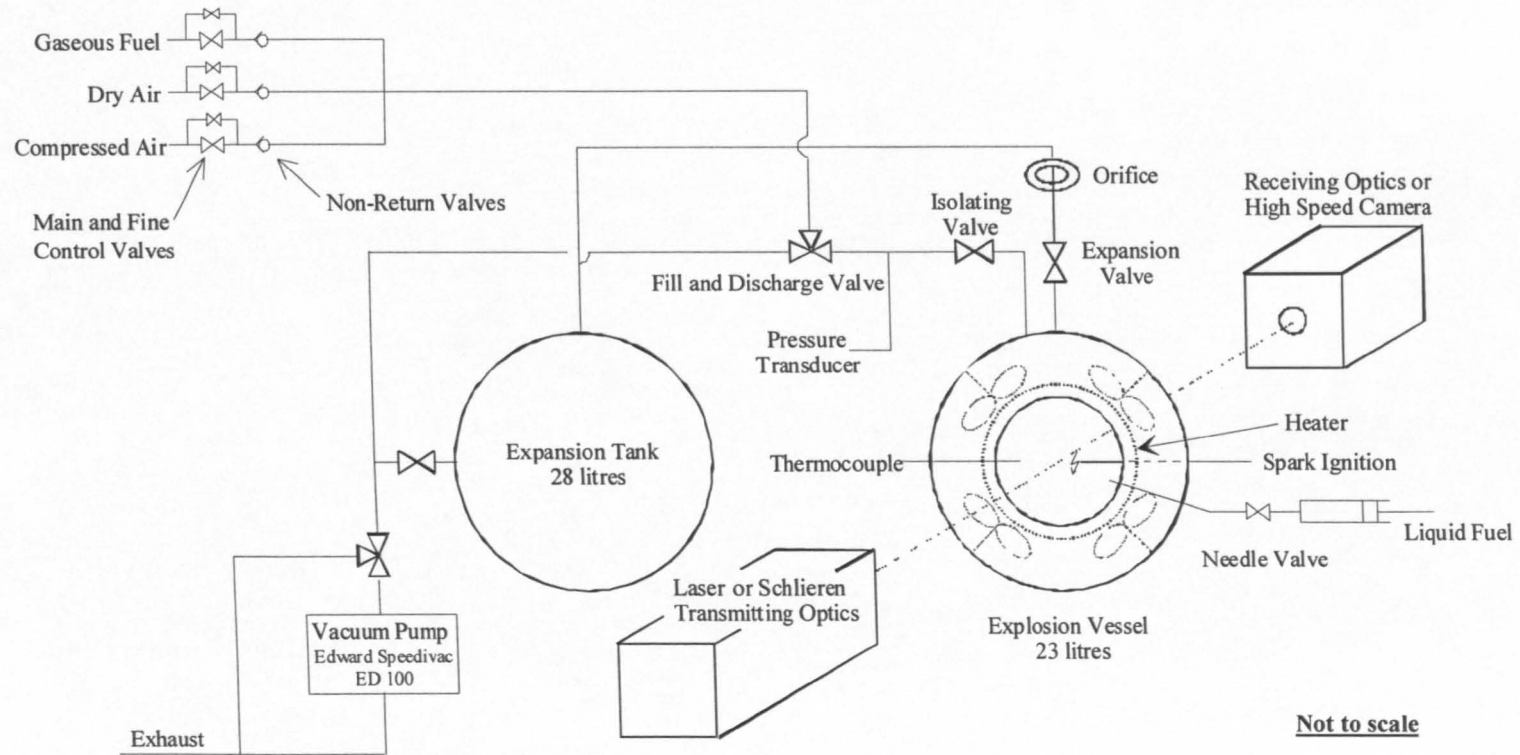


Figure 3.2: Schematic of combustion apparatus with schlieren system. Reproduced from Atzler (1999).



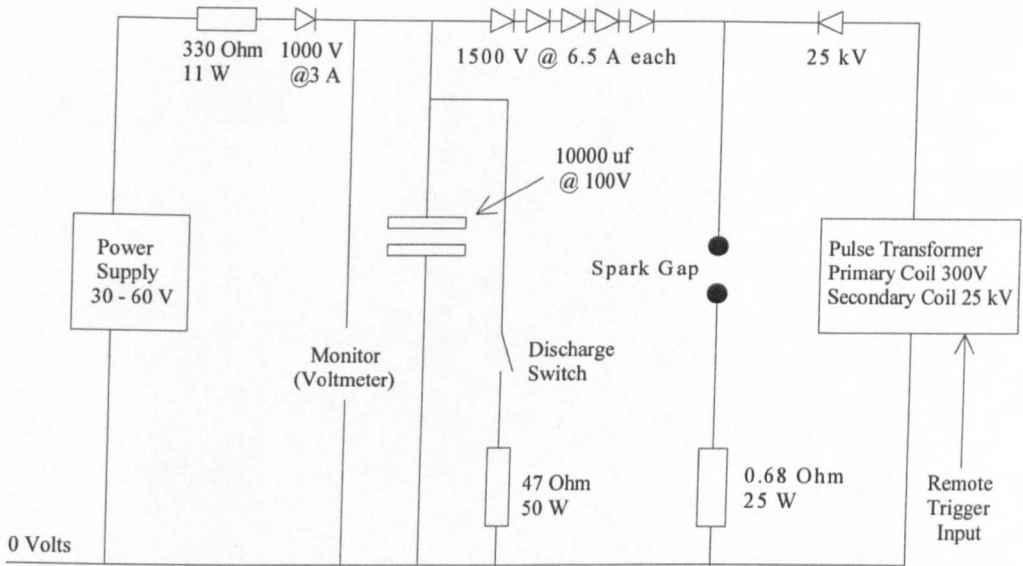


Figure 3.3: Circuit diagram for fixed energy ignition unit. Reproduced from Atzler (1999).

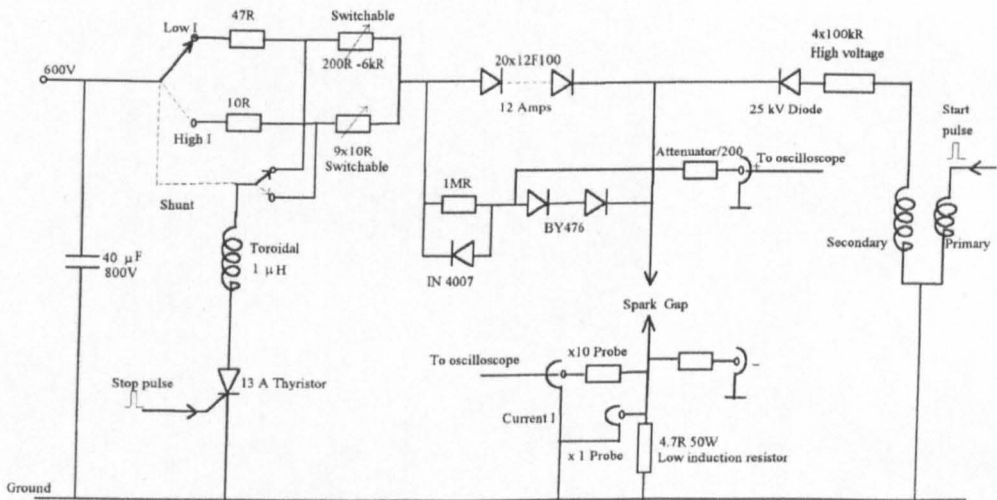


Figure 3.4: Circuit diagram for variable energy ignition unit. Reproduced from Ali (1995).

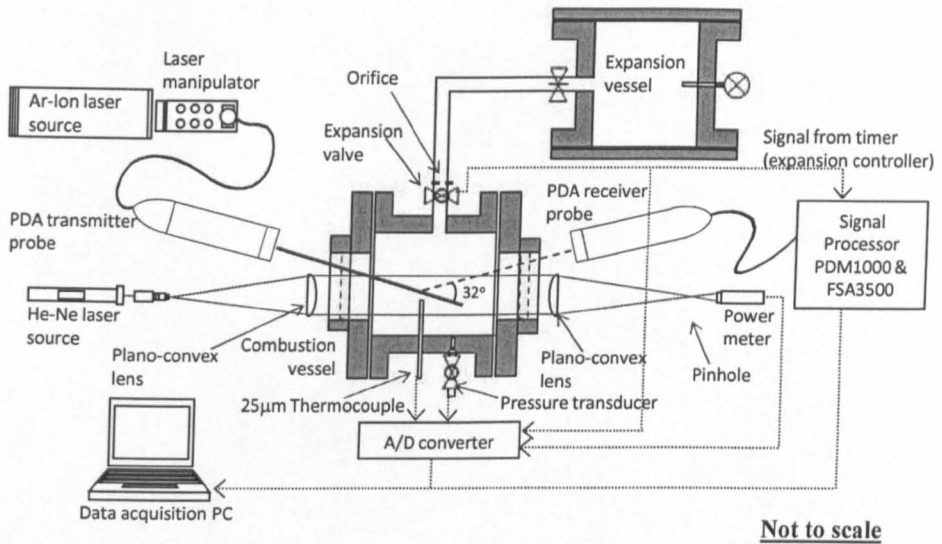


Figure 3.5: PDA system and laser attenuation apparatus for aerosol characterisation experiment.

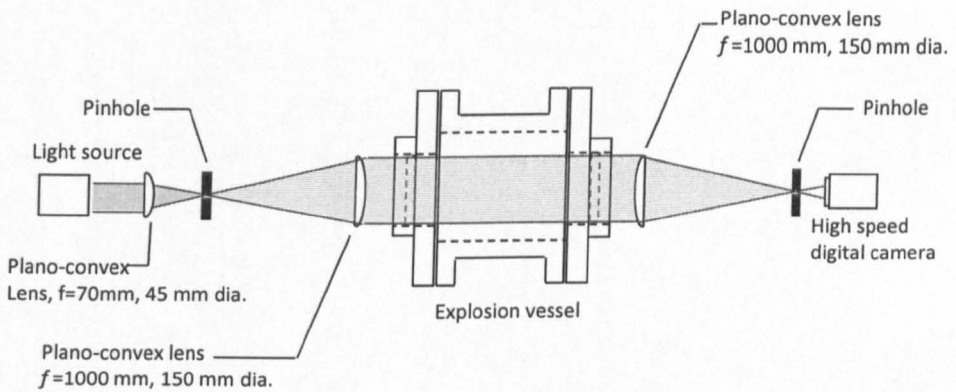


Figure 3.6: Experimental setup for high speed schlieren cine photography

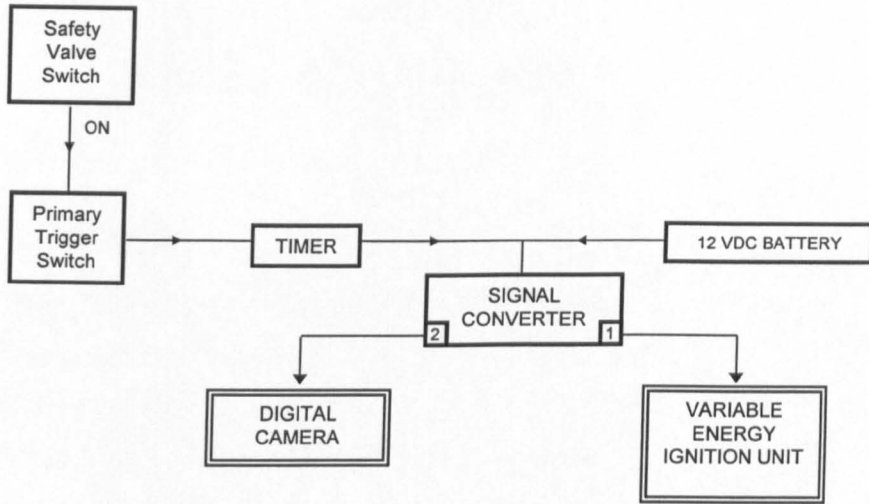


Figure 3.7: Schematic of control circuit for ignition and schlieren cine photography.

## Chapter 4

### Characterisation of Aerosol Mixtures

#### 4.1 Introduction

This chapter presents an analysis of the aerosol mixture composition, in terms of gaseous and liquid fractions, and the experimental results of cold calibration studies of aerosol mixture. In this characterisation study, aerosol mixtures of iso-octane and ethanol were calibrated, without combustion, to obtain the temporal variation of pressure, temperature, droplet size and number density as function of time during expansion, under laminar and turbulent conditions. In Section 4.2, a theoretical analysis to calculate the liquid-vapour equivalence ratio is presented. It is based on the thermodynamic principle that, given any two properties of a system, in this case pressure and temperature, any other property such as here the liquid fraction can be calculated. In Section 4.3, experimental data on pressure and temperature variations during the expansion process are presented. The results of droplet size measurements, using the Phase Doppler Anemometry technique, are shown in Section 4.4. In Section 4.5, experimental data on laser attenuation measurements are presented and these are used to estimate the variation of droplet number density throughout the aerosol formation and development. A brief discussion of effect of impurities and factors that might affect droplet formation is presented in Sections 4.6 and 4.7, respectively.

#### 4.2 Determination of aerosol properties

During the expansion of a fuel-air mixture, the vapour phase of the pure substance is brought to a supercooled state by the rapid drop of pressure. Further, when the pressure is dropped beyond the point of saturation, the mixture then undergoes a phase change. This process can be explained in schematic diagrams of pressure-specific volume,  $P$ - $v$ , and temperature-entropy,  $T$ - $s$ , as shown in Fig. 4.1, with two extreme assumptions: constant specific entropy (dashed line) and constant temperature (dotted line). During expansion, the temperature of the vessel is,

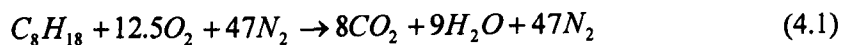
essentially, constant. The mixture temperature reduces due to expansion but receives heat from the vessel. If the expansion is fast, the heat transfer from the vessel will be negligible; hence the process is isentropic. Conversely, if the expansion is slow, the process will be at constant temperature.

By considering first, the isentropic case, at the start of expansion (point 1), the fuel is completely vaporised and superheated. At this time, the system is in gas phase equilibrium until saturation of the fuel vapour is reached at point 2, when its partial pressure is equal to its vapour pressure, as shown in Figs. 4.1a and 4.1b. As the expansion continues, the mixture goes into the two-phase regime towards point 3. Here a fraction of the fuel is in the liquid phase and the rest is in the vapour phase. However, if the expansion was at constant temperature, from point 1 to point 4, due to the heat supplied from the vessel, the fuel vapour would never reach the saturation point and the mixture would remain in the vapour phase throughout expansion. In reality, as discussed in Section 4.3, the expansion process is very close to isentropic.

In a two-phase mixture, as shown in Fig. 4.1 between points 2 and 3, the fractions of liquid and vapour of a substance are important parameters for the determination of the aerosol properties. The calculation procedure is demonstrated below for iso-octane and results are shown for both fuels, iso-octane and ethanol, in Sections 4.3 to 4.5.

#### 4.2.1 Gas phase equilibrium

The molar composition of a stoichiometric mixture of iso-octane and air can be calculated from the stoichiometric equation



For a non-stoichiometric mixture, the reactants on the left hand side of Eq. (4.1) can be expressed by



where  $\phi_{ov}$  is the overall equivalence ratio. Normalising to one mole of reactants yields

$$1 \text{ mole reactants} = \frac{\phi_{ov}}{59.5 + \phi_{ov}} C_3H_{18} + \frac{59.5}{59.5 + \phi_{ov}} \text{Air} \quad (4.3)$$

From Eq. (4.3), the mole fractions of air and fuel are

$$\frac{n_a}{n} = \frac{59.5}{59.5 + \phi_{ov}} \quad (4.4)$$

and

$$\frac{n_f}{n} = \frac{\phi_{ov}}{59.5 + \phi_{ov}} \quad (4.5)$$

where  $n_a$ ,  $n_f$ , and  $n$  are the numbers of moles of air, fuel and the total mixture. The ratio of the partial pressures of two gaseous species is equal to their mole fractions, such that

$$\frac{P_a}{P_f} = \frac{n_a}{n_f} \quad (4.6)$$

where  $P_f$  and  $P_a$  are the fuel and air partial pressures. Equation (4.6) is valid only for an ideal gas and cannot be used for liquid. Following from Eqs. (4.5) and (4.6), the partial pressure of the fuel can be determined by

$$P_f = P \frac{\phi_{ov}}{59.5 + \phi_{ov}} \quad (4.7)$$

#### 4.2.2 Mass fraction and equivalence ratio

The stage at which the fuel is completely vaporised and superheated, such that it is well away from saturation conditions, is defined by the ideal gas law

$$P_f = \frac{n_f \bar{R} T}{V} \quad (4.8)$$

where  $V$  is the volume occupied by the mixture and  $\bar{R}$  is the universal gas constant. Close to saturation conditions, the ideal gas law must be modified to account for the changed compressibility of the gas, using the compressibility factor,  $Z$ .

$$P_f = Z \frac{n_f \bar{R} T}{V} \quad (4.9)$$

Compressibility factors were acquired from Fig. 4.2 which is reproduced from Cengel and Boles (1998). This chart shows generalised compressibility factors as a function of reduced pressure,  $P_r$  and temperature,  $T_r$ , which are expressed by

$$P_r = \frac{P_f}{P_c} ; T_r = \frac{T}{T_c} \quad (4.10)$$

where  $P_c$  and  $T_c$  are the critical pressure and temperature. The critical properties for iso-octane and ethanol were obtained from Yaws (1992). For the present work, a rich iso-octane mixture at  $\phi_{ov}=2.0$ , expanded from 200 kPa, represents the worst case for estimating the changed compressibility factor. This mixture has a fuel partial pressure at the onset of condensation of 5.4 kPa, which yields a value of  $P_r$  of  $2.1 \times 10^{-3}$ . Also, the value of  $T_r$  at 290 K is 0.53. The calculated value of  $P_r$  is far off the scale to the left of Fig. 4.2, but extrapolation of the curves with a constant value of  $T_r$  shows that  $Z$  is close to unity. A value of  $Z$  close to unity was also obtained for ethanol. Therefore  $Z$  was disregarded in the present analysis. The total number of moles of fuel in the explosion vessel at the start of expansion, when all fuel was fully vaporised, can be expressed using Eqs. (4.7) and (4.8), by

$$n_{f1} = \frac{P_{f1}V}{\bar{R}T_1} = \frac{\phi_{ov}}{59.5 + \phi_{ov}} \frac{P_1V}{\bar{R}T_1} \quad (4.11)$$

where suffix 1 denotes the state of the mixture immediately prior to the start of expansion. In an ideal system, saturation of the fuel vapour is reached when its partial pressure is equal to its vapour pressure. In the wet region, the partial pressure cannot be used to characterise the total fuel content because some of it is liquid. However, the gaseous portion of the fuel can be approximated by the assumption

$$P_f = P_v \quad (4.12)$$

where  $P_v$  is the vapour pressure of the fuel. This is calculated from the measured temperature by

$$\log P_v = A - \frac{B}{T + C} \quad (4.13)$$

where  $T$  is the temperature and the coefficients are  $A = 6.81189$ ,  $B = 1257.84$  and  $C = 220.735$  (Yaws, 1992).

At saturation conditions, the ideal gas law is not strictly valid. However, it does give a good approximation. Using Eqs. (4.8) and (4.12), the number of moles of gaseous fuel in the wet mixture can be estimated by

$$n_{fg2} = \frac{P_v V}{RT_2} \quad (4.14)$$

where suffix 2 denotes the point of the mixture at any time in the wet region (Fig. 4.1) and  $g$  represents the vapour state. The liquid molar fraction of fuel can be expressed in terms of the gaseous fraction as

$$\frac{n_{fl}}{n_f} = \frac{(n_f - n_{fg})}{n_f} = 1 - \frac{n_{fg}}{n_f} \quad (4.15)$$

In the current apparatus, the expansion of the mixture from a fixed-volume vessel into an expansion tank introduces an additional problem. The total amount of mixture in the explosion vessel decreases during the process. However, it is assumed that  $\phi_{ov}$  in the vessel, irrespective of the phase of the fuel, remains constant during expansion. This assumption is reasonable on the grounds that condensed drops and the remaining fuel vapour-air mixture are essentially at the same temperature and the droplets are small enough to follow the flow. As droplets condense from the gas phase at the local flow velocity, they are transported out of the bomb at the same rate as that of the gaseous mixture (Atzler, 1999). The values of  $n_f$  within the wet regime must be calculated by assuming a constant mixture composition because the method presented in Eq. (4.11) does not account for the liquefied fuel. Constant mixture composition implies

$$\frac{n_{a1}}{n_{f1}} = \frac{n_{a2}}{n_{f2}} \quad (4.16)$$

Hence

$$n_{f2} = n_{f1} \frac{n_{a2}}{n_{a1}} \quad (4.17)$$

Using Eq. (4.4), the initial number of moles of air is

$$n_{a1} = \frac{59.5}{59.5 + \phi_{ov}} \frac{P_1 V}{RT_1} \quad (4.18)$$

The number of moles of air in the wet region is



$$n_{a2} = \frac{P_{a2}V}{RT_2} = \frac{(P_2 - P_v)V}{RT_2} \quad (4.19)$$

Substituting Eqs. (4.11), (4.18) and (4.19) into Eq. (4.17) yields

$$n_{f2} = \frac{\phi_{ov} (P_2 - P_v)V}{59.5 RT_2} \quad (4.20)$$

Substituting Eqs. (4.14) and (4.20) into Eq. (4.15) yields

$$\frac{n_{f2}}{n_{f2}} = 1 - \frac{59.5P_v}{\phi_{ov}(P_2 - P_v)} \quad (4.21)$$

The mass of gaseous fuel and air present in the combustion vessel at condition 2 can be calculated from the molar mass of fuel,  $M_f$ , and air,  $M_a$  by

$$m_{f2} = n_{f2}M_f \quad (4.22)$$

$$m_{a2} = n_{a2}M_a \quad (4.23)$$

The instantaneous mass of liquid fuel can be determined by

$$m_{f2} = m_{f2} \frac{n_{f2}}{n_{f2}} \quad (4.24)$$

The mass fraction of fuel in the liquid and gas phases (*lmf* and *gmf*) are given by

$$lmf = \frac{m_{f2}}{m_{f2}}, \quad gmf = \frac{m_{fg2}}{m_{f2}} = \frac{m_{f2} - m_{f2}}{m_{f2}} \quad (4.25)$$

The gaseous and liquid equivalence ratios can be calculated by

$$\phi_g = \frac{(F/A)}{(F/A)_{stoic}} = \frac{(m_{fg2}/m_{a2})}{(F/A)_{stoic}} \quad (4.26)$$

and

$$\phi_l = \phi_{ov} - \phi_g \quad (4.27)$$

where  $F/A$  is the fuel-air ratio. The stoichiometric fuel-air ratio can be calculated from Eqs. (4.1) and (4.2)

$$(F/A)_{stoic} = \frac{M_f}{59.5M_a} \quad (4.28)$$

### 4.3 Pressure and temperature variation

Pressure and temperature are important parameters for the calculation of gaseous and liquid fractions of fuel-air mixture at any instant during expansion. In addition to mixture composition, data on these are essential prerequisites for the analysis of the combustion process, discussed in Chapter 5. This section presents experimental values of pressure and temperature variation as a function of time from the start of expansion for two fuels at a wide range of  $\phi_{ov}$  under laminar and turbulent conditions, as summarised in Table 4.1. The pressure and temperature measurements were obtained simultaneously with the droplet size and number density.

#### 4.3.1 Initially quiescent conditions

Figure 4.3 shows typical variations of pressure and temperature during the expansion of a stoichiometric iso-octane and air mixture from an initial temperature and pressure of 303 K and 200 kPa. Following the start of expansion until the start of condensation, the measured temporal variations of temperature and pressure exhibited an isentropic relationship as indicated by the dashed line in Fig. 4.3. This can be expressed by

$$\frac{T_2}{T_1} = \left( \frac{P_2}{P_1} \right)^{\frac{\gamma-1}{\gamma}} \quad (4.29)$$

where  $\gamma$  is isentropic expansion index. Using the ratio of specific heats of the iso-octane-air mixture, the value of  $\gamma$  is 1.35. At the start of nucleation, the measured temperature deviated from that of Eq. (4.29) because the mixture no longer acts like an ideal gas. The temperature remains higher than that suggested by Eq. (4.29) because of the latent heat of condensation. Marquez (2003) suggested that there is an additional factor that may affect the measured temperature due to the thermocouple which tends to act as a nucleation site, resulting in a higher temperature at the thermocouple than in the free stream. Similar trends of the variation of pressure and temperature during the expansion of a stoichiometric ethanol and air mixture is shown in Fig. 4.4 in which the start of condensation was approximately 0.7 seconds after the start of expansion.

Shown in Fig. 4.5 are the variations of measured pressure and temperature of iso-octane and air mixtures at  $\phi_{ov}$  between 0.8 and 2.0, expanded from 200 kPa and 303 K. The pressure varies little with variation in  $\phi_{ov}$ . However, temperature remains nearly independent of  $\phi_{ov}$  only to the start of condensation, indicated by the solid circles on each curve. This is because of the transition to non-ideal gas behaviour as discussed above.

### 4.3.2 Turbulent conditions

Figure 4.6 shows typical variations of pressure and temperature as a function of time during expansion of stoichiometric iso-octane and air mixture at an initial condition of 200 kPa, 303 K and  $u'$  of 1.0 m/s. For turbulent conditions, the orifice size was 25 mm, as discussed in Section 3.2.2, to compensate for the higher rate of droplet evaporation as a result of a higher rate of heat transfer from the vessel due to the turbulence flow. Also shown in Fig. 4.6 are curves of the variation of temperature with time for isentropic expansion of an ideal gas ( $\gamma = 1.35$ ) and for expansion with a polytropic index of 1.21. It is shown that under turbulent conditions, the expansion process is far from adiabatic and this is due to the high turbulence convective heat transfer from the vessel walls.

Shown in Fig. 4.7 is the variation of pressure and temperature of stoichiometric iso-octane and air mixture at different  $u'$  between 1.0 and 4.0 m/s and at similar initial conditions to those in Fig. 4.6. Under turbulence, there is no significant effect of  $u'$  on the variation of pressure with time. However, in temperature variation, there is a slight increment in temperature with  $u'$  prior to condensation. During condensation, the increment in temperature becomes significant due to enhanced heat transfer resulting in more rapid evaporation of droplets.

## 4.4 Droplet size distribution

This section presents measurements of the temporal variation of droplet size in terms of individual and averaged diameter as a function of time throughout the expansion of fuel and air mixtures. The measurements were performed using Phase Doppler Anemometer as described in Section 3.5.1.

#### 4.4.1 Initially quiescent conditions

Figure 4.8 shows a typical variation of individual and averaged droplet diameter with time for stoichiometric iso-octane-air aerosols when expanded from initial conditions of 200 kPa and 303 K. The diamond symbols represent individual measurements while the solid circles and the solid curve represent averaged values. Also shown in Fig. 4.8, by the crosses and chain dashed line, are values of standard deviation of droplet diameter,  $\sigma_D$ , which was obtained from

$$\sigma_D = \sqrt{\frac{\sum (D - D_{10})^2}{n}} \quad (4.30)$$

where  $D$  and  $D_{10}$  are the individual and linear averaged droplet diameter, respectively. In most cases, the present system could not adequately detect the onset of condensation. However, this was resolved by extrapolating the curve fit of  $D_{10}$  to zero. During the early stage of droplet formation, up to 3.5 seconds, a narrow distribution of droplet diameter was obtained, as supported by the small value of  $\sigma_D$ . After this period, significant scatter was recorded before the size of droplet reduced and further disappeared from the expanded mixture. This was probably due to droplet evaporation by heat transfer from the explosion vessel.

Figure 4.9 shows a typical variation with time of individual and averaged droplet diameter and  $\sigma_D$  for stoichiometric ethanol-air aerosols, expanded from initial conditions of 200 kPa and 313 K. In general, a similar trend to that of aerosol for iso-octane discussed above, was obtained for ethanol. The onset of droplet formation was obtained at approximately 0.7 seconds after the start of expansion. Since the condensation of ethanol started earlier than iso-octane, the maximum attainable droplet diameter in ethanol was greater than in iso-octane. The probable reason for ethanol's experiencing an earlier start of condensation is because of its being more volatile than iso-octane.

Figure 4.10 shows the spatial variation of individual droplet diameters for stoichiometric iso-octane aerosol measured at six locations within the field of view of the windows (Marquez, 2003). The solid line represents a curve fit through the experimental values and the chain dashed line represents  $\sigma_D$ . Because the measurements of individual droplet diameter at different locations were obtained from different experiments, values of  $\sigma_D$  represent the combined effect of spatial and shot to shot experiment variability. It is shown in Fig. 4.10 that although  $\sigma_D$

increases slightly with time, the spatial variation is low, which typically is below 2  $\mu\text{m}$ . Clearly, this low value of  $\sigma_D$  demonstrates the near monodispersed distribution of  $D_{10}$  and the excellent repeatability in the present explosion vessel. All combustion studies in the present work were undertaken during the first few milliseconds, while droplet diameter could be considered monodispersed. Clearly, this simplifies analysis during combustion studies because variation in droplet diameter can be neglected. Further, many studies report the use of various volume and area weighted averages such as  $D_{32}$  and  $D_{20}$  as described in Section 2.5. However, for monodispersed droplets, they all reduce to the same value (Hayashi and Kumagai, 1975; Cameron and Bowen, 2001).

Shown in Fig. 4.11 is the temporal variation of  $D_{10}$  with time for iso-octane aerosols expanded from an initial pressure of 200 kPa and initial temperature of 303 K, at values of  $\phi_{ov}$  between 0.8 and 1.4. Each curve was obtained from a single expansion and the limit was determined from the start of droplet formation until the end of the narrow distribution of droplet diameter (at which  $\sigma_D \leq 2 \mu\text{m}$ ). The scatter of the individual data is indicated by the error bars. The onset of droplet formation is a strong function of  $\phi_{ov}$ , being at 1.2 seconds after the start of expansion for  $\phi_{ov}$  of 1.4 and at later times for leaner mixtures. The richer mixtures experience earlier start of condensation due to higher values of  $P_v$ , as described in Section 4.2. A similar trend of temporal variation of  $D_{10}$  with time also was obtained in ethanol aerosols as shown in Fig. 4.12.

#### 4.4.2 Turbulent conditions

Figure 4.13 shows the temporal variation of  $D_{10}$  for iso-octane aerosols expanded from 200 kPa and 303 K, at values of  $\phi_{ov}$  between 0.8 and 1.4 with  $u'$  of 1.0 m/s. The solid line in Fig. 4.13 represents the curve fit through the experimental values. The scatter of the individual droplet diameter is indicated by the error bars. The variation in droplet diameter with time is similar to that in Fig. 4.11, except that droplet formation is much faster under turbulence than for initially quiescent conditions. This was due to the quicker expansion rate as a result of the use of a larger orifice, as described in Section 3.2.2. It is interesting to note that the maximum attainable value of  $D_{10}$  is slightly smaller under turbulent than for initially

quiescent conditions. This was probably due to the higher rate of heat transfer as discussed in Fig. 4.7

Shown in Fig. 4.14 is the temporal variation of  $D_{10}$  with time for stoichiometric iso-octane aerosols, expanded from initial conditions of 200 kPa and 303 K, at a wide range of  $u'$ . The values of  $u'$  were varied between 0.5 and 4.0 m/s. The solid line represents the curve fit through the experimental values of  $D_{10}$  at  $u' = 0.5$  m/s. It is shown in Fig. 4.14 that the influence of  $u'$  on the onset of droplet formation is not significant, however the maximum attainable of  $D_{10}$  decreased as  $u'$  increased.

## 4.5 Droplet number density

An estimation of droplet number density,  $N_D$ , was based on measurement of laser power attenuation and  $D_{10}$ , as described in Section 3.5.2. The attenuation in the intensity of the laser beam is given as a ratio of the voltage output ( $V/V_o$ ) of the laser power meter. This section presents measurements of laser power attenuation and  $N_D$  as a function of time throughout expansion under initially quiescent and turbulent conditions.

### 4.5.1 Initially quiescent conditions

Shown in Fig. 4.15 are the variations of  $V/V_o$  and  $N_D$  with time during the expansion of iso-octane and air mixtures, at values of  $\phi_{ov}$  between 1.0 and 1.6, at similar initial pressures and temperatures. The repeatability of the experiment was good, as indicated by several laser attenuation measurements at  $\phi_{ov} = 1.0$ . Following the start of expansion, the value of  $V/V_o$  remained constant until it reduced after the onset of condensation. This corresponds well with the determination of onset of droplet formation by extrapolation to zero of the experimental values of  $D_{10}$ , as explained in Section 4.4.1. After the onset of condensation,  $V/V_o$  decreased with time due to the combined effect of an increase in droplet size and droplet number density, until a minimum value was reached. After this,  $V/V_o$  increased due to droplet evaporation. Using this ratio and  $D_{10}$  measurement,  $N_D$  was estimated based on the Beer-Lambert law, as described in Section 3.5.2. It is shown in Fig. 4.15 that immediately after the start of condensation,  $N_D$  rose rapidly to an approximately constant value, in the order of  $10^{10}$ , before it experienced a slight reduction. Similar

results and trends of  $N_D$  at different  $\phi_{ov}$  are also shown in Fig. 4.15 and this indicates that the variation in  $\phi_{ov}$  did not have a significant effect on  $N_D$ .

Figure 4.16 shows the variations of  $V/V_o$  and  $N_D$  with time during the expansion of ethanol and air mixtures, at values of  $\phi_{ov}$  between 0.6 and 1.2, and at initial conditions of 200 kPa and 313 K. Similar to Fig. 4.15, the onset of condensation is shown to be a function of  $\phi_{ov}$ , with richer mixtures condensing earlier than lean ones. It is shown in Fig. 4.16 that ethanol aerosols had lower number densities ( $\sim 10^9 \text{ m}^{-3}$ ) than those of iso-octane ( $\sim 10^{10} \text{ m}^{-3}$ ). The probable reason for this is due to the latent heat of ethanol being higher than that of iso-octane. The estimation of  $N_D$  can be used further to estimate a mean inter-drop distance,  $l_D$ . Annamalai and Ryan (1992) showed that  $l_D$  can be estimated by

$$l_D = \frac{1}{\sqrt[3]{N_D}} \quad (4.31)$$

Figure 4.17 shows the typical calculated mass of liquid fuel as a function of time during expansion of stoichiometric iso-octane aerosols from initial conditions of 200 kPa and 303K. This is used to compare the mass of liquid fuel calculated from  $N_D$  and  $D_{I0}$  measurement (shown by crosses) by comparing with the mass of liquid calculated using measured pressure and temperature, as described in Section 4.22 (shown by circles). After the start of condensation, both results show a similar trend where the liquid mass increases with time as the fuel condenses. The comparison in Fig. 4.17 indicates that there is not much difference between mass of liquid fuel calculated by using  $N_D$ - $D_{I0}$  and measured pressure-temperature. Hence, this suggests that the estimation of  $N_D$  in the present work is likely to be reasonable.

#### 4.5.2 Turbulent conditions

Shown in Fig. 4.18 are the variations of  $V/V_o$  and  $N_D$  with time during the expansion of turbulent stoichiometric iso-octane and air mixtures, at values of  $u'$  between 1.0 and 4.0 m/s, at identical initial pressure and temperature. The repeatability of experiment under turbulent conditions was good, as indicated by several laser attenuation measurements at  $u'=1.0$  m/s. It is shown that the onset of condensation under turbulent conditions is independent of  $u'$ . However, the variation of  $N_D$  at highest  $u'$  (4.0 m/s) seems to be slightly smaller than at low  $u'$ . This is probably due to the higher rate of droplet evaporation as discussed in Fig. 4.7.

## 4.6 Effect of particles on aerosol formation

As described in Section 3.3.3, the repeatability of aerosol generation was maintained throughout experiment by using a clean dried air and a consistent mixture preparation procedure. However, since nucleation is affected by particles (Carey, 1992), it is interesting to investigate the effect of particles on the aerosol formation. In general, particles might have existed in the atmosphere or could result from various deliberate or intentional additions such as small droplets from partially evaporated fuel, from particulates such as smoke and fine dust, and even from particles adhering to the vessel walls that might be disturbed during mixture preparation. Whilst uncontrolled particles are detrimental to reliable experiments, their controlled introduction might be beneficial in providing a means of varying and controlling  $N_D$  and  $D_{10}$ .

The present Section reports results from the variation of particle inclusion in the mixture. Such particles were introduced by two techniques. The first involved variation of the settling time between liquid fuel injection and clean air addition into the main vessel. This variation might affect the degree of evaporation of liquid fuel and the degree to which particles that might have adhered to the wall were disturbed by the inflow of the reactants. The second technique involved deliberate introduction of small particles (smoke from incense sticks). Although it was not possible to quantify the amount of smoke injected, careful preparation and experimentation helped to ensure consistency. The technique was to fill an empty syringe with smoke by placing the open end of the syringe (with plunger removed) over a burning incense stick to allow the smoke to fill the syringe. The plunger was then refitted and adjusted until it contained 10 ml of smoke. The smoke was then injected into the vessel prior to liquid fuel injection.

Shown in Fig. 4.19 are the variations of pressure and temperature with time during the expansion of stoichiometric iso-octane and air mixtures under different preparation conditions. The thick solid line represents a mixture with clean dried air and 40 seconds settling time, the dashed line represents a mixture with 10 seconds settling time and the thin line represents a mixture with the inclusion of 10 ml of smoke. It is shown that the variation of pressure with time is independent of the method of mixture preparation. The variations of temperature variation were initially similar. However, after the start of nucleation, the mixture with 10 seconds settling



time and that with 10 ml of smoke had a slightly higher temperature by between 3% and 4% than the mixture with clean air and 40 seconds of settling time.

Shown in Fig. 4.20 are the corresponding variations of  $D_{10}$  with time for those mixtures in Fig. 4.19. Immediately after the start of condensation, the variation of  $D_{10}$  with time was a strong function of the method of mixture preparation. That with clean air and 40 seconds of settling time exhibited the greatest influence of time on  $D_{10}$ . Such differences became progressively more prominent later during expansion. The mixture with clean air and 40 seconds settling time displayed the largest size of  $D_{10}$  variation, typically by 40-50% higher than that with 10 seconds settling time. The mixture with the inclusion of smoke resulted in  $D_{10}$  being of similar magnitude to that mixture with 10 seconds settling time but the time dependence was a little different. Shown in Fig. 4.21 are the variations of laser power attenuation and  $N_D$  with time for those mixtures in Fig. 4.19. It is shown that the time of onset of condensation was nearly the same in all cases. However, the attenuation profile was different, with clean air and 40 seconds settling time displaying less attenuation than the other mixtures, typically by between 60-70%. This significant difference is reflected in the variation of  $N_D$  with time. Figure 4.21 clearly shows that the effect of the inclusion of particulates can increase the number density of droplets by an order of magnitude.

It is shown above that the existence of particles in the expanded mixture had a significant influence in the development of  $D_{10}$  and  $N_D$ . In the present work, it is unclear whether changes in settling time were due to evaporated fuel or due to dust particulates that were disturbed during mixture preparation. However, in the case of smoke addition, it is clear that any contamination during mixture preparation would result in a difference in  $D_{10}$  and  $N_D$ . Clearly, this issue must be minimised by following a standard mixture preparation procedure, as described in Section 3.3. Any changes to the standard procedure might result in inconsistency of aerosol calibration which would lead to ambiguity in the aerosol combustion studies.

## 4.7 Summary of aerosol characterisation

Throughout the experiments to calibrate aerosol mixtures, discussed in Sections 4.3 to 4.6, several factors have been identified which may have a significant influence on the aerosol formation and characteristics. Aerosol

generation by expansion was influenced by the following parameters: initial pressure and temperature, equivalence ratio, fuel volatility, expansion rate, mixture flow and impurities. Most of these parameters affected the onset of condensation which in turn affected the variation in  $D_{10}$ . In this Section, these parameter are discussed with respect to the results presented in Sections 4.3 and 4.4 and the thermodynamic considerations illustrated in the  $P$ - $v$  diagram in Fig. 4.1. This schematic provides a qualitative understanding of the expansion and condensation processes in the present work. A full quantitative analysis would require consideration of the compressibility factor and non-equilibrium, or supersaturation, theory embodied in the Wilson line (Marquez, 2003).

Shown in Fig. 4.22a is the variation of  $D_{10}$  with instantaneous pressure that recorded during mixture expansion at different initial pressures of 200 kPa and 300 kPa. In both experiments, the initial temperature was identical. In Fig. 4.22b, schematic representation of these expansion processes are illustrated on a  $P$ - $v$  diagram. Both figures are related by the point of condensation start. As indicated by the experimental results in Fig 4.22a, the onset of condensation for the mixture with high initial pressure of 300 kPa occurred at higher instantaneous pressure than that with initial pressure of 200 kPa. This was due to their different values of  $P_f$ , as expressed by Eq. (4.7), and being equal to  $P_v$  when the condensation is started (described in Section 4.2). Further, the maximum attainable  $D_{10}$ , was higher for the higher initial pressure. This was related to the higher difference between the saturation and instantaneous pressure at which  $D_{10}$  was measured.

Figure 4.23a shows the effect of initial temperature on the expansion of stoichiometric ethanol and air mixtures at initial pressure of 200 kPa. Here the mixtures were expanded from initial temperature of 313 K and 333 K. Similar to Fig. 4.22b, Fig. 4.23b shows schematic representation of these expansion process on a  $P$ - $v$  diagram. It is clear from Fig. 4.23a and 4.23b that the onset of condensation occurred at higher instantaneous pressure for the mixture with the lower initial temperature. This was related to the lower values of  $P_v$  at the saturation line during expansion. As given in Eq. (4.13), increasing the initial temperature resulted in an increase in the value of  $P_v$ . Hence, the higher the initial temperature, the greater the difference in  $P_v$ , being equal to  $P_f$  at the point where the condensation occurred.

The equivalence ratio was also found to have an effect on the generation of aerosols. Shown in Fig. 4.24 are data from the expansion of iso-octane and air

mixtures from initially quiescent conditions at 200 kPa and 303 K at  $\phi_{ov} = 1.0$  and 1.4. In Fig. 4.24a, the mixture with the higher  $\phi_{ov}$  experienced condensation at higher instantaneous pressure than the lower  $\phi_{ov}$ . A similar reason applies as discussed in relation to Fig. 4.22 where, in this case, increasing  $\phi_{ov}$  results in increasing  $P_f$ . Figure 4.24b shows schematically that different  $\phi_{ov}$  results in a different saturation line (due to different  $P_f$ ) with the line for higher  $\phi_{ov}$  being nearer to the initial condition (1). Although the schematic of the expansion of each mixture should follow a different process path, the actual variations were small, as shown in Fig. 4.5, and in the present work were considered to be negligible.

Figure 4.25 shows the comparison of different fuels, between iso-octane and ethanol on aerosol formation. Both mixtures were expanded from identical initial conditions. It is shown in Fig. 4.25a that ethanol condensed at a higher instantaneous pressure than iso-octane. The reason for this is shown schematically in Fig 4.25b. Because ethanol was more volatile (high value of  $P_v$ ) than iso-octane (Yaws, 1992), it has a higher saturation line, at which  $P_v$  located closer to the initial condition, (1), than iso-octane.

Figure 4.26 shows the effect of expansion rate on the generation of aerosol. In the present work, the difference in expansion rate was obtained by changing the diameter of the orifice plate, as described in Section 3.2.2. It is shown in Fig. 4.26a that the higher expansion rate, in this case corresponding to the 8.5 mm orifice, resulted in condensation at a higher instantaneous pressure than for the 6.0 mm orifice. The reason for this is shown schematically in Fig. 4.26b where it is related to the quicker rate of pressure drop towards the saturation point. Further, for the mixture with high instantaneous pressure at condensation, the amount of fuel condensed was higher than for those with low instantaneous pressure and this correlates well with the high value of maximum attainable  $D_{10}$ .

Table 4.1: Initial (pre-expansion) conditions for aerosol characterisation experiment in present work.

Regime	Fuel	$P_{in}$ (kPa)	$T_{in}$ (K)	$\phi_{ov}$	orifice (mm)	$u'$ (m/s)
Laminar	Iso-octane $C_8H_{18}$	160	303	0.8, 0.9, 1.0, 1.1, 1.2, 1.4, 1.6, 2.0	6	-
		180				
		200				
	Ethanol $C_2H_5OH$	140	313	0.6, 0.8, 1.0, 1.2		
		160				
		180				
		200				
	Turbulent	Iso-octane $C_8H_{18}$	100	303		
200			25			
100			0.8, 1, 1.4, 1.6, 2.0		-	1
200					25	

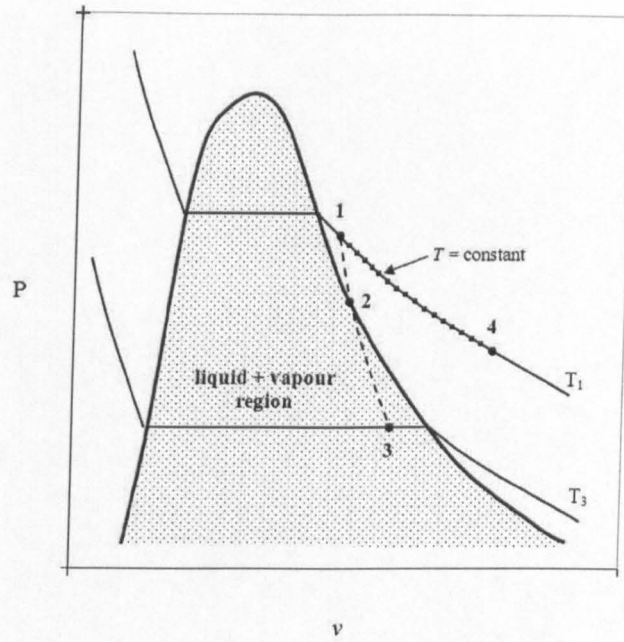
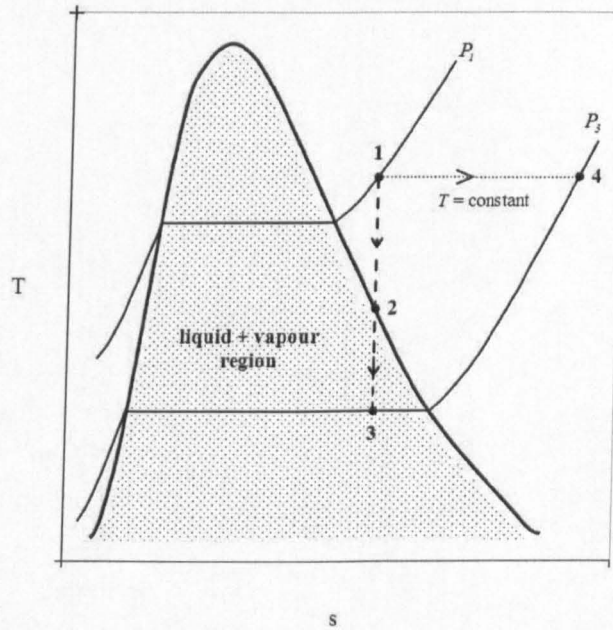
(a)  $P$  -  $v$  diagram(b)  $T$  -  $s$  diagram

Figure 4.1: Expansion paths for phase change in present work on (a)  $P$ - $v$  diagram, and (b)  $T$ - $s$  diagram. Reproduced from Sulaiman (2007).

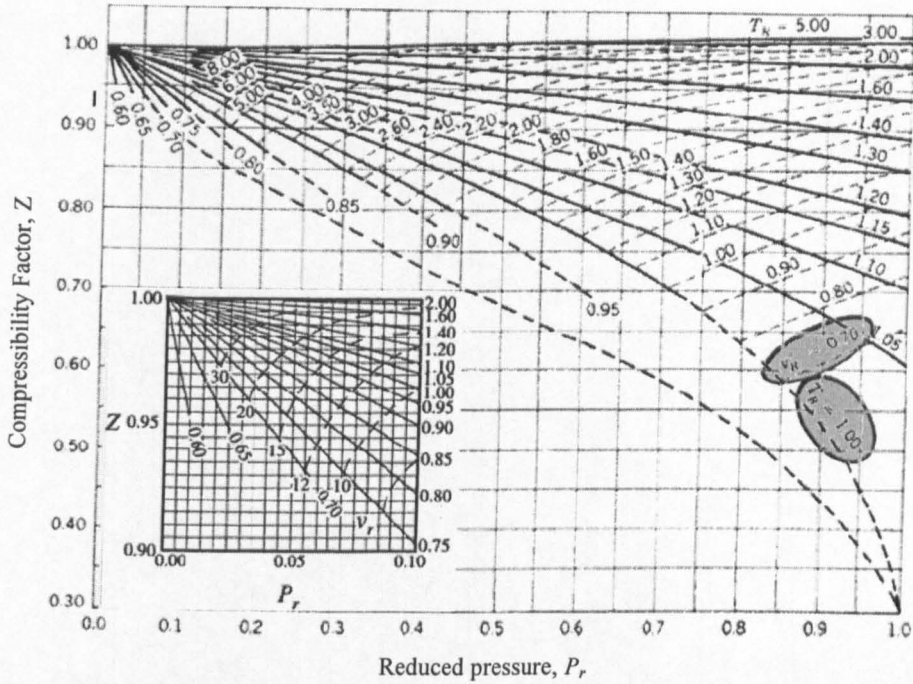


Figure 4.2: Generalised compressibility chart for low pressure condition. Reproduced from Cengel *et al.* (1998).

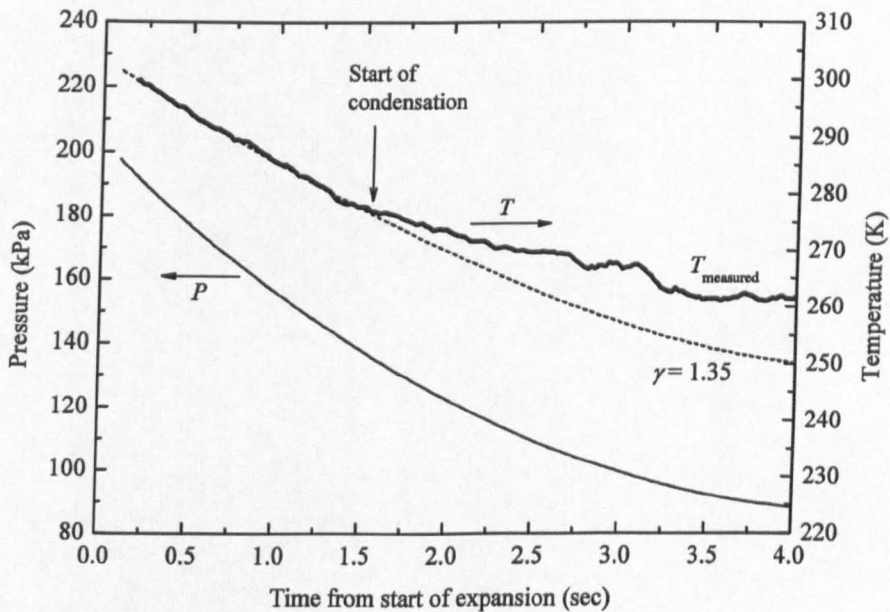


Figure 4.3: Variation of pressure and temperature with time during the expansion of initially quiescent stoichiometric iso-octane and air mixture from 200 kPa and 303 K.

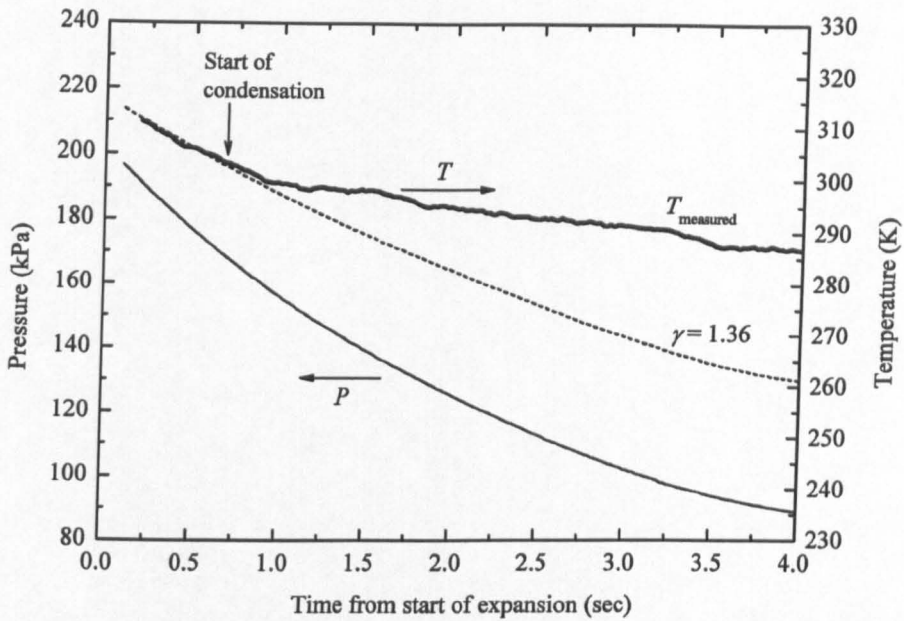


Figure 4.4: Variation of pressure and temperature with time during expansion of initially quiescent stoichiometric ethanol and air mixture from 200 kPa and 313 K.

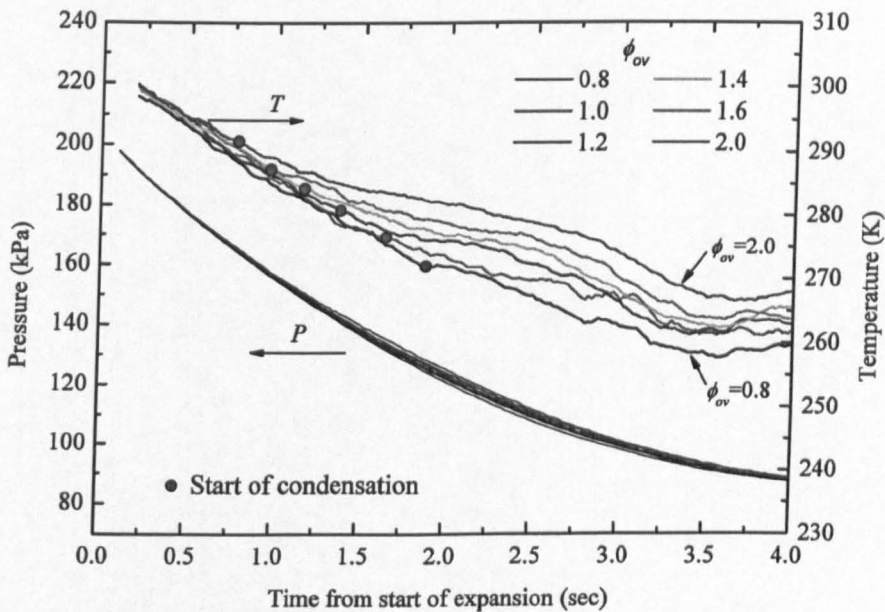


Figure 4.5: Variation of pressure and temperature with time for initially quiescent iso-octane and air mixtures at various  $\phi_{ov}$ . All mixtures were expanded from 200 kPa and 303 K.

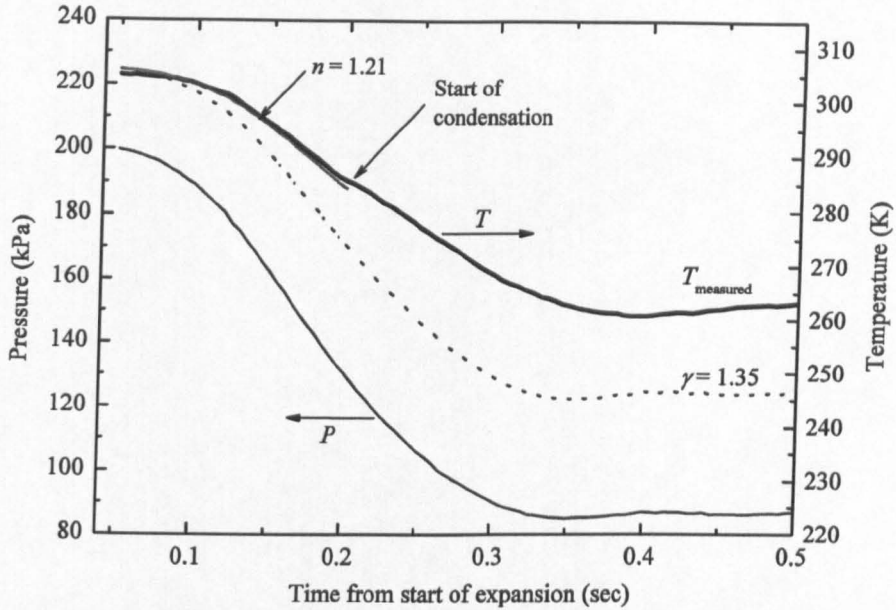


Figure 4.6: Variation of pressure and temperature with time for stoichiometric turbulent iso-octane and air mixture expanded from 200 kPa and 303 K at  $u'$  of 1.0 m/s.

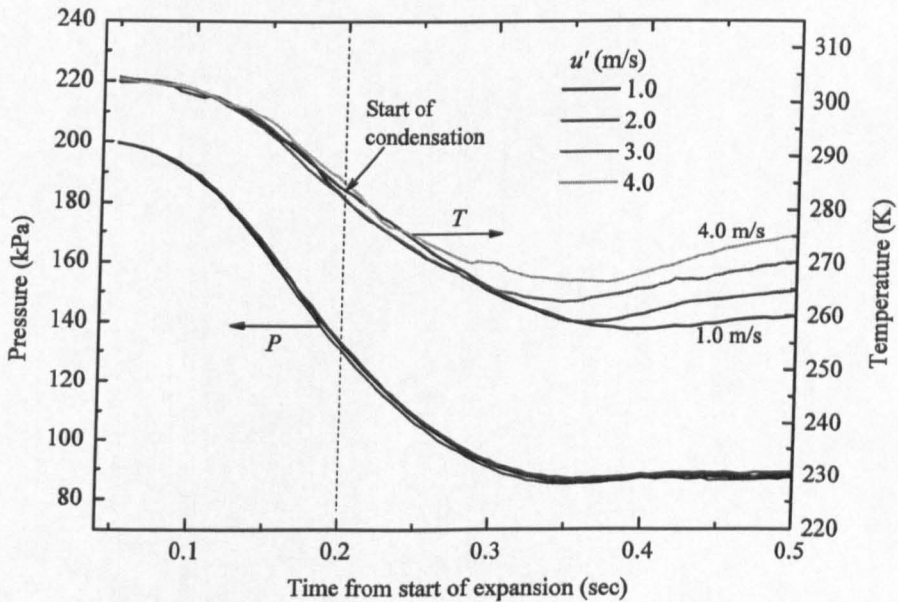


Figure 4.7: Variation of pressure and temperature with time for stoichiometric turbulent iso-octane and air mixtures at various  $u'$ . All mixtures were expanded from 200 kPa and 303 K.



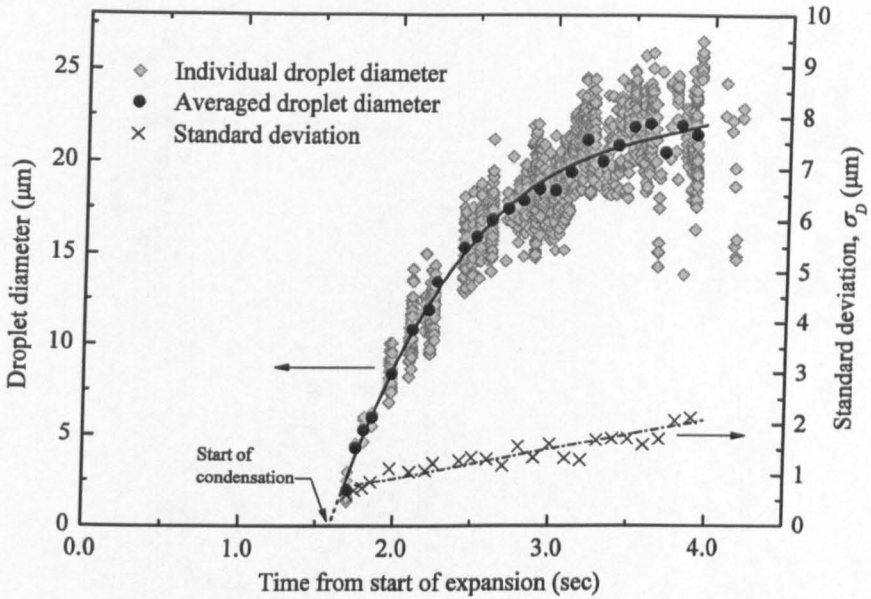


Figure 4.8: Variation of individual and averaged droplet diameter,  $D_{10}$ , and standard deviation,  $\sigma_D$ , with time for initially quiescent stoichiometric iso-octane and air mixture expanded from 200 kPa and 303 K.

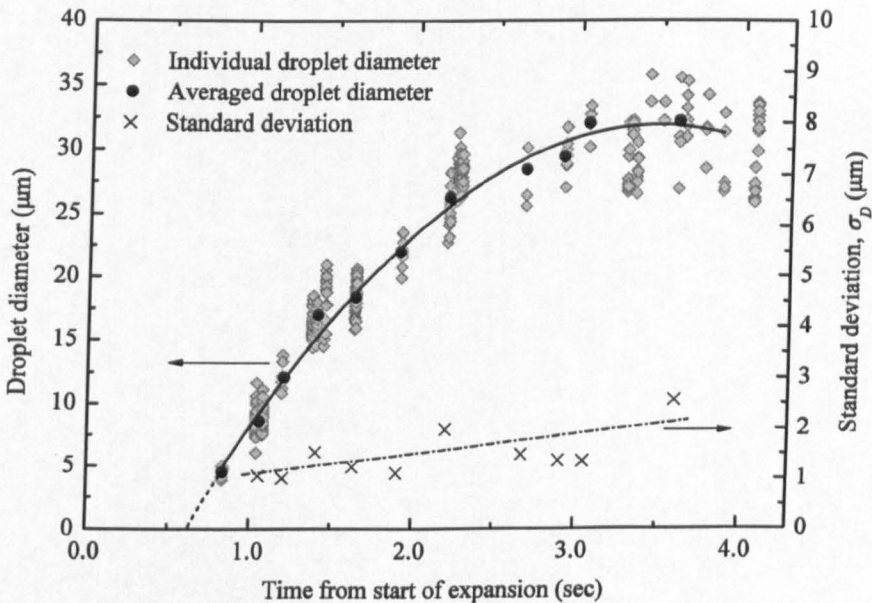


Figure 4.9: Variation of individual and averaged droplet diameter,  $D_{10}$ , and standard deviation,  $\sigma_D$ , with time for initially quiescent stoichiometric ethanol and air mixture expanded from 200 kPa and 313 K.

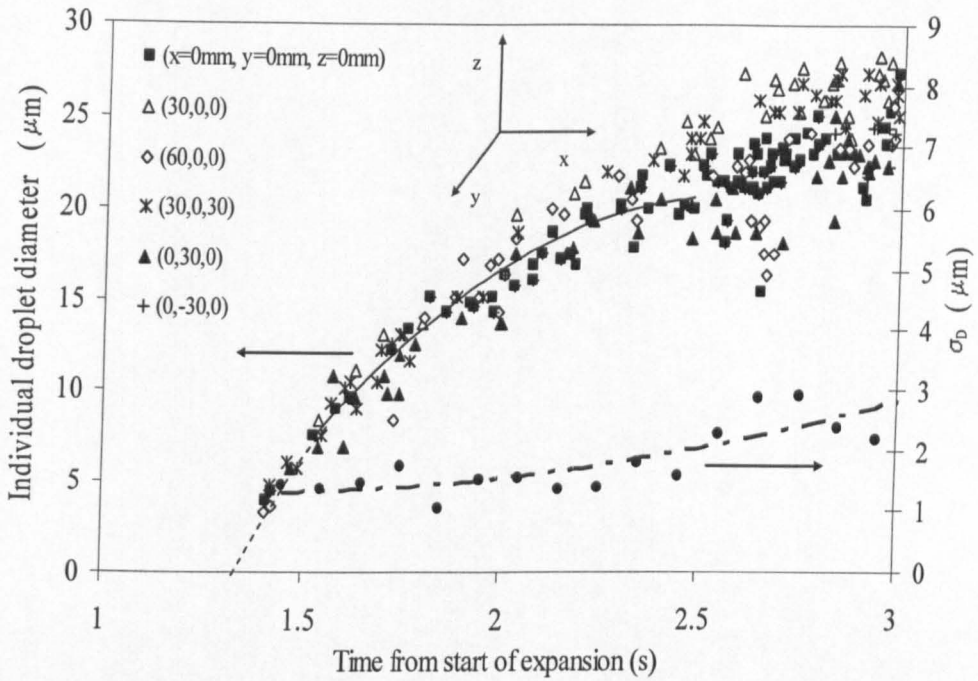


Figure 4.10: Spatial variation of individual droplet diameter and  $\sigma_D$  with time for stoichiometric iso-octane and air mixture expanded from 250 kPa and 303 K at six different positions in explosion vessel. Reproduced from Marquez (2003).

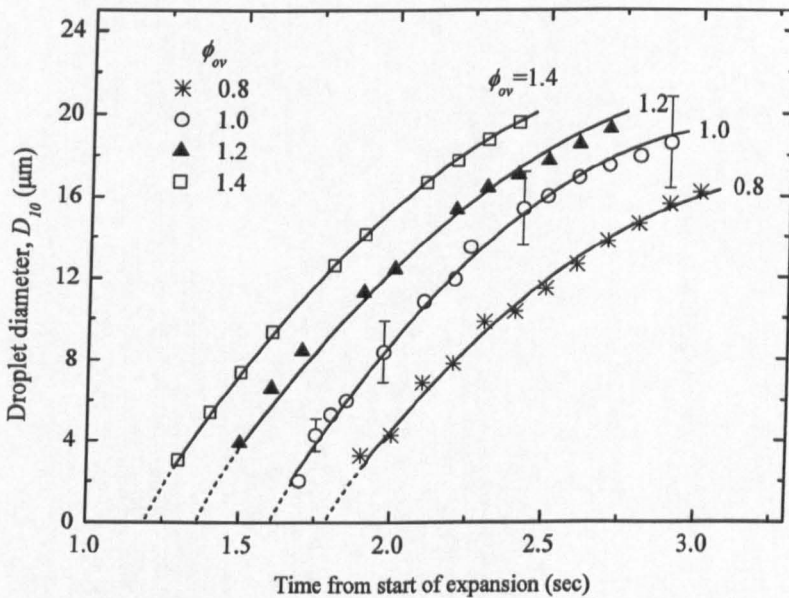


Figure 4.11: Variation of  $D_{10}$  with time for initially quiescent iso-octane and air mixtures at various  $\phi_{ov}$ . All mixtures were expanded from 200 kPa and 303 K.

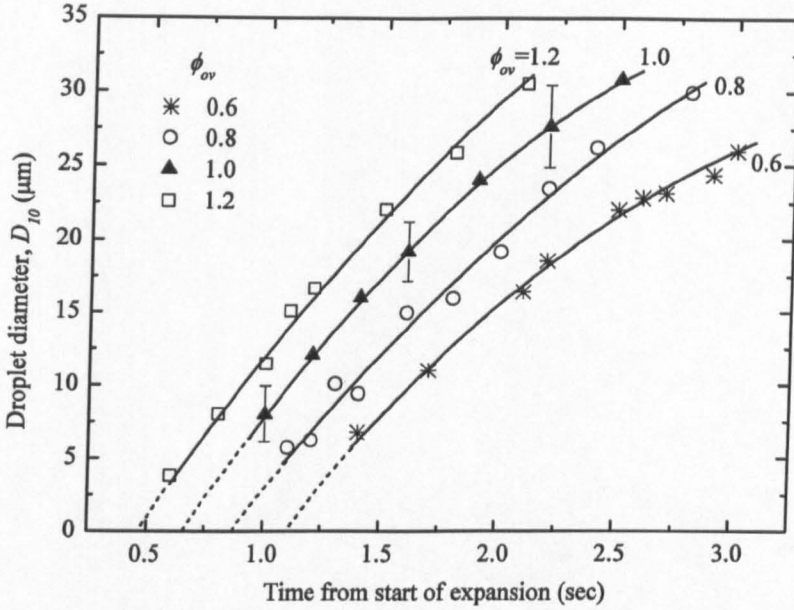


Figure 4.12: Variation of  $D_{10}$  with time for initially quiescent ethanol and air mixtures at various  $\phi_{ov}$ . All mixtures were expanded from 200 kPa and 313 K.

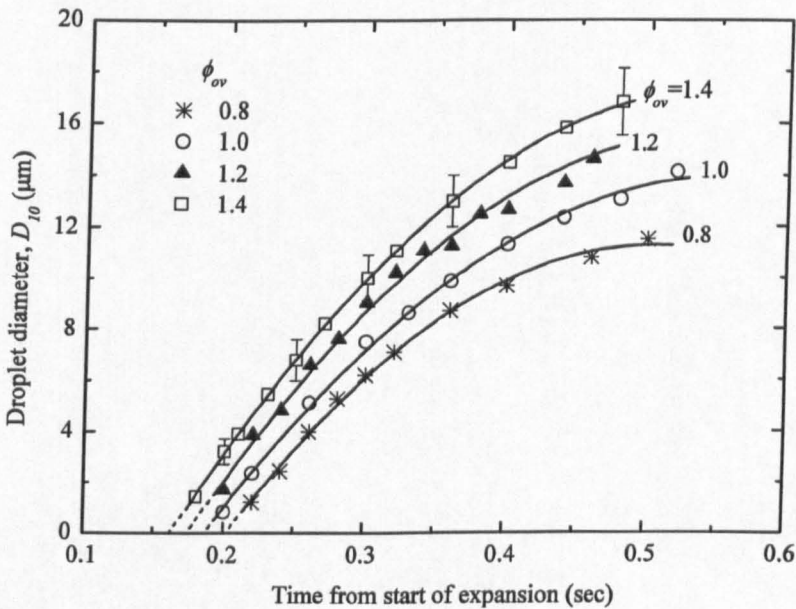


Figure 4.13: Variation of  $D_{10}$  with time for turbulent iso-octane and air mixtures at various  $\phi_{ov}$ . All mixtures were expanded from 200 kPa and 303 K at  $u'$  of 1.0 m/s.

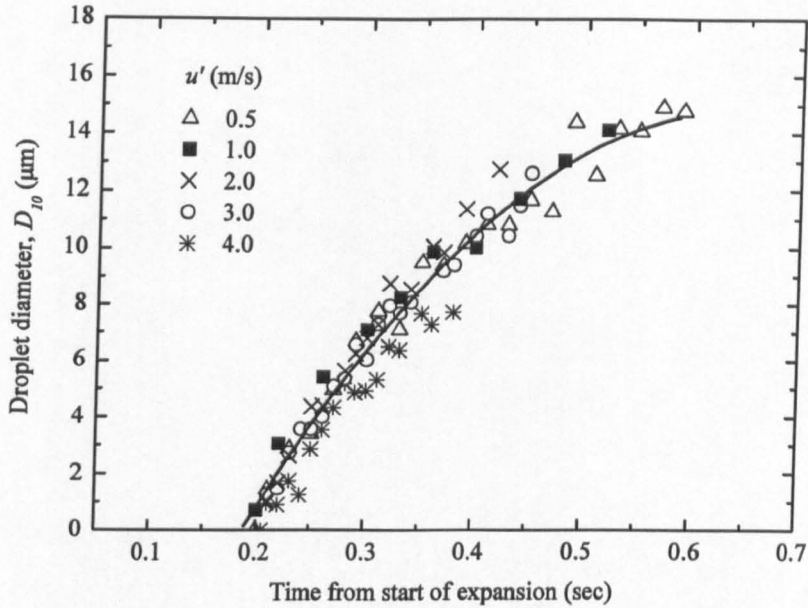


Figure 4.14: Variation of  $D_{10}$  with time for turbulent stoichiometric iso-octane and air mixtures at various  $u'$ . All mixtures were expanded from 200 kPa and 303 K.

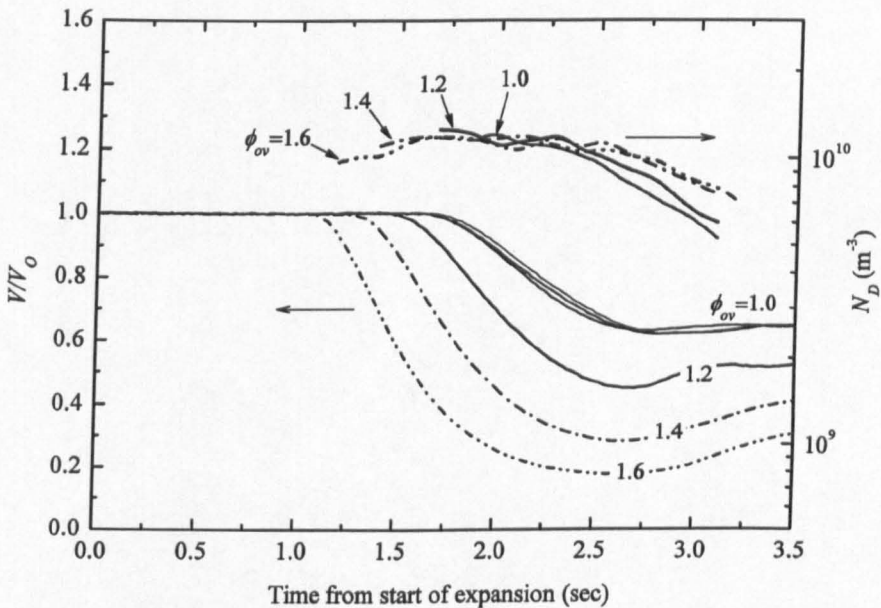


Figure 4.15: Variation of laser power attenuation and droplet number density with time for initially quiescent iso-octane and air mixtures at various  $\phi_{ov}$ . All mixtures were expanded from 180 kPa and 303 K.

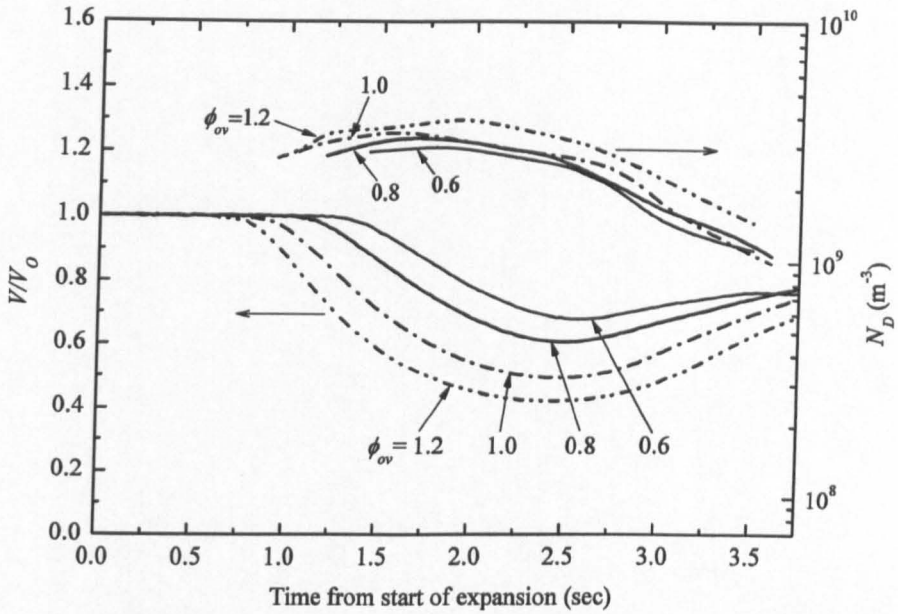


Figure 4.16: Variation of laser power attenuation and droplet number density with time for initially quiescent ethanol and air mixtures at various  $\phi_{ov}$ . All mixtures were expanded from 200 kPa and 313 K.

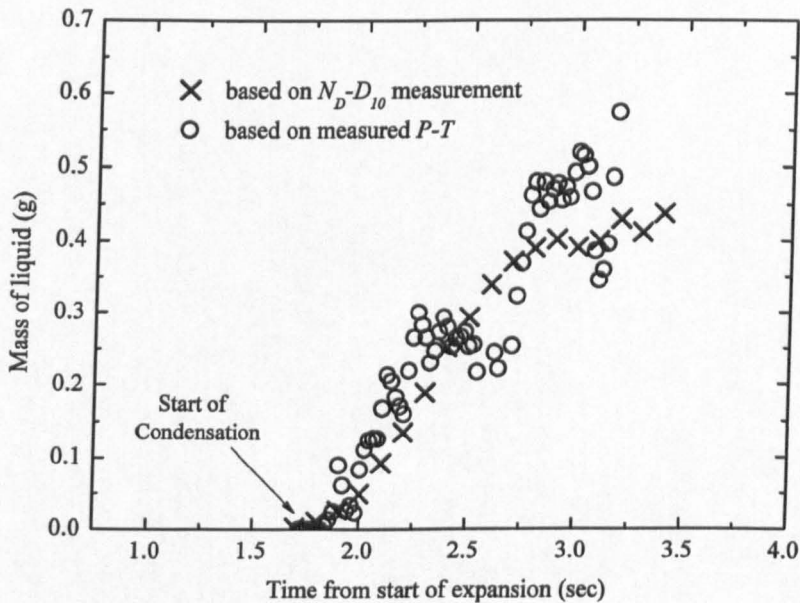


Figure 4.17: Variation in calculated mass of liquid fuel with time for stoichiometric iso-octane air mixture. Mixture was expanded from initial conditions of 200kPa and 303K.

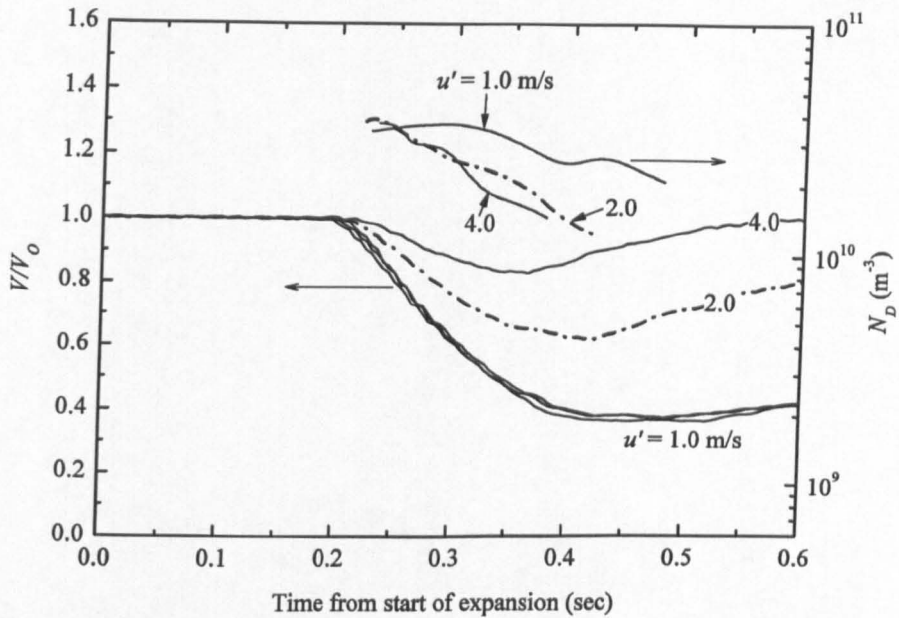


Figure 4.18: Variation of laser power attenuation and droplet number density with time for turbulent stoichiometric iso-octane and air mixtures at various  $u'$ . All mixtures were expanded from 200 kPa and 303 K.

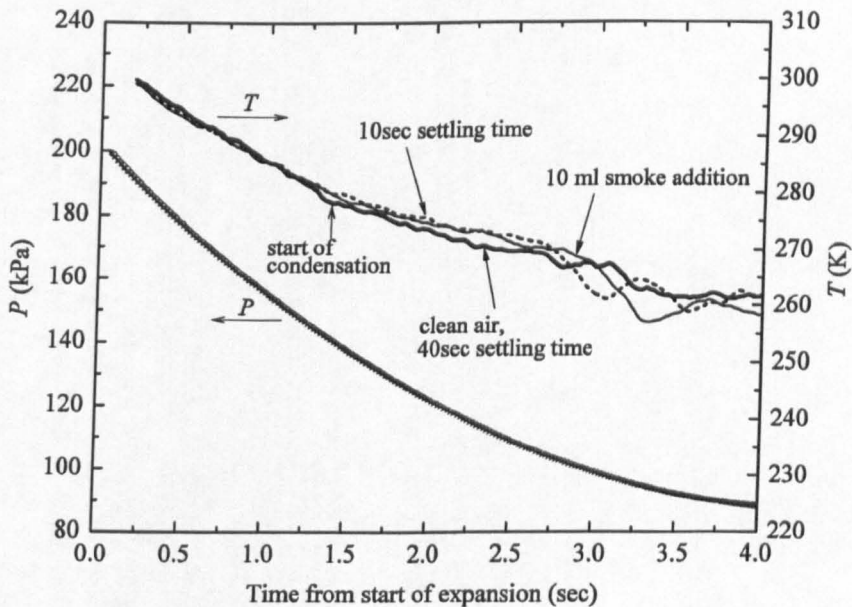


Figure 4.19: Variation of pressure and temperature with time during expansion of initially quiescent stoichiometric iso-octane and air mixtures from 200 kPa and 303 K under different mixture preparation conditions.

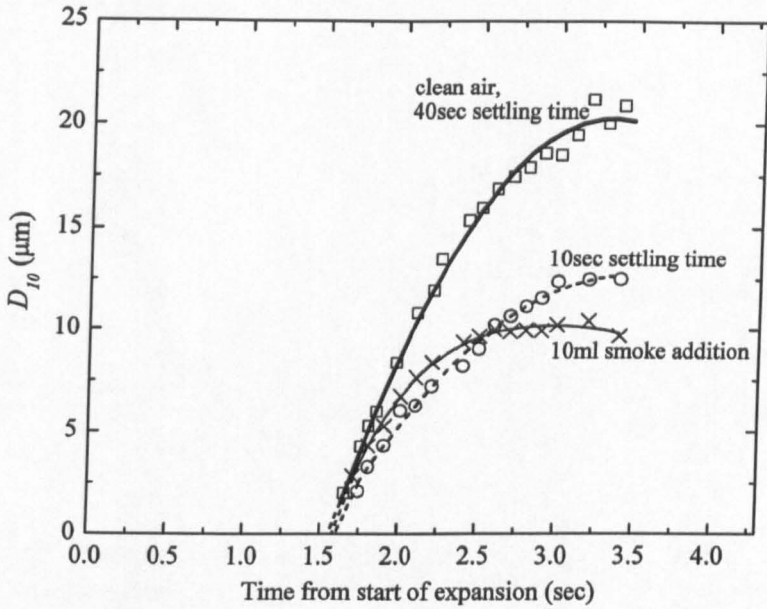


Figure 4.20: Variation of  $D_{10}$  with time for expanded mixtures in Fig. 4.18.

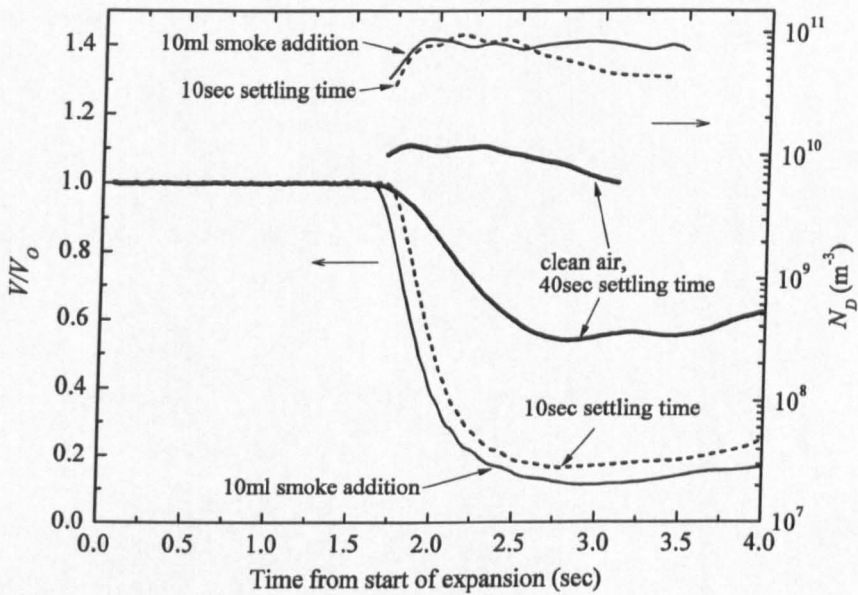


Figure 4.21: Variation of laser power attenuation and  $N_D$  with time for expanded mixtures in Fig. 4.18.

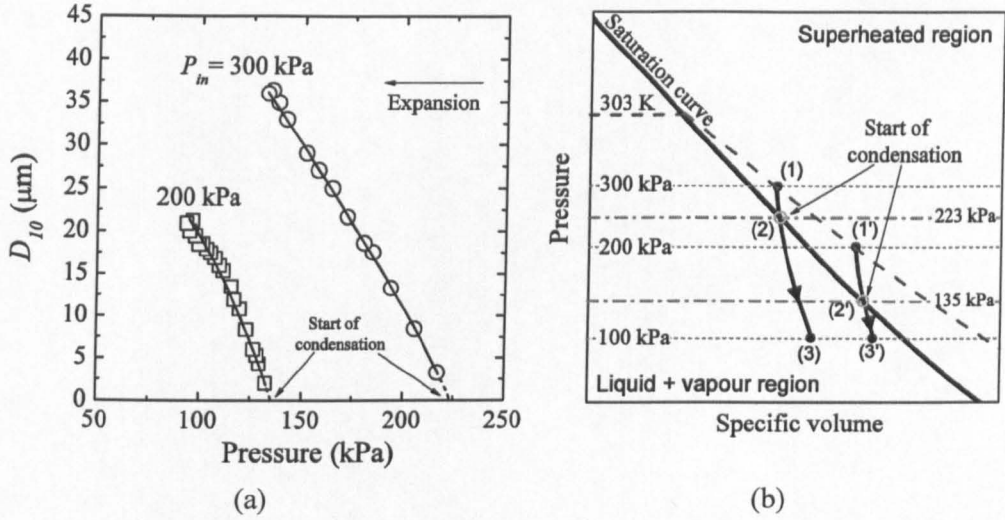


Figure 4.22: Comparison of aerosol generation at different initial pressures: (a) variation of  $D_{10}$  with instantaneous pressure and (b) schematic representation of expansion process on a  $P$ - $v$  diagram. Stoichiometric iso-octane and air under initially quiescent conditions at initial temperature of  $303$  K.

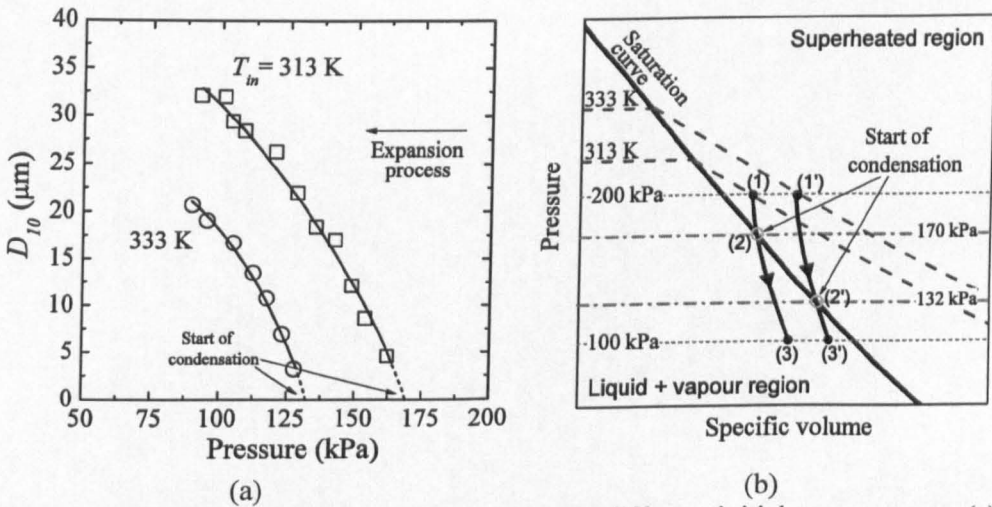
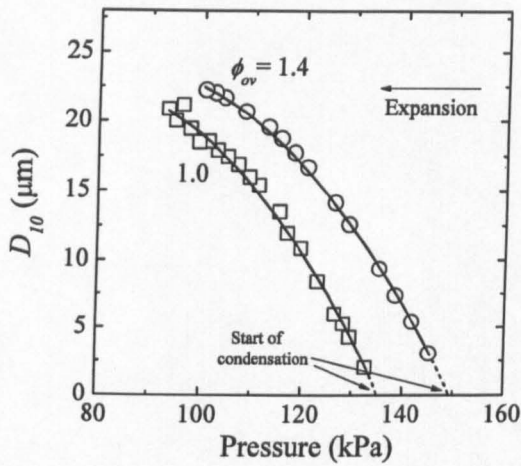
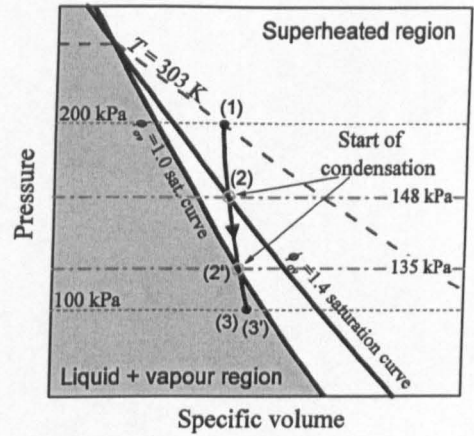


Figure 4.23: Comparison of aerosol generation at different initial temperatures: (a) variation of  $D_{10}$  with instantaneous pressure and (b) schematic representation of expansion on  $P$ - $v$  diagram. Stoichiometric ethanol and air under initially quiescent conditions at initial pressure of  $200$  kPa.



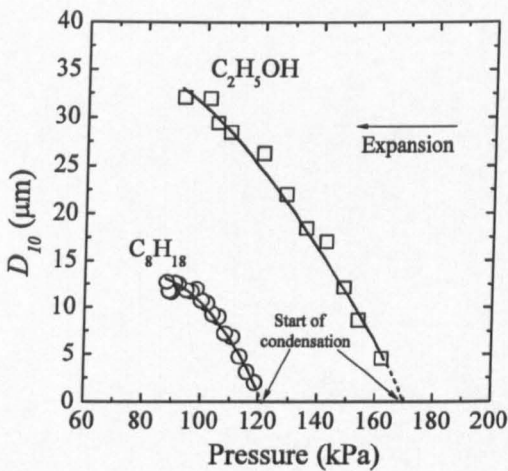


(a)

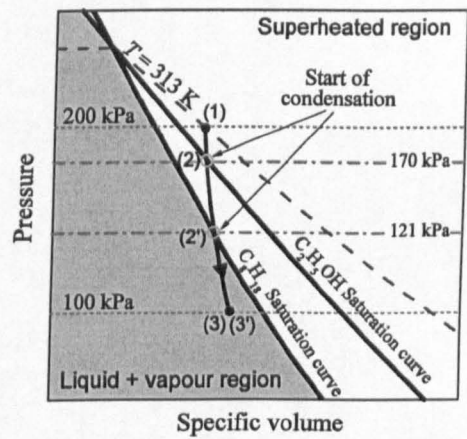


(b)

Figure 4.24: Comparison of aerosol generation at different  $\phi_{ov}$ : (a) variation of  $D_{10}$  with instantaneous pressure and (b) schematic representation of expansion on  $P$ - $v$  diagram. Both mixtures were iso-octane and air, expanded from initially quiescent conditions at 200 kPa and 303 K.

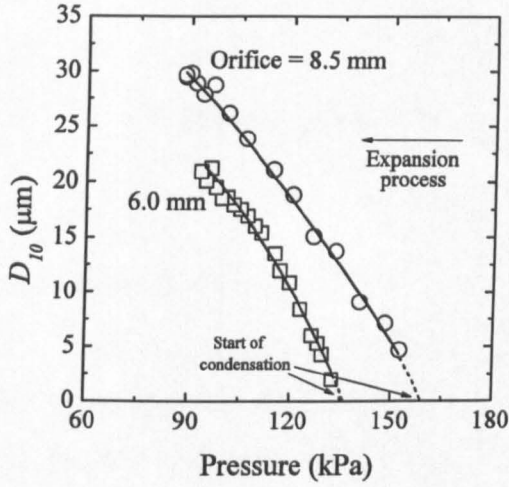


(a)

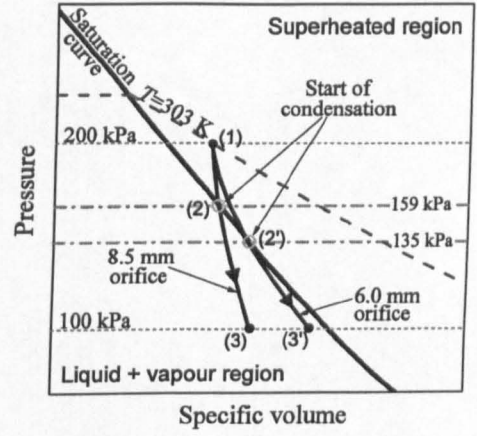


(b)

Figure 4.25: Comparison of aerosol generation at different types of fuel: (a) variation of  $D_{10}$  with instantaneous pressure and (b) schematic representation of expansion on  $P$ - $v$  diagram. Both mixtures were expanded from 200 kPa and 313 K at initially quiescent and stoichiometric conditions.



(a)



(b)

Figure 4.26: Comparison of aerosol generation at different expansion rates: (a) variation of  $D_{10}$  with instantaneous pressure and (b) schematic representation of expansion on  $P$ - $v$  diagram. Stoichiometric iso-octane and air under initially quiescent conditions at 200 kPa and 303 K.

## Chapter 5

### Flame Observations and Burning Rates

#### 5.1 Introduction

This chapter presents the experimental results of aerosol combustion under initially quiescent and turbulent conditions. Burning rates of laminar and turbulent flames have been derived by the spherical expanding flame technique discussed in Section 2.3. Effect of droplets was investigated by comparing flames of gaseous mixtures with those of aerosols at similar initial conditions. Flame observations of initially quiescent aerosol and gaseous flames are presented in Section 5.2. This includes observations during the ignition stage and throughout flame development at different  $\phi_{ov}$  and  $D_{10}$ . Measurements of laminar burning rates of aerosol and gaseous flames are presented in Section 5.3, together with those of Markstein length,  $L_b$  and unstretched burning velocity,  $u_l$ . The experimental results are also compared with those from other researchers. In Section 5.4, observations of aerosol and gaseous flames under turbulent conditions are presented, followed in Section 5.5 by measurements of their turbulent burning rates. Burning results of laminar ethanol-air flames are presented in Section 5.6.

#### 5.2 Observations of laminar iso-octane-air flames

In this section, observations of flame structure within aerosol and gaseous flames at a range of initial conditions are presented. Flame images were acquired by schlieren imaging as described in Section 3.5.3.

##### 5.2.1 Flame development with different ignition systems

Shown in Fig. 5.1a is a sequence of gaseous flame development at initial conditions of  $\phi_{ov} = 1.2$ , 100 kPa and 303 K, ignited using a fixed energy ignition unit, described in Section 3.2.3.1. Also shown in each image is the time from the

start of spark. It is shown in Fig. 5.1a that after the spark was initiated, a bright spot was exhibited at the centre of the flame and lasted for about 8 ms after ignition. After 16 ms, the flame surface started to display small bumps at random locations across the flame front. As the flame propagated further, these bumps enlarged but there was no cell division. On further investigation, it was found that the fixed energy ignition unit has a spark duration of several milliseconds which has the obvious effect of melting the electrode. Since this produced inconsistent observation, as discussed in Section 6.2, the ignition unit was changed to a variable energy ignition unit, as described in Section 3.2.3.2.

Shown in Fig. 5.1b is a sequence of isooctane-air gaseous flame development ignited using the variable energy ignition unit. The initial condition of gaseous mixture was identical to that in Fig. 5.1a. A smooth surface on the flame front was observed throughout flame propagation in Fig. 5.1b and was seen to be stable throughout observation. Small cracks were visible on the right and left side of the flame surface after 16 ms from ignition and these were originated due to the interaction between flame and the spark electrode. A similar observation of flame propagation was found when the same experiment was repeated. Although the flame structure in Fig. 5.1a is different from that in Fig. 5.1b due to the appearance of small bumps, such phenomena did not cause any difference to the rate of flame propagation. Nevertheless, in order to avoid misinterpretation of flame observation between aerosol and gaseous flames in the present study, the use of the variable energy ignition unit was employed throughout the rest of the experiments. See Section 6.2 for further details.

### 5.2.2 Ignition

Figure 5.2 shows sequences of schlieren images of gaseous and aerosol flame kernels for fuel rich mixtures,  $\phi_{ov} = 1.4$ , during the first 3 ms after ignition. Measurements for  $D_{10}$  of 5  $\mu\text{m}$ , 14  $\mu\text{m}$  and 20  $\mu\text{m}$  are shown. At these conditions, aerosol temperatures were varied between 275 K and 282 K, and pressures between 104 kPa and 110 kPa. For gaseous flames, the conditions were 285 K and 110 kPa. All mixtures were ignited using the same spark electrode at identical ignition energy using the variable ignition unit, described in Section 3.2.3.2. Up to three experiments, denoted 1, 2 and 3 in Fig. 5.2, were recorded at each condition.

It is shown in Fig. 5.2 that the size of flame kernel within 3 ms after ignition was an inverse function of  $D_{10}$ , with the gaseous flame being the largest. This trend indicates that the initial flame development of a gaseous flame was faster than for aerosol flames. However, this trend was reversed for the fuel lean mixtures, as shown in Fig. 5.3 for gaseous and aerosol flame at  $\phi_{ov} = 0.9$ . In contrast to the trend presented for the richer mixtures in Fig. 5.2, Fig. 5.3 shows that for lean mixtures, the size of flame kernel was smallest in the gaseous flame and largest in the aerosol flame at  $D_{10} = 20 \mu\text{m}$ . Clearly, this difference in flame size within the first 3 ms is a function of the complex interaction between ignition, diffusion and burning and this is discussed in Section 6.4.1.

### 5.2.3 Aerosol and gaseous flame development

Shown in Fig. 5.4 are schlieren images showing the growth of three expanding laminar iso-octane-air flames at  $\phi_{ov} = 1.2$ . The circular boundary (150 mm in diameter) represents the optical access windows. The black horizontal object in each of images was the spark electrode holder. Figure 5.3a shows a gaseous mixture ignited at 107 kPa and 283 K, while Figs. 5.3b and 5.3c show aerosol mixtures with  $D_{10} = 5 \mu\text{m}$  and  $14 \mu\text{m}$ , ignited between 279-280 K and 100-105 kPa. Since there were negligible differences in initial pressure and temperature, it is assumed that the differences in the flame structure between Figs. 5.4a and 5.4c were entirely due to the presence of droplets.

For the gaseous mixture, the flame had a smooth surface and was nearly spherical throughout observation. The long cracks visible on the flame surface were initiated by the perturbation by the spark electrode and then persisted throughout the range of observation. For the aerosol mixture in Fig. 5.4b, initially, the flame structure was similar to that in the gaseous mixture. However, differences started to appear at about 10 ms after ignition. At about this time, small cracks and cells appeared that progressively increased throughout flame growth. As  $D_{10}$  increased from  $5 \mu\text{m}$  (Fig. 5.4b) to  $14 \mu\text{m}$  (Fig. 5.4c), this development of cracks and cells became more prominent as indicated by the earlier onset of cracks and cells of about 6 ms after ignition. Clearly, such observations demonstrate that aerosol flames are more unstable than those of equivalent gaseous flames, which manifests itself in

earlier onset of cellularities that would not be present in gaseous flames at similar conditions.

Figure 5.5 shows a comparison between schlieren images of flames within aerosol and gaseous iso-octane-air mixtures at  $\phi_{ov}$  ranging from 0.8 to 2.0 and  $D_{10}$  up to 20  $\mu\text{m}$ . In all cases, the flame radius was approximately 48 mm which was the largest at which most flames could be fully observed through the windows at a wide range of equivalence ratios. This was less than the radius of the windows and is used to compare the flame structure between gaseous and aerosol mixtures in the later stage of flame propagation. Also shown in each flame image is the time from ignition. The aerosol mixtures were ignited at between 265-290 K and 93-125 kPa and gaseous mixtures were ignited at between 278-293 K and 95-125 kPa. The slight differences in initial pressure and temperature were unavoidable due to the method of aerosol generation using condensation technique as described in Section 4.7. For gaseous flames, the flame structure was smooth for lean and stoichiometric mixtures, indicating a stable flame. At  $\phi_{ov} = 1.2$ , the flame surface displayed a few long cracks, or large cells. At  $\phi_{ov} = 1.4$ , a large number of small cells were obtained, but at increasing  $\phi_{ov}$ , the cellular structure appeared to diminish. Conversely, for aerosol flames, the degree of cellularity was more prominent, indicative of more unstable flames. Furthermore, the tendency towards unstable flame propagation was promoted with an increase in  $D_{10}$ . For example, at  $\phi_{ov} = 1.0$ , the gaseous flame appeared smooth but a gradual transition to cellular structure was observed with an increase in  $D_{10}$ . However, it is interesting to observe that this trend was more apparent up to  $D_{10} = 14 \mu\text{m}$ . At a larger  $D_{10}$ , for instance at 20  $\mu\text{m}$ , the density of cells reduced, but the flame structure seems to be slightly distorted. Even the aerosol flame at  $\phi_{ov} = 0.8$ , which appeared smooth up to a droplet size of 14  $\mu\text{m}$ , presented a considerably distorted structure at  $D_{10} = 20 \mu\text{m}$ . Further results that related with this comparison is addressed in Section 5.3.2. Nevertheless, Fig. 5.4 clearly demonstrates that aerosol flames are more unstable than an equivalent gaseous flame and this observation is more pronounced for richer mixtures.

### 5.3 Laminar burning rates in iso-octane-air mixtures

Burning rates of quiescent aerosol mixtures were measured at a range of initial conditions. These were compared to burning rates of gaseous mixtures at similar conditions by igniting the mixture during expansion but before the onset of condensation.

#### 5.3.1 Flame speed development of gaseous mixtures

Shown in Figs. 5.6 and 5.7 are the variations of flame speed with time, radius and stretch, for gaseous iso-octane-air mixture at pre-ignition conditions of  $\phi_{ov} = 0.9$ , 97 kPa and 279 K. This is a typical data of gaseous flame development that has been described by many workers (Ali, 1995; Haq, 1998; Gillespie *et al.*, 2000) and explained in Section 2.3.1. It is shown in Fig. 5.6b that the flame might be considered to be fully developed approximately at radii larger than 20 mm, as denoted by point (1). This is indicated by the reduced gradient of flame speed against radius.

As shown in Fig 5.7, after a smooth propagating flame is established at point (1), the fundamental property of a laminar flame can be determined by a linear extrapolation of the region (1) to (2) to zero stretch (continuous line in Fig. 5.7), as described in Section 2.3.1. In determining the best linear extrapolation method that takes into account all data in region (1) to (2), two possible linear extrapolations were identified, as denoted by  $L_{b,min}$  and  $L_{b,max}$ , and the average value is calculated. From the flame speed at zero stretch,  $S_s$ , the laminar burning velocity,  $u_l$ , can be calculated using Eq. (2.11). The slope of this linear extrapolation represent the sensitivity of the flame speed to stretch rate and is known as the Markstein length,  $L_b$ . In the present plot of Fig. 5.7, the value of  $L_b$  is of positive sign and its significance is explained in Section 2.3.1.

#### 5.3.2 Aerosol flame speed and comparisons with gaseous flames

Shown in Figs. 5.8 and 5.9 are the variations of flame speed with radius and stretch rate for three aerosol flames at  $D_{f0} = 5 \mu\text{m}$  and  $\phi_{ov} = 0.8$  (squares),  $\phi_{ov} = 1.0$  (triangles) and  $\phi_{ov} = 1.2$  (circles). In Fig. 5.8, corresponding schlieren photographs of the flames at a maximum viewable radius are shown. As in Fig. 5.7, the solid lines

in Fig. 5.9 are linear fits to the data points at which the flames were stable and were used to determine  $S_f$  and  $L_b$ . The leanest mixture,  $\phi_{ov} = 0.8$ , in Figs. 5.8 and 5.9, was the slowest among those shown and was stable throughout the observed period. This is indicated by the smooth flame surface shown in Fig. 5.8. This flame was also affected by buoyancy in the later stages, as depicted by the corresponding schlieren photograph in Fig. 5.8, in which a smaller spacing can be seen between flame edge and window edge at the top in comparison to the bottom side. The flame in the stoichiometric mixture was also smooth and stable throughout propagation, as indicated by the photograph in Fig. 5.8. The flame of the richest mixture,  $\phi_{ov} = 1.2$ , shown in Figs. 5.8 and 5.9, was the fastest throughout the observation and also displayed a high degree of cellularity. In all the flames shown in Figs 5.8 and 5.9, a gradual increase in flame speed,  $S_n$ , was noticeable. However, at a critical radius, the flame for the richest mixture,  $\phi_{ov} = 1.2$ , became unstable and later began to accelerate. This is shown clearly in Fig. 5.9 and is described in Section 5.3.3.

Figure 5.10 shows the variations of flame speed with time and radius of aerosol and gaseous iso-octane-air mixtures at  $\phi_{ov} = 0.9, 1.4$  and  $2.0$ . The pressure and temperature are indicated for each curve (graphs plotted against time and radius used the same data) and, for the aerosol mixtures, values of  $D_{10}$  and  $\phi$ , also are indicated. For clarity, each plot shows average values from up to three explosions with associated error bars. In Fig. 5.10f, for the aerosol mixture with  $D_{10} = 14\mu\text{m}$ , data from all three explosions are plotted along with the corresponding error bars. In general, the scatter of experimental data was slightly larger for the lean mixtures, Figs. 5.10a and 5.10b, possibly by 20 to 60%, than for the richer mixtures, Figs. 5.10c to 5.10f.

In the lean flames of Figs. 5.10a and 5.10b, gaseous flames developed slower than aerosol flames. After 30 ms from ignition, all flames seem to have reached an approximately constant value, although aerosol flames at  $5\mu\text{m}$  and  $14\mu\text{m}$  exhibited small fluctuations. A notable exception to this trend was that at  $D_{10} = 20\mu\text{m}$ , where significant oscillations in flame speed were observed throughout propagation. Further results of this phenomenon are addressed in Section 5.3.5.

In the rich flames, shown in Figs. 5.10c and 5.10d, gaseous flames developed faster than aerosol flames within the first 7 ms after the start of ignition. Conversely, the aerosol flames had lower flame speeds during this early stage, but attained higher



subsequent values throughout the later period of observation. This acceleration, relative to that of the gaseous mixture, was associated with flame instabilities, as shown in Fig. 5.5. For the very rich flames,  $\phi_{ov} = 2.0$ , shown in Figs. 5.10e and 5.10f, the development of aerosol flames was remarkable in that they show a dramatic increase in flame speed compared to that in the gaseous phase and this increases rapidly with  $D_{10}$ . Such acceleration leads to a significant burning rate enhancement relative to the gaseous flames.

Although the temperature was not constant for all of the curves in Fig. 5.10, the differences in each figure were negligible in all comparisons except for Figs. 5.10a and 5.10b. Here, the temperature associated with different curves varied by  $14^\circ\text{C}$ , with the gaseous flames being at the highest temperature. This results in a higher gaseous flame speed, possibly by up to 5% (Lawes *et al.*, 2006), than for the coldest aerosol mixture. Hence, for identical temperatures, the effect of  $D_{10}$  on the flame speed might be a little greater than is shown in Figs. 5.10a and 5.10b. Nevertheless, the overall trends would be unchanged.

In the present work,  $S_{n,48}$ , which corresponds to the flame speed at a radius of approximately 48 mm was used to characterise the burning rate at the later stage of flame propagation. It should be noted that  $S_{n,48}$  is not a fundamental parameter. This parameter was chosen because there was some difficulty to determine unstretched flame speed,  $S_s$  for flames that cellular immediately after the ignition period (described in Section 5.3.3). In addition, the use of  $S_s$  in aerosol flames does not properly describe the effect of droplets on flame propagation. Since the determination of  $S_s$  does not account for flame acceleration due to instabilities, the variation of  $S_s$  as a function of equivalence ratio can be represented by the results of unstretched burning velocity,  $u_l$ , as described in Section 5.3.4. Shown in Fig. 5.11 are the variations of flame speed, measured at a radius of 48 mm,  $S_{n,48}$ , at a wide range of  $\phi_{ov}$ , for gaseous and aerosol iso-octane-air mixtures at similar initial pressures and temperatures. This plot shows the stretched flame speed that corresponds to the schlieren images as shown in Fig. 5.5. The symbols in Fig. 5.11 represent the average value of up to three measurements at each condition and the curves were best fits through the experimental data points. It is shown in Fig. 5.11 that at lean and stoichiometric flames, the effect of droplet size was not significant on the measured  $S_{n,48}$ . However, for increasingly rich flames,  $S_{n,48}$  became a strong

function of  $D_{10}$ . This was particularly significant at very high  $\phi_{ov}$  and large  $D_{10}$  (20  $\mu\text{m}$ ). The curve at  $D_{10} = 18 \mu\text{m}$  appeared to be in a transition regime at which droplets were reducing the burning rate at rich mixtures ( $1.1 \leq \phi_{ov} \leq 1.6$ ), but increasing it at very rich mixtures ( $\phi_{ov} \geq 1.8$ ). At bigger droplet sizes ( $D_{10} > 18 \mu\text{m}$ ), the effect was even more dramatic, which can be observed at  $D_{10} = 20 \mu\text{m}$ , where the very rich aerosol mixture ( $\phi_{ov} = 2.0$ ) burns nearly as fast as a gaseous stoichiometric mixture.

### 5.3.3 Flames with early onset of instabilities

Figure 5.12 shows four graphs of flame speed with stretch rate of rich gaseous and aerosol iso-octane-air mixtures at  $\phi_{ov} = 1.4$ . In the gaseous flame of Fig. 5.12a, the flame had a steady increase in flame speed and the flame front remained smooth and stable, as a result of the high stretch rate. As the flame expanded, the stretch rate is reduced. As stretch rate is reduced further, a point was reached where the flame became unstable and cellularity develops and this is associated with a significant increase in flame speed. As denoted in Fig. 5.12a, the point at which the flame speed begins to accelerate rapidly with decreasing stretch rate is expressed as  $Pe_{cl}$ , as defined in Section 2.3.2. For the aerosol flame at  $D_{10} = 5 \mu\text{m}$ , shown in Fig. 5.12b, a similar trend of flame speed variation with stretch rate was found as in the gaseous flame in Fig. 5.12a, except that the onset of acceleration which denoted by  $Pe_{cl}$  was earlier than gaseous in Fig. 5.12a and the acceleration of flame speed due to cellularity became more pronounced. The influence of  $Pe_{cl}$  on aerosol flame instabilities is discussed in Section 6.4.3. At a larger  $D_{10}$ , as in Figs 5.12c and 5.12d, cellularity was seen to develop immediately after the ignition period in aerosol flames. This is indicated by significant acceleration in flame speed at stretch rate,  $\alpha = 0.4 \text{ ms}^{-1}$ . As a result, the linear extrapolation for calculating the unstretched laminar burning properties such as  $L_b$  and  $S_r$  could not be determined.

### 5.3.4 Markstein length and unstretched burning velocity

Figure 5.13 shows the variations of  $L_b$  (defined in Section 2.3.1) for iso-octane gaseous and aerosol flames at a wide range of  $\phi_{ov}$ . Each plot shows average

values, as depicted in Fig. 5.7, from up to three experiments, and a best fit curve was obtained for each condition. For values of  $\phi_{ov}$  less than about 1.3, gaseous flames had the highest positive values of  $L_b$ , which reduced with increasing  $D_{10}$  and  $\phi_{ov}$ . However, at values of  $\phi_{ov}$  greater than 1.3,  $L_b$  became negative and decreased with decreasing  $D_{10}$ . It is interesting to note that the gradient of  $L_b$  with  $\phi_{ov}$  reduces with  $D_{10}$  such that an extrapolation of the data in Fig. 5.13 to  $D_{10} = 20 \mu\text{m}$  might yield a constant value of  $L_b$  as indicated by the dotted line.

Shown in Fig. 5.14 are the variations of  $u_l$  (defined in Section 2.3.1) over a wide range of  $\phi_{ov}$  for gaseous and aerosol iso-octane-air mixtures. This plot shows the average value of the experimental data. The value of  $u_l$  was obtained by application of Eq. (2.11) to experimental results such as those shown in Fig. 5.9. The solid line in Fig. 5.14 was obtained by drawing a best fit curve through the experimental results for gaseous mixtures. The scatter in the gaseous data is indicated by error bands. It is clear from Fig. 5.14 that the average value of  $u_l$  of an aerosol mixture is similar to that of an equivalent gaseous mixture. This observation is further strengthened by the fact that data points for aerosol mixtures lie within the error bands of an equivalent gaseous mixture. This might suggest that the laminar burning velocity of an aerosol iso-octane-air mixture probably remains unaffected by droplets within the range of the present work. This conclusion differs from that for flame speed shown in Fig. 5.11 because the latter includes the influence of instabilities while the former does not.

Shown in Fig. 5.15 are the variations of  $u_l$  with  $D_{10}$  for iso-octane-air mixtures at  $\phi_{ov}$  of 0.8, 1.0 and 1.2 at a range of pressures and temperatures. Also shown are the data points from previous measurements (Lawes *et al.*, 2006; Sulaiman, 2007) using the same apparatus as in the present work. For  $\phi_{ov} = 0.8$ , the present data is available only up to  $D_{10} = 5 \mu\text{m}$  because flame oscillations (addressed in Section 5.3.5) prevented reliable measurements thereafter. Further, in the case of  $\phi_{ov} = 1.2$  and  $D_{10}$  greater than  $10 \mu\text{m}$ , values of  $u_l$  could not be determined due to the early onset of instabilities, as explained in Section 5.3.3. It is shown in Fig. 5.15 that, in general, the present measurements showed good agreement with those taken previously. Reasons for the ability of the previous authors to obtain data at conditions not possible by the present author are unclear. For overall stoichiometric

mixtures, the present results show a slightly higher value than the previous results by up to 10%. This was probably due to differences in the initial pressure.

### 5.3.5 Oscillating flames

Shown in Fig. 5.16 is the variation of flame speed with radius for an oscillating flame of iso-octane-air aerosol at  $\phi_{ov} = 0.8$ ,  $D_{10} = 14 \mu\text{m}$ ,  $P = 95 \text{ kPa}$  and  $T = 273 \text{ K}$ . Also shown in Fig. 5.16 are corresponding schlieren images at selected radii to indicate the structure of flame surface. At approximately 6 mm radius, the flame speed reaches a minimum value, indicated by point (1), as the effects of the spark decayed. After this point, the flame speed begins to accelerate until it reaches a maximum, indicated by point (2) in Fig. 5.16. At this point, the flame displayed a mildly cellular surface structure. As the flame developed further, it slowed down until it reached a second minimum, at which the flame surface appeared smooth, as shown by point (3) in Fig. 5.16. This phenomenon was repeated throughout observation with alternating maximum and minimum in the flame speed, together with cellular and smooth flame structure.

Figure 5.17 shows the variations of flame speed with time for iso-octane-air aerosol at  $\phi_{ov} = 0.8$ , pressures between 93 and 120 kPa and temperatures between 263 and 276 K. The droplet sizes were 0  $\mu\text{m}$  (thin continuous line), 5  $\mu\text{m}$  (thick continuous line), 14  $\mu\text{m}$  (dash dot line) and 20  $\mu\text{m}$  (dash line). The symbols in Fig. 5.17 have been removed for clarity. It is indicated in Fig. 5.17 that large flame oscillations in the iso-octane aerosol mixture occurred for aerosols at  $D_{10} = 14 \mu\text{m}$  and  $D_{10} = 20 \mu\text{m}$ , as depicted by large fluctuations in flame speed throughout observation. These fluctuations in flame speed were accompanied by a periodic appearance and disappearance of cellular flame structure, as shown in Fig. 5.16. It is interesting to note that the flame oscillation frequency is a clear function of  $D_{10}$  as indicated by the larger time interval between the peaks with the larger  $D_{10}$ . These oscillations are in a good agreement with those obtained in the previous work as described in Section 2.6.4. Although this represents an interesting aside to the present work, further investigation is beyond the scope of the present study.

## 5.4 Turbulent flame observations

This section presents observations of aerosol and gaseous flames of iso-octane and air mixtures under turbulent conditions. The effect of fine droplets up to 14  $\mu\text{m}$  in diameter on turbulent flames was examined at various values of  $u'$  between zero and 4.0 m/s.

### 5.4.1 Ignition

Shown in Fig. 5.18 are sequences of schlieren images of gaseous and aerosol flame kernels for fuel-lean mixtures,  $\phi_{ov} = 0.9$ , at  $u' = 0.5$  m/s during the first 3 ms after ignition. Measurements for  $D_{10}$  of 5  $\mu\text{m}$  and 10  $\mu\text{m}$  are shown. At these conditions, the temperatures of the aerosols varied between 268 and 277 K and pressures between 97 and 108 kPa. For gaseous flames, the conditions at ignition were 293 K and 100 kPa. Similarly, as previously discussed in Section 5.2 relating to laminar flames, the variation in pre-ignition conditions was inevitable due to the droplet generation method. Ignition of all mixtures was initiated at the centre of the combustion vessel at identical ignition energy, as described in Section 3.2.3. Up to five experiments were recorded and measured at each condition.

It is shown in Fig. 5.18 that for  $\phi_{ov} = 0.9$ , the size of flame kernel was an inverse function of droplet size, with the gaseous flame being the largest at all times. However, this trend was reversed for fuel rich mixtures at  $\phi_{ov} = 1.2$ , as shown in Fig. 5.19. Similar to Fig. 5.18, the aerosols in Fig. 5.19 varied at similar values of  $D_{10}$  and also had a slight difference of pressure and temperature during ignition. In contrast to the trend presented for lean mixtures in Fig. 5.18, it is seen in Fig. 5.19 that for rich mixtures, the size of flame kernel was smallest in gaseous flame and biggest in aerosol flame at  $D_{10} = 10$   $\mu\text{m}$ . Clearly, the difference in the flame size within the first 3 ms can cause differences in early flame propagation rates. This is discussed in Section 6.5.1, together with the reversal trend between development in fuel-lean and fuel-rich conditions under turbulent conditions.

### 5.4.2 Aerosol and gaseous flame development

Shown in Fig. 5.20 are schlieren images of the growth of three expanding iso-octane-air flames at  $u' = 0.5$  m/s and  $\phi_{ov} = 0.9$  during the first 30 ms of flame

propagation. Within the first 5 ms, all flames had a smooth surface with mild wrinkles due to turbulence. At 10 ms, all flames had clear wrinkles which progressively increased throughout the rest of flame growth. During these observations, the gaseous flame was largest relative to the aerosol flames which indicates that it had faster propagation. The two aerosol flames, initially, displayed nearly similar flame sizes until 15 ms. However, after 15 ms, the aerosol flame at  $D_{10} = 10 \mu\text{m}$  appeared slightly larger in size and had more wrinkles relative to the aerosol flame at  $D_{10} = 5 \mu\text{m}$ . Although such observations in flame structure were obtained from a single experiment, consistency of observation was obtained in up to five experiments at each condition.

Figure 5.21 shows a comparison of flame growth and development similar to Fig. 5.20 but in this case for fuel rich mixtures at  $\phi_{ov} = 1.2$ . The flames in Fig. 5.21 are similar to those in Fig. 5.19 except only one flame was selected at each condition. Initially, all flames started to show wrinkles due to turbulence as early as 3 ms after ignition started. Such wrinkles developed gradually throughout the flame growth and became more intensified towards a large flame. It is interesting to note that the degree of wrinkling in the case of aerosol flames was slightly higher relative to the gaseous flame, in which the aerosol flame at  $D_{10} = 10 \mu\text{m}$  had the highest degree of wrinkling. It is also shown in Fig. 5.21 that the aerosol flame at  $D_{10} = 10 \mu\text{m}$  had the largest flame size compared to the other flames throughout the observation, which indicates the fastest propagation. Clearly, this observation, obtained in a fuel-rich mixture, is reversed from the observation in a fuel lean mixture in Fig. 5.20.

Shown in Fig. 5.22 are schlieren images of the development of three expanding iso-octane-air flames at  $\phi_{ov} = 1.2$  under the highest measured turbulent condition of  $u' = 4.0 \text{ m/s}$ . At these conditions, the temperatures of the aerosols were varied between 267 and 277 K and pressures between 93 and 106 kPa. For gaseous flames, the conditions at ignition were 293 K and 100 kPa. The same comment applied as in Fig. 5.18 about the variation in pre-ignition conditions between aerosol and gaseous mixtures. It is shown in Fig. 5.22 that there were insignificant differences in the structure of these three flames throughout observation. However, since the level of turbulence was the highest in the present work ( $u' = 4.0 \text{ m/s}$ ), the flame kernel was significantly more wrinkled and distorted than those of lower

turbulence, as in Fig. 5.21. As a result of higher turbulence, the flame propagation in Fig. 5.22 was faster than in Fig. 5.21, as indicated by the time scale in the two Figures.

Shown in Fig. 5.23 are schlieren images of aerosol and gaseous iso-octane-air flames at  $\phi_{ov} = 0.9$  and at different values of  $u'$  between zero and 2.0 m/s. The images are limited to  $u' \leq 2.0$  m/s due to a failure to ignite the mixtures at higher levels of  $u'$ . All images were taken at a mean flame radius of 40 mm. This radius was the largest at which most flames were observed. Also shown in each flame image is the time from ignition. For the gaseous mixture at  $u' = 0$ , the flame was smooth and nearly spherical. As  $u'$  increased from 0.5 to 2.0 m/s, the flames started to wrinkle and deform considerably relative to the laminar flame. The degree of wrinkling was also shown qualitatively to increase with  $u'$ . In the case of aerosol flames, a slightly unstable flame with small bumps was found for laminar aerosol flame at  $D_{10} = 10 \mu\text{m}$ . As  $u'$  increased from 0.5 to 1.0 m/s, the flames started to wrinkle and the degree of wrinkling increased as  $u'$  increased. However, at  $u' = 2.0$  m/s, the flame images were unusual, in that both aerosol flames were obstructed by unknown 'black clouds' (Sulaiman, 2007). These were observed at random locations near the flame front and started to appear approximately between 8 and 10 ms after ignition and increased in quantity throughout flame propagation. The observation of 'black clouds' was significant because they seem to be visible only in aerosol flames. This is addressed in Section 6.2.

Figure 5.24 shows a similar comparison of flame structure between gaseous and aerosol flames as in Fig. 5.23 but in this case for fuel-rich mixtures at  $\phi_{ov} = 1.2$  and  $u'$  between zero and 4.0 m/s. Under quiescent conditions,  $u' = 0$ , the gaseous flame was smooth and nearly spherical. However, the corresponding aerosol flames showed unstable structure with cracks and cells and the level of cellularity was increased as  $D_{10}$  increased. In low turbulence,  $u' = 0.5$  m/s, the structure of aerosol flames still displayed more wrinkles than in the gaseous flame, indicating that droplet induced flame instabilities were still present. However, at  $u' = 1.0$  to 4.0 m/s, the difference in flame structure between aerosol and gaseous mixtures was much less obvious, suggesting that increasing levels of turbulence eventually dominate over any effects of cellular instabilities.

## 5.5 Turbulent burning rates in isooctane-air mixture

Following the observations in Section 5.4, this section presents measurements of turbulent burning rates for both gaseous and aerosol iso-octane-air flames. The calculation procedures are described in Section 2.3.3.

### 5.5.1 Flame speed development in gaseous mixtures

Shown in Fig. 5.25 are the variations of radius with time for turbulent gaseous iso-octane-air mixtures at  $\phi_{ov} = 1.2$ , 100 kPa and 303 K for two different  $u'$ : 0.5 and 4.0 m/s. The asterisk markers represent the results for  $u' = 0.5$  m/s and the circles represent those for  $u' = 4.0$  m/s. For each condition, up to five experiments were recorded. It is shown in Fig. 5.25 that the variation of flame radius with time is a strong function of  $u'$ . As the flames propagated further, the flame radius at  $u' = 4.0$  m/s is shown to be always higher than that of  $u' = 0.5$  m/s.

Shown in Figs. 5.26 and 5.27 are the measured turbulent flame speeds, plotted against time and radius after ignition for the mixtures in Fig. 5.25. The turbulent flame speed was calculated using Eq. (2.29). The scatter of the results was small for  $u' = 0.5$  m/s but remarkably high for  $u' = 4.0$  m/s, possibly by up to a factor of 4. This uncertainty was consistent with random variations associated with turbulence (Nwagwe *et al.*, 2000) and was probably due to real cyclic variations rather than to experimental errors. It is shown in Figs. 5.26 and 5.27 that a regime of spark affected propagation in early stages, as described for laminar flames in Section 2.3.1, was also exhibited in the turbulent flames. The effect of turbulence on flame propagation was significant throughout the flame growth, which is shown in Figs. 5.26 and 5.27 where the flame speed increased with  $u'$  and became more prominent as the flame developed further.

### 5.5.2 Aerosol flame speed and comparisons with gaseous flames

Figure 5.28 shows the variations of flame speed with time and radius for gaseous and aerosol lean mixtures,  $\phi_{ov} = 0.9$ , and values of  $u'$  at 0, 0.5 and 1.0 m/s. The results are limited to  $u' \leq 1.0$  m/s due to obscuration of the flame edge by the 'black clouds' at  $u' = 2.0$  m/s, as shown in Fig. 5.23 and discussed in Section 6.2. The ignition pressure and temperature are indicated for each curve (graphs plotted



against time and radius used the same data) and, for the aerosol mixtures, the values of  $D_{10}$  (5 $\mu\text{m}$ , 10 $\mu\text{m}$ , 14 $\mu\text{m}$ ) and  $\phi$ , also are indicated. For clarity, each plot shows the average value of between three and five explosions with associated error bars. In Fig. 5.28c, for the gaseous mixture, data from all five explosions are plotted along with the corresponding error bars. In general, the scatter of experimental data was small for quiescent mixtures but it increased with  $u'$ . This was probably due to random variations associated with turbulence as described in Section 5.5.1.

It is shown in all data in Fig. 5.28 that a regime of spark affected period was visible within 10 ms after the start of ignition. After this period, the propagation of flame in quiescent mixture displayed evidence of flame speed stabilisation while the propagation of turbulent flame displayed a sustained increase in flame speed with time and radius. For quiescent mixtures, shown in Figs. 5.28a and 5.28b, the propagation of aerosol flames was faster than that of gaseous flames throughout the observation. However, at low turbulence, where  $u' = 0.5$  m/s, the trend was reversed to that of  $u' = 0$  m/s, where gaseous flames developed faster than aerosol flames throughout the propagation. As  $u'$  increased to 1.0 m/s, the variation of flame speed with time and radius was seen to be independent of the presence of droplets.

Shown in Figs. 5.29 and 5.30 are similar plots to those in Fig. 5.28, but for fuel rich mixtures at  $\phi_{ov} = 1.2$ , and values of  $u'$  at 0, 0.5 and 1.0 m/s (Fig. 5.29) and  $u'$  at 2.0 and 4.0 m/s (Fig. 5.30). The general trend in all data in Figs. 5.29 and 5.30, after the spark affected period of about 3 ms, was a sustained increase in flame speed with time and radius. The flame growth rate was also increased with  $u'$ . In the quiescent mixtures of Figs. 5.29a and 5.29b, gaseous flames developed faster than aerosol flames within the first 5 ms before reaching an approximately constant value of about 2.5 m/s. Conversely, the two aerosol flames developed slower than the gaseous flames but continued to accelerate throughout the period of observation and the maximum flame speed increased with  $D_{10}$ . This acceleration was associated with flame instabilities due to droplets, as shown in Fig. 5.24.

At  $u' = 0.5$  m/s, as shown in Figs. 5.29c and 5.29d, the effect of  $D_{10}$  on flame propagation was still obvious, where both aerosol flames propagated faster than gaseous flames, particularly in the later stage. This enhancement is consistent with the increase in cellular structure of aerosol flames compared with that of gaseous flames, as shown in Fig. 5.24. As  $u'$  increased to 1.0 m/s, as shown in Figs. 5.29e

and 5.29f, the variation of flame speed with time and radius between gaseous and aerosol flames was not consistent. Initially, all flames propagated with nearly the same rate. After 5 ms, aerosol flames at  $D_{10} = 5 \mu\text{m}$  developed slower than gaseous flames. Conversely, aerosol flames at  $D_{10} = 10 \mu\text{m}$  developed faster than aerosol flames at  $D_{10} = 5 \mu\text{m}$  and closer to that of gaseous flame propagation. This trend was unexpected and further discussion on this result is presented in Section 6.5.2. At higher turbulence,  $u' = 2.0$  and  $4.0$  m/s, as shown in Fig. 5.30, the difference in the flame speed variation with time and radius between gaseous and aerosol flames became less obvious.

As described in Section 5.3.2, it is important to recognise that the temperature was not constant for all comparisons in Figs. 5.28 to 5.30. For example, in Fig. 5.28, the highest temperature difference between gaseous and aerosol was up to 28 K, while in Figs. 5.29 and 5.30 it was up to 26 K, with the gaseous flames being at the highest temperature in each Figure. Such differences in temperature might result in increase of gaseous flame speed, possibly by up to 10% more than for aerosol mixture (Lawes *et al.*, 2006). Nevertheless, as explained in Section 5.3.2, this variation would not alter the overall trends of flame propagation due to the presence of droplets.

## 5.6 Burning rates of quiescent ethanol aerosol mixtures

In the present work, experimental investigation on combustion of droplet clouds has been extended to that of ethanol. The burning rates of quiescent ethanol aerosol mixtures were measured at near atmospheric pressures and temperatures. The effect of fine droplets between 5 and 31  $\mu\text{m}$  in diameter was examined at  $\phi_{ov}$  between 0.7 and 1.2. Comparisons of flame propagation were made between ethanol gaseous and aerosols mixtures at similar conditions.

### 5.6.1 Flame observations

Shown in Fig. 5.31 are schlieren images of the growth of three expanding laminar ethanol-air flames at  $\phi_{ov} = 1.2$ . Figure 5.31a shows a gaseous mixture ignited at 100 kPa and 300 K, while Figs. 5.31b and 5.31c show aerosol mixtures at 5  $\mu\text{m}$  and 12  $\mu\text{m}$ , ignited at between 298-300 K and 109-115 kPa. In general, a similar

observation of flame structure as in iso-octane-air flames in Fig. 5.4, was found in ethanol-air flames. For gaseous flames, smooth surface and nearly spherical flame were recorded throughout observation. For aerosol flames at  $D_{10} = 5 \mu\text{m}$ , development of cracks and cells on the flame surface was observed as early as 9 ms after the mixture ignited. However, for the  $12 \mu\text{m}$  droplets, the development of cracks and cells appeared to become less obvious than for flames at  $D_{10} = 5 \mu\text{m}$ .

Figure 5.32 shows a comparison between the flame structure at a flame radius of approximately 48 mm of gaseous and aerosol mixtures, for  $\phi_{ov}$  ranging from 0.8 to 1.2 and  $D_{10}$  up to  $31 \mu\text{m}$ . This comparison was similar to that for the iso-octane-air flames in Fig. 5.5, except that the range in  $\phi_{ov}$  was limited to 1.2. Also shown in each flame image is the time from ignition. The variation in pre-ignition conditions for ethanol-air mixture was unavoidable and varied between pressure of 96-119 kPa and temperature of 289-300 K. For gaseous flames, the flame structure was smooth and stable at a wide range of  $\phi_{ov}$ . Conversely, for aerosol flames, the flame structure displayed cracks and shallow cells. For lean and stoichiometric aerosol flames, the development of cracks and cells became pronounced as  $D_{10}$  increased to  $31 \mu\text{m}$ . However, for aerosol flames at  $\phi_{ov} = 1.2$ , the degree of cellularity was remarkable only for aerosol flames at  $D_{10} = 5 \mu\text{m}$  and gradually became less cellular with  $D_{10}$  larger than  $12 \mu\text{m}$ . It is interesting to note that, at a wide range of  $\phi_{ov}$ , increasing  $D_{10}$  beyond  $12 \mu\text{m}$  showed a slight distortion on the flame surface and this became apparent with leaner mixtures and bigger droplets.

### 5.6.2 Burning rates of laminar gaseous and aerosol mixtures

Shown in Fig. 5.33 is the variation of flame speed, at a radius of 48 mm,  $S_{n,48}$ , at a wide range of  $\phi_{ov}$ , for aerosol and gaseous ethanol-air mixtures at similar initial pressures and temperatures. Similar to iso-octane-air flames in Fig. 5.12,  $S_{n,48}$  was used as characteristic flame speed for comparing the burning rate between gaseous and aerosol mixtures in the present work. This plot shows the average value of the experimental data and the trend was obtained by drawing a best fit curve through the averaged data points. It is shown in Fig. 5.33 that in the lean flames, the effect of fine droplets, up to  $23 \mu\text{m}$ , was not significant on the measured  $S_{n,48}$ . However, as  $D_{10}$  increased to  $31 \mu\text{m}$ , there was a remarkable enhancement in the

measured  $S_{n,48}$ , possibly by up to 22 % than that of equivalent gaseous flames. However, for stoichiometric and rich flames, such a trend was reversed. Aerosol flames at 31  $\mu\text{m}$  showed slowest propagation than the other flames, possibly by up to 15 % slower than the equivalent gaseous flame. Although the effects of fine droplets up to 23  $\mu\text{m}$  was also insignificant on the measured  $S_{n,48}$  of rich flames, due to cellularity, as shown in Fig. 5.31, aerosol flames at 5 and 12  $\mu\text{m}$  had a slight enhancement on the measured  $S_{n,48}$  probably by up to 4 % than the equivalent gaseous flames. Two important observations can be made from the results in Fig. 5.33. First, the measured  $S_{n,48}$  was roughly independent of  $D_{10}$  up to 23  $\mu\text{m}$  throughout a wide range of  $\phi_{ov}$ . Second, as  $D_{10}$  increased beyond 23  $\mu\text{m}$ , there was a remarkable enhancement of  $S_{n,48}$  in the lean flames but a reduction of  $S_{n,48}$  in the rich flames.

Shown in Fig. 5.34 are the variations of  $L_b$  (defined in Section 2.3.1) for aerosol and gaseous flames of ethanol-air mixtures at a wide range of  $\phi_{ov}$ . Each plot shows average values and a best fit curve was obtained for each condition. In general, a similar trend of  $L_b$ , as shown by iso-octane-air flames in Fig. 5.13, was obtained for ethanol-air flames. For gaseous flames, as  $\phi_{ov}$  increased,  $L_b$  decreased. In case of aerosol flames, as  $D_{10}$  increased, the reduction in  $L_b$  was only appreciable up to  $\phi_{ov} = 0.9$ . For  $\phi_{ov}$  greater than 0.9, the reduction became less pronounced and further became insignificant to the  $\phi_{ov}$ .

Shown in Fig. 5.35 are the variations of  $u_l$  (defined in Section 2.3.1) with  $D_{10}$  for ethanol-air mixtures at  $\phi_{ov}$  of 0.8, 1.0 and 1.2 at a range of pressures and temperatures. Also shown in Fig. 5.35 by the cross symbols are the experimental values from Hayashi *et al.*, (1976). In general, the value of  $u_l$  in the present work, at each condition of  $\phi_{ov}$ , was shown to be slightly lower, possibly by up to 12% than those in Hayashi *et al.* (1976). This was probably due to the lower initial temperature in the present work, possibly by up to 38 K than that in Hayashi *et al.* (1976). This is supported by Bradley *et al.* (1998) who showed that, for stoichiometric gaseous flames, an increase in temperature of about 30 K would increase  $u_l$  by about 10%. Nevertheless, both values from the present work and from Hayashi *et al.* (1976) show a similar trend at each  $\phi_{ov}$ . At  $\phi_{ov} = 0.8$ , the results suggest that  $u_l$  was probably unchanged by the presence of droplets. However, at stoichiometric and  $\phi_{ov} = 1.2$ ,

droplets show an effect to the variation of  $u_l$  with  $D_{10}$  where it decreases as  $D_{10}$  increases.

Shown in Fig. 5.36 are the variations of  $u_l$  at a wide range of  $\phi_{ov}$  for gaseous and aerosol ethanol-air mixtures. Each plot shows average values and best fit curves were obtained for each condition with associated error bars. At  $\phi_{ov} = 0.7$ , only data up to  $12 \mu\text{m}$  were available, since the larger droplets (beyond  $12 \mu\text{m}$ ) experienced the oscillating phenomenon as described in iso-octane-air flames in Section 5.3.5. It is shown in Fig. 5.36 that the effect of droplet size was important to the variation of  $u_l$  at a wide range of  $\phi_{ov}$ . In the case of stoichiometric and rich flames, an increase in  $D_{10}$  caused a significant reduction in  $u_l$ . However, in lean flames, the reduction in  $u_l$  due to  $D_{10}$  occurred only up to  $D_{10} = 12 \mu\text{m}$ . As  $D_{10}$  increased beyond  $12 \mu\text{m}$ , the value of  $u_l$  appeared to increase. Also shown in Fig. 5.36, for comparison, is the smooth curve for gaseous iso-octane reproduced from Fig. 5.14. It clearly illustrates that ethanol flames are faster than iso-octane flames. Also, a comparison of Figs. 5.14 and 5.36 shows that ethanol is much more sensitive to  $D_{10}$  than iso-octane and this is discussed in Section 6.4.4.

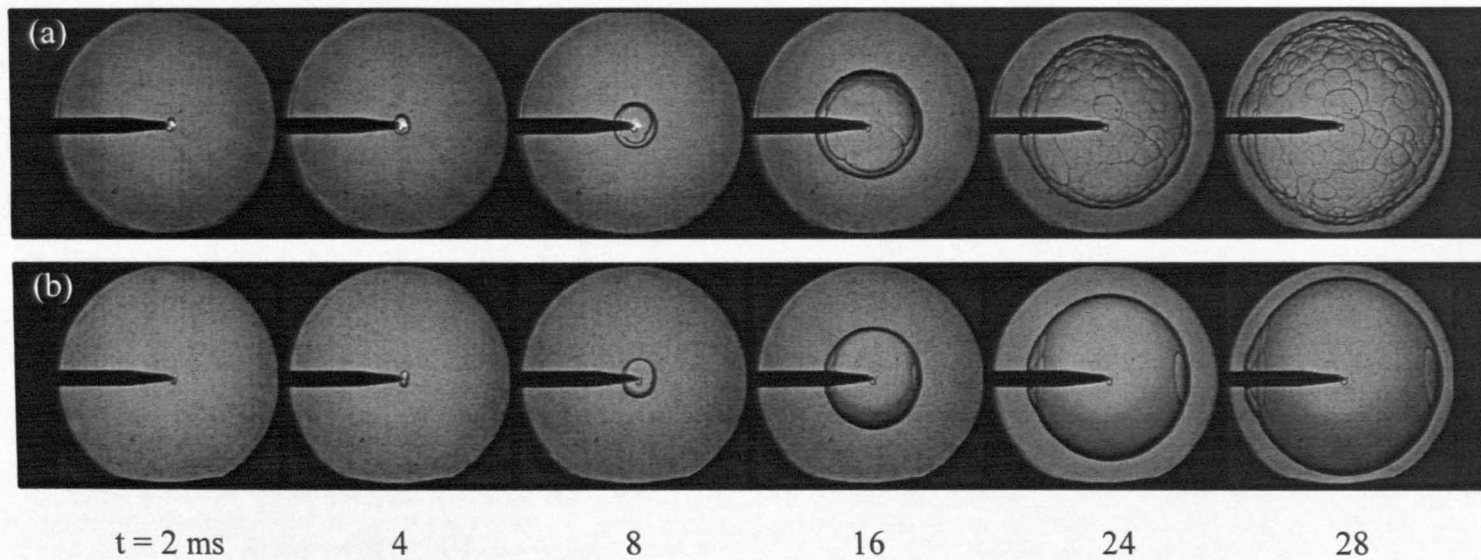


Figure 5.1: Comparison of effect of ignition system on laminar flame propagation for gaseous iso-octane-air mixtures at  $\phi_{ov}=1.2$ , 100 kPa and 303 K. (a) Fixed energy ignition unit, and (b) variable energy ignition unit.

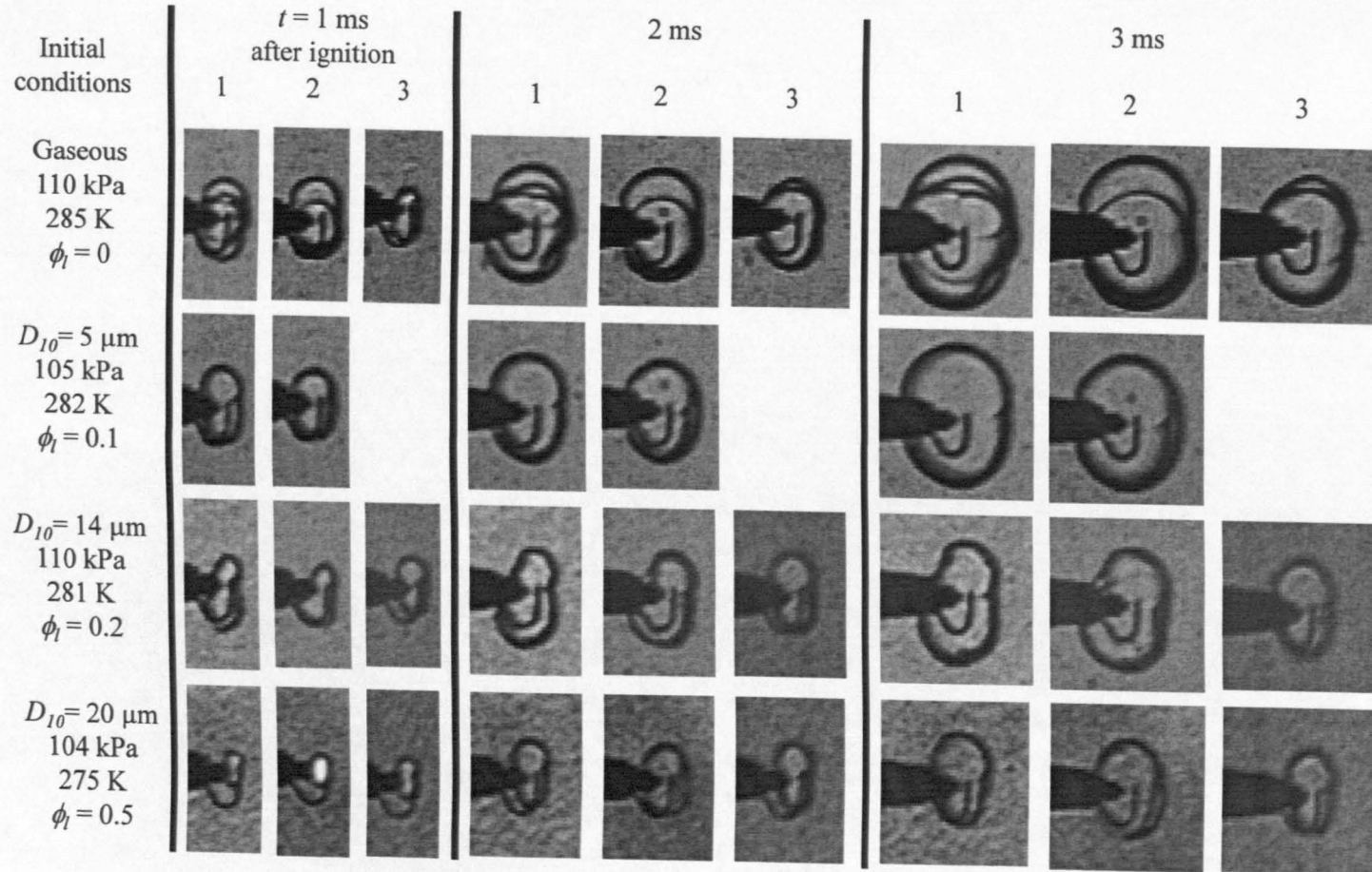


Figure 5.2: Effects of droplets on ignition and initial flame growth of initially quiescent iso-octane-air mixtures,  $\phi_{ov}=1.4$ .

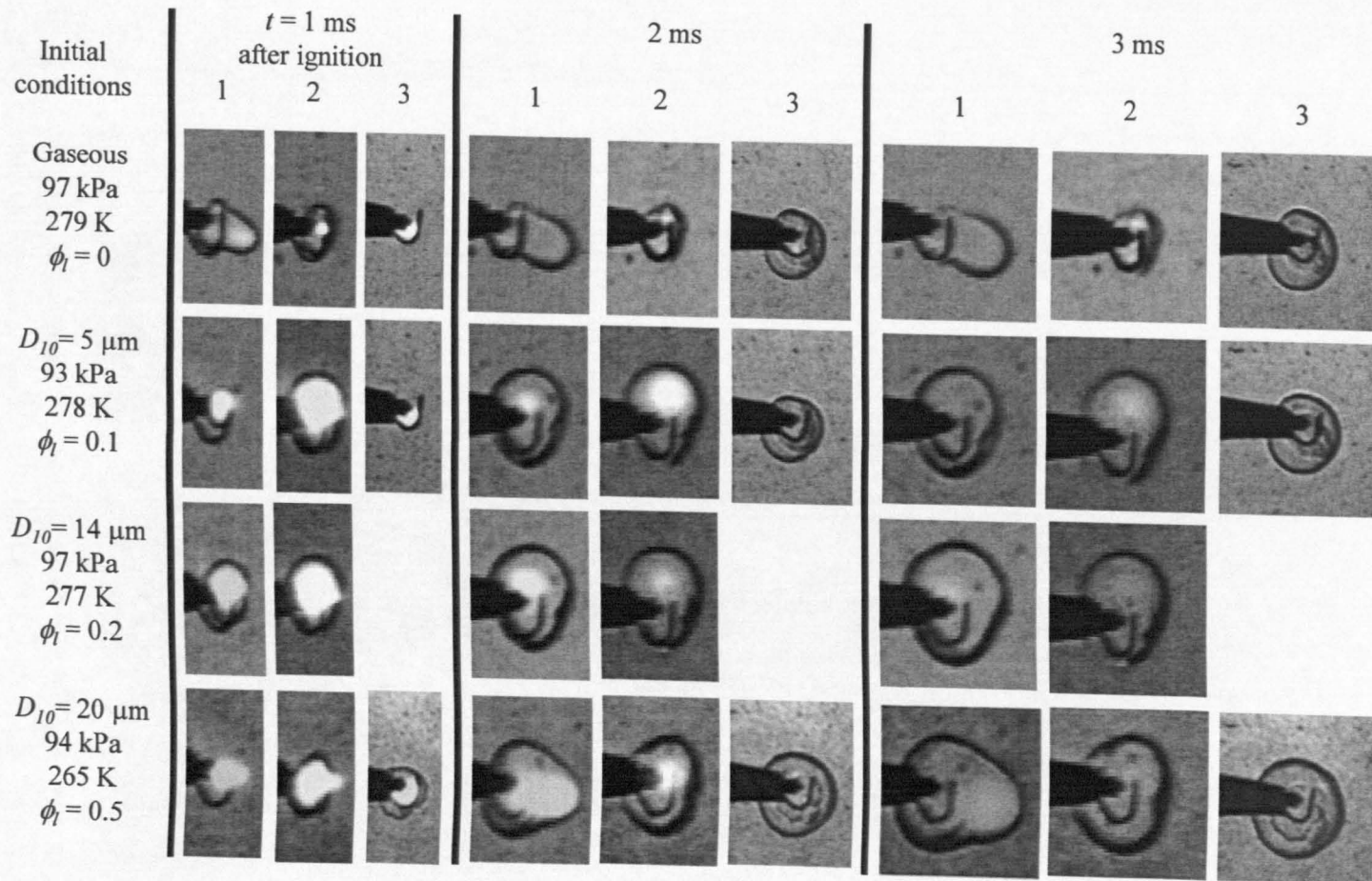


Figure 5.3: Effects of droplets on ignition and initial flame growth of initially quiescent iso-octane-air mixtures,  $\phi_{ov}=0.9$ .



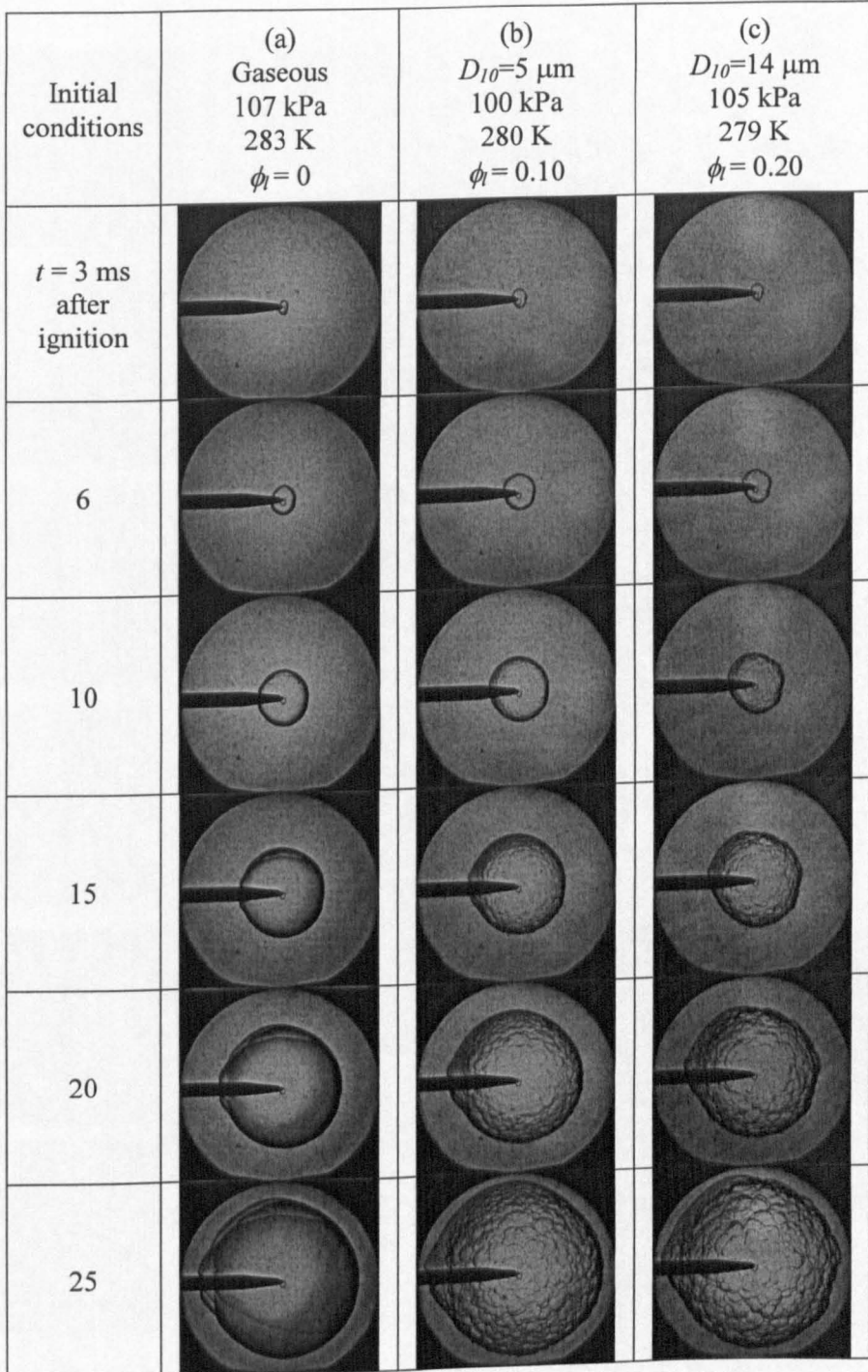


Figure 5.4: Typical development of laminar iso-octane-air flames at  $\phi_{ov} = 1.2$  for, (a) gaseous mixture, (b) aerosol at  $D_{10} = 5 \mu\text{m}$  and (c) aerosol at  $D_{10} = 14 \mu\text{m}$ .

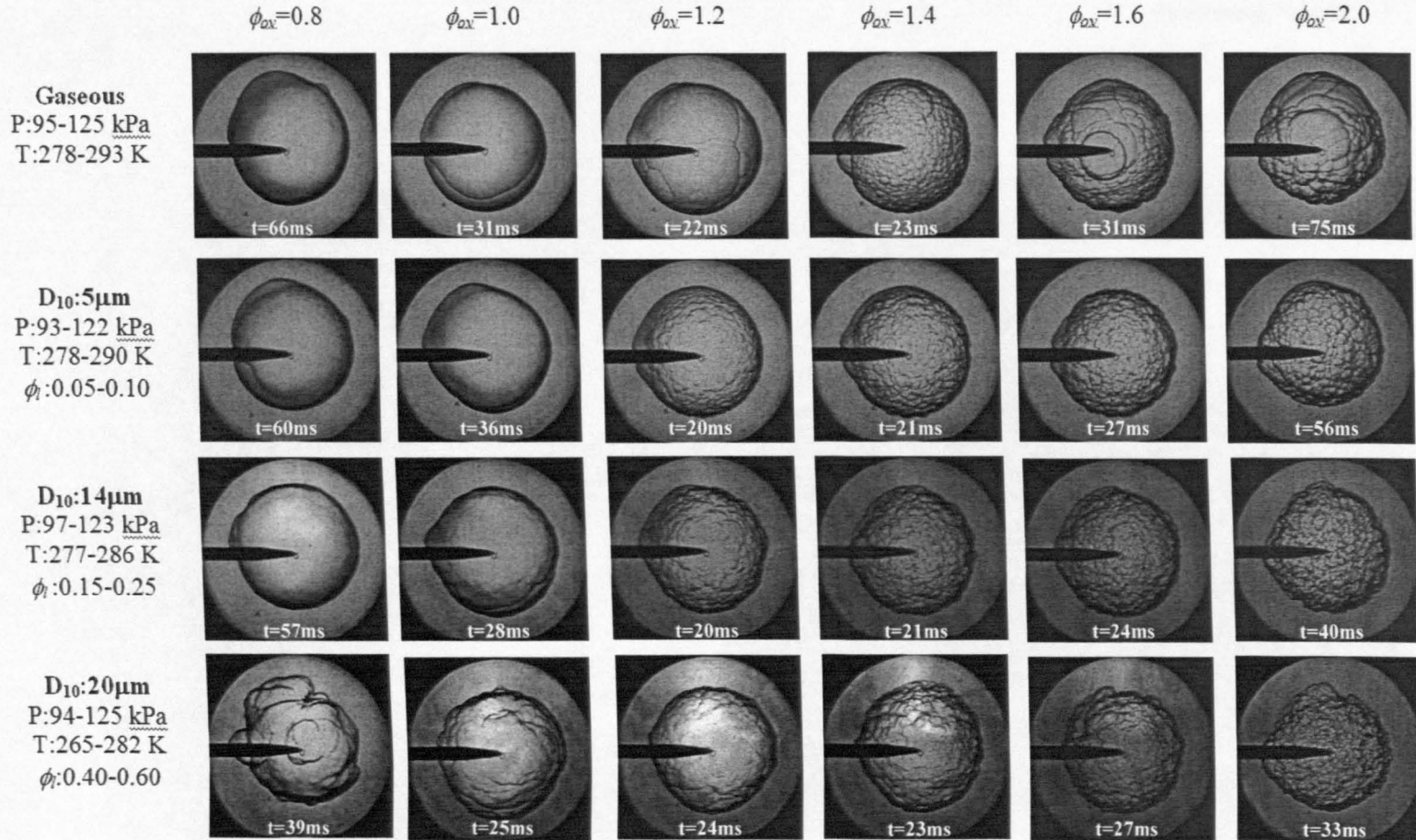


Figure 5.5: Comparison of flame schlieren images at radius approximately 48 mm for gaseous and aerosol iso-octane-air mixtures at various  $\phi_{ov}$  and  $D_{10}$ .

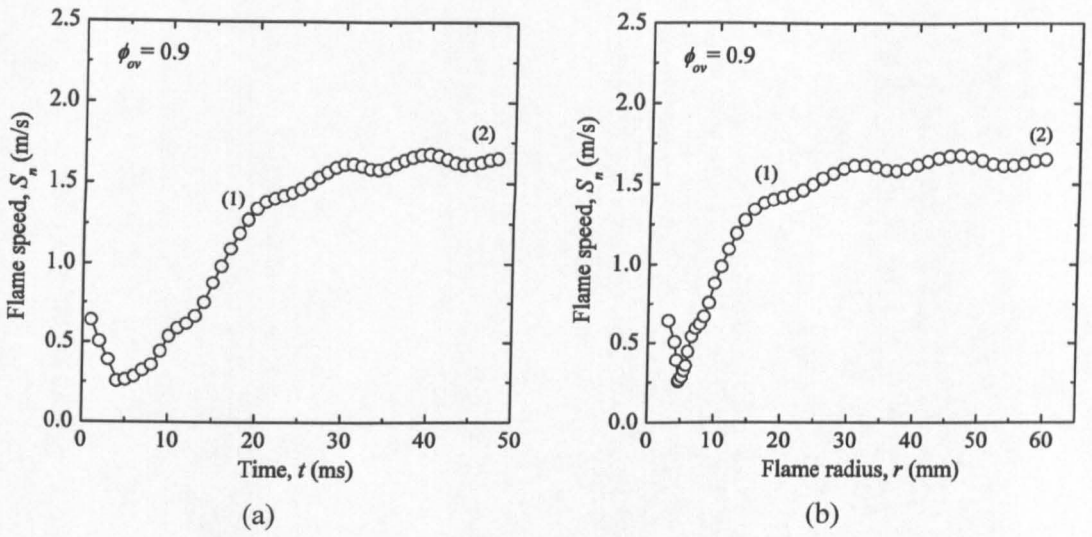


Figure 5.6: Variation of flame speed with (a) time, (b) radius, for gaseous iso-octane-air mixtures at  $\phi_{ov} = 0.9$ , 97 kPa and 279 K.

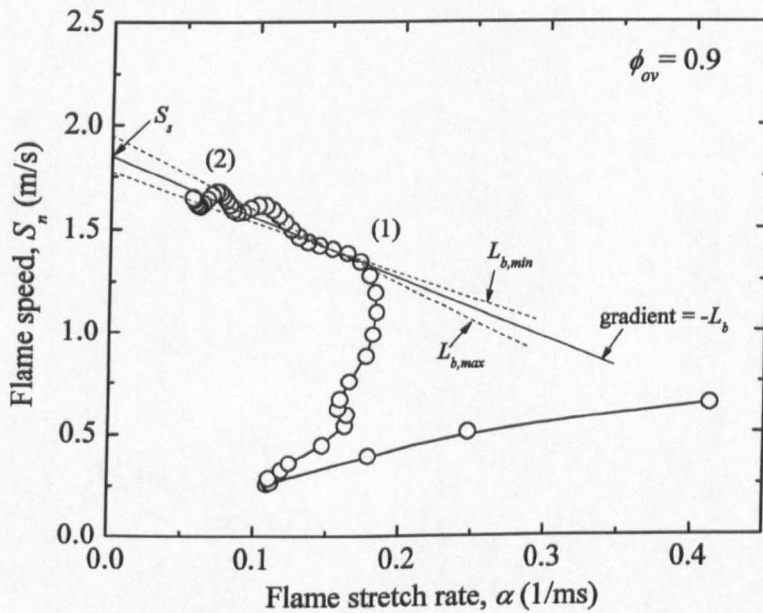


Figure 5.7: Variation of flame speed with stretch rate for the gaseous flame in Fig. 5.6.

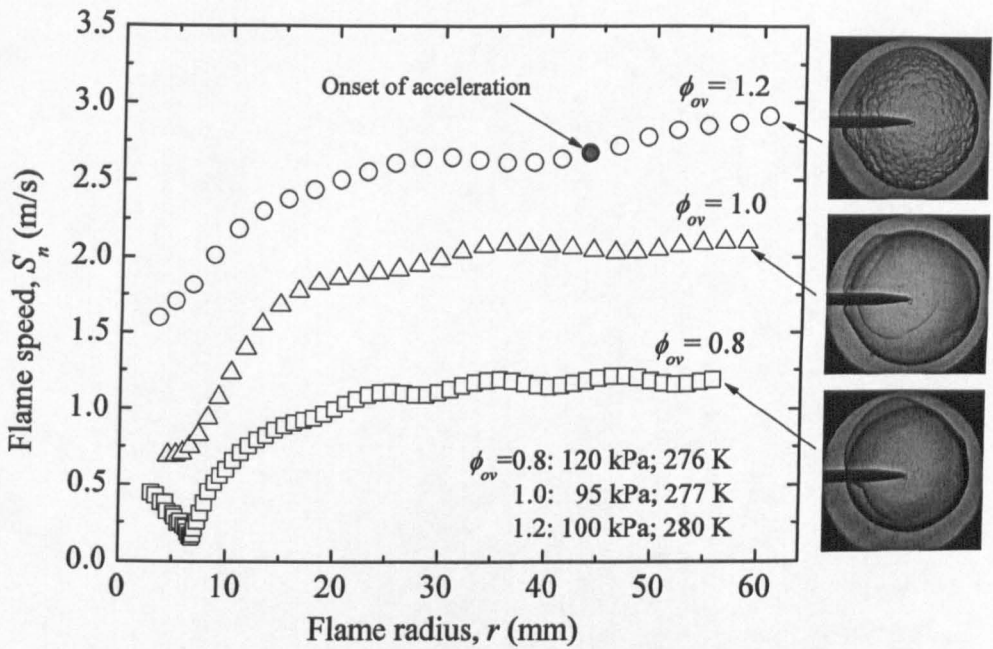


Figure 5.8: Variation of flame speed with radius for aerosols iso-octane-air mixture at  $D_{10} = 5 \mu\text{m}$  and at  $\phi_{ov} = 0.8, 1.0$  and  $1.2$ . Also shown for each case are last flame images within field of view of access windows.

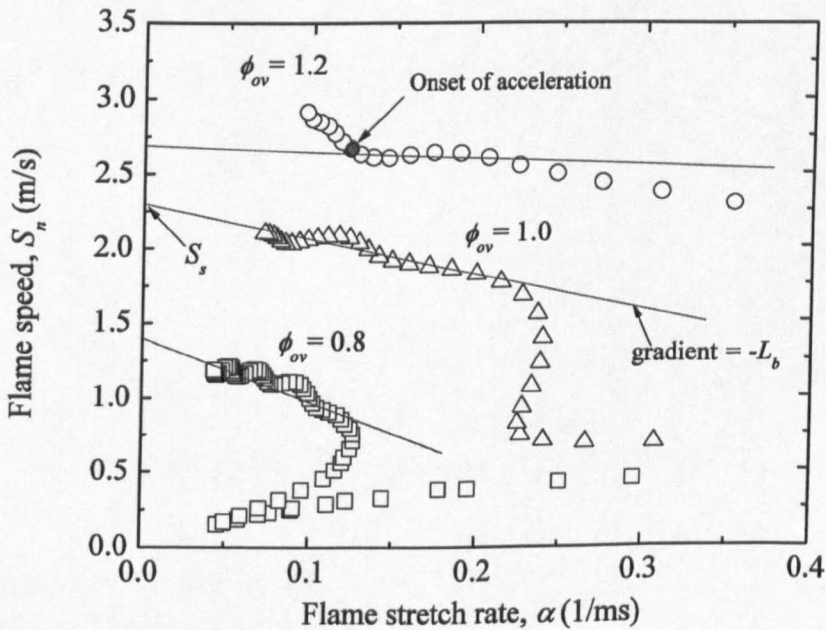


Figure 5.9: Variation of flame speed with stretch rate for aerosol flames in Fig. 5.8.

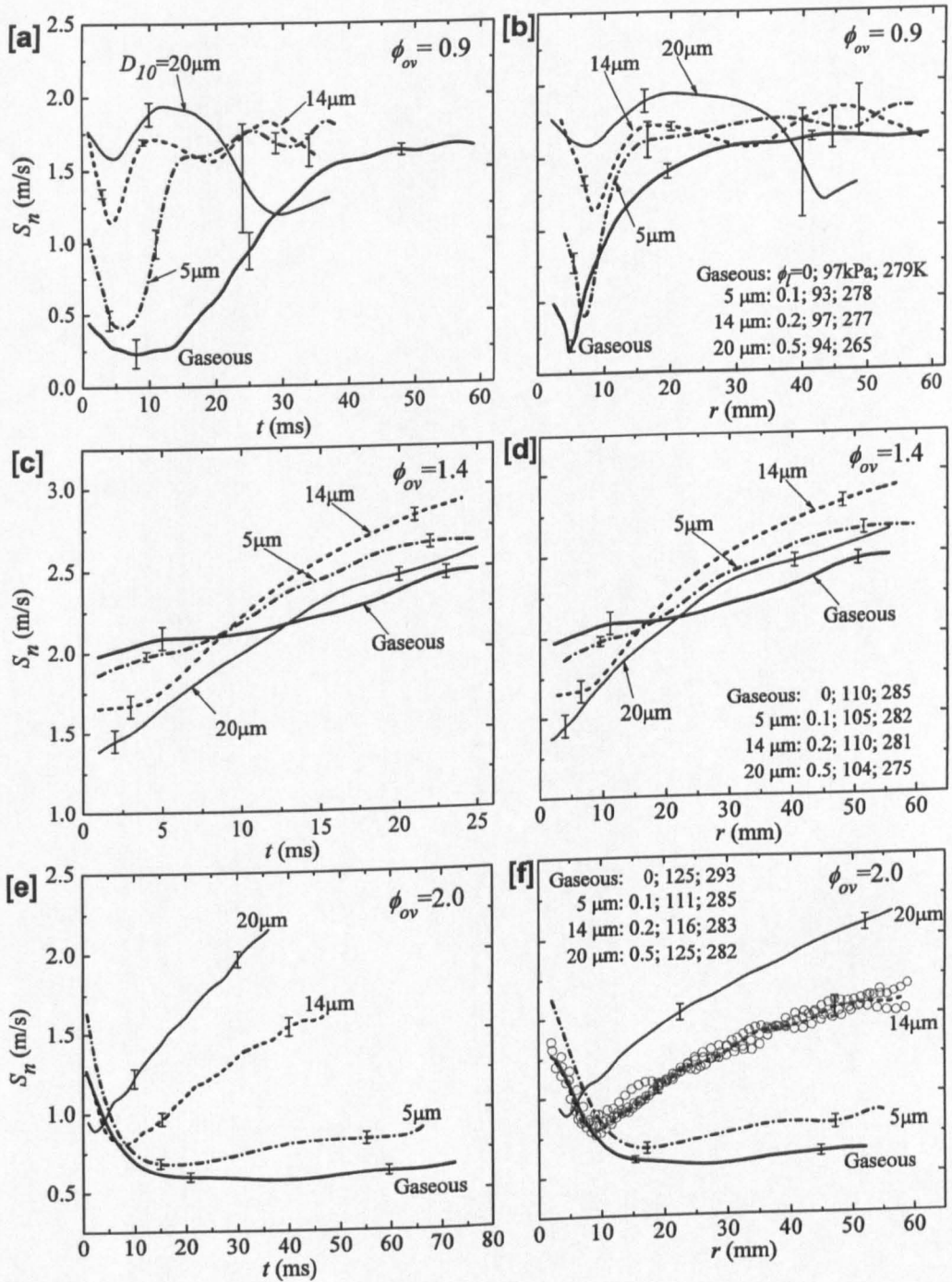


Figure 5.10: Variation of flame speed with time and radius for gaseous and aerosol iso-octane-air mixtures at  $\phi_{ov} = 0.9, 1.4$  and  $2.0$ .

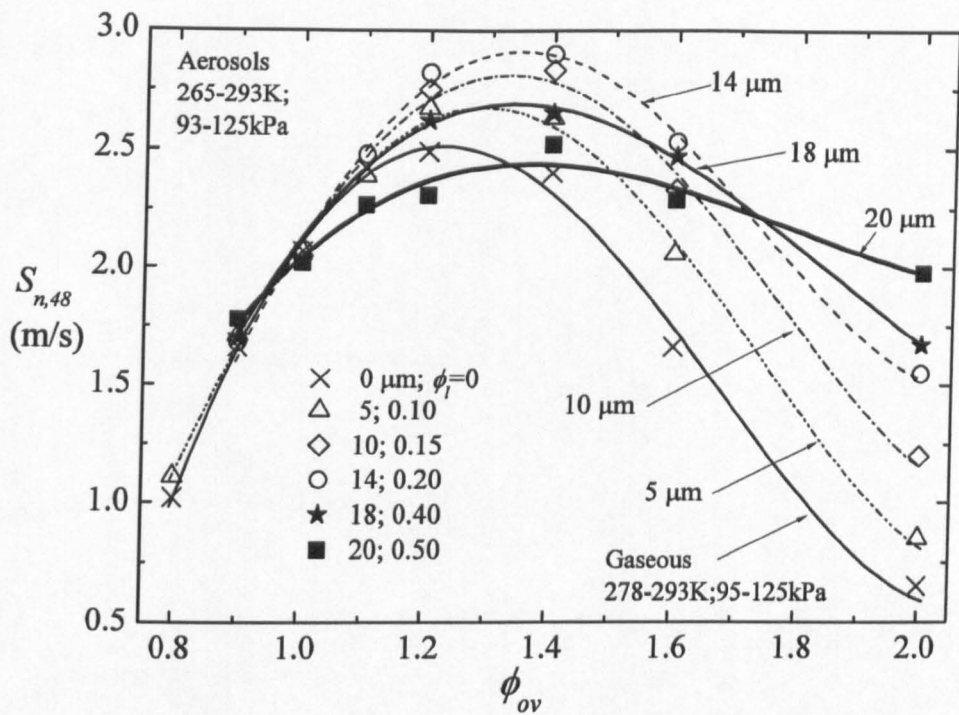


Figure 5.11: Comparison of  $S_{n,48}$  for gaseous and aerosol iso-octane-air at various  $\phi_{ov}$ .

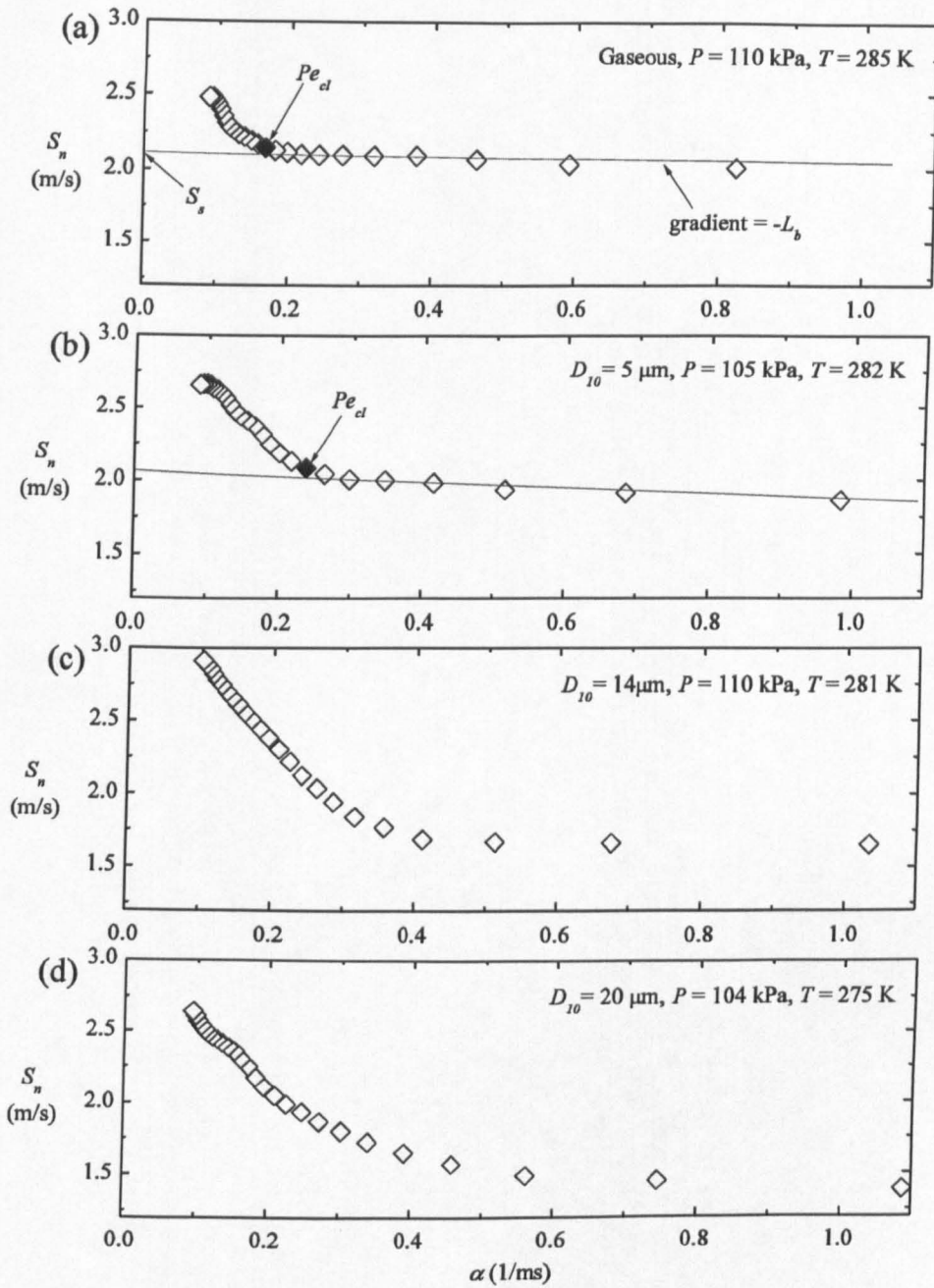


Figure 5.12: Typical variation of flame speed with stretch rate for iso-octane-air mixtures at  $\phi_{ov} = 1.4$  for (a) gaseous, (b) aerosol at  $D_{10} = 5$   $\mu\text{m}$ , (c) aerosol at  $D_{10} = 14$   $\mu\text{m}$  and (d) aerosol at  $D_{10} = 20$   $\mu\text{m}$

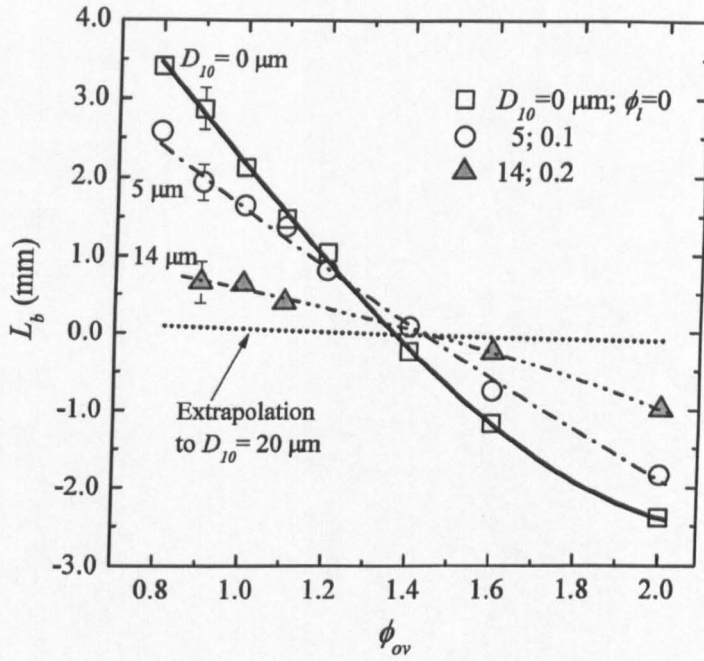


Figure 5.13: Effect of fuel droplets on relationship between  $\phi_{ov}$  and  $L_b$  of iso-octane-air mixtures.

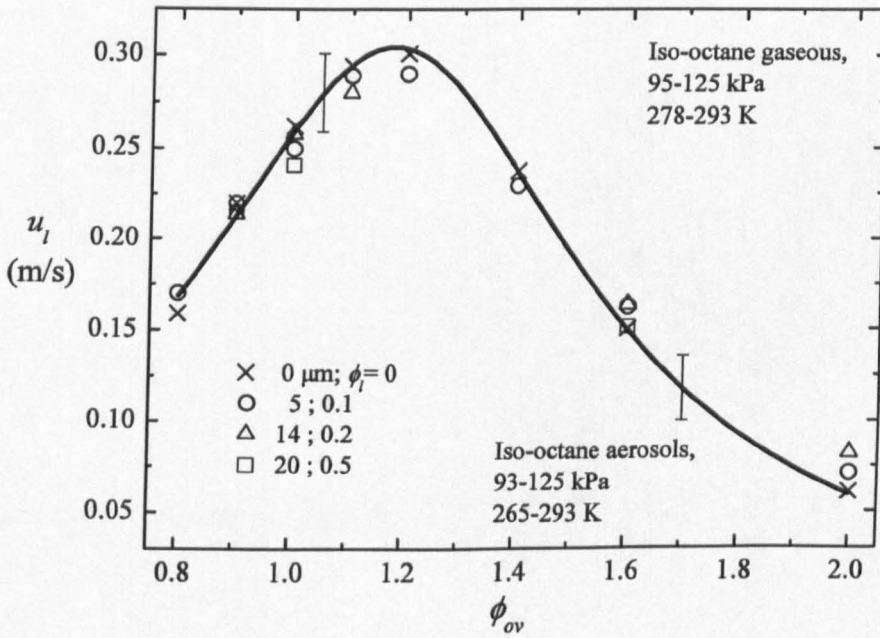


Figure 5.14: Variation of averaged  $u_l$  with  $\phi_{ov}$  and  $D_{10}$  for iso-octane-air mixtures.



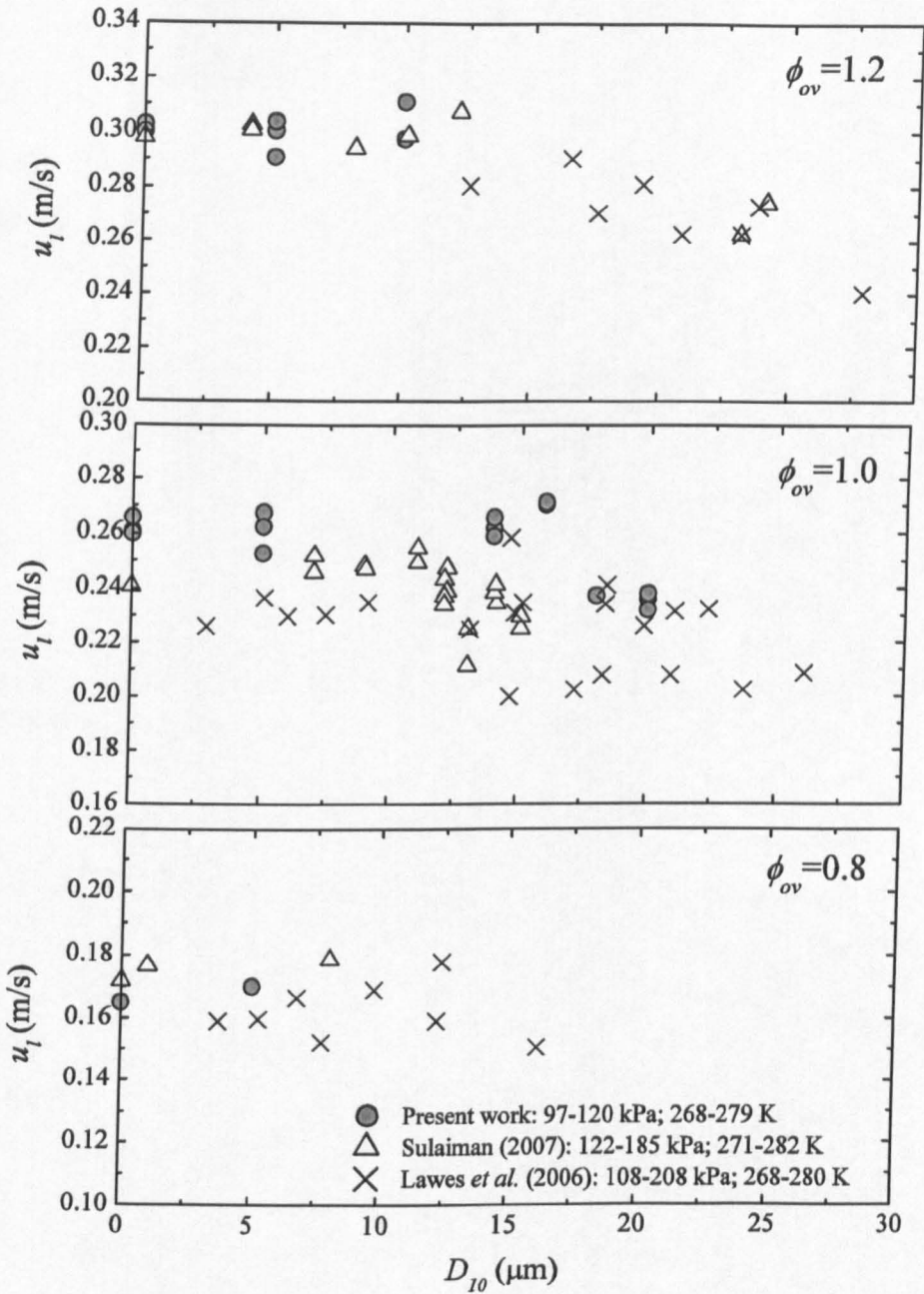


Figure 5.15: Variation of  $u_i$  with  $D_{10}$  for iso-octane-air mixtures at  $\phi_{ov} = 0.8, 1.0$  and  $1.2$ .

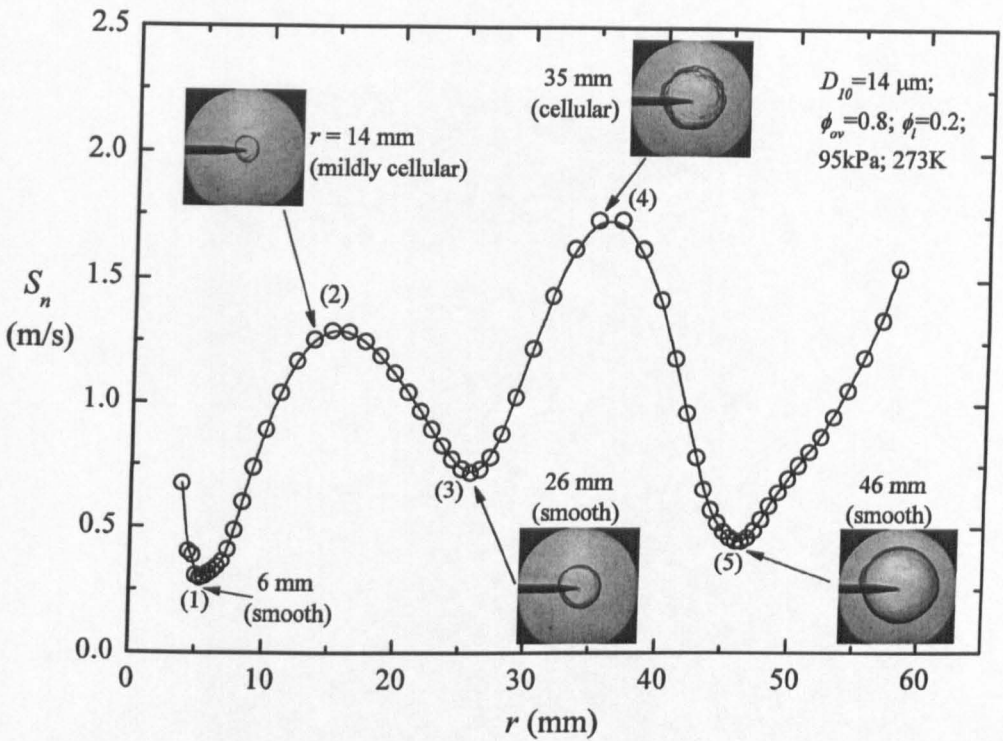


Figure 5.16: Typical variation of flame speed with radius for oscillating flame of iso-octane-air aerosol mixture. Also shown are corresponding schlieren images throughout propagation.

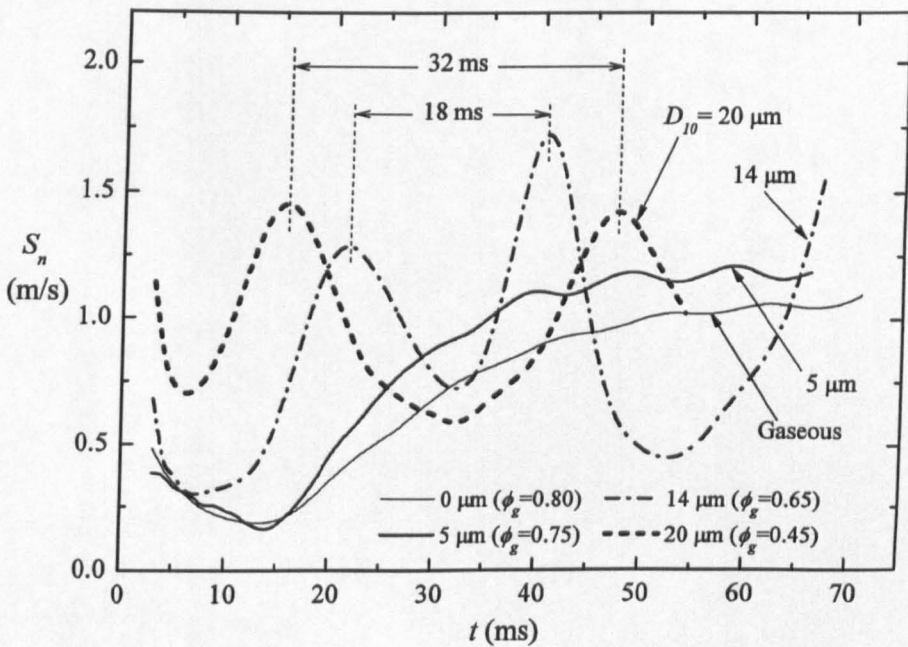


Figure 5.17: Variation of flame speed with time for iso-octane-air aerosol at  $\phi_{ov} = 0.8$  at  $D_{10}$  between 0 and 20  $\mu\text{m}$ , pressures between 93 and 120 kPa and temperatures between 263 and 276 K.

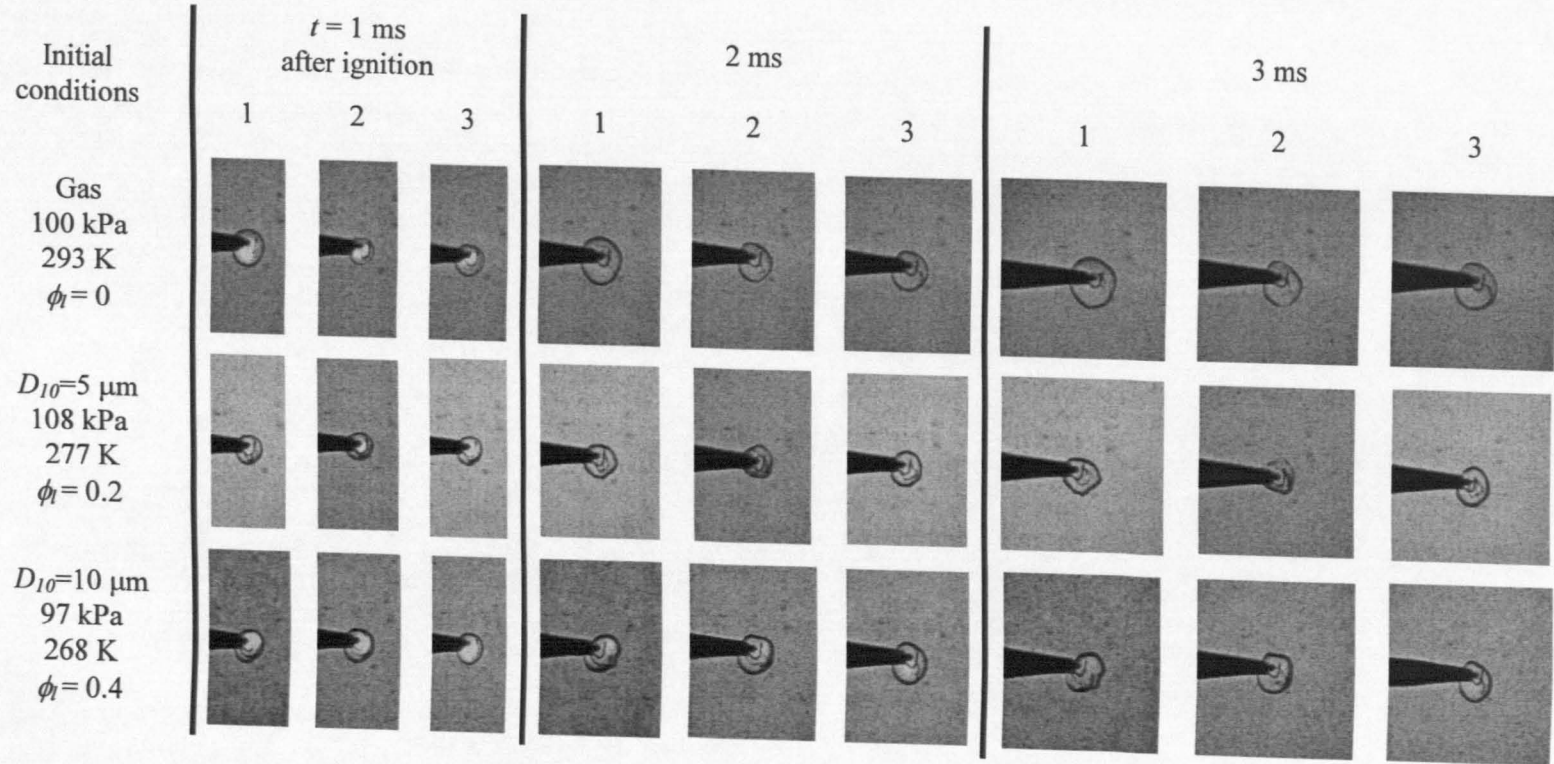


Figure 5.18: Effects of droplets on early stage of flame propagation under turbulent condition,  $u' = 0.5$  m/s for iso-octane-air mixtures at  $\phi_{ov} = 0.9$

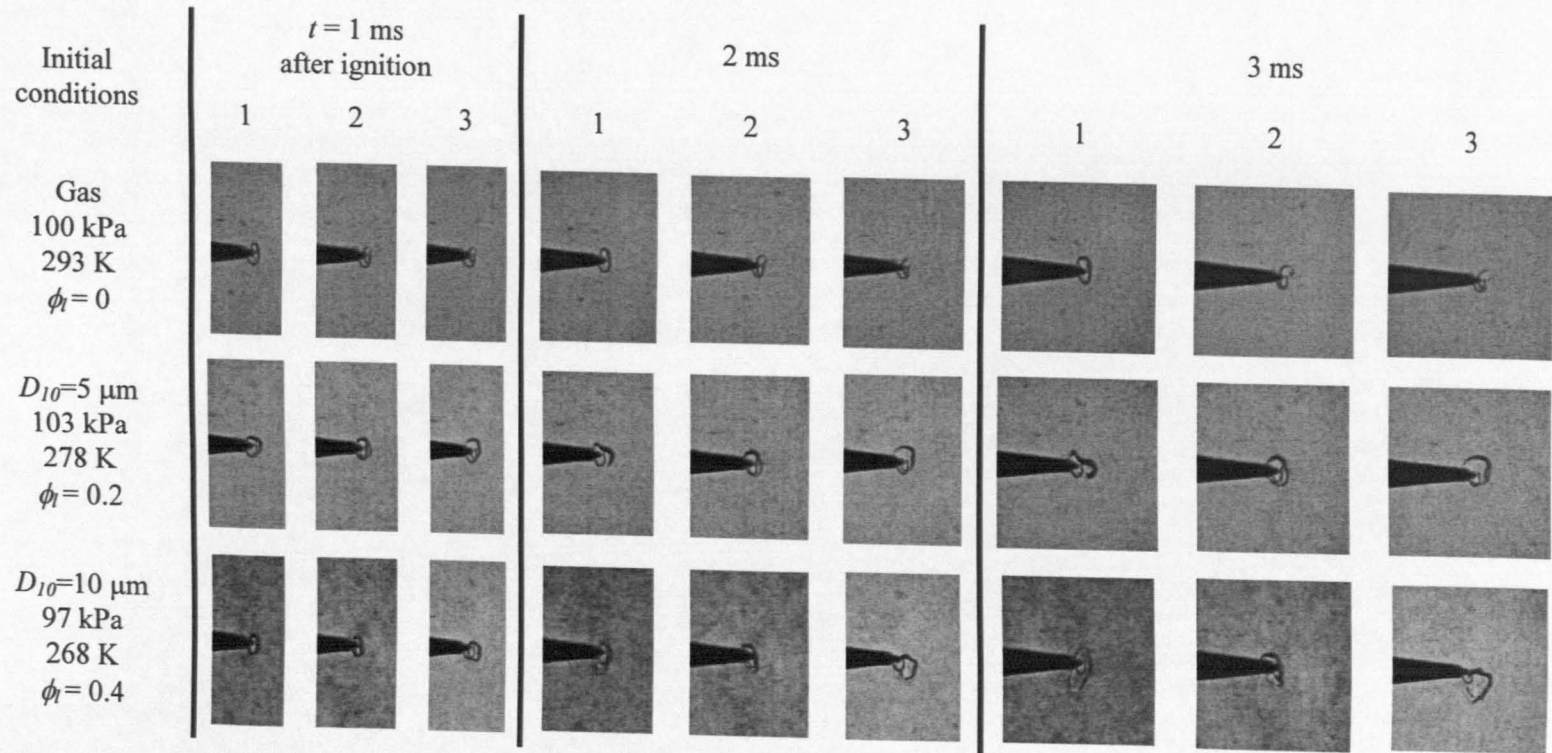


Figure 5.19: Effects of droplets on early stage of flame propagation under turbulent condition,  $u' = 0.5$  m/s for iso-octane-air mixtures at  $\phi_{ov} = 1.2$

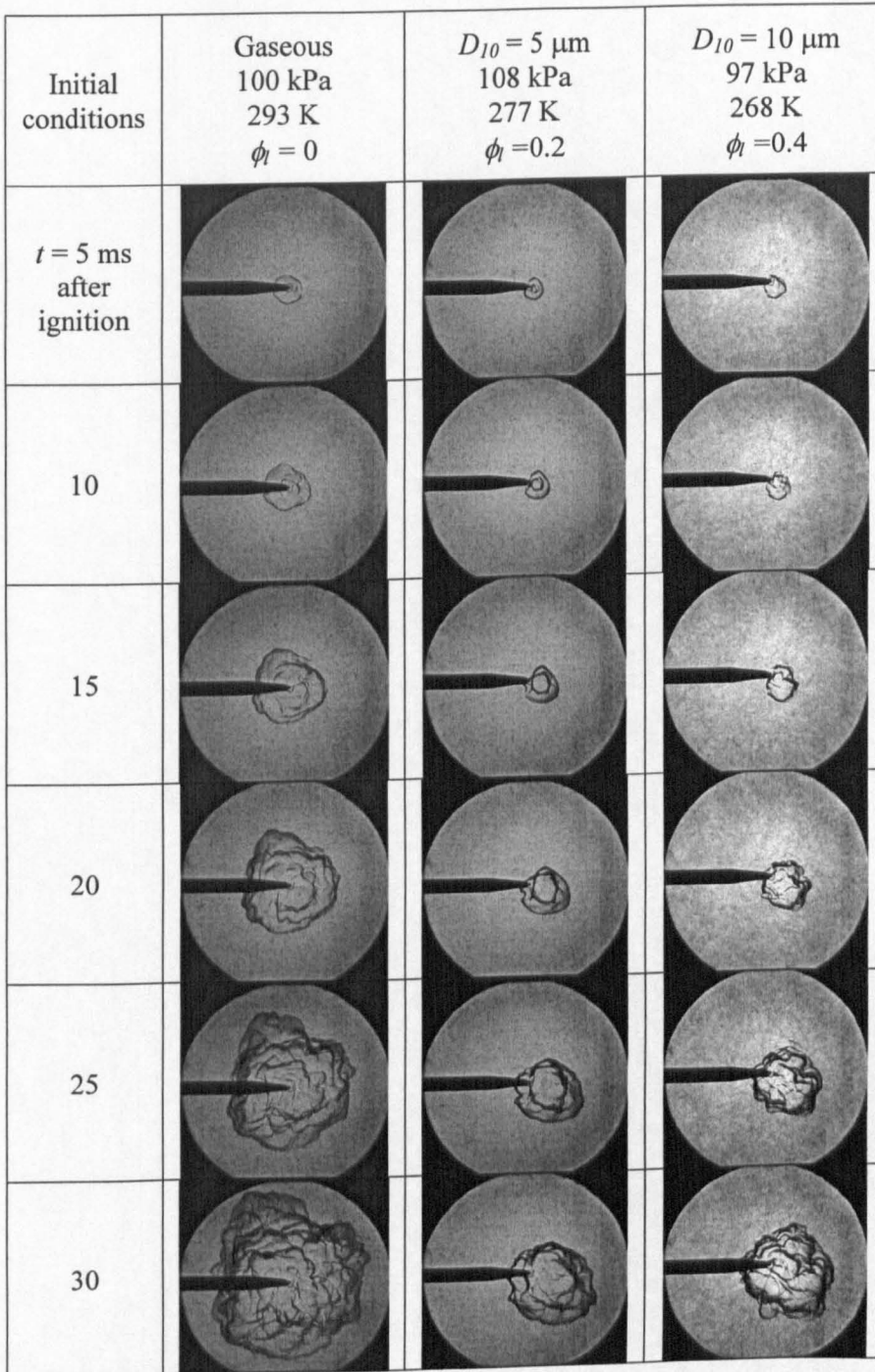


Figure 5.20: Typical development of turbulent gaseous and aerosol flames propagation at  $u' = 0.5 \text{ m/s}$  and  $\phi_{ov} = 0.9$

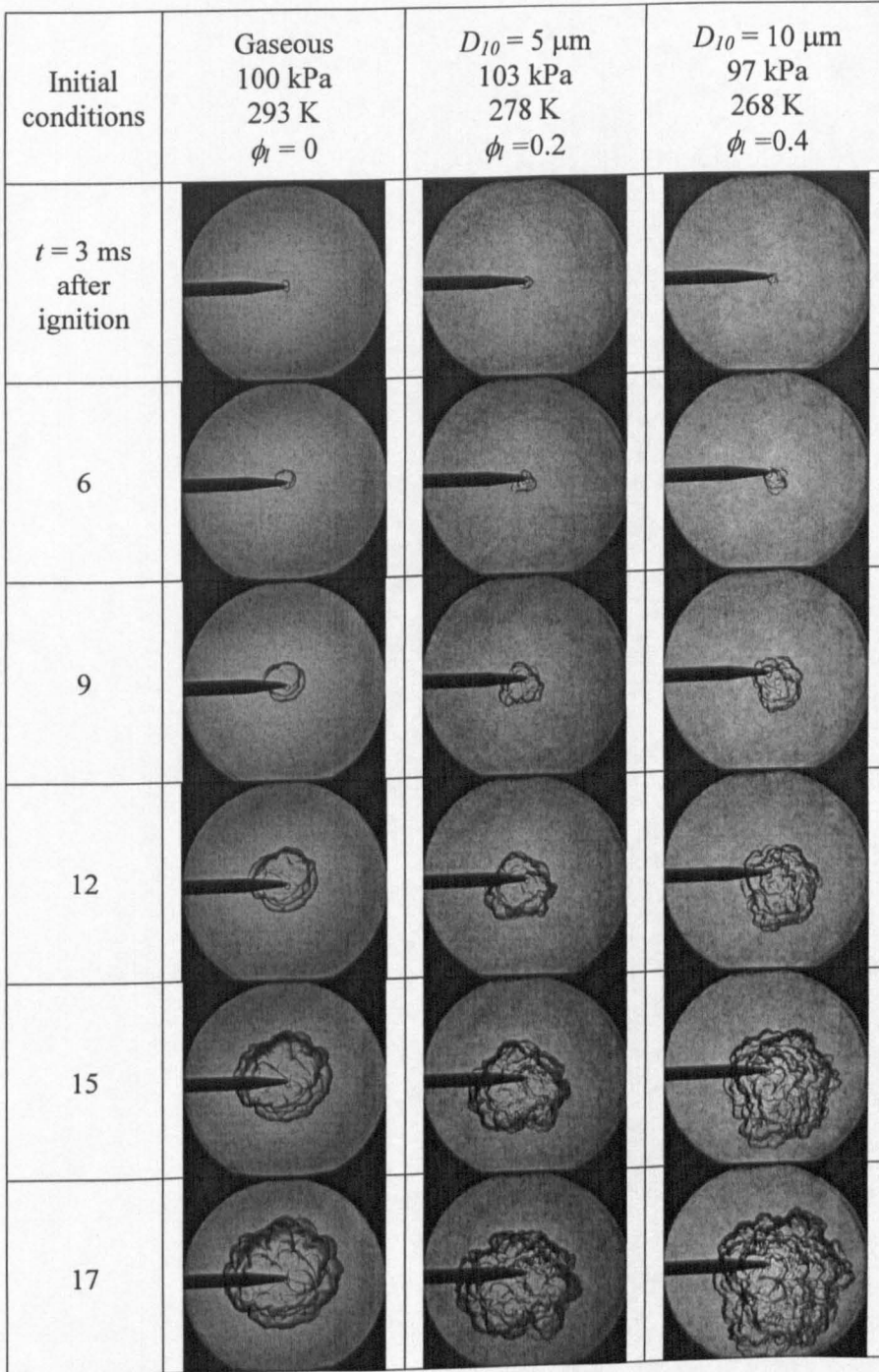


Figure 5.21: Typical development of turbulent gaseous and aerosol flames propagation at  $u' = 0.5 \text{ m/s}$  and  $\phi_{ov} = 1.2$

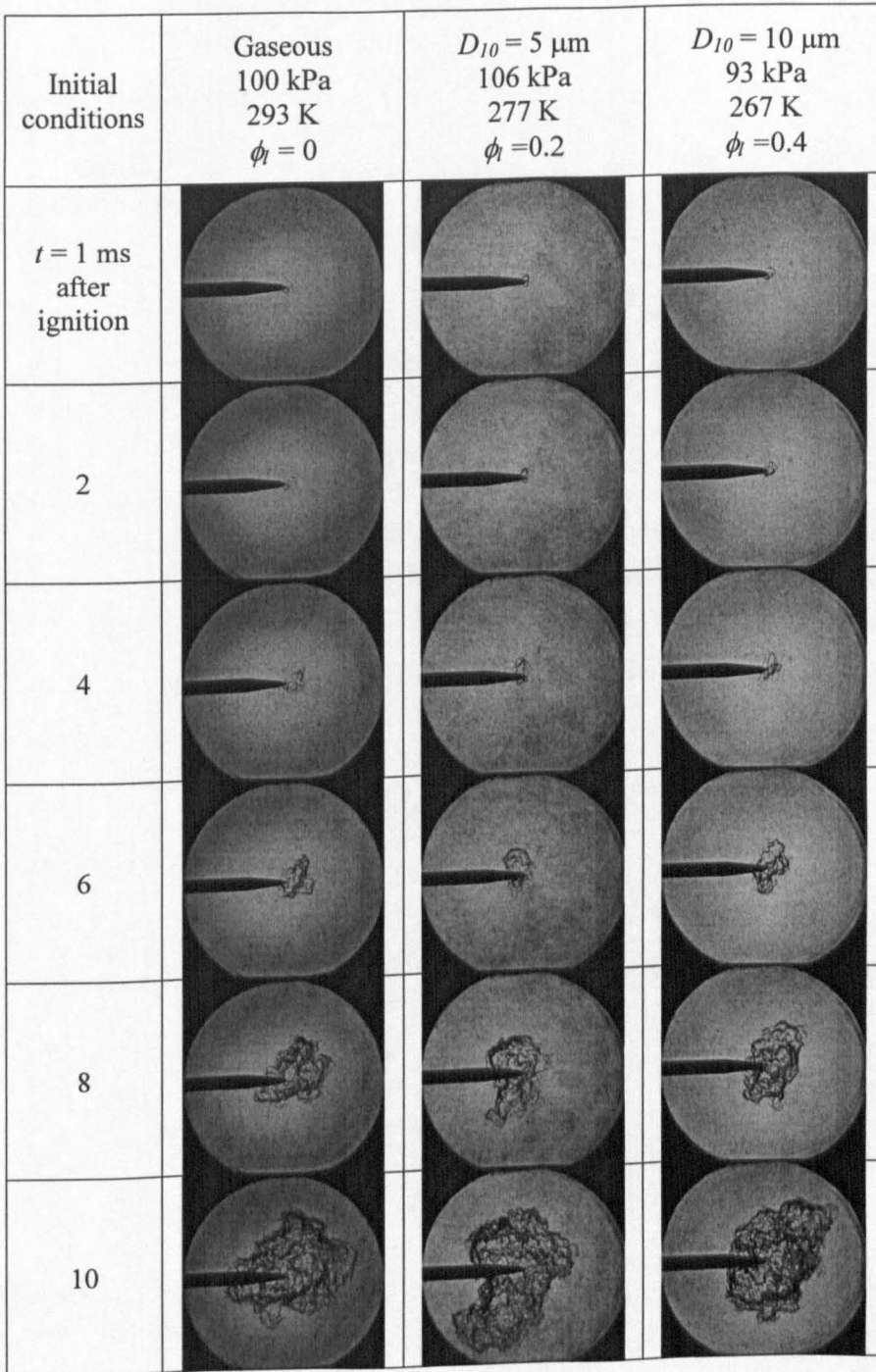


Figure 5.22: Typical development of turbulent gaseous and aerosol flames propagation at  $u' = 4.0 \text{ m/s}$  and  $\phi_{ov} = 1.2$ .

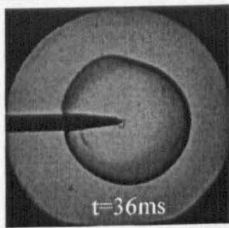
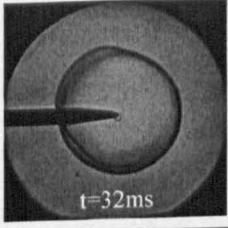
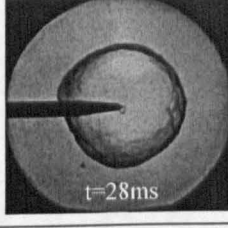
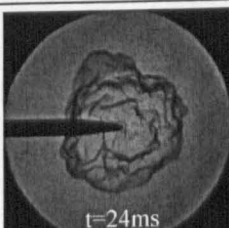
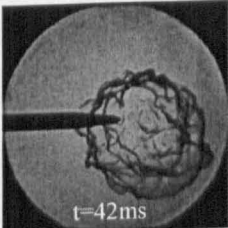
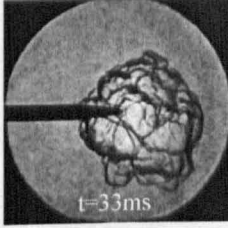
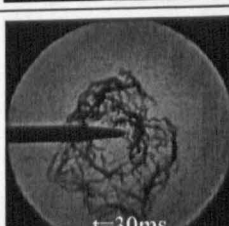
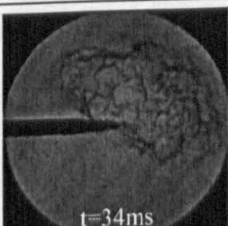
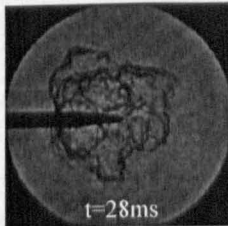
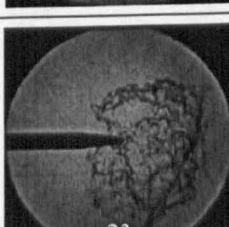
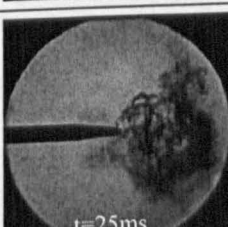
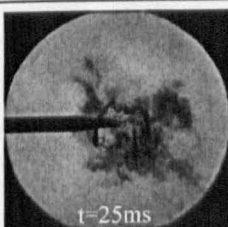
Initial conditions	Gaseous 97-100 kPa 279-297 K $\phi_l = 0$	$D_{10} = 5 \mu\text{m}$ 93-110 kPa 277-279 K $\phi_l = 0.2$	$D_{10} = 10 \mu\text{m}$ 92-97 kPa 267-277 K $\phi_l = 0.4$
$u' = 0 \text{ m/s}$	 A smooth, spherical flame structure with a sharp interface, observed at $t=36\text{ms}$ .	 A smooth, spherical flame structure with a sharp interface, observed at $t=32\text{ms}$ .	 A smooth, spherical flame structure with a sharp interface, observed at $t=28\text{ms}$ .
0.5	 A highly wrinkled and irregular flame structure, observed at $t=24\text{ms}$ .	 A highly wrinkled and irregular flame structure, observed at $t=42\text{ms}$ .	 A highly wrinkled and irregular flame structure, observed at $t=33\text{ms}$ .
1.0	 A highly wrinkled and irregular flame structure, observed at $t=30\text{ms}$ .	 A highly wrinkled and irregular flame structure, observed at $t=34\text{ms}$ .	 A highly wrinkled and irregular flame structure, observed at $t=28\text{ms}$ .
2.0	 A highly wrinkled and irregular flame structure, observed at $t=23\text{ms}$ .	 A highly wrinkled and irregular flame structure, observed at $t=25\text{ms}$ .	 A highly wrinkled and irregular flame structure, observed at $t=25\text{ms}$ .

Figure 5.23: Typical flame structure at radius approximately 40 mm of turbulent gaseous and aerosol flames at  $\phi_{ov}=0.9$ .



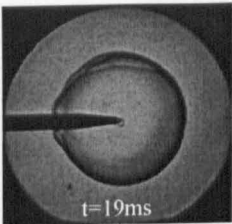
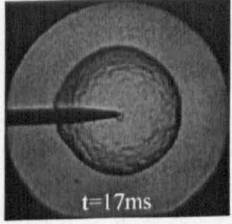
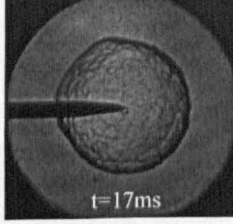
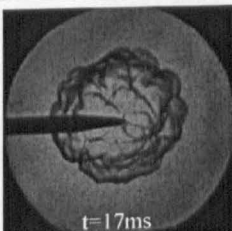
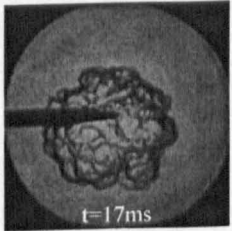
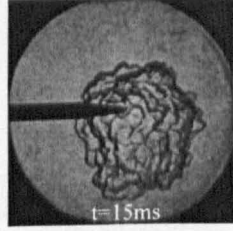
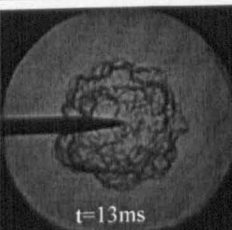
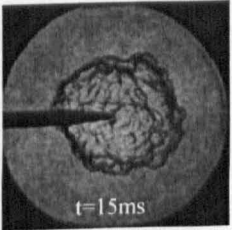
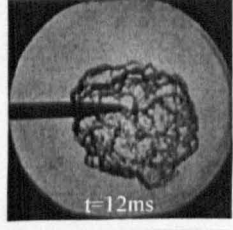
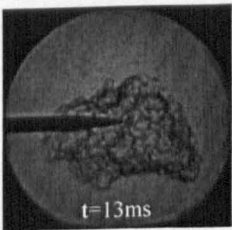
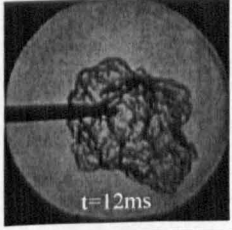
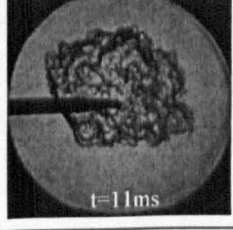
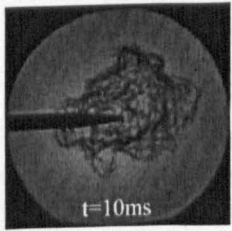
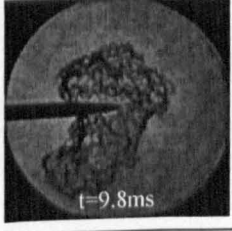
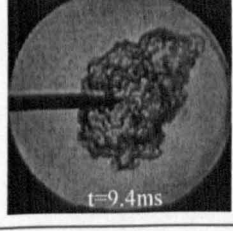
Initial conditions	Gaseous 100-105 kPa 283-295 K $\phi_1 = 0$	$D_{10} = 5 \mu\text{m}$ 100-111 kPa 275-280 K $\phi_1 = 0.2$	$D_{10} = 10 \mu\text{m}$ 93-105 kPa 267-279 K $\phi_1 = 0.4$
$u' = 0 \text{ m/s}$	 t=19ms	 t=17ms	 t=17ms
0.5	 t=17ms	 t=17ms	 t=15ms
1.0	 t=13ms	 t=15ms	 t=12ms
2.0	 t=13ms	 t=12ms	 t=11ms
4.0	 t=10ms	 t=9.8ms	 t=9.4ms

Figure 5.24: Typical flame structure at radius approximately 40 mm of turbulent gaseous and aerosol flames at  $\phi_{ov}=1.2$ .

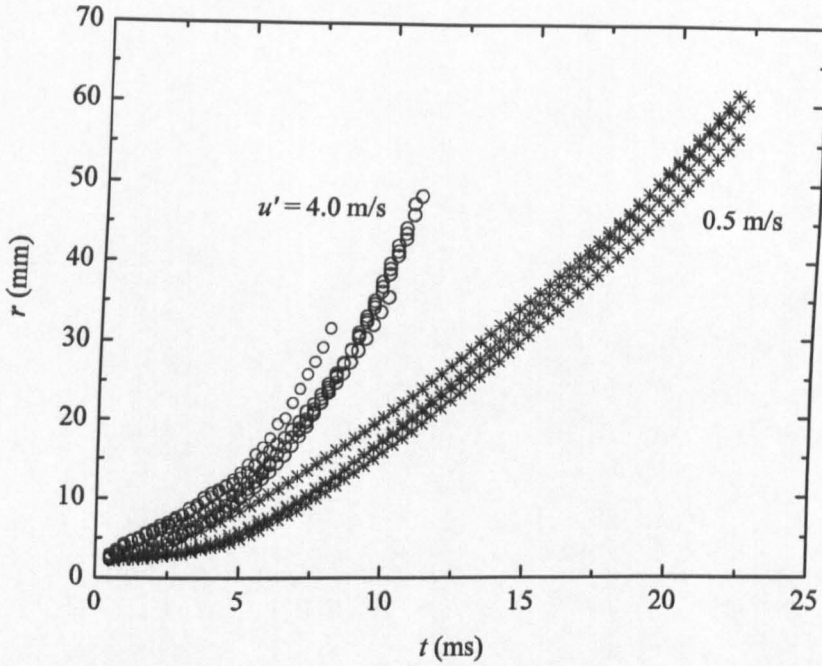


Figure 5.25: Flame radius against time for turbulent gaseous iso-octane-air at  $\phi_{ov} = 1.2$ , 100 kPa, 303 K and  $u'$  of 0.5 and 4.0 m/s.

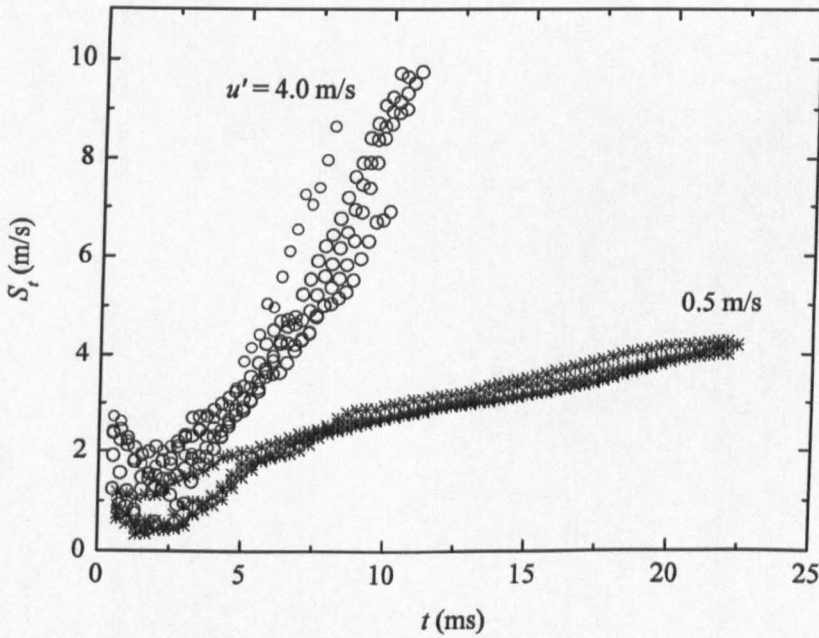


Figure 5.26: Variation of  $S_t$  with time for turbulent gaseous flames in Fig. 5.25.

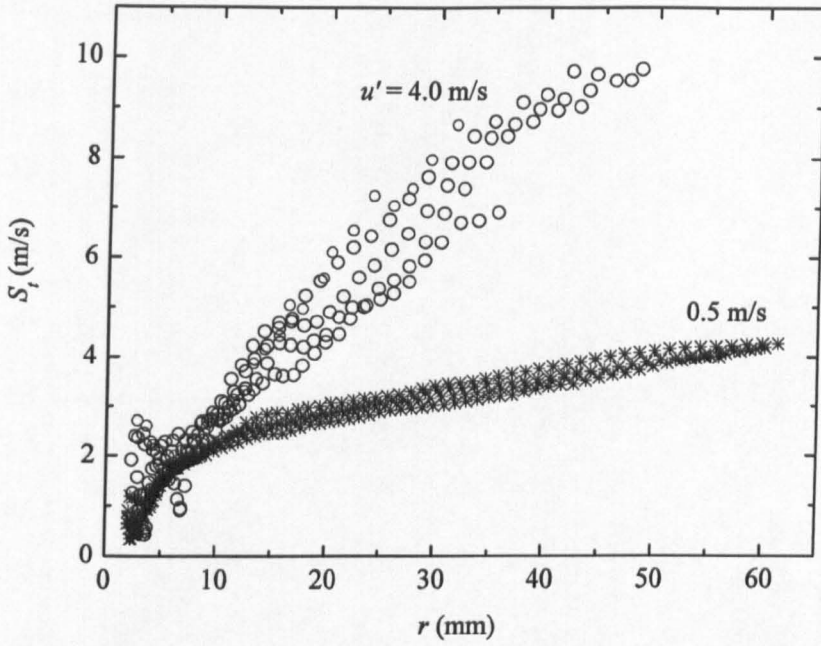


Figure 5.27: Variation of  $S_t$  with radius for turbulent gaseous flames in Fig. 5.25.

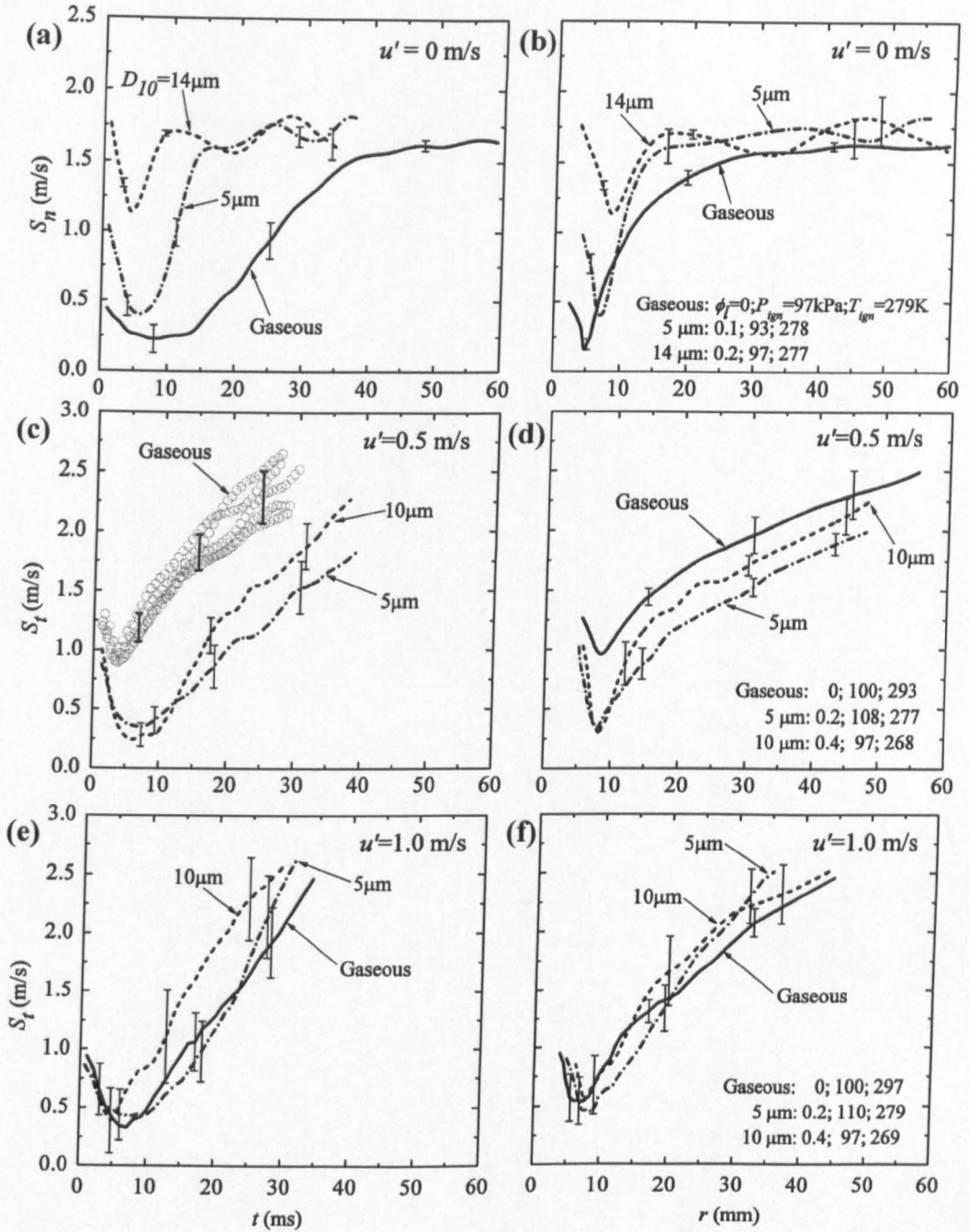


Figure 5.28: Variation of flame speed with time, radius and  $u'$  for iso-octane-air gaseous and aerosol mixtures at  $\phi_{ov} = 0.9$ .

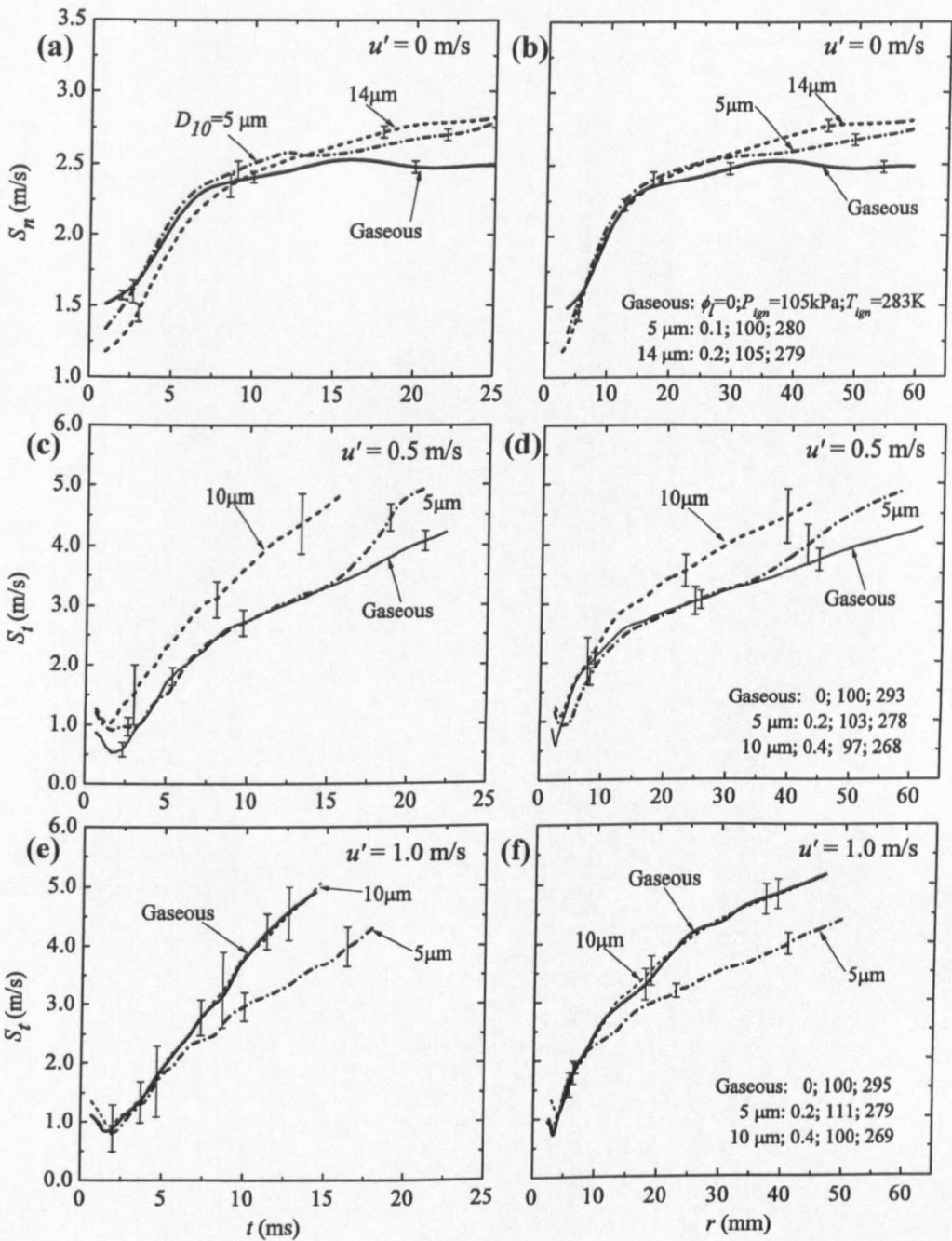


Figure 5.29: Variation of flame speed with time and radius for iso-octane-air gaseous and aerosol mixtures at  $\phi_{ov} = 1.2$  and  $u'$  of 0, 0.5 and 1.0 m/s.

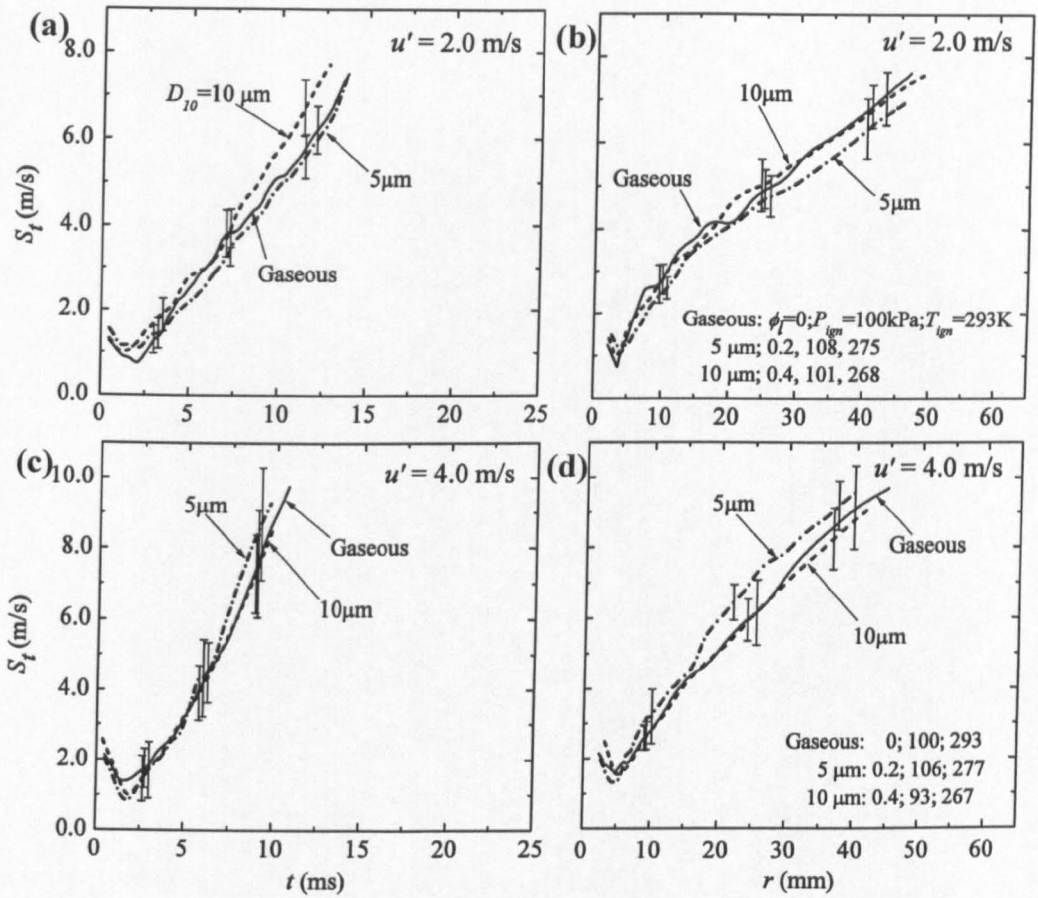


Figure 5.30: Variation of flame speed with time and radius for iso-octane-air gaseous and aerosol mixtures at  $\phi_{ov} = 1.2$  and  $u'$  of 2.0 and 4.0 m/s.

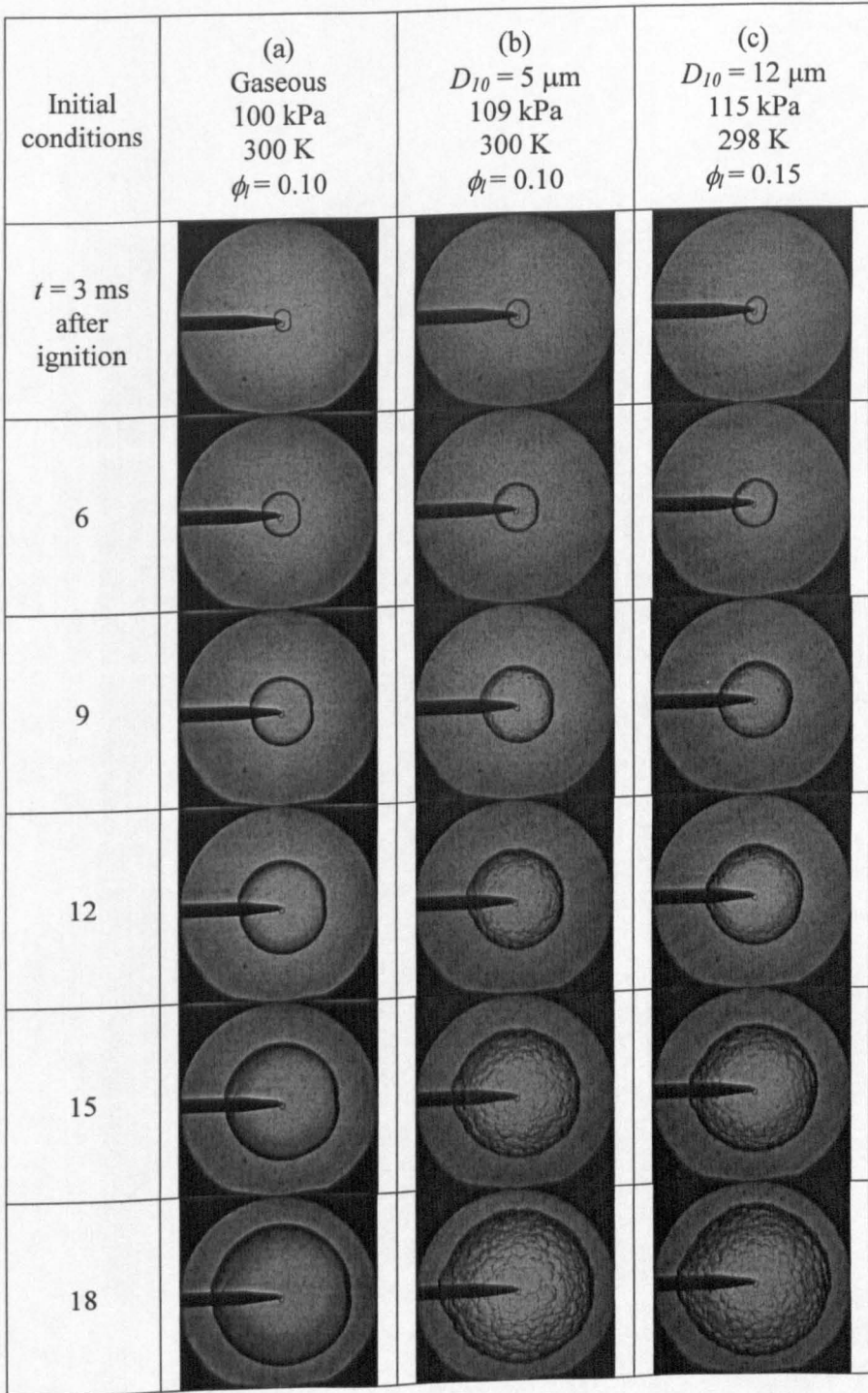


Figure 5.31: Typical development of laminar ethanol-air flames at  $\phi_{ov}=1.2$  for, (a) gaseous mixture, (b) aerosol at  $D_{10} = 5 \mu\text{m}$  and (c) aerosol at  $D_{10} = 12 \mu\text{m}$ .

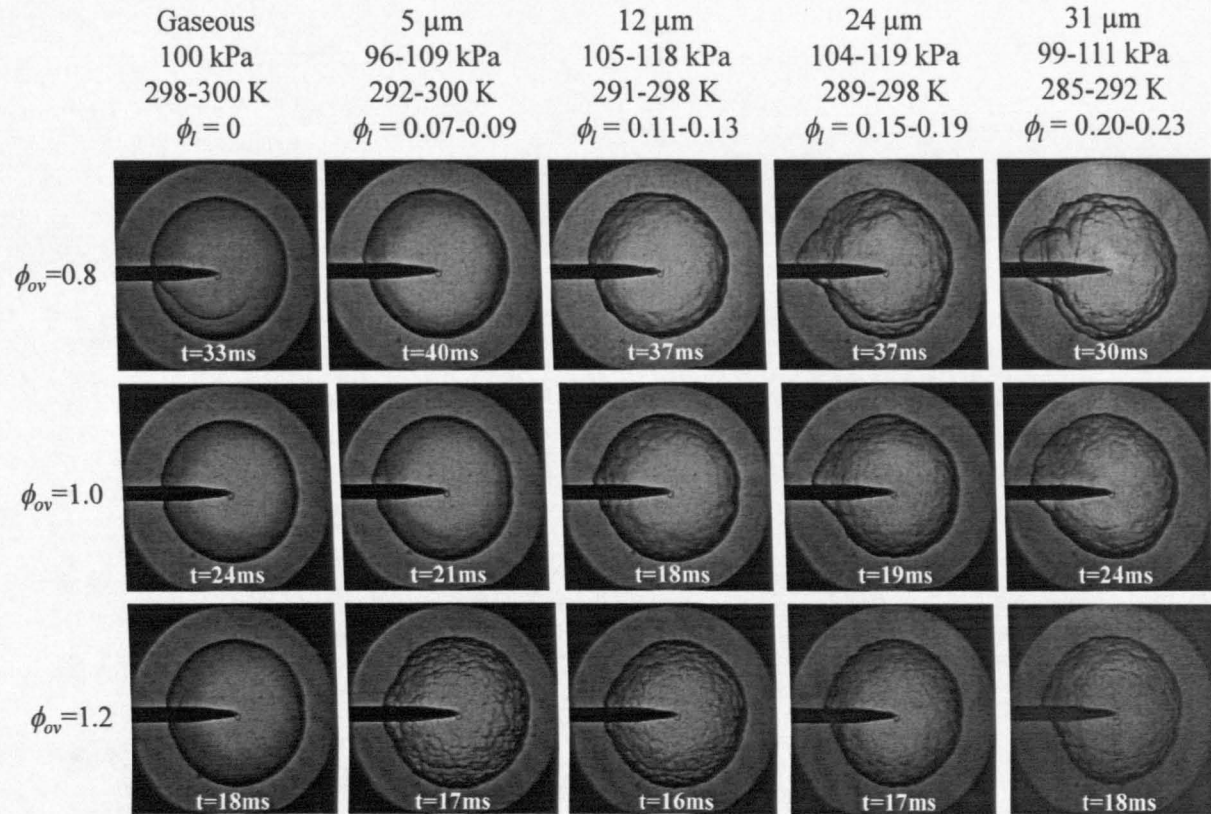


Figure 5.32: Comparison of flame schlieren images at radius approximately 48 mm for gaseous and aerosol ethanol-air mixtures at various  $\phi_{ov}$  and  $D_{10}$ .



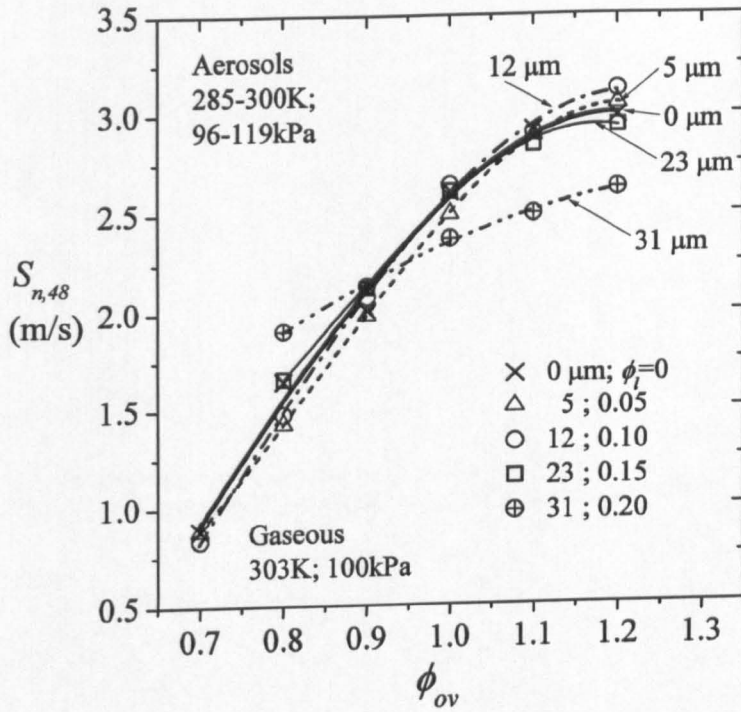


Figure 5.33: Comparison of  $S_{n,48}$  for gaseous and aerosol ethanol-air at various  $\phi_{ov}$ .

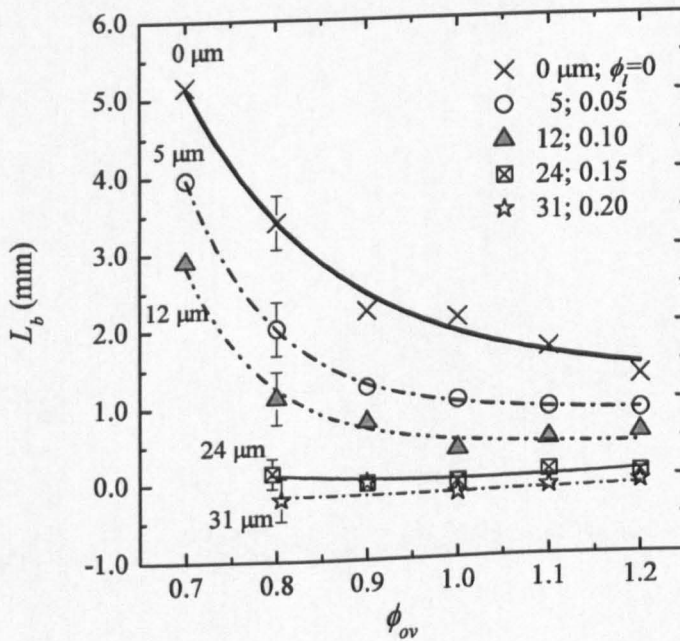


Figure 5.34: Effect of fuel droplets on relationship between  $\phi_{ov}$  and  $L_b$  of ethanol-air mixtures.

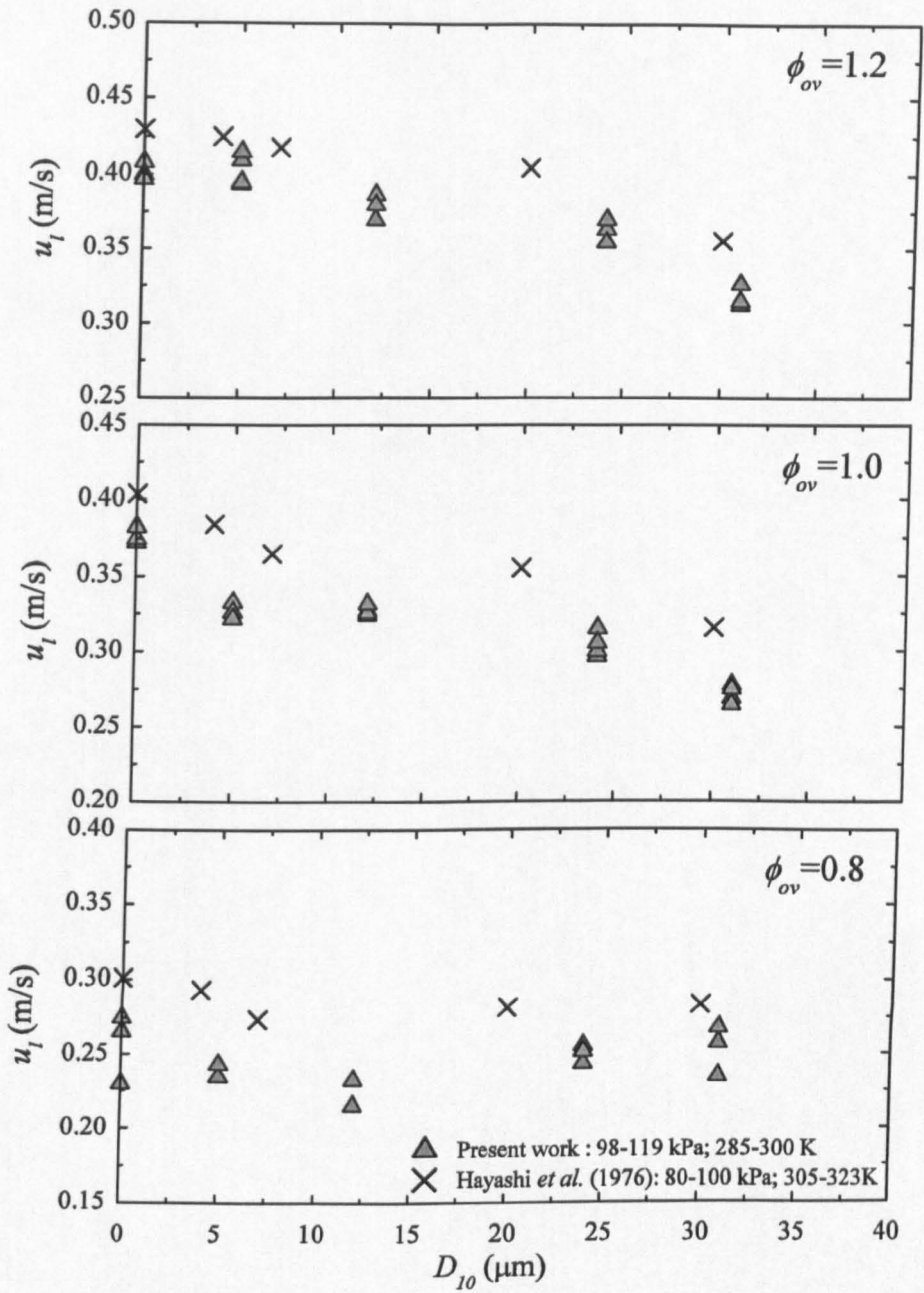


Figure 5.35: Variation of  $u_l$  with  $D_{10}$  for ethanol-air mixtures at various  $\phi_{ov} = 0.8, 1.0$  and 1.2.

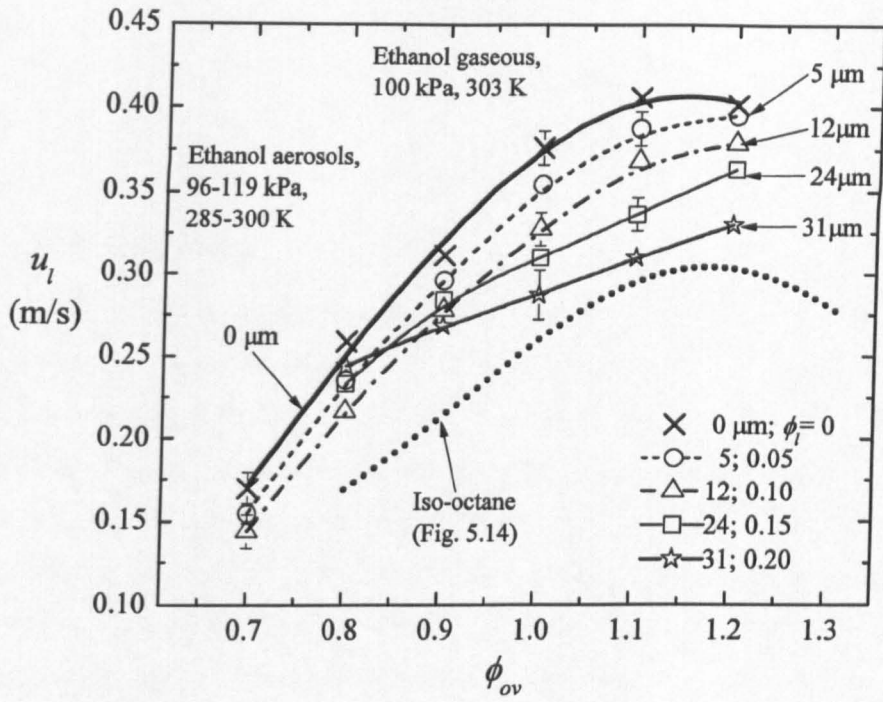


Figure 5.36: Variation of averaged  $u_l$  with  $\phi_{ov}$  and  $D_{10}$  for ethanol-air mixtures. Also shown is the variation of averaged  $u_l$  with  $\phi_{ov}$  for gaseous iso-octane-air mixtures as in Fig. 5.14.

## **Chapter 6**

### **Discussions**

#### **6.1 Introduction**

This Chapter contains a discussion of laminar and turbulent burning results that were presented in Chapter 5. This is placed in context in relation to previous experimental and theoretical works. In Section 6.2, the effect of using different ignition systems on comparisons with previous work is discussed. This is followed in Section 6.3, by discussion of droplet evaporation under laminar and turbulent conditions. In Section 6.4, the effects of droplets on laminar flames are discussed. This includes discussion on the effects of droplets during the early stage, later stage propagation, flame instabilities and unstretched burning velocity. Finally, the effect of droplets in turbulent flames is discussed in Section 6.5.

#### **6.2 Effect of ignition unit on comparisons with previous work**

In the earlier stages of the present study, ignition of combustible mixtures was performed using a large spark from a fixed energy ignition unit, described in Section 3.2.3.1. This system was used for obtaining good consistency of results when comparing with previous works that used the same ignition system (Atzler, 1999; Marquez, 2003; Sulaiman 2007). However, there have been problems with its use which were reported by Sulaiman (2007), but no action was taken to mitigate the problem. These issues are discussed below and the present author changed the ignition unit to the one described in Section 3.2.3.2.

Shown in Figs. 5.1a and 5.1b are sequences of gaseous flame development taken with the previous ignition unit and with the one used throughout this study. As described in Section 5.2.1, flame observation with the previous unit showed the existence of bright spots in the early stage of flame development and the appearance of bumps on the flame structure at random locations in the later stage of propagation. These structures were not observed with the present unit. This has been

investigated by Sulaiman (2007) who used natural light imaging as shown in Fig. 6.1. Here, a sequence of natural light images of a spark in air (without fuel) is shown at 100 kPa and 303 K using the previous unit, described in Section 3.2.3.1. A bright spot was remained at the spark location for about 12 ms after spark ignition. More importantly, after 6 ms from ignition, splashes of bright objects were emitted from the spark kernel. Sulaiman (2007) suggested that these splashes were fragments of molten metal from the electrode as a result of high ignition temperature. He also demonstrated that the observation of black clouds in turbulent aerosol flames, as shown in Fig. 6.2, was related to the interaction between molten metal and droplets. The present author believes that the most likely reason for these phenomena is the excessive energy and long spark duration in the previous ignition unit. The use of a large ignition energy and long spark duration can cause the tip of the electrodes to melt. Further, this long spark duration is unhelpful in the ignition process since, after about a millisecond, the flame has propagated, far from the spark kernel, as shown in Fig. 5.1a. Therefore, the present author used another ignition unit, with a smaller spark duration, as described in Section 3.2.3.2, and this resulted in successful ignition of combustible mixtures. However, due to the use of different ignition systems, care must be used in any comparison of results from both systems. This is discussed below.

Shown in Fig. 6.3 is a graph of flame speed against time for gaseous flames presented in Fig. 5.1b and from Sulaiman (2007) at exactly similar conditions. The cross symbols with chain-dashed curve represent flames ignited using the previous unit and the square symbols with solid curve represent flames ignited using the present unit. In the early stage of propagation, within 6 ms after ignition, the previous unit produced flame relatively overdriven than the present unit. This is an expected result owing to higher ignition energy. Between 6 ms and 14 ms, both the curves start to converge towards attaining identical values of flame speed. After about 16 ms, both curves are similar although the propagation by the previous unit shows slightly higher values of  $S_n$  by about 2%. It is suggested that this difference was due to mild cells and bumps on the flame surface that generated due to interaction of molten metal with the flame front. As the flame propagated further and the effect of molten metal subsided, both the propagations became almost identical. Therefore, on the basis of the results in Fig. 6.3, the present author suggests that

usage of different ignition system does not produce any significant difference in the measurement of burning rates. However, the use of ignition with excessive energy might produce an unstable flame structure which is although not a real flame instability, but may lead to mistaken conclusions on interpretation of flame cellularities.

### 6.3 Evaporation of droplets in laminar and turbulent flames

As described in Section 2.6.1, the understanding of droplet evaporation is important for investigating the combustion of droplets. For this, it is imperative to investigate the range of droplets that is fully evaporated during or prior to combustion in the present work. However, the present experiments did not allow a simple analysis of droplet evaporation. This is because at ignition, the initial temperature was low (normally less than 280 K) and the mixture was in the wet regime. Clearly, there is no evaporation at these conditions. Evaporation can only occur when conditions change, such as when droplets advance into a higher temperature zone, within the preheat region of the flame.

Although the present experimental conditions are difficult to simulate, an attempt is made here to estimate droplet evaporation of a single droplet instantaneously placed into air at a given condition. Figure 6.4 shows variation of droplet lifetime,  $\tau_D$ , estimated from Eq. (2.42), with droplet diameter for isooctane at 100 kPa and 273 K. The dashed line represents  $t_i$ , defined as the time taken for a droplet, at a burning rate,  $u_n$ , to reach a reaction zone located within a distance of preheat zone. Haq (1998) showed that the preheat zone thickness was typically of the order of half a millimeter (see Section 6.4.1). Using this value and burning rates of stoichiometric isooctane, yields a critical droplet diameter, of about 35  $\mu\text{m}$ , below which droplets fully evaporate before reaching the reaction zone. Since this value is larger than the droplet diameter studied in the present work, this suggests that there is no droplets penetrate the reaction zone and result in a single phase flame propagation. Yet, this estimation contradicts the result of Sulaiman (2007) who showed at certain conditions, droplets can survive the flame front. However, in a real situation, for example in combustion engines, droplets are likely to fully evaporate before reaching the reaction zone since the initial condition of combustion is much higher than the present work. Although the estimation in Fig 6.4 suggests that

droplets are fully evaporated, it is likely that rapid increase in volume expansion due to evaporation and inevitable heterogeneous mixture in the reaction zone due to improper mixing could have significant effect on flame instability.

For turbulent combustion, the above model is used but the evaporation constant is changed to that expressed in Eq. (2.45). Yet, the use of laminar burning rate to estimate the critical droplet diameter under turbulence conditions raises some doubts. Shown in Fig. 6.5 is the illustration of turbulent flame with burning rate,  $u_t$ , and the droplets ahead of the flame front. The turbulent flame thickness is much thicker than laminar flame thickness as a consequence of the flame becoming wrinkled by an ever-increasing range of turbulent wavelengths as it propagates (Abdel-Gayed *et al.*, 1987). For analysing droplet evaporation, one can simply say that the turbulent burning rates and flame brush thickness are the appropriate values to take into account. Yet, both values are difficult to define. In laminar flame, the temperature profile across the reaction zone is well defined (see Section 6.4.1). However, in turbulent flame as in Fig. 6.5, it is difficult to define the temperature profile because of flame wrinkles. Hence, for an individual droplet, it evaporates quicker because of turbulence, but it does not know about the flame until it gets close to the flame. To a first approximation, the flame can be treated as a stretched laminar flamelet as the flame, locally, propagates with laminar burning velocity. Justification for this argument is given by the modified Borghi diagram as described below.

Shown in Fig. 6.6 is a modified Borghi diagram that has been adopted fairly widely in the literature to indicate combustion regimes (Abdel-Gayed *et al.*, 1989). On y-axis, the ratio of  $u'/u_l$  represents the magnitude of turbulence relative to the laminar burning velocity. High values of  $u'/u_l$  will cause a large amount of flame wrinkling leading to increased flame surface area and turbulent flame brush thickness. On x-axis, the ratio of  $L/\delta_l$  represents the size of turbulent eddies relative to the laminar flame thickness. This is important since, as discussed below, large eddies will wrinkle the flame surface while eddies that are smaller than the flame thickness will exist within the reaction zone and may alter the local heat and mass diffusion processes. The regime at the bottom left, for which the turbulent Reynolds number,  $R_L$  is less than one represents laminar flames. The regime at the bottom right in which  $u'/u_l$  is less than one represents a wrinkled flame. In this regime,

turbulence wrinkles the flame surface but the smallest scales are too slow or contain too little energy to disrupt the flame. In the corrugated flamelets regime, the velocity of turbulent eddies is such that they can cause the flame to fold back on itself to cause reacted gas pockets. In the distributed reaction zone, the chemical lifetime,  $\tau_c$ , is larger than the lifetime of the smallest turbulent eddies,  $\tau_\eta$ . Hence, the flame will not have enough time to burn a small eddy before that eddy breaks up. In the well stirred reactor, where  $\tau_c$  is larger than the largest eddies lifetime,  $\tau_L$ , the reacting mixture is being continuously broken up by the fast but short lived eddies. Shown by the symbols in Fig. 6.6 are data from the present author. They were calculated from the experimental data in Section 5.3. They clearly show that the data reported in this thesis lie within the wrinkled laminar and corrugated regimes. Hence, locally, these flames approximate that of a stretched laminar flamelet. This approximation is consistent with Bradley (1992) who shows that a turbulent flame in an engine can often be regarded as an array of laminar flamelets with no turbulence structure residing within them.

Shown in Fig. 6.7 is the variation of droplet lifetime with droplet diameter for stoichiometric isooctane-air aerosols at a different value of  $u'$ . It is shown in Fig. 6.7 that there is an increase in a critical droplet diameter below which a droplet is fully evaporated as  $u'$  increases. Clearly this suggests that the rate of droplet evaporation improved due to the turbulence. Since the present work investigates only the effect of droplets up to 10  $\mu\text{m}$  diameter under turbulent condition, this estimation suggests that the droplet is fully evaporated before it reaches the reaction zone and propagates as a gaseous flame. Nevertheless, the results of turbulent flames in Section 5.5 suggest that there was a difference between aerosol and gaseous flames propagation. This is further discussed in Section 6.5.

#### **6.4 Effect of droplets on laminar flames**

In this Section, some of the important aspects of laminar flame propagation in quiescent aerosols are addressed. The effect of droplets during the early stage of propagation is discussed in Section 6.4.1. In the later stage of flame propagation, some of the aerosol flames became cellular in structure and resulted in higher burning rates relative to the equivalent gaseous flame. This enhancement in burning



rates is discussed in Section 6.4.2 and the relationship with flame instabilities is discussed in Section 6.4.3. Finally, the effect of droplets on the determination of unstretched burning velocity is discussed in Section 6.4.4.

#### 6.4.1 Early stage of flame propagation

It is shown in Section 5.2.2 (Figs. 5.2 and 5.3) that the initial growth of flame kernel in aerosol mixtures was different than in gaseous mixtures. This difference was shown to be a function of droplet size and equivalence ratio. Shown in Fig. 6.8 is the variation of flame speed with time for the first 10 ms of flame development for the lean and rich flames represented in Figs. 5.2 and 5.3. Figure 6.8a shows that for lean mixtures, an increase in  $D_{10}$  resulted in an increase in flame speed. However, for the rich mixtures in Fig. 6.8b, the trend is reversed. These results contradict previous arguments by Hayashi and Kumagai (1975, 1976) that droplets can increase burning rate by reducing, towards stoichiometric, the value of  $\phi_g$  of very rich flames. The same argument would result in the flame speed of lean flames being lower than the equivalent gaseous flame which, clearly, is not the case in Fig. 6.8a.

Ballal and Lefebvre (1978) showed that the influence of droplets on initial flame kernel growth can be related to the difference in the minimum ignition energy,  $E_{min}$ . They defined  $E_{min}$  as the amount of energy required to heat a sphere of gas/droplet (whose diameter is equal to the quenching distance) to its adiabatic flame temperature. Figure 6.9 shows the variation of  $E_{min}$  with droplet size for isooctane-air mixtures at 1 atm and  $\phi = 0.65$  (Ballal and Lefebvre, 1978). It demonstrates the strong dependence of  $E_{min}$  on droplet size, where  $E_{min}$  is proportional to the cube of droplet size. Although this illustrates how droplets might affect the early stage propagation in terms of ease of ignition, it does not explain the contradictory trends of Fig. 6.8.

A more convincing explanation, was proposed by Atzler (1999, 2001) and described in Section 2.6.4 in which oscillating flames were explained by droplet inertia. Following ignition of a quiescent aerosol mixture, the spark produces very rapid expansion of the gas in front of the flame. However, droplets have inertia which causes their velocity to lag behind that of the expanding gas. This results, for lean mixtures, in an increase in equivalence ratio at the flame front towards that for maximum flame speed, which is at about  $\phi = 1.1$  for iso-octane (Bradley *et al.*,

1998), as shown in Fig. 6.8a. Similarly, richer mixtures become, local to the flame front, even richer with a corresponding reduction in flame speed, as shown in Fig. 6.8b.

As described in Section 2.6.4 (Fig. 2.14), Atzler *et al.* (2001) predicted the relationship between droplet velocity, local  $\phi$  and the resultant velocities of flame speed, gas velocity and burning velocity near the flame front of an oscillation flame. This prediction was extended from ignition, through flame development and into the oscillations. For the present purposes, only the developing phase of flame development is of interest. Therefore, Fig. 2.14 has been adapted in Fig. 6.10 to show only that regime. Considering a developing flame, initially at time = 0, the spark is initiated which results in a rapid flame expansion as discussed above. A short time later, the flame has grown, but droplets lag behind. This results in an increase in local  $\phi$  as shown by point 1. At a later time (point 2), droplet velocity,  $u_d$ , starts to catch up with the gas velocity,  $u_g$ . This results in a lower  $\phi$  and thus increases  $u_l$ . As  $u_l$  increases, the effect is to increase  $S_n$  and  $u_g$  and therefore affects  $u_d$  as well. Ultimately, (for a non-oscillating flame) it reaches steady state, with no relative slip velocity between droplet and gas phase. The local  $\phi$  and burning velocities then become equal to those of the overall mixture.

Evidence of the effect of droplet inertia on laminar flame propagation can be strengthened by considering the response time of droplets to the gas velocity fluctuation ahead of the flame. Using Stoke's law and the equation of motion, Drain (1980) derived an expression to predict the maximum droplet diameter,  $D$  that will faithfully follow a flow velocity fluctuation of frequency,  $f_u$

$$D = \left( \frac{0.4\mu}{\rho_D f_u} \right)^{1/2} \quad (6.1)$$

where  $\mu$  is the viscosity of gas flow and  $\rho_D$  is the density of the droplet. The  $f_u$  can be related to the time taken to accelerate the cold gas ahead of a flame to the velocity of the burned gas and is given by  $f_u = 2u_l/\delta$  where  $\delta$  is the flame thickness in terms of the velocity profiles, as illustrated schematically in Fig. 6.11. For the present work, data on gas velocity profiles within an isooctane-air mixture at atmospheric conditions were not available. However shown in Fig. 6.12 are typical profiles of gas temperature and velocity in a methane-air flame at 0.16 atm (Bradley *et al.*, 1994). It

shows that the velocity goes from a value of about 0.5 m/s to 3.5 m/s in about 4 mm for this low pressure flame. For the atmospheric pressure flames studied in the present work, this distance is less but unknown. Shown in Fig. 6.13 are profiles of various parameters, including temperature for a methane-air flame at 1 atm and 300 K (Haq, 1998). By assuming the profile of gas velocity is similar to that for temperature as in Fig. 6.12, it suggests that the gas velocity rises, in Fig. 6.13, from rest to its maximum value in about 0.8 mm. Making the final assumption that the profile for methane and isooctane are not too dissimilar, the gas velocity for the present isooctane-air mixtures probably rises in about 0.8 mm. Using the present data for the stoichiometric flame speed yields a frequency of gas velocity of 1.25 kHz. Substitution of this value into Eq. (6.1) gives the maximum droplet diameter that will faithfully follows the gas flow. However, in the ignition stage, due to rapid expansion following the spark, Akindele (1980) showed that the gas velocity is much higher (by up to a factor of 4) than that in steady state propagation. This results in an increase of frequency of gas velocity up to about 5 kHz, and a maximum droplet diameter of only 1.5  $\mu\text{m}$ . Clearly, this value is significantly smaller than the lowest droplet diameter studied in the present work. Hence, this approximate analysis by the present author supports the view that droplet inertia is a plausible cause of the differences in early stage propagation between aerosol flames and gaseous ones.

#### 6.4.2 Later stage of flame propagation

In Section 5.3.2, it is shown, through Figs. 5.10 and 5.11, that during the later stage of flame development, the droplets lead to an increase in the rate of aerosol flame propagation relative to that of gaseous mixtures. Such enhancement was significant, particularly at rich conditions.

Using the results in Fig. 5.11, the droplet induced enhancement in the flame speed was quantified by normalising  $S_{n,48}$  for the aerosol mixture with that for the gaseous mixture,  $S_{n,48g}$  at the same  $\phi_{ov}$ . Figure 6.14 shows the effect of  $\phi_{ov}$  on the relationship between normalised flame speed and droplet size. The solid curves were obtained by drawing a best fit curve through data points at each  $\phi_{ov}$ . From these curves, the dashed curve was deduced which shows, approximately, the variation of maximum flame speed enhancement with droplet size and  $\phi_{ov}$ . It is seen that the

maximum flame speed enhancement occurs at larger droplet diameters as  $\phi_{ov}$  increases. It is probable that small droplets evaporate quickly near the reaction zone (Section 6.3) and, hence, are not significant to burning. As droplet diameter increases, there is a complex interaction between droplet evaporation, instabilities and variations in gaseous phase equivalence ratio which can significantly affect burning.

An attempt to further generalise the data in Fig. 6.14 by normalising the droplet diameter with flame thickness,  $\delta_f$ , as shown in Fig. 6.15 by the solid curves. Also shown in Fig. 6.15 are data for ethanol mixtures (chain dashed curves). Figure 6.15 suggests that for isooctane and ethanol mixtures, generality is obtained, with a maximum enhancement of flame speed at about  $D_{10}/\delta_f = 0.18$ . If this generalisation is proven to be universal, it has interesting consequences for engine combustion. For example, at the high pressures that occur in engines, the flame thickness is less than in the present work, suggesting that enhancement exists only for very small droplets. Further research is required in order to study aerosol flame propagation at high pressure.

### 6.4.3 Instabilities in aerosol flames

An important observation based on the quantification of burning rate enhancement in Section 6.4.2 was a significant enhancement in laminar flame speed compared to the gaseous flame, particularly at fuel rich conditions and optimum droplet size (at which maximum enhancement occurs). It is suggested by the present author and also by several workers (Hayashi *et al.*, 1976; Atzler, 1999; Sulaiman; 2007) that this enhancement can be attributed to the instability of the flame front by droplets which increases the flame surface area and promotes propagation. This Section discusses this instability in aerosol flames and presents a comparison with instabilities in gaseous flames.

As shown in Fig. 5.5, aerosol flames are more unstable than an equivalent gaseous flame. In order to quantify the instability of aerosol and gaseous flames, a critical Peclet number,  $Pe_{cl}$  (defined in Section 2.3.2) was measured at a wide range of  $\phi_{ov}$ . Shown in Fig. 6.16 is the variation of  $Pe_{cl}$  with  $D_{10}$  for isooctane-air aerosol flames at different  $\phi_{ov}$ . It was not possible to determine the values of  $Pe_{cl}$  for most gaseous flames since they were smooth throughout the observable period of

propagation (resulting in large, but unmeasurable in the present work, values of  $Pe_{cl}$ ). However, with a known value of  $Ma_{sr}$  for the gaseous flames, the value of  $Pe_{cl}$  was estimated using Eq. (2.25). It is shown in Fig. 6.16 that the measured  $Pe_{cl}$  is an inverse function of  $D_{10}$ , with the gaseous flame ( $D_{10} = 0$ ) showing the highest value of  $Pe_{cl}$  at any  $\phi_{ov}$ .

As explained in Section 2.3.2,  $Pe_{cl}$  can be correlated with  $Ma_{sr}$  to demonstrate some generality of the onset of flame instabilities. For this, the correlation of Bradley *et al.* (2009) which plots  $Pe_{cl}$  against  $Ma_{sr}$  has been extended in Fig. 6.17 to include the influence of aerosols in terms of the dimensionless group  $D_{10}/\delta_l$ . The curves for different values of  $D_{10}/\delta_l$  were obtained from experiments at  $D_{10}$  between 5 and 20  $\mu\text{m}$ , pressures between 93 and 125 kPa, and temperatures between 265 and 293 K. It is clearly shown in Fig. 6.17 that the trend in the effect of  $Ma_{sr}$  on  $Pe_{cl}$  is similar to that for gaseous flames, but that the magnitude is smaller. As the ratio of  $D_{10}/\delta_l$  increases, its effect is to reduce the value of  $Pe_{cl}$  which indicates earlier onset of flame instabilities.

Although  $Pe_{cl}$  has been used extensively for quantifying flame instabilities (Bradley *et al.*, 1998; Gu *et al.*, 2000), this dimensionless number is, perhaps, not physically appropriate because onset of instabilities is more directly related to a reduction in flame stretch rather than to flame radius. In a recent work, Bradley *et al.* (2009) proposed the critical Karlovitz stretch factor,  $K_{cl}$  (defined in Section 2.3.2) as a further practical parameter for quantifying the onset of flame instability since it is expressed in terms of the critical stretch rate at the onset of flame instability. Shown in Fig. 6.18 is the variation in  $K_{cl}$  with  $Ma_{sr}$  for iso-octane-air aerosols in terms of dimensionless group  $D_{10}/\delta_l$ . These data were obtained by reprocessing the data in Fig. 6.17 using Eq. (2.26). It is shown in Fig. 6.18 that the trend in the effect of  $Ma_{sr}$  on  $K_{cl}$  is similar to that of gaseous flames, except that the magnitude of  $K_{cl}$  is larger in aerosol than in gaseous flames. As  $Ma_{sr}$  reduces to negative values, the flame stretch regime in which stable flames occur becomes narrower. With the increase in  $D_{10}/\delta_l$  at 0.4 and above, it indicates that the initial flame becomes unstable almost immediately.

Several possible reasons related to droplets in the reaction zone have been proposed by previous workers to explain instabilities in aerosol flames. Hayashi *et al.* (1976) suggested that droplets obstructed the path of the flame, producing a

distortion of the flame front and consequently, flame acceleration. For this reason, Atzler (1999) investigated the effect of non-evaporating hollow glass spheres in a laminar flame of gaseous isooctane-air. With careful experimental preparation, he obtained similar number density and spacing of glass spheres to those of droplets in an aerosol mixture. From observations of flame propagation with and without glass spheres, Atzler (1999) found that the flame front was smooth in both cases, and the glass spheres did not produce any change in the burning rates. Clearly, this suggests that particles in the reaction zone do not cause instability of the flame front.

Another mechanism that might be responsible for the instability of aerosol flames was suggested by Atzler (1999), to be due to the heat loss from the flame and rapid local expansion through droplet evaporation. In an attempt to investigate these effects, Atzler (1999) introduced water droplets using the condensation technique in a gaseous propane-air mixture. A similar premixed flame of gaseous propane-air was used to compare the difference in the flame structure and the burnig rates. Shown in Fig. 6.19 are schlieren images of the resulting flame of gaseous propane-air with and without water droplets at a radius of 60 mm. Both mixtures were ignited centrally at nearly identical conditions which is close to that of the experiments in the present work. It is clearly shown in Fig. 6.19 that there was a well developed cellular structure in a mixture with water droplets as compared to the smooth flame in a mixture without water droplets. Atzler (1999) demonstrated that the corresponding flame speed due to this cellularity increased by about 13 % more than the smooth one. This suggests that the heat loss from the flame due to evaporation of water (or fuel) droplets has a significant role in the development of flame instabilities. Moreover, it was shown theoretically by Greenberg *et al.* (1999), using linear stability analysis, that the effect of heat loss due to droplet evaporation plays a dominant role in the manifestation of instabilities in a spray flame.

The influence of heat loss from the flame due to presence of water droplets can be described in terms of heat and mass diffusion effects embodied in the Lewis number,  $Le$ , which is defined by the ratio of the thermal diffusivity to the mass diffusivity of the reactant. Water droplets near the flame front will absorb the heat as they evaporate. This reduces the thermal diffusion from the reaction zone, but is unlikely to change the mass diffusion. As shown by Joulin and Clavin (1979) that the influence of heat loss is to produce a shift of  $Le$  to a lower value. Hence, the

presence of water droplets is likely to reduce  $Le$ . As described in Section 2.3.2, lower values of  $Le$  (less than unity) result in a greater propensity of the flame to cellularity.

#### 6.4.4 Unstretched burning velocity of isooctane and ethanol aerosols

One of the objectives of the present work was to investigate the fundamental unstretched laminar burning velocity,  $u_l$ , in aerosol mixtures. Iso-octane was used as a primary fuel for the present study and the results for  $u_l$  were presented in Section 5.3.4 for different droplet diameters between 5 and 20  $\mu\text{m}$  and at equivalence ratios between 0.8 and 2.0. In addition, the present study also investigated the burning rates of ethanol aerosols under quiescent conditions, as presented in Section 5.6. For ethanol, the effects of fine droplets, between 5 and 31  $\mu\text{m}$  in diameter were examined at equivalence ratios between 0.7 and 1.2.

It is shown in Figs. 5.14 and 5.36 that the variation of  $u_l$  with  $\phi_{ov}$  for iso-octane and ethanol aerosols were different since ethanol flames are much more sensitive to  $D_{10}$  than iso-octane flames. In order to describe this difference, normalisation of  $u_l$  for the aerosol mixture with that for the gaseous mixture at the same  $\phi_{ov}$  was calculated and plotted as a function of  $D_{10}$ . Figure 6.20 shows these plots for stoichiometric iso-octane and ethanol aerosol mixtures. The symbols in both mixtures represent the average data points from Figs. 5.14 and 5.36 and the curves are best fits through the data points. The small range of  $D_{10}$  in isooctane relative to that of ethanol was due to the lower volatility of the fuel as described in Section 4.7. It is shown in Fig. 6.20 that, at stoichiometric conditions, both mixtures showed a reduction of  $u_l$  as  $D_{10}$  increased. However, the reduction of  $u_l$  in ethanol was higher than that of iso-octane, by about 13 % at  $D_{10} = 12 \mu\text{m}$ .

The probable reason for the different trends in the reduction of  $u_l$  in Fig. 6.20 was due to the difference in the thermodynamics properties of the fuel. To explain this, a simplified model of droplet evaporation, as discussed in Section 6.3, is used to compare the droplet lifetime of isooctane and ethanol aerosols. Shown in Fig. 6.21 is the variation of droplet lifetime,  $\tau_D$  with droplet diameter,  $D_{10}$  for stoichiometric isooctane and ethanol aerosols at 100 kPa and 273 K. It is shown that the variation of  $\tau_D$  with  $D_{10}$  was a strong function of fuel where  $\tau_D$  in ethanol displayed a larger value than that of isooctane at the same  $D_{10}$ . This was caused by two factors. First,

the heat of vaporisation for ethanol was about three times higher than that of isooctane, which makes the droplet temperature rise slower in the case of ethanol and further reduces the rate of evaporation. Second, the heat of combustion for isooctane was nearly twice as high as that of ethanol, which accelerates the heat release rate and enhanced the evaporation rate near the reaction zone. As a result, both factors resulted in a reduction of fuel vapour near the reaction zone due to insufficient droplet evaporation particularly for ethanol aerosols. For a larger droplet ( $D_{10} \geq 30 \mu\text{m}$ ), the reduction of evaporation rate is expected to be greater, as shown by the significant reduction of  $u_t$  in ethanol as compared to the gaseous flames in Fig. 6.20.

## 6.5 Effect of droplets on turbulent flames

This Section discusses a comparison of burning results between aerosols and gaseous mixtures under turbulent condition. In the present work, the investigation of the effect of fuel droplets under turbulent conditions was divided into two stages of flame propagation: early stage and later stage. In the early stage, the flame is characterised by transitions from ignition to spark assisted propagation and then to developing self sustained propagation. These result in high gradients and high flame stretch. In the later stage, near steady state turbulent flame propagation dominates flame development. The early stage of propagation is discussed below and later stage propagation is addressed in Section 6.5.2

### 6.5.1 Early stage propagation

It is demonstrated in Section 5.5.2 that the early stage of turbulent flame propagation was different between aerosol and gaseous mixtures particularly at low  $u'$ . Although such difference was found in the laminar study discussed in Section 6.4.1, the trend in the laminar case was different. Shown in Fig 6.22 are the variations of flame speed with time and  $D_{10}$  for the first 8 to 11 ms of flame development under turbulent conditions of  $u' = 0, 0.5$  and  $1.0$  m/s. For each  $u'$ , the plot of flame speed with time for fuel-lean ( $\phi_{ov} = 0.9$ ) and fuel-rich ( $\phi_{ov} = 1.2$ ) mixtures was given in the left and right side of Fig. 6.22, respectively, to indicate the trend at a wide range of  $\phi_{ov}$ . Under quiescent conditions, as shown in Figs. 6.22a and



6.22b, the droplets cause an increase in the flame speed of lean aerosol mixtures but decrease that of rich ones. A possible reason for this is discussed in Section 6.4.1.

However, at low turbulence of  $u' = 0.5$  m/s, as shown in Figs 6.22c and 6.22d, the rate of early flame development has opposite trends to those for the laminar flames in Figs. 6.22a and 6.22b. They appear to follow the trends expected from consideration of  $\phi_g$  in which flame speed is changed directly in relation to the gaseous phase equivalence ratio. A possible reason for this is due to turbulence induced droplets motion before flame initiation which might dominate over those resulting from the flame, negating the effect of droplet inertia. Evidence for this mechanism is given by estimating the maximum droplet diameter that will faithfully follow the flow as expressed in Eq. (6.1) by Drain (1980). Under turbulence conditions, the frequency,  $f_u$  can be related to the time scale of turbulence flow inside the vessel. At  $u' = 0.5$  m/s, the maximum diameter of isooctane droplet that faithfully follows the flow was three times bigger than the largest droplet size studied under the present turbulent conditions.

The further data at  $u' = 1.0$  m/s in Figs. 6.22e and 6.22f show that the difference in early flame propagation between aerosol and gas mixtures became less significant. This suggests that as turbulence increase, any droplets effect is being diminished due to the additional contribution from externally generated turbulence. This is further discussed in Section 6.5.2.

### 6.5.2 Later stage propagation

In Section 5.5.2, the burning rates of turbulent gaseous and aerosol flames are presented as a function of time and radius at a different  $u'$  throughout flame development. Although the comparison demonstrates some dissimilarity between aerosol and gaseous flame propagation, the difference was not clearly defined since the development of turbulent flame is influenced by the degree of turbulence spectrum (Abdel-Gayed *et al.*, 1987). To make a better comparison between aerosol and gaseous propagation, the burning rate at selected radius was quantified by normalising flame speed for the aerosol with that for the gaseous at the same  $\phi_{ov}$ . Figures 6.23 and 6.24 show the effect of normalised droplet diameter,  $D_{10}/\delta_l$  and  $u'$  on the flame speed normalisation at two different  $\phi_{ov}$ : 1.2 and 0.9, at a flame radius of 40 mm. This radius was the largest at which most flames were observed and also

the integral length scale of turbulence in the vessel (Lawes, 1987). Abdel-Gayed *et al.* (1987) showed that a turbulent flame of 40 mm radius is considered to be 60% fully developed. Further, at this radius, the effects of ignition were probably negligible and the initial droplet velocity lag due to inertia has probably decayed to near zero.

It is shown in Figs. 6.23 and 6.24 that droplets can have contradictory effects on developed flame speed. For initially quiescent conditions, flame speed is enhanced by 10 % as  $D_{10}/\delta_l$  is increased to about 0.22 for  $\phi_{ov} = 1.2$  and by 6 % as  $D_{10}/\delta_l$  is increased to about 0.15 for  $\phi_{ov} = 0.9$ . At low level of turbulence of  $u' = 0.5$  m/s, the trends for the rich and lean mixtures were different. The flame speed of the rich mixture was clearly enhanced as  $D_{10}/\delta_l$  increased, to a maximum value of 30 % at  $D_{10}/\delta_l$  of about 0.22. However, data for the lean mixture, in Fig. 6.24, at this level of turbulence appear confusing, showing an initial reduction in flame speed (enhancement less than unity) before the enhancement increases towards unity at  $D_{10}/\delta_l$  of approximately 0.18. A similar trend of flame speed reduction-enhancement was found in the case of rich mixture, in Fig. 6.23, when  $u' = 1.0$  m/s. Data for the lean mixture at  $u' = 1.0$  m/s displayed insignificant variation of flame enhancement with  $D_{10}/\delta_l$ . At high  $u'$ , as shown in Fig. 6.23, the effect of droplets on the flame propagation becomes, ultimately, insignificant within the range of droplet sizes reported in the present work.

In order to generalise the results in Figs. 6.23 and 6.24, the ratio of rms turbulent velocity to the laminar burning velocity,  $u'/u_l$ , was used to characterise the transition from laminar condition (zero value) to the turbulent condition at a wide range of  $\phi_{ov}$ . Shown in Fig. 6.25 is the effect of  $D_{10}/\delta_l$  on the flame speed normalisation as a function of  $u'/u_l$ . The solid lines represent the results from  $\phi_{ov} = 1.2$  and the chain dashed lines represent the results from  $\phi_{ov} = 0.9$ . For roughly similar values of  $u'/u_l$ , for both  $\phi_{ov}$ , a similar trend of flame speed enhancement due to droplets can be observed. Under laminar conditions ( $u'/u_l = 0$ ), there was a significant increase in a flame speed as  $D_{10}/\delta_l$  increased. This, most likely, was due to increased in flame instability and wrinkling by the droplets as discussed in Section 6.4.3. However, at higher turbulence ( $u'/u_l \geq 4.8$ ), there was no significant enhancement of flame speed due to the droplets. Wrinkling by turbulence probably

dominates over that due to flame instabilities. This was due to the increased turbulent wrinkling coupled with a reduction in cellular instability due to increased flame stretch (Abdel Gayed *et al.*, 1987). Interestingly, it is shown in Fig. 6.25 that the transition from laminar condition ( $u'/u_t = 0$ ), to highly turbulence ( $u'/u_t = 4.8$ ) was rather complicated. Within this range, there appears to be a transition regime, between instabilities dominated, and turbulence dominated regimes. For example, at  $u'/u_t = 1.7$ , this trend suggests that instabilities and turbulence work together, where there was a greater enhancement than for a simple gaseous flame at the same turbulence condition. However, at  $u'/u_t$  between 2.3 and 3.3, the trend suggests that droplets counteract the effects of turbulence which resulted in the reduction of flame speed. This reduction becomes less significant and negligible as  $D_{10}/\delta_l$  increased to about 0.2. To clarify the trend in this transition regime, a cross plot of data in Fig. 6.25 is plotted at a fixed value of  $D_{10}/\delta_l$ . Shown in Fig. 6.26 is a variation of flame speed normalisation with a different ratio of  $u'/u_t$  at  $D_{10}/\delta_l$  of about 0.11. It is shown that the normalised flame speed is fluctuated (increased and then decreased) by approximately 14% from the unity before it became constant when  $u'/u_t$  reached of about 5. One might argue that this transition is likely due to experimental error. However, each of the data represents up to five experiments which suggest that this phenomenon might be real.

Based on the results in Figs. 6.25 and 6.26, it is interesting to note that the effect of droplets on turbulent flame propagation is significant for a smaller value of  $u'/u_t$  up to about 5. As described in Section 2.6.5, some previous works found contradict effects of droplets on turbulent flames. Mizutani and Nakajima (1973a) observed that the addition of kerosene drops into a low turbulence ( $u' = 0.13$  m/s) propane-air flame yielded a higher burning rate than for the propane-air flame alone. However, Sulaiman (2007) demonstrated that the burning rate of turbulent isooctane aerosol with droplets  $4 \mu\text{m}$  was lower than that of gaseous flames at  $u' = 1.0$  m/s. By estimating the experimental conditions in both previous works, their results fall roughly within the transition regime as shown in Fig. 6.25. In the case of Mizutani's work, the ratio of  $u'/u_t$  is about 0.7 while in the case of Sulaiman's works, the ratio of  $u'/u_t$  is about 3.5. This implies that the enhancing effects resulted in Mizutani's work while the reduction effect is found in Sulaiman's work. Nevertheless, both

works did not report any contradictory effects due to droplets, since their conditions were limited to a certain value of  $u'$ . Hence, it is proposed that Fig. 6.25 presents a generalisation of the effect of droplets on turbulent flames and thus could be applied for any mixture conditions.

As a conclusion, an important finding pertaining to the effects of droplets on turbulent flame was a significant enhancement of burning rates which appeared in a low turbulence condition, but became progressively less important as turbulent wrinkling became dominant. Between low and high turbulence, there was a transition regime where turbulent aerosol flames were found to be lower than those of gaseous flames. In the real situation, since all flames start with laminar and time is required for turbulent flame structure to be fully developed, the above phenomena might be important to understand the initial stages of combustion in engines. In some other applications, the present results might be relevant for understanding and quantifying potential hazards posed by releases of two-phase combustible liquid vapour mixtures.

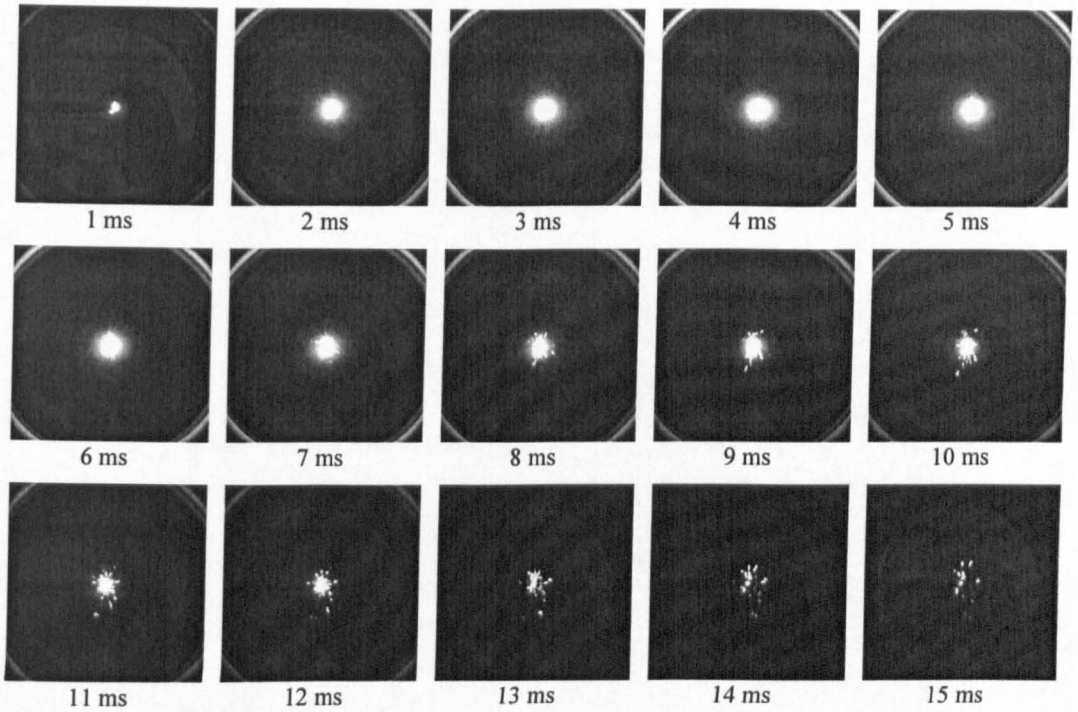


Figure 6.1: Natural light imaging of spark ignition in air using fixed energy ignition unit at 100 kPa and 303 K. Reproduced from Sulaiman (2007).

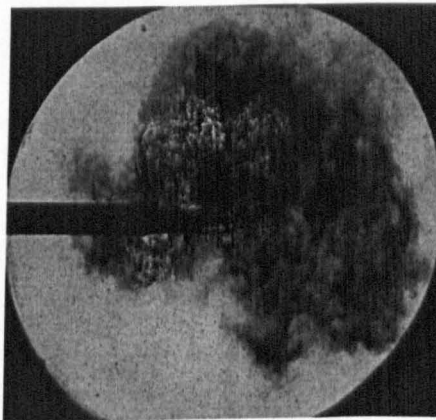


Figure 6.2: Schlieren image of black clouds in turbulent stoichiometric iso-octane aerosol flame at  $u'=4.0$  m/s, ignited by fixed energy ignition unit. Reproduced from Sulaiman (2007).

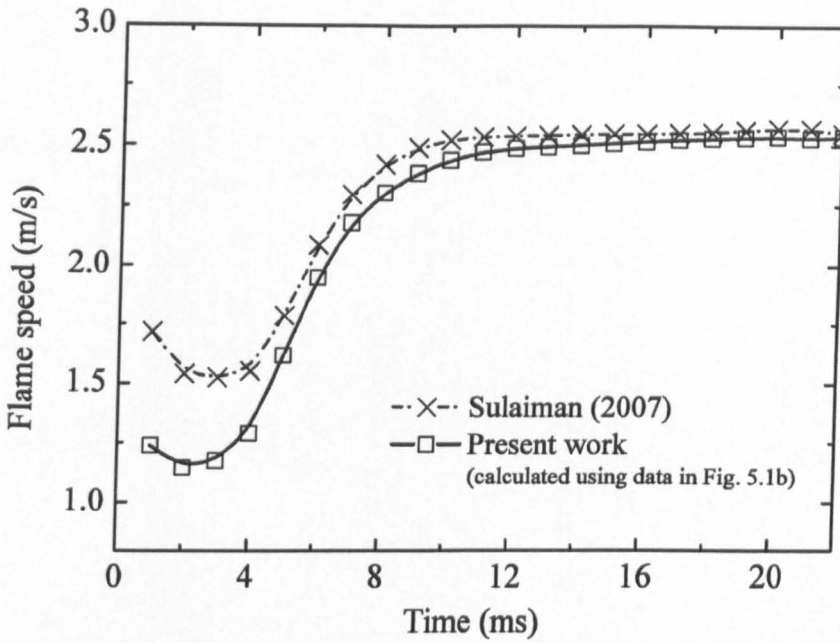


Figure 6.3: Variation of flame speed with time for gaseous isooctane-air mixtures at  $\phi_{ov}=1.2$ , 100 kPa and 303 K.

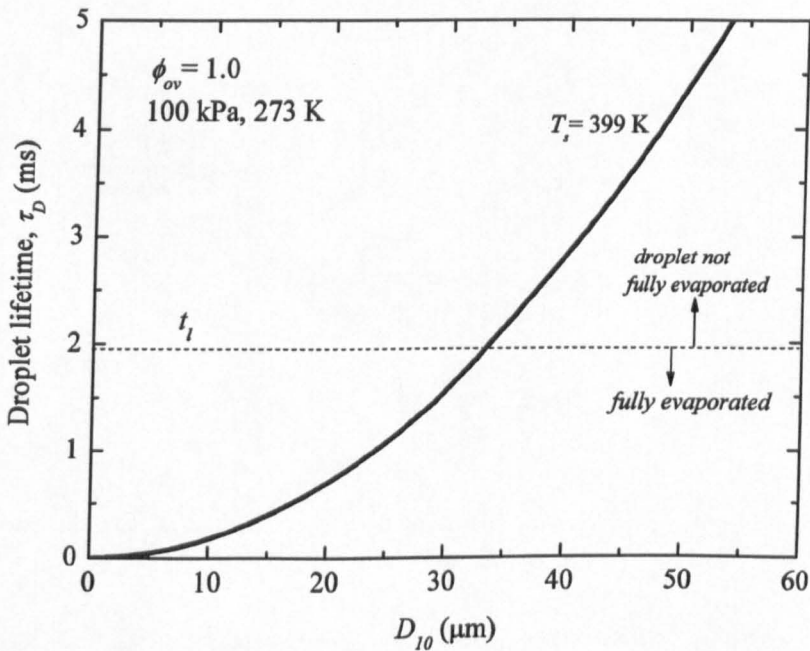


Figure 6.4: Estimation of droplet lifetime using  $D^2$ -law for stoichiometric iso-octane-air aerosol at 100 kPa and 273 K, assuming  $T_\infty = 2275$  K.

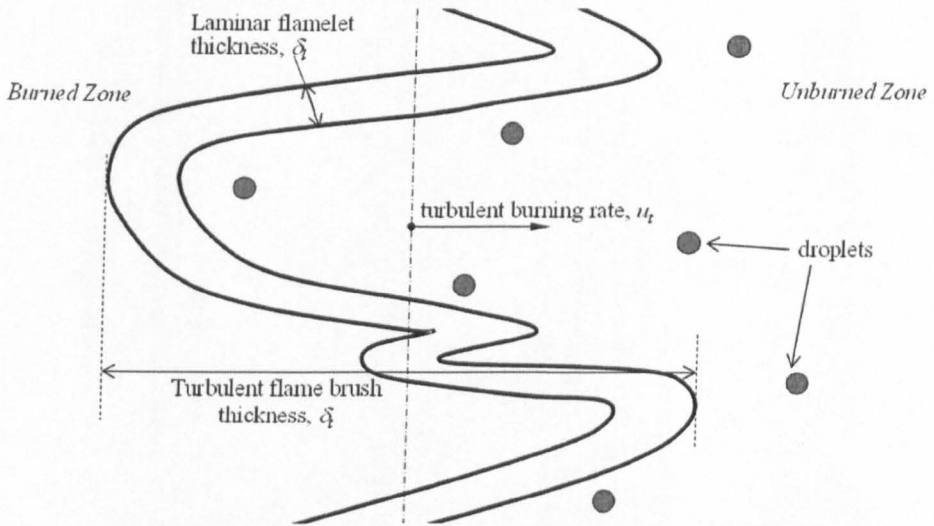


Figure 6.5: Illustration of turbulent flame and region ahead of the flame.

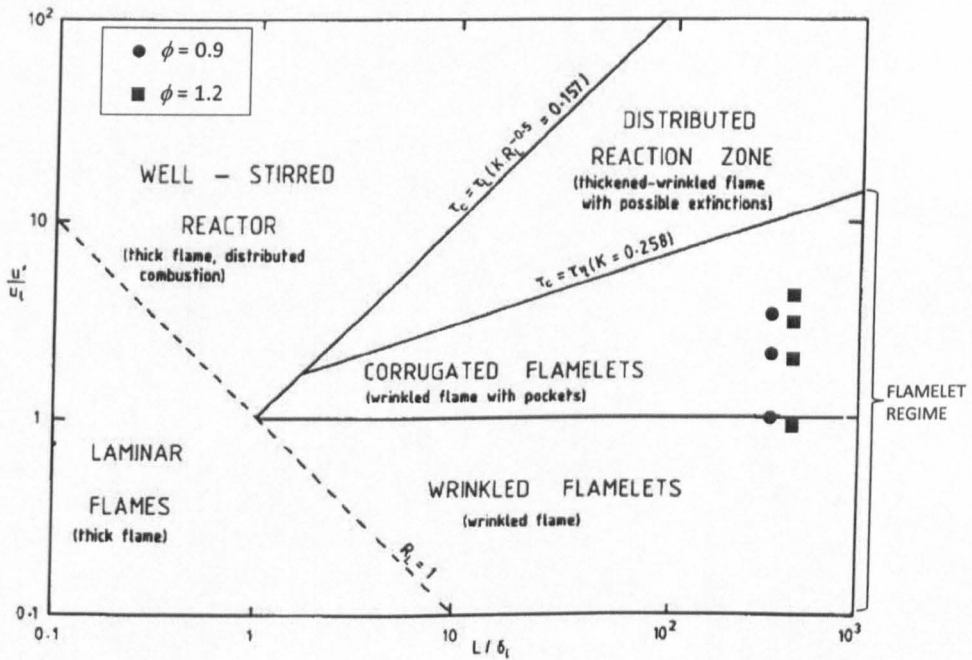


Figure 6.6: A modified Borghi phase diagram showing different regimes in turbulent combustion (Abdel-Gayed *et al.*, 1989).

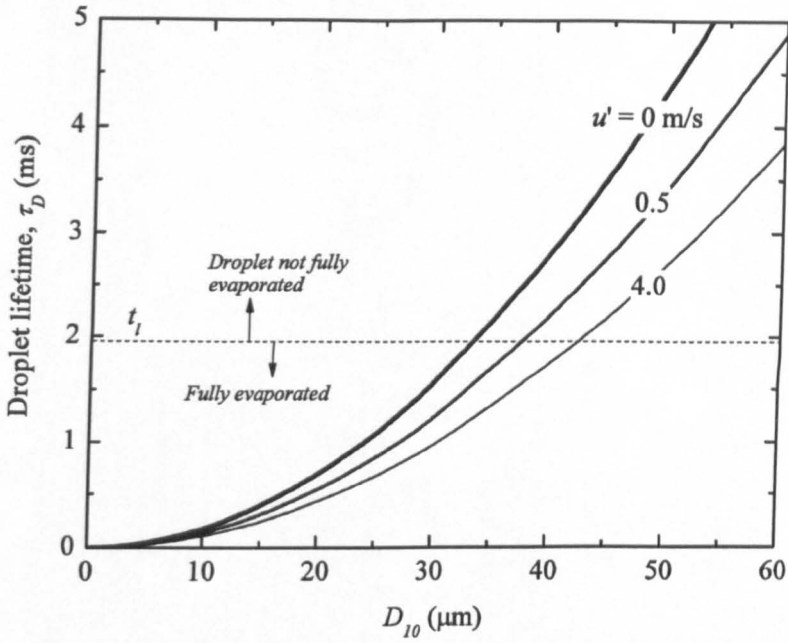


Figure 6.7: Effect of turbulence on estimation of droplet lifetime using  $D^2$ -law for stoichiometric iso-octane-air aerosol at 100 kPa and 273 K, assuming  $T_\infty = 2275$  K.

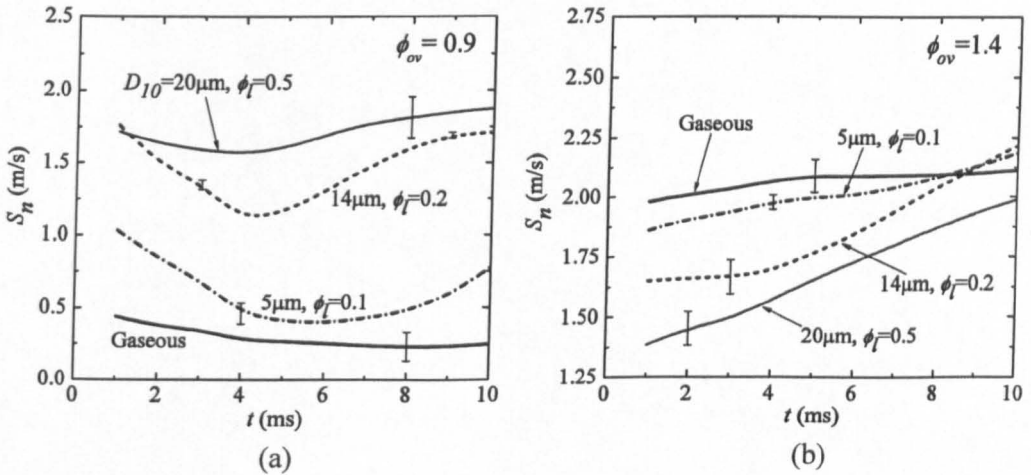


Figure 6.8: Variation of  $S_n$  with time during early stage of flame propagation of iso-octane-air mixtures at, (a) fuel-lean mixture, (b) fuel-rich mixture.



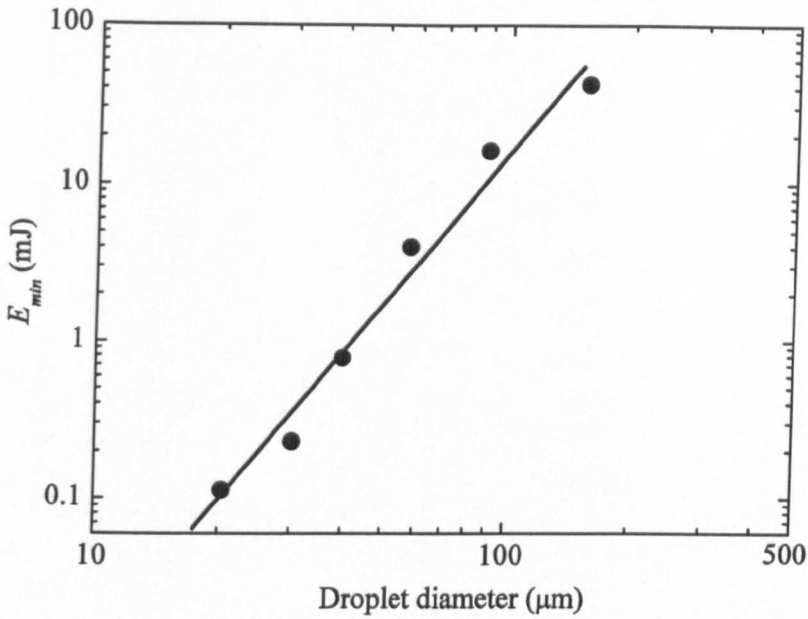


Figure 6.9: Effect of droplet diameter on minimum ignition energy of isooctane sprays. Adapted from Ballal and Lefebvre (1978).

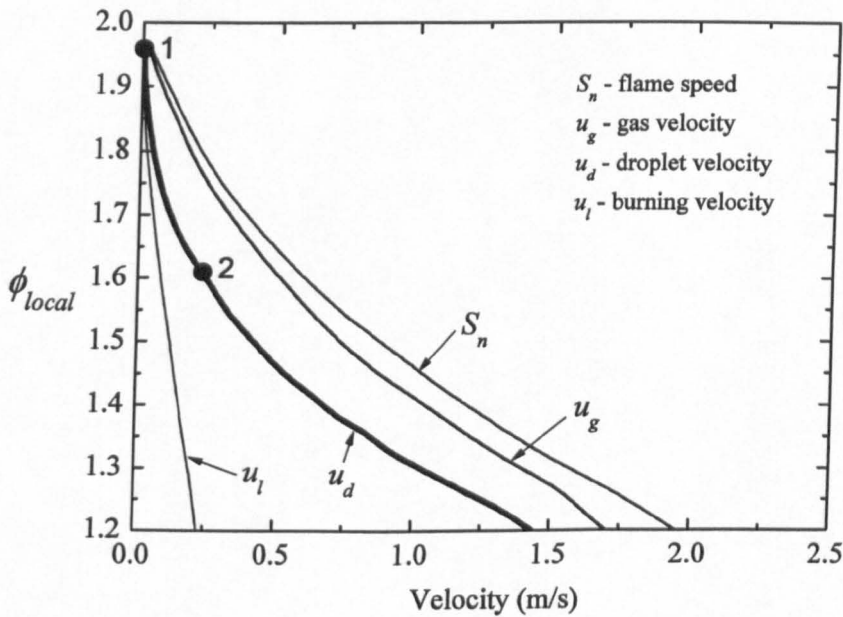


Figure 6.10: Effect of variation of  $u_D$  on local equivalence ratio at reaction zone and resulting values of  $S_n$ ,  $u_g$  and  $u_l$  for aerosol mixture at  $\phi_{ov} = 1.0$ . Adapted from Atzler *et al.* (2001).

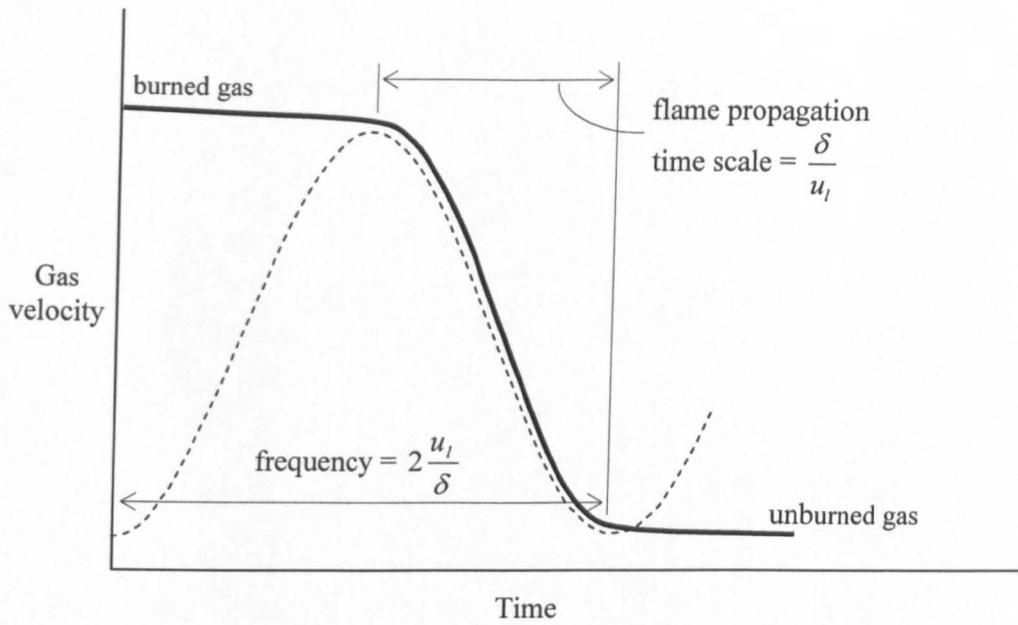


Figure 6.11: Gas velocity at a point in space as an unconfined flame propagation past.

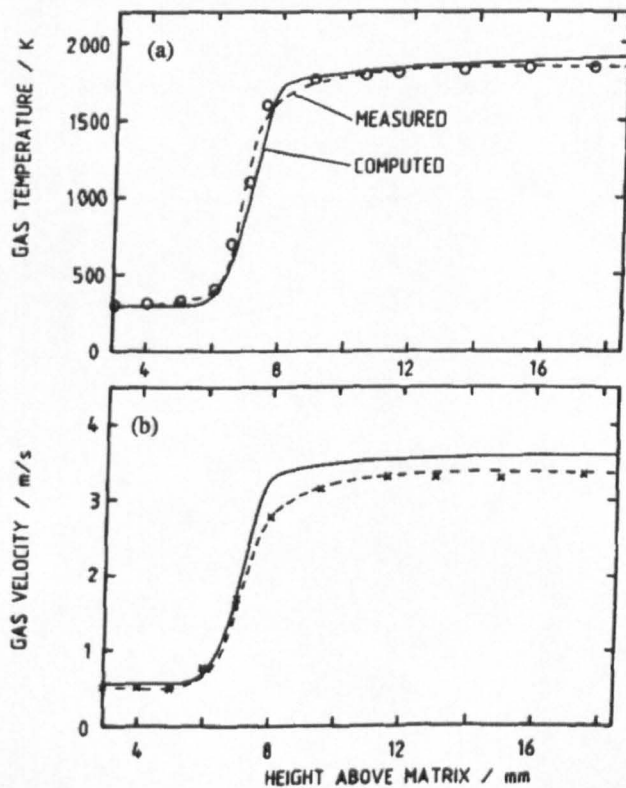


Figure 6.12: Measured and computed gas temperature and velocity for a methane-air flame at 0.16 atm and  $\phi = 1.07$ . Reproduced from Bradley *et al.* (1994).

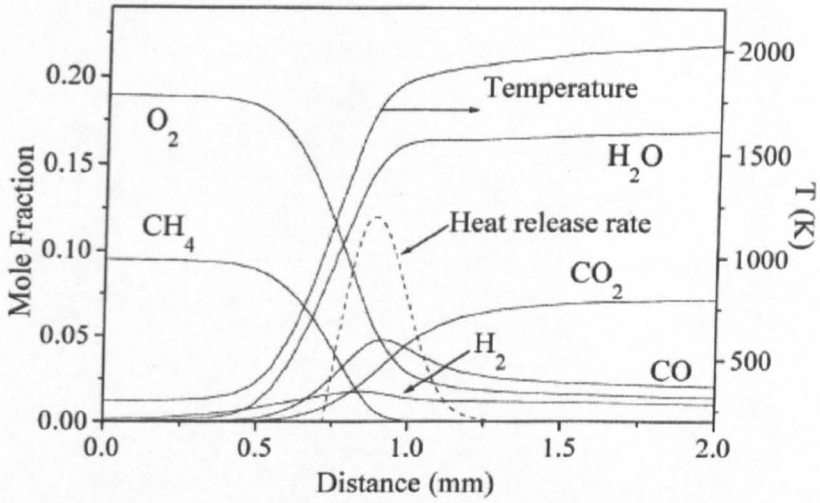


Figure 6.13: Computed composition and temperature profiles for stoichiometric methane-air mixture at 1 atm and 300 K. Reproduced from Haq (1998).

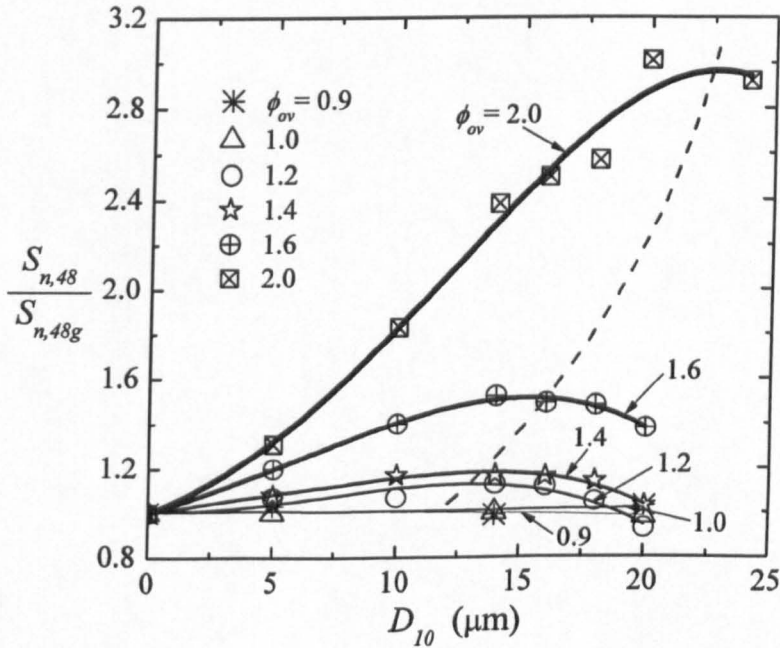


Figure 6.14: Variation of normalised flame speed with  $D_{10}$  and  $\phi_{ov}$  for isoctane-air aerosol mixtures.

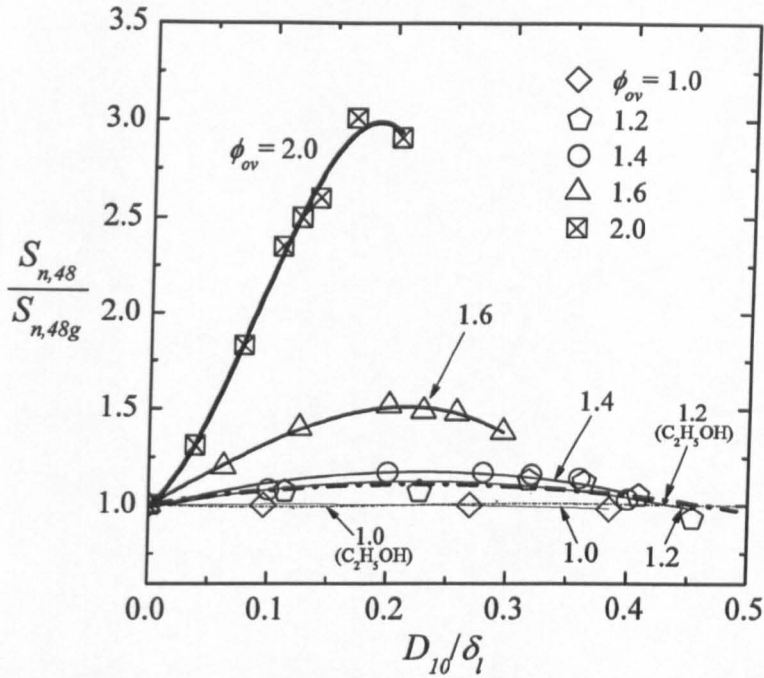


Figure 6.15: Variation of normalised flame speed with normalised droplet diameter and  $\phi_{ov}$ ; solid curves are for iso-octane and chain dashed curves are for ethanol.

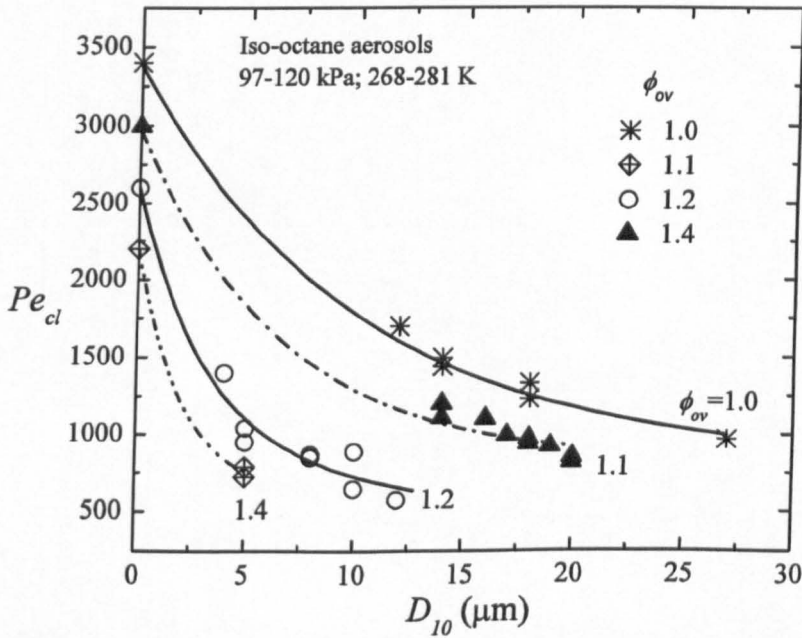


Figure 6.16: Variations of  $Pe_{cl}$  with  $D_{10}$  at different  $\phi_{ov}$  for iso-octane-air aerosol flames.

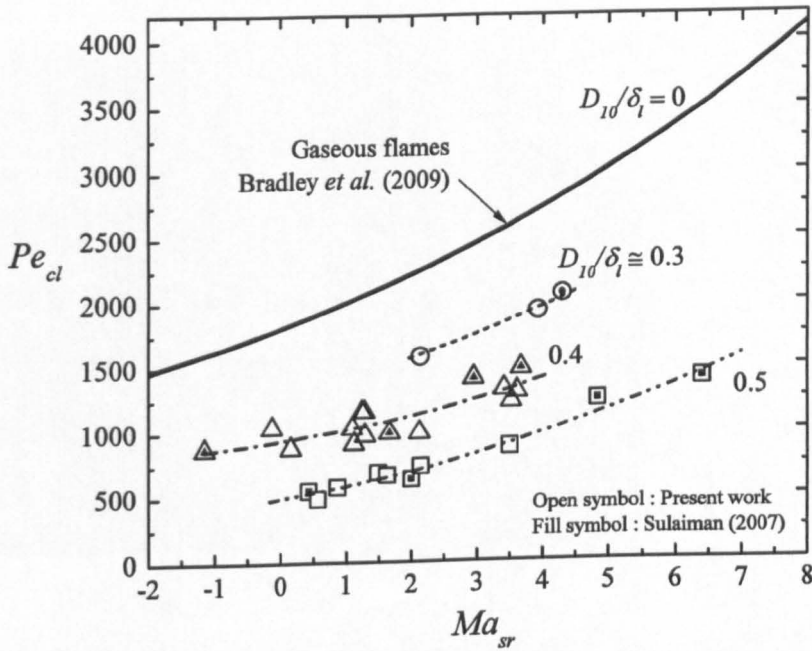


Figure 6.17: Variations of  $Pe_{cl}$  with  $Ma_{sr}$  for iso-octane-air aerosol flames. Also shown, curve fit for gaseous flames (Bradley et al., 2009).

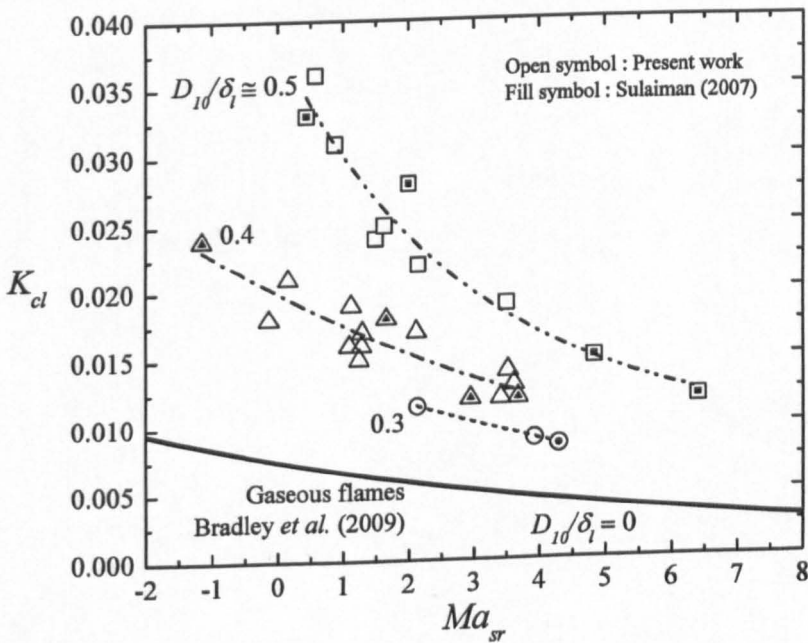


Figure 6.18: Variations of  $K_{cl}$  with  $Ma_{sr}$  for iso-octane-air aerosol flames. Also shown curve fit for gaseous flames (Bradley et al., 2009).

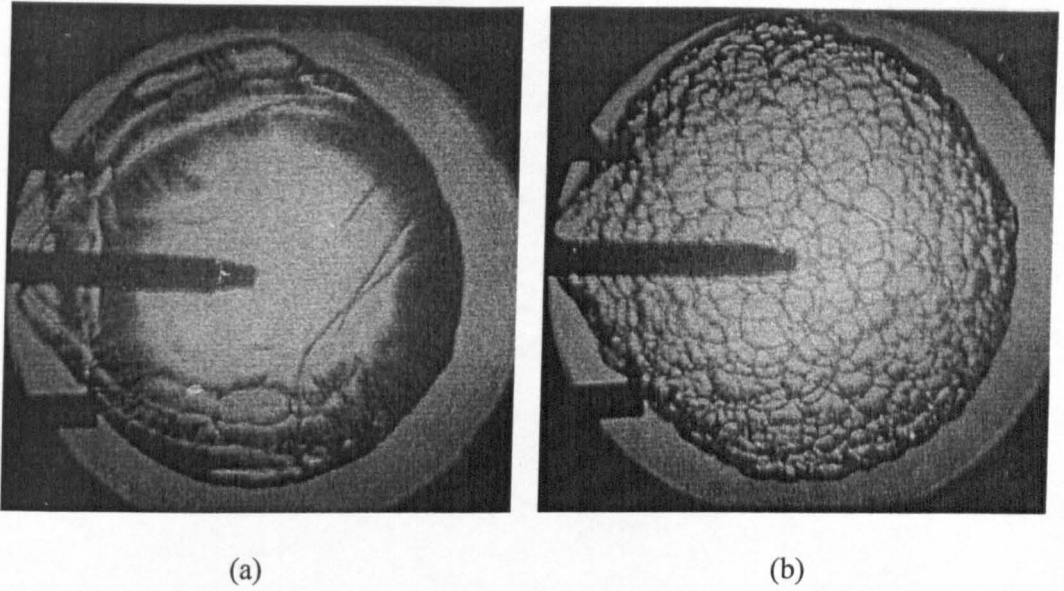


Figure 6.19: Comparison of laminar flame structure of propane-air mixtures at 60 mm radius, (a) without water, (b) with water aerosol, at  $\phi_{ov} = 1.3$ , 105-110 kPa, 260-265 K. Reproduced from Atzler (1999).

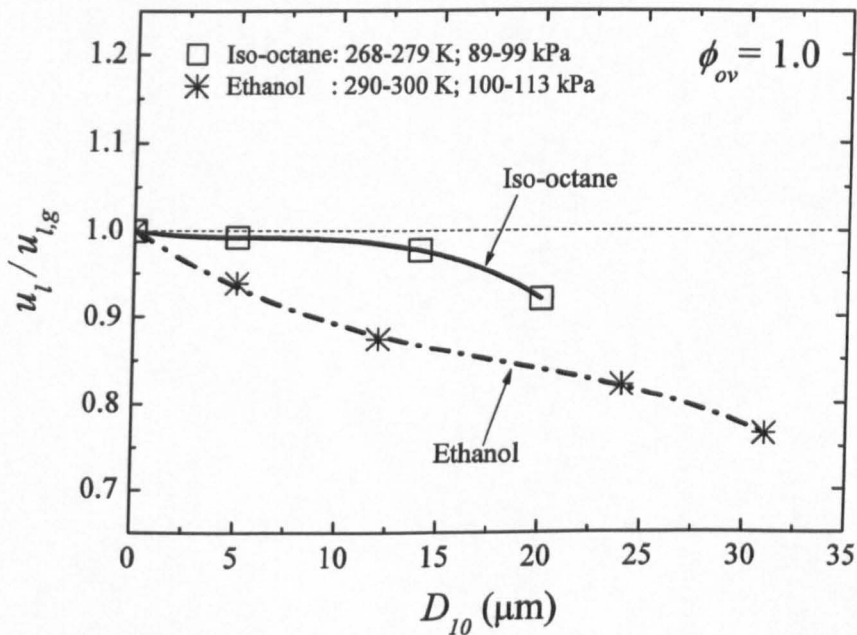


Figure 6.20: Effect of  $D_{10}$  on normalised unstretched burning velocity of iso-octane and ethanol aerosol mixtures at stoichiometric condition.

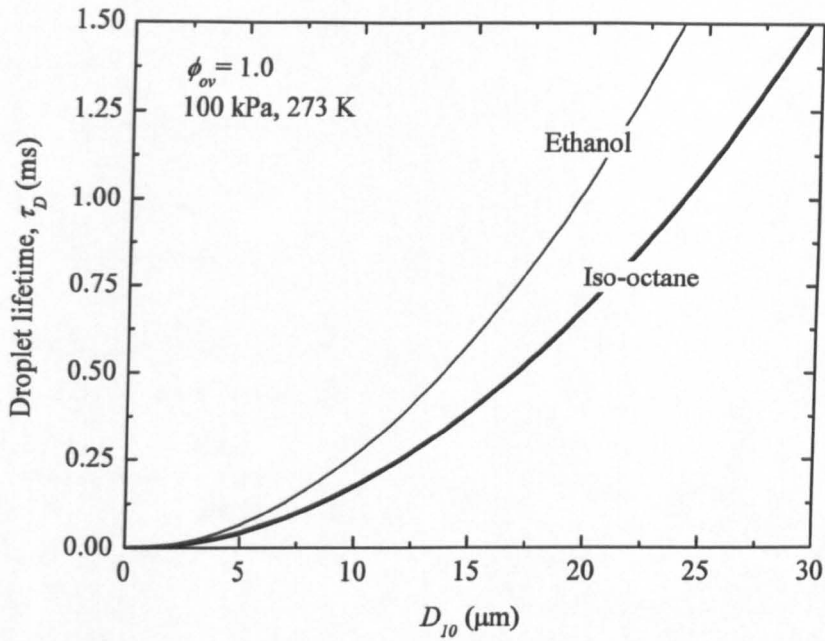


Figure 6.21: Estimation of droplet lifetime using  $d^2$ -law for stoichiometric iso-octane and ethanol aerosols at 100 kPa and 273 K, assuming  $T_\infty = 2275$  K.

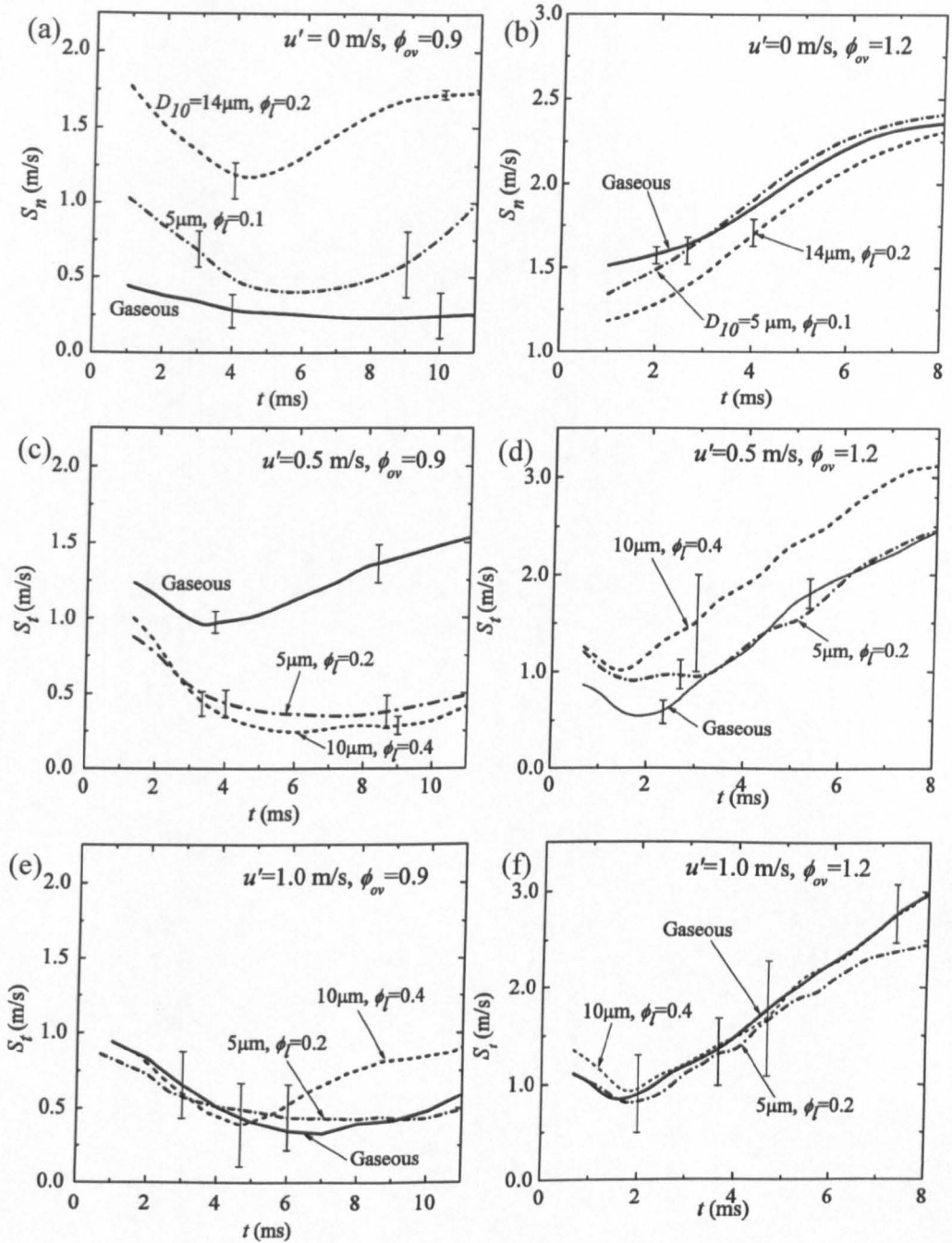


Figure 6.22: Variation of flame speed with time and  $u'$  during early stage of flame propagation of isooctane-air mixtures at  $\phi_{ov} = 0.9$  and 1.2.



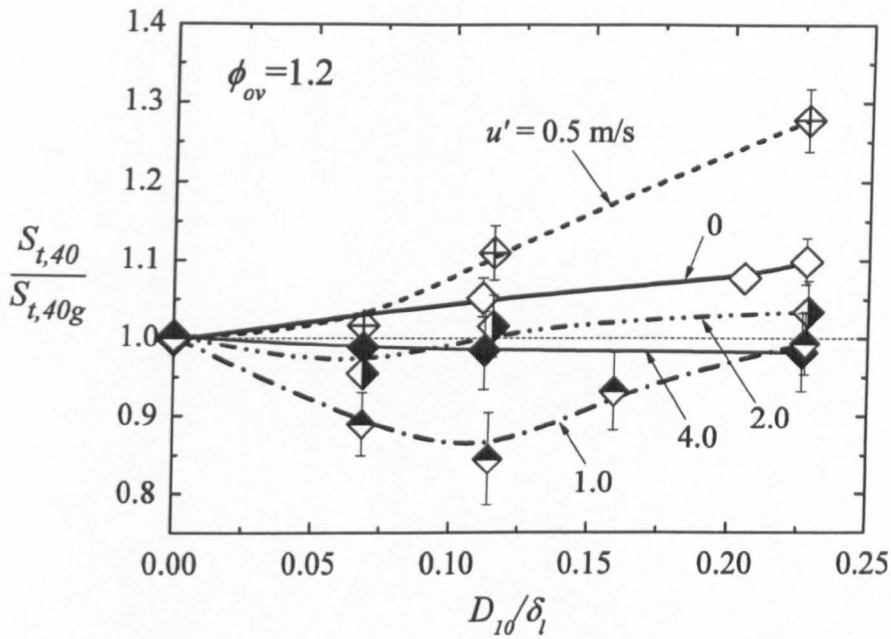


Figure 6.23: Variation of flame speed normalisation at a radius of 40 mm with different normalised droplet diameter and  $u'$  of isoctane-air mixtures at  $\phi_{ov} = 1.2$ .

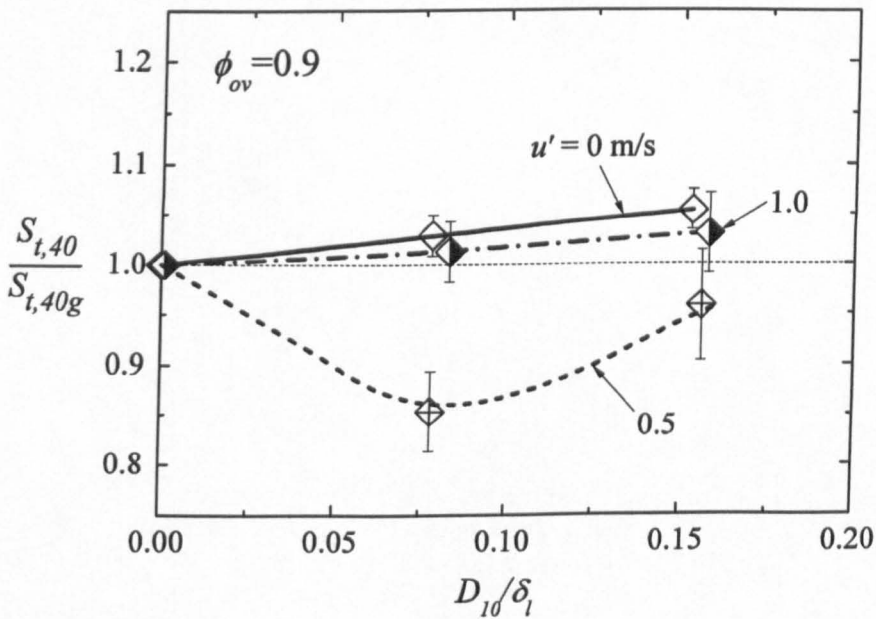


Figure 6.24: Variation of flame speed normalisation at a radius of 40 mm with different normalised droplet diameter and  $u'$  of isoctane-air mixtures at  $\phi_{ov} = 0.9$ .

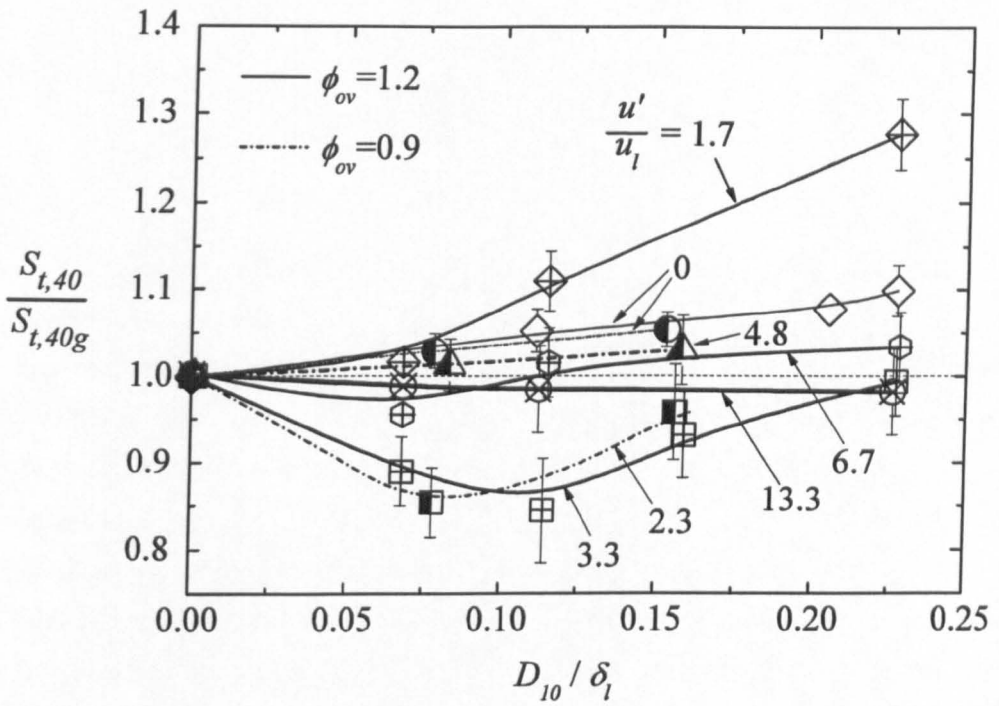


Figure 6.25: Variation of flame speed normalisation with normalised droplet diameter,  $D_{10}/\delta_l$ , as a function of ratio of  $u'/u_l$ .

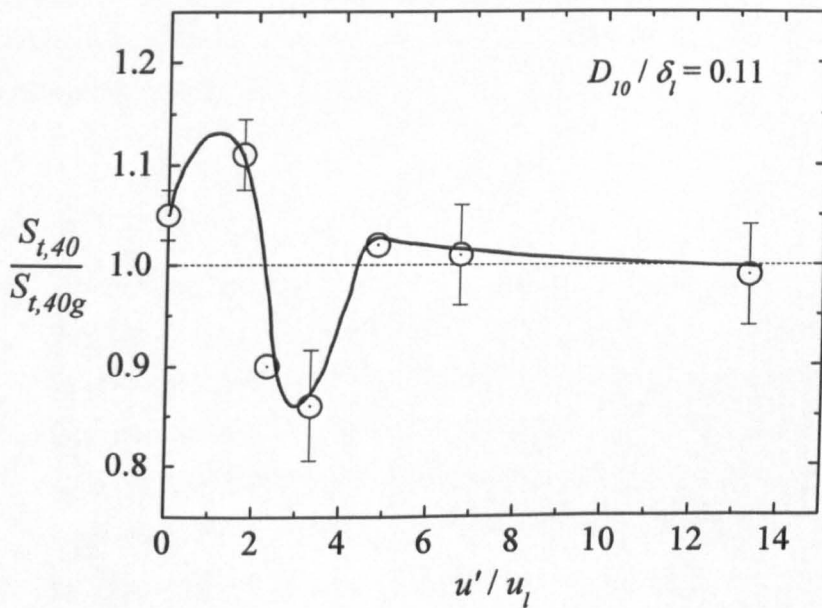


Figure 6.26: Variation of flame speed normalisation at different ratio of  $u'/u_l$  and  $D_{10}/\delta_l = 0.11$ .

## **Chapter 7**

### **Conclusions and Suggestions**

Experimental studies of aerosol combustion under quiescent and turbulence conditions have been conducted to quantify the differences in the flame structure and burning rates between aerosol and gaseous mixtures. Homogeneously distributed and near monodispersed aerosol clouds were generated using a thermodynamic condensation method. Using schlieren photography, spherically expanding flames, following central ignition, were recorded to investigate the flame structure and propagation rate. The effects of fine droplets on flame propagation were investigated at a wide range of equivalence ratios for isooctane and ethanol droplet, vapour and air mixtures. For quiescent mixtures at some conditions, significant enhancement of burning rate was observed, as addressed in Section 5.3.2, and possible reasons for this enhancement were discussed in Section 6.2.2. Similar observations of burning rate enhancement were observed under low turbulence conditions but this became negligible at higher turbulence. A summary of the conclusions obtained from the present work are presented in Section 7.1. This is followed by several suggestions for further work in Section 7.2.

#### **7.1 Conclusions**

1. Aerosols of two different fuels, iso-octane and ethanol, were investigated in this study. Aerosol mixtures were generated by condensation through controlled expansion of a gaseous fuel-air mixture from the combustion vessel into the secondary vessel, as described in Section 3.3. This proved to be highly successful in producing well defined aerosol mixtures with nearly equal size and homogeneously distributed. Conversely, conventional means of generating two phase mixtures, such as through use of fuel injection, produce a highly heterogeneous mixture which is affected by the induced flow field as described in Section 2.4.

2. The characteristics of the aerosol mixtures were calibrated by in-situ measurements, for a wide range of equivalence ratios, without combustion, to obtain temporal variation of pressure, temperature, droplet size and number density with reference to the time from start of expansion. It was shown in Section 4.4 that the aerosol was near monodispersed as indicated by the low standard deviation of droplet diameter and that  $D_{10}$  was a strong function of time.
3. The repeatability of aerosol generation was maintained throughout the work by using clean dried air and using a consistent mixture preparation methodology as described in Section 3.3. This was shown, in Section 4.6, to be very important, because existence of particles in the expanded mixture, either from the atmosphere or due to incomplete evaporation, had a significant influence on the development of  $D_{10}$  and  $N_D$ .
4. The present study investigated spherically expanding flames. Although the experimental methods and their theoretical descriptions are well established and have been used by many researcher for gaseous combustion (as discussed in Section 2.3), aerosol combustion presents additional challenges that include quantification of the effect of droplets on flames, in terms of burning rate and flame front structure. Data on burning properties for gaseous and aerosol mixtures were investigated under near atmospheric conditions. For quiescent mixtures, the effect of fuel droplets up to 31  $\mu\text{m}$  diameter was examined. In turbulent flames, the effect of droplets up to 14  $\mu\text{m}$  was investigated at various values of  $u'$  up to 4.0 m/s.
5. Throughout the entire range of combustion experiments presented in Sections 5.2 and 5.3, the pressure of the mixture at ignition was maintained between 93 and 125 kPa, while the temperature was maintained between 265 and 293 K. This range was unavoidable due to the variation of saturation temperature with fuel partial pressure and to the method of generating droplets by expansion as described in Section 4.7. Nevertheless, based on the empirical correlations in Lawes *et al.* (2006), the differences in pressure have a negligible effect on burning rate, and those in temperature can affect it only by up to 9 %. In the opinion of the present author, the overall trends obtained from the present

work would be unchanged due to slight inconsistencies in pressure and temperature.

6. Based on measurements of unstretched laminar burning velocity of aerosol mixtures (Section 5.3.4), and on heat transfer and droplet evaporation calculations (Section 6.3), the droplets were found to evaporate completely in the preheat zone, particularly for very small droplets, and this results in single phase flame propagation, as indicated by small changes of  $u_l$  of about 8 % between isooctane gaseous and aerosol mixtures. In a case where there was a significant difference in  $u_l$ , as in ethanol aerosol mixtures presented in Section 5.6.2, this was caused by a reduction of fuel vapour in the reaction zone as a result of incomplete evaporation of droplets. Based on this difference, it is concluded that ethanol flames are much more sensitive to droplets than are isooctane flames due to the difference in the thermodynamic properties of the fuel, as discussed in Section 6.4.4.
7. As presented in Section 5.2.1 and discussed in Section 6.2, the use of an ignition system with large energy and long spark duration, as used by Sulaiman (2007), does not produce any significant difference in the measurement of burning rates compared with that of present work. However, such a system might produce fragments of molten metal from the electrodes as a result of high spark kernel temperature and long spark duration. Further, the interaction between the molten metal and the flame front resulted in an unstable flame structure as shown in Fig. 5.1a. Although this is not a real flame instability as described in Section 5.3.3, it may lead to incorrect conclusions on the interpretation of flames with early onset of instabilities. Such difficulties were eliminated in the present work by using an ignition unit which capable in controlling the spark duration and energy as described in Section 3.2.3.2.
8. The initial growth of laminar flame kernel in aerosol mixtures was different from in gaseous mixtures. This difference was found to be a function of droplet size and equivalence ratio, as shown in Section 5.2.2. It is concluded that such a difference was due to the effect of droplet inertia which leads to local enrichment in equivalence ratio. This is supported by the analysis of droplet inertia in Section 6.4.1, in which it is concluded that the droplets used

in the present work are unlikely to faithfully follow the gas flow ahead of the flame.

9. In the later stages of laminar flame propagation, an enhancement in flame speed was observed for aerosol flames as compared to that of gaseous flames as shown in Fig. 5.11. This enhancement was significant at very high  $\phi$  and large  $D_{10}$  (relative to the present work). This enhancement was likely due to the more rapid development of flame instabilities in aerosol than in gaseous flames, which in turn increased the flame surface area and burning rate. As discussed in Section 6.4.3, the mechanism behind this flame instability was probably related to the heat loss from the flame in vaporising the droplets, accompanied by the local rapid expansion of fuel volume through droplet evaporation. Increase in droplet diameter not only intensified the propensity but also triggered an earlier onset of instabilities.
10. Based on the quantification of laminar flame speed in Section 6.4.2, a generalisation of flame speed enhancement in aerosol flames was obtained, as shown in Fig. 6.15. The ratio of  $D_{10}/\delta_l$  has been proven by the present author to be useful in quantifying the effect of droplets on flame propagation. It is shown in Fig. 6.15 that for isooctane and ethanol mixtures, the maximum enhancement of flame speed occurred at about  $D_{10}/\delta_l = 0.18$ .
11. In order to quantify the instabilities in aerosol flames, the dimensionless numbers,  $Pe_{cl}$  and  $K_{cl}$  provide valuable insight and data for a wide range of conditions, as reported in Section 6.4.3. Two relationships were plotted in terms of  $Pe_{cl}$  with  $Ma_{sr}$  and  $K_{cl}$  with  $Ma_{sr}$  to generalise the phenomena of flame instabilities. It is shown in Figs. 6.17 and 6.18 that the ratio of  $D_{10}/\delta_l$  has been proven to be useful in demonstrating the influence of droplets on laminar flame instability.
12. In the early development of turbulent flames, presented in Section 5.5.2, the propagation of aerosol flames was different from the gaseous flames, particularly at low  $u'$ . The aerosol flames appear to follow the trends expected from consideration of  $\phi_g$  in which flame speed directly related to the gaseous phase equivalence ratio. A possible reason for this is due to the turbulence that counteracted the effect of droplet inertia, which is an important mechanism

when in initially quiescent. This is supported by the estimation of maximum droplet diameter that faithfully follows the turbulence flow in Section 6.5.1. It is shown that this is three times bigger than the largest droplet diameter studied under present turbulent conditions. Hence, it is concluded that under turbulent condition, the droplet is likely to follow the gas flow ahead of the flame.

13. In the later stages of turbulent propagation, aerosol flames were found to be more wrinkled than gaseous flames in low turbulence, as shown in Fig. 5.21. This is consistent with the enhancement of turbulent flame speed in aerosol mixtures as discussed in Section 6.5.2. This enhancement was probably due to the flame instability and wrinkling by the droplets which might be dominant as compared to the effect of low turbulence. However, at higher turbulence, the enhancement of flame speed become insignificant within the range of droplet sizes reported in the present work. This concludes that as turbulence increases, any droplet effect is being diminished due to the additional contribution from externally generated turbulence.
14. From the quantification of turbulent flame speed in Section 6.5.2, the present work has produced a generalisation of the effect of droplets on turbulent flames as shown in Fig. 6.25. This generalisation enables identification of whether the aerosol flame is dominated by flame instability or generated turbulence. It is shown that there was a transition range between laminar and high turbulence conditions in which the aerosol flame propagation was influenced between instability and turbulence dominated regimes. As a result, the flame speed enhancement due to droplets under this transition range was rather complex. Further research is required to investigate this transition range.

## 7.2 Suggestions for further work

1. Combustion experiments with larger droplet diameter ( $D_{10} > 30 \mu\text{m}$  for laminar experiments and  $D_{10} > 15 \mu\text{m}$  for turbulent experiments) are required in order to provide further evidence to support conclusion of the present work. This is important because a larger range of droplet diameters exists in conditions such as those in gas turbines (Lefebvre, 1989).

2. The effect of particles on aerosol formation is investigated in Section 4.6 and this emphasizes the importance of maintaining a standard procedure of aerosol mixture preparation to obtain a good consistency of aerosol generation. Yet, the present investigation did not quantify the size and density of the particles involved. Since nucleation is significantly affected by particles (Carey, 1992), it is interesting to extend the present investigation by varying the density and size of particles. This might be beneficial in providing a means of varying and controlling  $N_D$  and  $D_{10}$  of generated aerosol mixtures.
3. A study of the effect of water aerosol in a gaseous propane-air mixture was conducted by Atzler (1999) using the present vessel. It was shown that mixtures containing water aerosol burned faster than in purely gaseous mixtures. However, the amount of water used in Atzler's experiment was not properly quantified. Therefore, a good method of quantifying the amount of water in the present vessel is required. In addition, precise characterisation of water aerosols is essential to further quantify any enhancement on flame propagation due to the water droplets.
4. Experiments at higher pressures are recommended in order to investigate the effect of pressure on aerosol combustion. Although a similar study has been made by Nomura *et al.* (2007) using ethanol aerosols at pressure up to 1000 kPa, this work was limited to droplet diameters of 8.5 and 11  $\mu\text{m}$  and measurements of flame speed at a radius of 10 mm. The maximum safe operating pressure of the current vessel is only 300 kPa at ignition. Therefore the use of high pressure vessel, the Leeds Mk-2 bomb, is recommended as this would allow initial pressures of up to 1400 kPa.
5. The present work did not investigate a minimum ignition energy (defined in Section 6.4.1) to ignite aerosol mixture at a wide range of conditions. This probably offers an interesting extension to the present work, particularly that related to the effect of droplets in the early stage of flame propagation.
6. In order to advance the clarification of the effect of droplets on turbulent flame, the use of optical technique such as laser sheet imaging is recommended to visualise the droplets with and without flame, at different time steps, for different turbulence level and overall equivalence ratio. From



such observations, data on droplet lifetimes or vaporisation times can be deduced and compared with the turbulence time scales and characteristic chemical time scales. Although similar attempts have been made by Sulaiman (2007), but his observations were obscured by the phenomenon of black clouds as described in Section 6.2.

7. As discussed in Section 6.5.2, there was a transition regime between laminar and high turbulence aerosol flames in which the flame propagation was influenced between instability dominated and turbulence dominated regimes. Since the present work did not provide many data (at different  $u$ ) within this transition regime, there is a need for detailed investigation. This may provide additional evidence to assess the mechanism which controls the turbulent aerosol flame propagation within this transition regime.

## References

- Abdel-Gayed R. G., Bradley D. & Lawes M., Turbulent Burning Velocities: A General Correlation in Terms of Straining Rates, Proc. Roy. Soc. London, A414, pp. 389-413, 1987
- Abdel-Gayed R. G., Bradley D., Lung, F.K.K., Combustion Regimes and the Straining of Turbulent Premixed Flames, Combustion and Flame, Vol. 76, pp. 213-218, 1989.
- Abdel-Gayed, R. G., Al-Khishali, K. and Bradley, D., Turbulent Burning Velocities and Flame Straining in Explosions, Proc. Roy. Soc. London, A391, pp. 393-414, 1984.
- Abdel-Gayed, R. G., Bradley, D., Lawes, M., and Lung, F., Premixed Turbulent Burning During Explosion, 21st Symposium (International) on Combustion, The Combustion Institute, pp. 497-504, 1986.
- Akamatsu, F., Nakabe, K., Mizutani, Y., Katsuki, M., and Tabata, T., Structure of Spark-Ignited Spherical Flames Propagating in a Droplet Cloud, in Developments in Laser Techniques and Applications to Fluid Mechanics (ed. R.J. Adrian, *et al.*), Springer-Verlag, Berlin, pp. 212-223, 1996.
- Akindele, O. O., Fundamentals of Spark Ignition With Reference to Engines, PhD Thesis, School of Mechanical Engineering, University of Leeds, 1980.
- Ali, Y., Fundamentals of Turbulent Combustion Related to Gasoline Engines, PhD Thesis, School of Mechanical Engineering, University of Leeds, 1995.
- Annamalai K. and Ryan W., Interactive Processes in Gasification and Combustion, Part I: Liquid Drop Arrays and Clouds, Progress in Energy and Combustion Science, Vol. 18, pp. 221-295, 1992.
- Ashurst W. T., Darrieus-Landau Instability, Growing Cycloids and Expanding Flame Acceleration, Combustion Theory Modelling, pp. 405-428, 1997.
- Atzler, F., Demoulin, F. X., Lawes, M. and Lee, Y., Oscillations in the Flame Speed of Globally Homogeneous Two Phase Mixtures, Proceedings of the 18th International Colloquium on the Dynamics of Explosions and Reactive Systems, Paper No. 83, 2001.
- Atzler, F., Fundamental Studies of Aerosol Combustion, PhD Thesis, School of Mechanical Engineering, University of Leeds, 1999.
- Bachalo, W. D., Rudoff, R. C., Brena de La Rosa, A., Mass Flux Measurements of a

High Number Density Spray System Using the Phase Doppler Particle Analyser, AIAA, 26<sup>th</sup> Aerospace Sciences Meeting, Nevada, p11, 1988.

Ballal, D. R. and Lefebvre, A. H., Flame Propagation in Heterogeneous Mixtures of Fuel Droplets, Fuel Vapor and Air, 18th Symposium (International) on Combustion, The Combustion Institute, pp. 321-328, 1981.

Ballal, D. R. and Lefebvre, A. H., Ignition and Flame Quenching of Quiescent Fuel Mists, Proc. R. Soc. London, A364, pp. 277-294, 1978.

Ballal, D. R., and Lefebvre, A. H., The Influence of Spark Discharge Characteristics on Minimum Ignition Energy in Flowing Gases, Combustion and Flame, Vol. 24, pp. 99-108, 1975.

Bechtold, J. K., and Matalon, M., Hydrodynamic and Diffusion Effects on the Stability of Spherically Expanding Flames, Combustion and Flame, Vol. 67, pp. 77-90, 1987.

Bowen, P.J. and Cameron, L.R.J., Hydrocarbon Aerosol Explosion Hazards: A Review, Process Safety and Environmental Protection, Vol. 77, pp. 22-30, 1999.

Bradley, D., Gaskell, P. H., Gu, X. J. and Sedaghat, A., Premixed Flamelet Modelling: Factors Influencing the Turbulent Heat Release Rate Source Term and the Turbulent Burning Velocity, Combustion and Flame, Vol. 143, pp. 227-245, 2005.

Bradley, D., and Harper, C. M., The Development of Instabilities in Laminar Explosion Flames, Combustion and Flame, Vol. 99, pp. 562-572, 1994

Bradley, D., Chen, Z., El-Sherif, S., Habik, S. E., John, G., Dixon-Lewis, G., Structure of laminar Premixed Carbon Methane Air Flames and Ultrafine Coal Combustion, Combustion and Flame, Vol. 96, pp. 80-96, 1994.

Bradley, D., Gaskell, P. H., and Gu, X. J., Burning Velocities, Markstein Lengths and Flame Quenching for Spherical Methane-Air Flames: A Computational Study, Combustion and Flame, Vol. 104, pp. 176-198, 1996.

Bradley, D., Haq, M. Z., Hicks, R. A., Kitagawa, T., Lawes, M., Sheppard, C. G. W. and Woolley, R., Turbulent Burning Velocity, Burned Gas Distribution, and Associated Flame Surface Definition, Combustion and Flame, Vol. 133, pp. 415-430, 2003.

Bradley, D., Hicks, R. A., Lawes, M., Sheppard, C. G. W., and Woolley, R., The Measurement of Laminar Burning Velocities and Markstein Numbers of Iso-Octane-Air and Iso-Octane-n-Heptane-Air Mixtures at Elevated Temperatures and Pressures in an Explosion Bomb, Combustion and Flame, Vol. 115, pp.126-144, 1998.

- Bradley, D., How Fast Can We Burn, 24<sup>th</sup> International Symposium on Combustion, The Combustion Institute, pp. 247-262, 1992.
- Bradley, D., Instabilities and Flame Speeds in Large-Scale Premixed Gaseous Explosions, Phil. Trans. R. Soc. London, A357, pp. 3567- 3581, 1999.
- Bradley, D., Lau, A.K.C. and Lawes, M., Flame Stretch Rate as a Determinant of Turbulent Burning Velocity, Phil. Trans. R. Soc. London, A338, pp. 359-387, 1992.
- Bradley, D., Lawes, M., Liu, K., Verhelst, S., Woolley, R., Laminar Burning Velocities of Lean Hydrogen-Air Mixtures at pressures up to 1.0 MPa, Combustion and Flame, Vol. 149, pp. 162-172, 2007.
- Bradley, D., Lawes, M., Mansour, M. S., Explosion bomb measurements of Ethanol-Air Laminar Gaseous Flame Characteristics at Pressures up to 1.4 MPa, Combustion and Flame, Vol. 156, pp. 1462-1470, 2009.
- Bradley, D., Sheppard, C. G. W., Woolley, R., Greenhalgh, D. A., and Lockett, R. D., The Development and Structure of Flame Instabilities and Cellularity at Low Markstein Numbers in Explosions, Vol. 122, pp. 195-209, 2000.
- Burgoyne, J. H. and Cohen, L., The Effect of Drop Size on Flame Propagation in Liquid Aerosols, Proc. Roy. Soc. London, A225, pp. 375-392, 1954.
- Cameron, L. R. J. and Bowen, P. J., Novel Cloud Chamber Design for Transition Range Aerosol Combustion Studies, Process Safety and Environmental Protection, Vol. 79, pp. 197-205, 2001.
- Carey, V. P., Liquid-Vapour Phase Change Phenomena : An Introduction to the Thermophysics of Vaporisation and Condensation Processes in Heat Transfer Equipment, Hemisphere Publication, London, 1992.
- Cekalin, E. K., Propagation of Flame in Turbulent Flow of Two-Phase Fuel-air Mixture, 8<sup>th</sup> International Symposium on Combustion, pp. 1125-1129, 1962.
- Cengel Y. A., Boles, M. A., Thermodynamics : An Engineering Approach, 3<sup>rd</sup> Edition, McGraw Hill, Boston, 1998.
- Chan, K.K. and Jou, C.S., An Experimental and Theoretical Investigation of the Transition Phenomena in Fuel Spray Deflagration, Fuel, Vol. 67, pp. 1223-1227, 1988.
- Chiu, H. H. and Liu, T. M., Group Combustion of Liquid Droplets, Combustion Science and Technology, Vol. 17, pp. 127-142, 1977.
- Correa, S. M., and Sichel, M., The Group Combustion of a Spherical Cloud of Monodisperse Fuel Droplets, 19<sup>th</sup> International Symposium on Combustion, pp. 981-

991, 1982.

Drain, L. E., *The Laser Doppler Technique*, Wiley-Interscience Publishing, Chichester, 1980.

El-Banhawy, Y., and Whitelaw, J. H., *Experimental Study of the Interaction Between a Fuel Spray and Surrounding Combustion Air*, (1981), *Combustion and Flame*, Vol. 42, pp. 253-275, 1981.

Faeth, G. M., *Current Status of Droplet and Liquid Combustion*, *Progress in Energy and Combustion Science*, Vol. 3, pp. 191-224, 1977.

Gillespie, L., Lawes, M., Sheppard, C. G. W., and Woolley, R., *Aspects of Laminar and Turbulent Burning Velocity Relevant to S.I. Engines*, SAE Paper No. 2000-01-0192, 2000.

Godsave, G. A. E., *Studies of the Combustion of Drops in a Fuel Spray - The Burning of Single Drops of Fuel*, *Fourth Symposium (International) on Combustion*, The Combustion Institute, pp. 818-830, 1953.

Gökalp, I., Chauveau, C., Durox, D., Lacas, F., Legrand, B., Shafirovich, E., *Preliminary Analysis of a High Pressure Spray and Cloud Combustion Module for the ISS*, *Fifth International Microgravity Workshop*, Cleveland, Ohio, 1999.

Gökalp, I., Chauveau, C., Simon, O., Chesneau, X., *Mass Transfer from Liquid Fuel Droplets in Turbulent Flow*, *Combustion and Flame*, Vol. 89, pp. 286-298, 1992.

Greenberg, J. B., McIntosh, A. C., Brindley, J., *Instability of a Flame Front Propagating Through a Fuel-Rich Droplet-Vapour-Air Cloud*, *Combustion Theory Modelling*, Vol. 3, pp. 567-584, 1999.

Greenberg, J. B., Silverman, I. and Tambour, Y., *On Droplet Enhancement of the Burning Velocity of Laminar Premixed Spray Flames*, *Combustion and Flame*, Vol. 113, pp. 271-273, 1998.

Greenberg, J. B., *Stability Boundaries of Laminar Premixed Polydisperse Spray Flames*, *Atomization and Sprays*, Vol. 12, pp. 123-143, 2002.

Groff, G. E., *The Cellular Nature of Confined Spherical Propane-Air Flames*, *Combustion and Flame*, Vol. 48, pp. 51-62, 1982.

Gu, X. J., Haq, M. Z., Lawes, M., and Woolley, R., *Laminar Burning Velocity and Markstein Lengths of Methane-Air Mixtures*, *Combustion and Flame*, Vol. 121, pp. 41-58, 2000.

Haq, M. Z., *Fundamental Studies of Premixed Combustion*, PhD Thesis, School of Mechanical Engineering, University of Leeds, 1998.

- Harper, C. M., Turbulence and Combustion Instabilities in Engines, PhD Thesis, School of Mechanical Engineering, University of Leeds, 1989.
- Hayashi, S. and Kumagai, S., Flame Propagation in Fuel Droplet-Vapor-Air Mixtures, Proc. Combustion Institute, Vol. 15, pp. 445-452, 1975.
- Hayashi, S. and Kumagai, S., Sakai, T, Propagation Velocity and Structure of Flames in Droplet-Vapor-Air Mixtures, Combustion Science and Technology, Vol. 15, pp. 169-177, 1976.
- Health and Safety Executive (HSE), The Buncefield Incident 11 December 2005 Report, Vol. 1, ISBN 9780717662708, 2008.
- Health and Safety Executive (HSE), The Flixborough Disaster 1974: Report of the Court of Inquiry, London: H.M.S.O., ISBN 0113610750, 1975.
- Heywood, J. B., Internal Combustion Engine Fundamentals, McGraw Hill, 1988.
- Joulin, G., Clavin, P., Linear Stability Analysis of Nonadiabatic Flames: Diffusional-Thermal Model, Combustion and Flame, Vol. 35, pp. 139-153, 1979.
- Kwon, S., Tseng, L. -K., and Faeth, G. M., Laminar Burning Velocities and Transition to Unstable Flames in  $H_2/O_2/N_2$  and  $C_3H_8/O_2/N_2$  Mixtures, Combustion and Flame, Vol. 90, pp. 230-246, 1992.
- Law, C. K., Combustion Physics, Cambridge University Press, New York, 2006.
- Law, C. K., Dynamics of Stretched Flames, 22nd Symposium (International) on Combustion, The Combustion Institute, pp. 1381-1402, 1988.
- Lawes, M., Effects of Turbulence on Combustion in Engines, PhD Thesis, School of Mechanical Engineering, University of Leeds, 1987.
- Lawes, M., Lee, Y., Marquez, N., Comparison of Iso-octane Burning Rates Between Single-phase and Two-phase Combustion for Small Droplets, Combustion and Flame, Vol. 144, pp. 513-525, 2006.
- Lee, J., Yamakawa, M., Isshiki, S., Nishida, K., An Analysis of Droplets and Ambient Air Interaction in a D.I. Gasoline Spray Using LIF-PIV Technique, SAE Paper No. 2002-01-0743, 2002.
- Lefebvre, A. H., Atomization and Sprays, Hemisphere Publishing, New York, 1989.
- Lewis, B., Von Elbe, G., Combustion, Flames and Explosion of Gases, Academic Press, London, 1987.
- Liou, D., and Santavicca, D. A., A Model for Flame Kernel Growth at Aircraft Relight Conditions, 25<sup>th</sup> International Symposium on Combustion, pp. 261-268,

1994.

Lung, F. K. K., Spark Ignition and the Flame Propagation of Early Stages, PhD Thesis, School of Mechanical Engineering, University of Leeds, 1986.

Maly, R., and Vogel, M., Initiation and Propagation of Flame Fronts in Lean CH<sub>4</sub>-Air Mixtures by the Three Modes of the Ignition Spark, 17<sup>th</sup> International Symposium on Combustion, pp. 821-831, 1979.

Mandilas, C., Laminar and Turbulent Burning Characteristics of Hydrocarbon Fuels, PhD Thesis, School of Mechanical. Engineering, University of Leeds, 2008.

Marquez, N., Fundamental Studies of Aerosol Flames, PhD Thesis, School of Mechanical. Engineering, University of Leeds, 2003.

Mizutani, Y., and Nakajima, A., Combustion of Fuel Vapour-Drop-Air Systems: Part I, Open Burner Flames, Combustion and Flame, Vol. 20, pp. 343-350, 1973a.

Mizutani, Y., and Nakajima, A., Combustion of Fuel Vapour-Drop-Air Systems: Part II, Spherical Flames in a Vessel, Combustion and Flame, Vol. 21, pp. 351-357, 1973.*al.*, 1973b.

Mizutani, Y., and Nishimoto, T., Turbulent Flame Velocities in Premixed Sprays : Part I Experimental Study, Combustion Science and Technology, Vol. 6, pp. 1-10, 1972.

Mokhtar, A. S., Fundamental Study of Ignition and Combustion of Two Phase Flows at Gas Turbine Conditions, PhD Thesis, School of Mechanical. Engineering, University of Leeds, 2001.

Moreira, J. R., and Goldemberg, J., The Alcohol Programme, Energy Policy, Vol. 27, pp. 229-245, 1999.

Morley, C., Gaseq Equilibrium Code, <http://www.gaseq.co.uk>, 1994.

Myers, G. D. and Lefebvre, A. H., Flame Propagation in Heterogeneous Mixtures of Fuel Drops and Air, Combustion and Flame, Vol. 66, pp. 193-210, 1986.

Nakabe, K., Mizutani, Y., Hirao, T. and Tanimura, S., Burning Characteristics of Premixed Sprays and Gas-Liquid Coburning Mixtures, Combustion and Flame, Vol. 74, pp. 39-51, 1988.

Nicolas, P., Modelling of Air-Isocetane Aerosol Combustion in Laminar Media, PhD Thesis, School of Mechanical. Engineering, University of Leeds, 2009.

Nomura, H., Kawasumi, I., Ujiie, Y., Sato, J., Effects of Pressure on Flame Propagation in a Premixture Containing Fine Fuel Droplets”, Proceedings of the

Combustion Institute, Vol. 31, pp. 2133-2140, 2007.

Nomura, H., Koyama, M., Miyamoto, H., Ujiie, Y., Sato, J., Kono, M., Yoda, S., Microgravity Experiments of Flame Propagation in Ethanol Droplet-Vapor-Air Mixture, Proceedings of the Combustion Institute, Vol. 28, pp. 999-1005, 2000.

Nunome, Y., Kato, S., Maruta, K., Kobayashi, H., Niioka, T., Flame Propagation of n-Decane Spray in Microgravity, Proceedings of The Combustion Institute, Vol. 29, pp. 2621-2626, 2002.

Nwagwe, I. K., Weller, H. G., Tabor, G. R., Gosman, A. D., Lawes, M., Sheppard, C. G. W., Woolley, R., Measurements and Large Eddy Simulations of Turbulent Premixed Flame Kernel Growth, Proceedings of The Combustion Institute, Vol. 28, pp. 59-65, 2000.

Ofner, B., Phase Doppler Anemometry in: Optical Measurements: Techniques and Applications (F. Mayinger, F. and O. Feldmann, Eds), Springer, Berlin, pp. 135-143, 2001.

Ormsby, M. P., Turbulent Flame Development in a High-Pressure Combustion Vessel, PhD Thesis, School of Mechanical Engineering, University of Leeds, 2005.

Payne, A. L., Crowe, C. T., Plank, D. R., Laser Light Attenuation for Determining Loading Ratio in a Gas-solid Flow, Instrumentation in the Aerospace Industry, Vol 32, pp. 469-477, 1986.

Polymeropoulos, C.E., Flame Propagation in Aerosols of Fuel Droplets, Fuel Vapour and Air", Combustion Science and Technology. Vol. 40, pp. 217-232, 1984.

Rasbash, D.J., Review of Explosion and Fire Hazard of Liquefied Petroleum Gas, Fire Safety Journal, Vol. 2, pp. 223-236, 1979.

Richards, G. A. and Lefebvre, A. H., Turbulent Flame Speeds of Hydrocarbon Fuel Droplets in Air, Combustion and Flame, Vol. 78, pp. 299-307, 1989.

Schick, R. J., An Engineer's Practical Guide to Drop Size, Spraying Systems Co., Bulletin No. 459, 1997.

Shebeko, Y.N., Smolin, I.M., Korolchenko, A.Y., Shevchuk, A.P., Borodkin, A.N., Malkin, V.L., Simonov, O.A., Gurinovich, L.V., Popov S.A., Kolosov, V.A., Smirnov, E.V., Some Aspects of Fire and Explosion Hazards of Large LPG Storage Vessels, Journal of Loss Prevention Process Industry, Vol. 8, pp. 163-168, 1995.

Sivashinsky, G. I., Diffusional-Thermal Theory of Cellular Flames, Combustion Science and Technology, Vol. 15, pp. 137-146, 1977.

Spalding, D. B., The Combustion of Liquid Fuels, 4<sup>th</sup> Symposium (International) on



Combustion, The Combustion Institute, pp. 847-864, 1953.

Sulaiman, S. A., Burning Rates and Instabilities in the Combustion of Droplet and Vapour Mixtures, PhD Thesis, School of Mechanical Engineering, University of Leeds, 2007.

Syzmanski, W. W., and Wagner, P. E., Absolute Aerosol Number Concentration Measurement by Simultaneous Observation of Extinction and Scattered Light, *Journal Aerosol Science*, Vol. 3, pp. 441-451, 1990.

Tian-Yu, Xiang, H. Z., Zhen, W. Y., Some Factors Affecting Altitude Relighting Performance of Turbojet Engine Combustor, American Society of Mechanical Engineers, Gas Turbine Conference and Products Show, Houston, Texas, 9-12 March, 1981.

Turns, S. R., *An Introduction to Combustion: Concepts and Applications*, McGraw-Hill, New York, 2000.

Wilson, C. T. R., Condensation of Water Vapour in the Presence of Dust-free Air and Other Gases, *Proc. R. Soc. London*, Vol. 189, pp. 265-307, 1897.

Wu, C.K., Law, C.K., On The Determination of Laminar Flame Speeds From Stretched Flames, 20<sup>th</sup> International Symposium on Combustion, The Combustion Institute, pp. 1941-1949, 1984.

Yaws, C. L., *Thermodynamic and Physical Property Data*, Gulf Publications Co., Houston, 1992.

Zhao, F., Lai, M. C., Harrington, D. L., Automotive Spark-Ignited Direct-Injection Gasoline Engines, *Progress in Energy and Combustion Science*, Vol. 25, pp. 437-562, 1999.